MICROSTRUCTURAL, MECHANICAL AND ANTI-MICROBIAL CHARACTERIZATION OF ELECTRODEPOSITED AND DC MAGNETRON SPUTTER DEPOSITED COPPER COATINGS ON ALUMINIUM

Thesis

Submitted in partial fulfillment of the requirements for the

degree of

DOCTOR OF PHILOSOPHY

by

ARUN AUGUSTIN

DEPARTMENT OF METALLURGICAL AND MATERIALS

ENGINEERING

NATIONAL INSTITUTE OF TECHNOLOGY KARNATAKA

SURATHKAL, MANGALORE -575025.

JANUARY 2019

DECLARATION

I hereby declare that the Research Thesis entitled **"Microstructural, Mechanical and Anti-microbial Characterization of Electrodeposited and DC Magnetron Sputter Deposited Copper Coatings on Aluminium"** which is being submitted to the National Institute of Technology Karnataka, Surathkal, in partial fulfillment of the requirements for the award of the degree of Doctor of Philosophy in **Metallurgical and Materials Engineering** is a bonafide report of the research work carried out by me. The material contained in this Research Thesis has not been submitted to any University or Institution for the award of any degree.

<div align="right">

ARUN AUGUSTIN

Register Number: MT12F01

Department of Metallurgical and Materials Engineering

National Institute of Technology Karnataka (NITK), Surathkal

</div>

Place : NITK-Surathkal

Date : 19-01-2019

CERTIFICATE

This is to certify that the Research Thesis entitled **"Microstructural, Mechanical and Anti-microbial Characterization of Electrodeposited and DC Magnetron Sputter Deposited Copper Coatings on Aluminium"** submitted by **Arun Augustin (Register Number: MT12F01)** as the record of the research work carried out by his, is accepted as the Research Thesis submission in partial fulfillment of the requirements for the award of degree of Doctor of Philosophy.

Research Guides

Dr. Udaya Bhat K   Dr. K. Rajendra Udupa
Professor   Professor

Chairman – DRPC
Department of Metallurgical and Materials Engineering, NITK

ACKNOWLEGEMENT

Sona, Mr. Manzoor and Mr. Mebin Domnic for always being supportive, encouraging and loving. I also thank Ms. Rashmi Banjan for her support in using scanning electron microscope facility.

I am thankful to all Teaching and Non-Teaching staffs of Department of Metallurgical and Materials Engineering, NITK Surathkal, for the constant encouragement, support and guidance given to me during the entire period of my research work.

I would also like to express my heartfelt gratitude to all my well-wishers for their support and encouragement during my entire research work and I thank all those who directly / indirectly helped me to complete my doctoral thesis.

Last but not the least I am grateful to my Parents, my Wife and my Brother for being a constant support and encouragement during the entire period of my research.

ARUN AUGUSTIN

Abstract

Copper is a well-known antimicrobial metal which could be used in the form of coating on the aluminium touch surfaces, especially, those in hospitals. Experiments were conducted by copper coating on the double zincated aluminium samples by two processes, *viz* : i) Electrodeposition and ii) DC magnetron sputter deposition. Double zincation of the aluminium had been carried out, mainly, to improve the adhesion between the coating and the substrate. The electrodeposition was carried out by using two types of non-cyanide alkaline electrolyte: Bath-I (with ammonium nitrate) and Bath-II (without ammonium nitrate). In the case of electrodeposition, the coating characteristics were changed by varying the current density while in the case of DC magnetron sputter deposition, they were changed by varying the sputtering power. SEM characterization shows the nodular morphology of the deposits in the electrodeposited as well as the DC magnetron sputter deposited coating. TEM study of the coating shows that each nodule is made up of nano-sized crystallites. Moreover, the crystallite size varied with the coating parameters. XRD study of the coating revealed the texture and the microstrain of the coating. Further, the mechanical characteristics like hardness, scratch resistance and adhesion strength of the coatings has been determined. The scratch hardness and microhardness were significantly increased due to the nano-crystallinity, nano-twins and preferred texture of the coating. Adequate adhesion strength of the coating was observed in the cross-hatch cut test as well as in the pull-off adhesion test. Antimicrobial activity of the coating was evaluated against gram negative bacteria (*Escherichia coli*) and gram positive bacteria (methicillin-resistant *Staphylococcus aureus (MRSA)*). These pathogens are most harmful and ever present on the hospital touch surfaces. The colony forming unit (CFU) count of the bacteria on the copper coated samples was found to be less than that on the bulk copper. TEM and SEM analysis showed that *Escherichia coli* cells exposed to copper coating were found to be wrinkled and damaged because cell wall was broken and intracellular fluid was leaked. Whereas, in the case of *MRSA*, small pits were

developed on the copper treated cells. But the morphology of the cell was maintained due to the thick cell wall in the MRSA.

CONTENTS

LIST OF FIGURES

iv

A dm^{-2}, respectively.

point at a) initial stage and b) grown up stage.

x

LIST OF TABLES

Nomenclature

DC	Direct Current
HCAI	Health Care Associated Infection
ECDC	European Centre for Disease Prevention and Control
CFU	Colony Forming Unit
MRSA	Methicillin resistant *Staphylococcus aurous*
SEM	Scanning Electron Microscope
TEM	Transmission Electron Microscope
XRD	X-Ray Diffractometer
LPS	Lipopolysaccharide
FDA	Food and Drug Administration
EPA	Environmental Protection Agency
TEP	Tetra Ethylene Pentamine
PVD	Physical Vapor Deposition
RF	Radio Frequency
J_{ion}	Sputter Deposition Rate
V_{dc}	DC Applied Voltage
Ke_{av}	Kinetic Energy of Argon Ion Flux
T	Substrate Temperature
T_m	Target Temperature
r*	Critical Nucleus
$r*_{Twin}$	Critical Radius of the Twinned Nucleus
γ	Surface Energy/ Interfacial Tension
ΔG	Bulk Free Energy
FCC	Face Centered Cubic Structure
ε	Yield Stress
K_0	Hall Petch Constant
d	Crystallite Size
GPa	Giga Pascal
nm	Nano Meter

Hs	Scratch Hardness
F_N	Normal Force
b	Average Scratch Width
JIS	Japanese Industrial Standards
EDS	Energy Dispersive Spectroscope
A_s	Lattice Parameter of the Substrate
A_f	Lattice Parameter of the Film
SAED	Selected Area (Electron) Diffraction
$\dot{R}$	Equilibrium Deposition Rate
ΔGv	Chemical Free Energy Change Per Unit Volume
$\dot{R}_e$	Equilibrium Desorption Rate from the Film Nucleus
k_B	Bolzmann Constant
Ω	Atomic Volume
U	Density of Deformation Energy
β_{hkl}	Instrumental Broadening
λ	X-ray wave length
θ	Bragg's Angle
s	Elastic Compliances
E	Young's Modulus
m_i	Atomic Mass of the Bombarding (or Incident) Argon Ion
FWHM	Full Width Half Maxima
ICDD	International Centre for Diffraction Data
DNA	Deoxyribonucleic Acid

Chapter 1

INTRODUCTION

1.1 Introduction

Health Care Assisted Infections (HCAI) occurring from the contaminated surfaces, equipment and spreading from the hands of health care workers are becoming a severe problem in the health sector. According to CDC (Center for Disease Control and Prevention) reports, around two million patients are suffering from HCAI and cause $4.5 billion additional expenses yearly (Reed and Kemmerly 2009). To prevent the spread of infections from contaminated environments, global infection control community recommends the use of liquid hand soap, shampoo, and other personal hygiene products. But,the antimicrobial and anti-fungal agents in the above products are harmful to the human bodies. Hence, such products are under scrutiny by the Food and Drug Administration (FDA) of USA. Moreover, the evolutions of antibiotic resistant bacteria are a serious public health problem. In this context, the environmentally friendly antimicrobial metals, like copper, are getting more attention. Literature reports that the touch surfaces made of copper in hospitals are effective in preventing the growth and survival of microbes (Warnes et al. 2012, Marais et al. 2010, Molteni et al. 2010, Grass et al. 2011 and Isa et al. 2017). As a result, the touch surfaces in hospitals (example: door knobs, push plates, faucet handles, bed rails, and poles supporting intravenous fluid suppliers) are replaced with copper (antimicrobial copper Cu+, 2014). But the high cost and difficulty in machining of the copper are the major problems faced during fabrication. Alternatively, use of copper as coating on the aluminium touch surface is a feasible solution. Moreover, the coatings can offer better surface area, reduced grain size, ultra high purity (Lu et al. 2000), preferred texture and better mechanical properties

(Sanders et al. 1997) compared to the bulk copper. Copper on aluminium could be easily deposited using the techniques, like, sputtering and electrodeposition. In addition to that, the properties of the coating could be tuned to the requirement by varying deposition parameters. But, the challenge in engineering systems is to improve adhesive strength of the coatings on the aluminium. Durability of the coating in real time engineering applications is affected by limited value of the adhesive strength between the coated copper and the substrate aluminium. During the deposition of copper directly on aluminium, there is a large drop in the adhesive strength due to the presence of oxide layer on the aluminium (Lunder et al. 2002). This may be due to large lattice mismatching between the ceramic aluminium oxide and the metallic copper. The aluminium oxide can be easily replaced by the zinc by double zincation process (Willigan et al. 2014). Hence in the present work, copper has been deposited on the double zincated aluminium.

In the present work, the microstructural and mechanical characteristics of the electrodeposited as well as DC magnetron sputter deposited coating are explored. The microstructural analysis of the coating is carried out by scanning electron microscope (SEM), transmission electron microscope (TEM), x-ray diffractometer (XRD) and energy dispersive spectroscope (EDS). As a part of mechanical characterization, the coated sample is subjected to scratch hardness test as well as adhesion strength test because scratch resistance and adhesion strength are very essential mechanical properties of the antimicrobial coating. The antimicrobial test of the coating is carried out against gram negative bacteria (*Escherichia .coli)* and gram positive bacteria *(Methicillin-resistant Staphylococcus aureus).* The literature also reported that *Escherichia .coli (E.coli)* and *Methicillin resistant staphylococcus aureus (MRSA)* are the most frequent single pathogens causing HCAI in mixed patient population (Inweregbu et.al 2005).

1.2 Organization of theThesis

The dissertation has been divided into eight chapters. A brief chapter wise description of the thesis is as follows:

Chapter 1 gives an introduction to the research area.

Chapter 2 provides literature review on the significance of the antimicrobial touch surface, structure of microbes (gram negative and gram positive bacteria), copper coatings methods, such as, electrodeposition and sputter deposition techniques and microstructural, mechanical and antimicrobial characterizations of the copper coatings. The research gap identified from the literature survey is discussed in this chapter. The main objectives derived from the research gap and the scope of the planned work to be carried out are presented in this chapter.

Chapter 3 covers the details about the substrate preparation, electrodeposition and sputter deposition, microstructural characterization by using SEM, TEM, XRD, mechanical characterizations, like, hardness test and adhesion test, and antimicrobial characterization of the coating against *Escherichia .coli (E.coli) and* Methicillin resistant *staphylococcus aureus (MRSA)*.

Chapter 4 focuses on the microstructural and mechanical characteristics of the electrodeposited copper coatings. The results are given separately for Bath-I (electrolyte containing ammonium nitrate) and Bath-II (electrolyte doesn't contain ammonium nitrate). The microstructural characterizations include the study of the coating morphology using SEM, analysis of nano-crystallite using TEM, texture and microstrain study of the coating from the XRD profile. The mechanical characterizations include hardness measurement and adhesion strength study. The hardness of the coating is analyzed by scratch hardness test as well as microhardness test. The adhesion test of the coating includes cross-hatch cut test and pull-off adhesion test.

Chapter 5 focuses on the microstructural and mechanical characteristics of the DC magnetron sputter deposited copper coatings. The microstructural characterizations include the study of the coating morphology using SEM, analysis of nano crystallite using TEM, and texture study of the coating from the XRD profile. The mechanical characterizations include hardness measurement and adhesion strength study. The hardness of the coating is analyzed by using scratch hardness test as well as microhardness test. The adhesion test of the coating includes cross-hatch cut test and pull off adhesion test.

Chapter 6 covers the antimicrobial test results of both electrodeposited and sputter deposited coatings. The test results against gram negative bacteria *(E.coli)* and gram positive bacteria (*MRSA*) are presented separately. The results includes colony forming unit (CFU) count study and electron microscopic study (SEM, TEM and EDS) of the microbes.

Chapter 7 describes the detailed analysis and elaborate discussion on the results obtained by different experiments mentioned in chapter 4, 5 and 6. The discussions are presented as microstructural, mechanical and antimicrobial characteristics.

Conclusions and scope for further research: The conclusions obtained from the above chapters and scope for further research is given in this section.

Chapter 2

LITERATURE REVIEW

The review of the literatures related to antimicrobial touch surface, coating methods (electrodeposition and DC magnetron sputter deposition) and the microstructural and mechanical characteristics of the coating have been presented in the current chapter.

2.1 Antimicrobial Touch Surface

In the health care sectors, the patients as well as health care workers frequently comes in physical contact with the surfaces like door handles, bed rails, sink surfaces *etc.* Such surfaces act as the sources for spreading the pathogens from one person to another. These surfaces are generally called as touch surfaces in health care sectors. Based on the frequency of contact, touch surfaces are classified into three types: (i) high touch surfaces, (ii) medium touch surfaces and (iii) low touch surfaces. Bed rails, over-bed tables, IV pumps (a medical device that delivers fluids, such as nutrients and medications, into a patient's body in controlled amounts) and bed surfaces are some examples of high touch surfaces. Tubes, curtains, bedside tables, call bells, chairs and light switches are some examples of medium touch surfaces. Phones, trash cans, sink surfaces, soap dispensers, thermometers, mouse, keyboards, paper towels and dispensers are some of the examples of low touch surfaces (Huslage et al. 2010). Transmission of pathogens led to individual cases and multiple outbreaks of health care acquired infections (HCAI). This occurs in several ways: (i) contamination of the surfaces, (ii) contamination of the equipment and (iii) contamination of hands of health care workers and patients. Hence antimicrobial touch surfaces could be defined as the surfaces which can continuously kill the microbes coming from contaminated environment or inhibit their growth during its service period.

2.1.1 Significance of antimicrobial touch surfaces

Hospital care associated infections (nosocomial infections) are the major threats not only to the patients but also to the hospital workers as well. According to the World Health Organization (2011), health care associated infection (HCAI) is defined as: "An infection occurring in a patient during the process of care in a healthcare facility which was not present or incubating at the time of admission. This includes infections acquired in the hospital but appearing after discharge and also occupational infections among staff". Nosocomial infections can occur within 48 hours of hospital admission, three days of discharge or 30 days after an operation. They affect one in 10 patients admitted to hospitals (Inweregbu et al. 2005).

Based on the type of infections, the health care associated infections could be divided into six types, which are: (i) general health care infections, (ii) surgical site infections, (iii) ventilator associated pneumonia, (iv) blood stream infections, (v) health care associated pneumonia and (vi) urinary tract infections (Allegranzi et al. 2011). According to published data, 7.6% of mixed patient populations in high income countries have HCAI. The European Centre for Disease Prevention and Control (ECDC) estimated that 4.1 million patients are affected by approximately 4.5 million episodes of HCAI every year in Europe. As a result, 16 million extra days of hospital stay, 37 thousand deaths, and annual financial loss up to 7 billion Euros. Whereas in USA, the estimated HCAI incidence rate is 4.5% in 2002 (1.7 Million affected patients). This results in approximately 99000 deaths as well as an economic impact of 6.5 billion US$ per year. In low and middle income countries, data are not available at national level. The data acquired from 173 ICUs from Latin America, Asia, Africa, and Europe shows that crude excess mortality as 18.5%, 23.6%, and 29.3% for care associated urinary tract infections, health care associated bloodstream infections and ventilator associated infections, respectively. Studies showed that increased length of stay associated with HCAI varied between 5 to 29.5 days (World Health Organization, 2011). These details show that HCAI is a serious matter which requires more research attention.

It is estimated that 20% to 40% of HCAI have been attributed to cross infection *via* hands of health care personnel, who have become contaminated from direct contact with the patient or indirectly by touching contaminated environmental surfaces (Weber et al. 2010). These touch surfaces includes doorknobs, push plates, bed rails, faucet handles and poles supporting intravenous fluid supplies. The study carried out by Schmidt et al. (2012) explained over the 43 months of the analysis on samples recovered from 9,522 objects in 1,587 rooms across three study sites as following. The average microbial burden found for the six objects assessed in the clinical environment during the pre-intervention phase was 28 times higher (6,985 CFU/100 cm^2; 3,977 objects sampled) than levels commonly accepted as benign, <250 CFU/100 cm^2. The latter value exceeded for each object sampled. Bed rails were the most heavily burdened of the objects, averaging a concentration of 69 times greater than the level proposed as benign immediately after terminal cleaning or 17,336 CFU/100 cm^2, with a standard error of sampling of ± 2,896 CFU/100 cm^2. Methicillin-resistant *Staphylococcus aureus* (MRSA) and vancomycin-resistant *enterococcu*s (VRE) were frequently recovered from objects. Bed rails had average concentrations of 151 CFU of MRSA/100 cm^2 and of 667 VRE/100 cm^2 and nurse call buttons had averages of 146 CFU of MRSA/100 cm^2 and 16 CFU of VRE/100 cm^2. The average concentrations of gram negative bacteria on bed rails and call buttons were 57 and 109 CFU/100 cm^2, respectively, and the average concentration of gram negative bacteria resident on the monitors and tray tables were 5,914 and 8,572 CFU/100 cm^2, respectively, reflecting a small number of outliers from samples collected from hospital.

2.1.2 Common pathogens in touch surfaces

The common pathogens associated with nosocomial infections are Coagulase negative *Staphylococcus aureus, Pseudomonas aeruginosa, Enterococci species, Enterobacter species, Escherichia coli,* and *Candida albicans.* According to the reports of World Health Organization (2011), out of 13954 isolates collected from France, Germany and Italy, the infections occurred in the intensive care units (ICU) are due to the following

pathogens; *Staphylococcus aureus* (21.8%), *Enterobacteriaceae* (20.2%), *Pseudomonas species* (17.2%), *Enterococci* (10.0%), *Escherichia coli (E. coli)* (9.1%), *Candida species* (8.8%), coagulase negative *staphylococci* (7.0%), and *Acinetobacter species* (5.1%). Gram positive bacteria like methicillin resistant *Staphylococcus aureus* (MRSA) are the common causes of nosocomial infections. Inweregbu et al. (2005) reported that (MRSA) causes up to 60% of nosocomial infections in intensive care units (ICU). *E. coli* (20.1%) and *Staphylococcus aureus* (17.8%) were the most frequent single pathogens causing HCAI in mixed patient populations. Multiple studies strongly suggest that environmental contamination plays an important role in the transmission of methicillin-resistant *Staphylococcus aureus,* vancomycin resistant *Enterococcus species, Norovirus*, *Clostridium difficile*, and *Acinetobacter species*. All these pathogens survive for prolonged periods of time in the environment and the infections are associated with the frequent surface contamination in hospital rooms and health care worker hands (Weber et al. 2010).

2.1.2.1 Structure of *Escherichia coli* and *Staphylococcus aureus*

Escherichia coli and *Staphylococcus aureus* are the typical examples of gram negative and gram positive pathogens existing in hospital touch surfaces, respectively. Hence, these two bacteria are taken as the model for gram negative and gram positive bacteria, in the present study. *Escherichia coli* are rod shaped gram negative bacteria with approximately three micrometer in length and 0.5 micrometer in diameter. The scanning electron micrograph (SEM) of *Escherichia coli* is shown in Figure 2.1(a). *Staphylococcus aureus* are spherical in shape, with approximately one micrometer in diameter. The SEM micrograph of *Staphylococcus aureus* is shown in Figure 2.1(b).
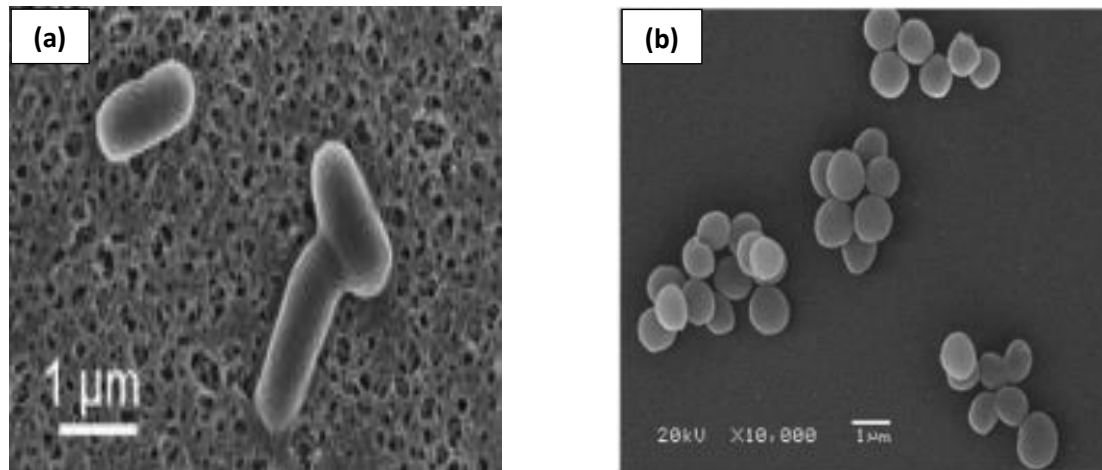
Figure 2.1 SEM micrograph of a) normal *E.coli* characterized by rod shape (Perreault et al. 2015) and b) normal *Staphylococcus aureus* characterized by grape like clusters (Zhang et al. 2013).

The outermost rigid structure is the cell wall which provides the general shape of the cell and functions to protect the cell from osmotic shock (Osmotic shock or osmotic stress is a physiologic dysfunction caused by a sudden change in the solute concentration around a cell, which causes a rapid change in the movement of water across its cell membrane). Cell wall of the bacteria is composed of peptidoglycan. It contains repeating disaccharide units (a polymer of N-acetylglucosamine and N-acetylmuramic acid), with amino acid side chains that are covalently linked to amino acid side chains from disaccharide units forming a stable cross linked structure. The designations 'gram positive' and 'gram negative' are based on fundamental differences in the components of the cell wall and associated structures. Owing to the uniqueness and the importance of the cell wall to bacterial viability, it is the target of many antimicrobial agents.

The gram negative bacteria like '*Escherichia coli*' cell walls are structurally and chemically more complex. The schematic representation of the cell wall structure is given in Figure 2.2 (a). Unique to 'gram negative bacteria' have an outer membrane, external to the cell wall, which acts as a permeability barrier to large molecules (Example; lysozyme) and hydrophobic molecules (Example; some antimicrobials). The space

between the outer membrane and the cell wall is known as periplasmic space, which is about 10 nm in thickness. The outer membrane is an asymmetric bilayer, which consists of an inner leaflet with phospholipids, much like those of the cytoplasmic membrane and an outer leaflet composed primarily of lipopolysaccharide (LPS). LPS is an endotoxin, which is toxic to human and is a potent activator of the immune response. So most of the gram negative bacterium are pathogenic. The LPS is responsible for many of the features of infections by gram negative bacteria including inflammation, fever, and shock. LPS is composed of three parts:

(a) Lipid A: It consists of a disaccharide backbone with attached fatty acids. It is an integral component of the outer membrane and is responsible for the endotoxin activity.

(b) Core polysaccharide: It is a branched polysaccharide of 9 – 12 sugars.

(c) The O-antigen portion: It consists of 50 – 100 repeating saccharide units, which is attached to the core polysaccharide and extends away from the bacterial surface. The O-antigen composition and structure can vary within a bacterial species and is often used to distinguish specific serotypes (Example; O157, strains of enterohemorrhagic *Escherichia coli*) (Schwechheimer and Kuehn 2015).

Whereas, in Gram positive bacteria, like, *Staphylococcus aureus* have a thick cell wall which is 90% peptidoglycan, with extensive cross-linking. The schematic representation of the cell wall is given in Figure 2.2(b). Teichoic acid and lipoteichoic acid present in the cell wall of gram positive bacteria are polymers of glycerol or ribitol phosphodiesters that contribute to the structure of the gram positive cell wall. The lipoteichoic acid present in the cell wall contains a fatty acid that anchors the cell wall to the cytoplasmic membrane. Additional cell wall associated proteins and polysaccharides may serve as antigenic determinants. But gram negative bacteria have thinner cell wall and do not contain teichoic or lipoteichioc acid.

(a)

LPS

Outer membrane

Periplasmic space

Plasma membrane

phospholipid   peptidoglycan

(b)

peptidoglycan

Lipoteichoic acid

Teichoic acid
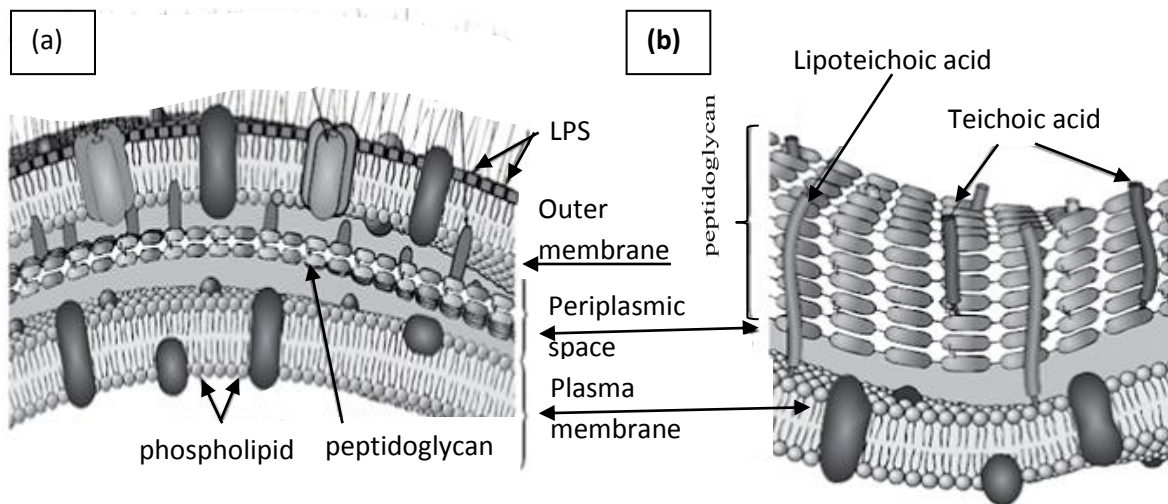
Figure 2.2 Schematic representation of the cell wall structure of a) gram negative and b) gram positive bacteria, respectively.

2.1.3 Antimicrobial metals

Metals have been used for their antimicrobial properties for thousands of years. For example, vessels made of copper and silver have been used for water disinfection and food preservation, since the time of the Persian kings. This practice was later adopted by the Phoenicians, Greeks, Romans and Egyptians. Settlers of North America dropped silver coins into transport containers to preserve water, wine, milk and vinegar, and a similar strategy was used by Japanese soldiers during Second World War to prevent the spread of dysentery (Lemire et al. 2013). Soft metals are functionally defined by their polarizability, which enables them to associate tightly with sulfhydryl groups. Broadly speaking, mercury(II), silver(I), copper(I), lead(II), cadmium(II), nickel(II), zinc(II), and cobalt(II) have substantial affinities for protein thiols, and they are toxic to bacteria. Toxicity is roughly in proportion to their affinities for sulfur. Use of silver and copper for drinking vessels of the classical period exploited the observation that these metals suppress spoilage. In the 20th century, silver and mercury in particular were applied as antibiotics to prevent or treat a variety of human infections. Today, mercury is still used in different parts of the world as a preservative for vaccines and seeds, silver tips have

11

been developed for catheters to resist biofilms, and both silver and copper coatings have been applied frequently to touched surfaces in hospitals in order to suppress nosocomial disease (Xu and Imlay 2012). The study carried out by Li et al. (2015) showed the excellent antimicrobial property of the copper nano-particle against *Staphylococcus aureus* and *E.coli,* within three hours. Truncated triangular silver nanoplates with {111} lattice plane as the basal plane displayed the strongest biocidal action compared with spherical and rod-shaped nanoparticles and with silver in the form of $AgNO_3$. It is proposed that nanoscale size and the presence of {111} plane combine to promote this biocidal property (Pal et al. 2007). In addition to pure metals, metal oxides and cuprous compounds like Cu_2S, CuI and CuCl have high levels of biocidal efficiency. But compared to cupric compounds, cuprous compounds are showing higher antimicrobial activity (Sunada et al. 2012). Ondok et al. (2010) reported that anatase structure of TiO_2 exhibits strong biocidal activity against *E.coli* .

2.1.3.1 Advantages of copper in antimicrobial touch surface applications

To prevent the infections from contaminated environments, globally practiced approaches are use of liquid hand soaps, shampoos, and other personal hygiene products. 'Triclosan' is used as the antimicrobial and antifungal agents in the above products. Studies have shown that triclosan causes liver fibrosis and cancer in laboratory mice by molecular mechanisms which are expected to be relevant in humans also (Yueh et al. 2014). So triclosan is under scrutiny by the Food and Drug Administration (FDA). Moreover, the evolutions of antibiotic resistant bacteria are the challenge to global infection control community. In this contest, copper is gaining more significance due to its environmental friendliness and continuous killing power for pathogens (Yasuyuki et al. 2010).

Literatures reports that copper has the multifaceted attacking ability by multiple mechanisms (Borkow and Gabbay 2005). Compared to other antimicrobials, copper can offer antimicrobial activity in 24/7. In addition to it, copper is the only solid metal touch surface approved by the US Environmental Protection Agency (EPA) (Sunada et al.

2012). Antimicrobial efficacy of copper is scientifically proven to be far more effective than silver containing coatings. Moreover copper has the advantages, like, safe to use and never wearing out (antimicrobial copper Cu+, 2014). Copper remains effective even after repeated wet and dry abrasion and recontamination conditions. Natural oxidation does not impair efficacy of copper. Copper has excellent mechanical properties as well as complete recyclability (European Copper Institute, 2012). Hence, as an antimicrobial touch surface, copper is getting more preference.

2.1.3.2 Mechanism of antimicrobial activity of copper

Most of the literatures agree that the primary target of attack of copper is the cell walls of bacteria (Santo et al. 2011, Warnes et al. 2012). This is because bacterial membranes contain polymers with highly electronegative chemical groups that serve as sites of adsorption of metal cations (Lemire et al. 2013). In the case of *E.coli* (gram negative bacteria), the cell damage is clearly observed in electron microscopic study (Li et al. 2015). In *E.coli*, negative charged liposaccharides have strong affinity to the positively charged cations, especially to the divalent cations (Warnes et al. 2012, Bai et al. 2007). So in copper surfaces, the cell wall gets oxidized and metal ions get reduced by redox reaction. Moreover in gram negative stains, bacteria have a very strong reducing environment of cytoplasm (Lemire et al. 2013). As a result dielectric properties of these cellular components get changed with copper treatment in a time and concentration dependent way. The permittivity of the outer membrane increases with the incubation time and the concentration of Cu^{2+}, possibly because polarizability of the outer leaflet of lipopolysaccharides is affected by Cu^{2+}. The conductivity of the periplasmic space decreased with the incubation time and the concentration of Cu^{2+}, possibly due to the damage of peptidoglycan. The decreased permittivity of the inner membrane is attributed to be caused by the disturbance of the lipid bilayer structure produced by Cu^{2+} incubation. The decreased cytoplasmic conductivity may be the consequence of the leakage of K^+ ions from it. The cytoplasmic permittivity decreased with Cu^{2+} treatment probably because of the leakage of its some components. In the case of gram negative

bacteria like *E.coli,* it is difficult to design antimicrobial agents because it has to cross the double membrane structure and periplasmic space (Warnes et al. 2012). This problem can be easily overtaken by disintegrating the cell wall of gram negative microbes by copper attack.

In the case of gram positive bacteria like *Staphylococcus aureus*, cell wall is thicker as compared to gram negative bacteria (Hong and Koo 2005). The cell wall of *Staphylococcus aerous* is made up of thick peptidoglycan layer which contain teichoic acid molecules. This gives negative charge to cell wall and it attracts positive charged cations (Li et al. 2015). Even though, the gram positive bacteria could maintain the cell integrity after copper treatment (Nie et al. 2010). The rapid killing of gram positive bacteria is not by membrane damage, but due to the loss of cell respiration (antimicrobial copper Cu+, 2015). Compared to gram negative cell, depolarization does not occur in the gram positive bacteria during the exposure to copper surface (Keevil 2003). But compared to *E.coli* (gram negative bacteria), *Staphylococcus aureus* (gram positive bacteria) has less resistance to copper (Li et al. 2015, Yousuf et al. 2016).

In addition to the membrane damage by direct attack of the copper ions, lipid peroxidation also causes the cell death (Lemire et al. 2013). In the presence of oxygen, hydroxyl radicles can damage the lipids and protein (Borkow and Gabbay 2005) because hydrogen peroxide is one of the strongest oxidizing agent rapidly destroying microorganism. Hydroxide radicals are generating from Fenton type reactions as given below (Grass et al. 2011).

$$Cu^+ + H_2O_2 = Cu^{2+} + OH^- + \cdot OH \qquad (2.1)$$

Where, $\cdot OH$ is hydroxyl radical

H_2O_2 could be produced from the metabolic reactions of bacteria (Sunada et al. 2012). So, copper can catalyze the radicals that promote membrane lipid peroxidation. This lipid peroxidation is initiated by the direct attack of poly-unsaturated fatty acids in membrane

by free radicals (Cabiscol et al. 2010). Sunada et al. (2012) reported that cuprous compound have more antibacterial and antifungal properties than cupric compounds. Reactive oxygen species is formed by redox reaction as given below

$$Cu^{2+} + o_2^{\cdot-} = Cu^+ + O_2 \tag{2.2}$$

$$Cu^+ + H_2O_2 = Cu^{2+} + OH^- + {}^{\cdot}OH \tag{2.3}$$

$$H_2O_2 + o_2^{\cdot-} = O_2 + OH^- + {}^{\cdot}OH \tag{2.4}$$

Where $o_2^{\cdot-}$ (super oxide) and H_2O_2 are produced by the bacteria during its metabolic reactions. Hence the redox cycling between Cu^{2+} and Cu^+ can catalyse the production of highly reactive hydroxyl radicals (Borkow and Gabbay 2005).

The study carried out by Xu and Imlay (2012) found that copper (I) exerted toxicity by destroying the iron-sulfur clusters of dehydratase family enzymes. These [4Fe-4S] clusters are directly involved in catalysis, as they bind substrate and serve as Lewis acids to promote the dehydration reaction. To do so, the clusters must be openly exposed to solvent, a trait not shared by the more familiar clusters that operate in electron transfer enzymes. A consequence is that copper (I) have access to the sulfur atoms of the cluster, and upon binding them it displaces the catalytic iron atoms. Activity is thereby abolished. Enzymes of this type are involved in key metabolic pathways, and their inactivation can arrest growth. Copper and silver have strong affinity to the sulfur and quickly destroy the solvent exposed iron-sulfur clusters of the aconitase-family dehydratase (Xu and Imlay 2012, Lemire et al. 2013, Macomber and Imlay 2009).

2.2 Copper Coating

The antimicrobial activity of the copper and the way of attack of the copper on the microbes are described in the previous sections. But the usage of the bulk copper has many disadvantages, like, wastage of material, difficulty of machining for complicated

shape, increased costs and more weight. The coating of the copper on the aluminium substrate could be taken as a feasible solution for the above problems. Moreover the microstructure of the coating could be tuned by controlling coating parameters. By adjusting the microstructure of the coating, the mechanical properties as well as morphological features of the coating could be tuned. The copper coating on the aluminium could be carried out mainly by the following methods

i) Electrodeposition

ii) Sputtering

iii) Electroless deposition

iv) Chemical vapor deposition

v) Electron beam deposition

Since electrodeposition and DC magnetron sputter deposition are used in the present work, detailed explanation on these two methods are given below.

2.2.1 Electodeposition

Electrodeposition is one of the most common methods of thin film coating in which deposition of the metallic ions on the cathode from the electrolyte using electric energy (Mattox 1998). Electroplating was first introduced by an Italian chemist, Brugnetell in 1805 (Tay et al. 2014). Electrodeposition has been recognized as the most technologically feasible and economically superior technique for production of the nanocrystalllie coatings with low residual porosity. Compared to other methods, the advantages of electrodeposition are: (a) low cost and industrial applicability, (b) ease of control, as the electrodeposition parameters could be easily tailored to meet the required crystal size, microstructure and chemistry of the products, (c) versatility, as the process could produce a wide variety of pore free coatings, (d) high production rates and (e) deposition could be

done on complex shaped substrates (Bharucha and Janjua 1973 and Rashidi and Amadeh 2008).

Copper could be deposited from two main types of plating solutions: (i) alkaline cyanide copper and (ii) acid sulfate copper. The alkaline cyanide bath is commonly used for the electronic applications while the acid copper bath is primarily used for decorative applications. Despite waste disposal problems, cyanide bath continues to be used owing to its superior throwing power. However, the use of cyanide salts in copper plating electrolytes has become environmentally disfavored because of ecological considerations. Accordingly, a variety of non-cyanide electrolytes for copper plating have been proposed for the replacements of the well-known and conventional commercially employed cyanide counterparts. Because of the environmental issues, non-cyanide alkaline copper plating solutions have found increasing popularity since the mid-1980s. The use of non-cyanide bath eliminates the inherent dangers of the cyanide in the production line, including: a) catastrophic accidental acidification of cyanide and b) harmful chemicals used to treat cyanide and the dangers of cyanide if a fire occurs. Therefore, it reduces the waste treatment costs for destroying the cyanide along with fire and liability insurance risks. Besides, this bath has higher throwing power (uniform deposit thickness) and smaller grained deposit than acidic and cyanide copper solutions (Hamid and Aal 2009). Moreover, the acidic plating bath has a disadvantage that, presence of hydrogen at the copper aluminium interface. This affects the adhesion strength of the coating (Bharucha and Janjua 1973), whereas, for alkaline bath, hydrogen evolution is absent (Sallee et al. 1994). In addition to the toxicity, cyanide bath have the disadvantage of photo resistive attack during plating process (De Almeida et al. 2002).

Sallee et al. (1994) has successfully deposited copper from the non-cyanide alkaline bath containing 0.745 M of copper nitrate, 0.79 M of tetra ethylene pentamine and 0.19M of ammonium nitrate. The bath has stable pH of 7.9, anodic current efficiency of 100% and cathodic current efficiency of 80%. In addition to copper nitrate, copper sulphate, copper acetate and copper chloride could also be used as copper salt because the production of

cupric ions is important when the salt is dissolved in water. The tetra ethylene pentamine (TEP) was used as a compexing agent because two nitrogen atoms in TEP are capable of forming a chelate with the divalent copper. The pH of the bath could be adjusted by adding ammonium hydroxide (Bharucha and Janjua 1973). The coating quality would be determined by the coating parameters, like, type of electrolyte, concentration of ions, pH, bath temperature, degree of agitation, substrate and counter electrode geometry and material, over potential and/or current density, mode of deposition (d.c. versus pulse plating or galvanostatic versus potentiostatic), and presence of additives in the electrolyte (Ebrahimi and Ahmed 2003). Among these, coating current density has a direct relationship with grain (crystallite) size. In general, high current densities promote grain refinement because an increase in the current density results in a higher over potential that increases the nucleation rate (Rashidi and Amadeh 2008 and Sallee et al. 1994). The theoretical model of nickel electroplating showed the linear relationship between log (d) and log (i), where 'd' is the grain size and 'i' is the coating current density (Rashidi and Amadeh 2008). But decrease in grain size with increase in current density is only up to a certain value. Tay et al. (2014) reported that in their bath, crystallite size decreased with increasing current density, up to 50 mA/cm^2 and crystallite size increased after that. The study carried out by Grujicic and Pesic (2002) explained that at deposition potential of 300 mV, the copper nucleation density was 3.75×10^7 nuclei per cm^2 and at 500 mV, it was 7.32×10^7 nuclei per cm^2. In addition to the deposition current density, nucleation rate depends on the bath pH, temperature, compositions and impurities (Balaraju and Rajam 2005). At higher temperatures, the ion supply to the cathode is increased. The velocity (diffusion and migration) of the metal ions and inhibitor molecules are functions of temperature (Natter and Hempelmann 1996). So the acceleration in nucleation cause fine grain and reverse results in coarse grain (Natter and Hempelmann 1996 and Balaraju and Rajam 2005). During the growth stage, (111) crystal orientation is preferred because cubic structure gives the lowest surface energy along (111) plane (Kang et al. 2002). Generally, nodular morphology is obtained in the copper electrodeposition, at room temperature. But it is reported that, on increasing the temperature to 45 °C, the

morphology of the copper deposition on the aluminium substrate has changed from globular to nodular shape (Kanungo et al. 2003, Okamoto et al. 2009).

In order to understand the mechanism of the electrodeposition and the growth behavior of the coating in detail, the movement of the cations in the bath needs to be discussed. Hence the concept of electrical double layer in the electrolyte is briefly given below.

2.2.1.1 Concept of electrical double layer

According to the Grahame triple layer model, the region near to the cathode could be divided into three regions *viz.* i) Inner Helmholtz layer (IHL), ii) Outer Helmholtz layer (OHL) and iii) Diffuse layer (Delgado et al. 2007).

IHL is a layer of partially or fully dehydrated specifically adsorbed ions. IHL is bounded by the surface and the inner Helmholtz plane (IHP). OHL is located between the IHP and the OHP. OHL is the layer of the centers of hydrated ions. Bath parameters, such as the concentration of individual ion species, use of complexing agents and their concentration, temperature, illumination or irradiation influences the nucleation process as these parameters could directly influence the inner row (Stern layer) of the Helmoholtz double layer. Bath temperature controls the rate of diffusion of ions from the diffusion to Helmohltz layer, the convection current and stability of any complex (Ray 2015). The schematic representation of the electrical double layer is shown in Figure 2.3.

The basic idea in the interpretation of the ion-specific behavior is that when attracted to the interface, cations may become dehydrated and thus get closer to the electrode. Each cation undergoes this to a different extent. This difference in the degree of the dehydration and the difference in the size of ions results in the specific behavior of the cations. Ions that are partially or fully dehydrated are in contact with the electrode. This contact adsorption of ions allows short range forces (Example; electric image forces) to act between the metal electrode and the ions, in addition to the conventional electrostatic Coulombic forces (Delgado et al. 2007).

19
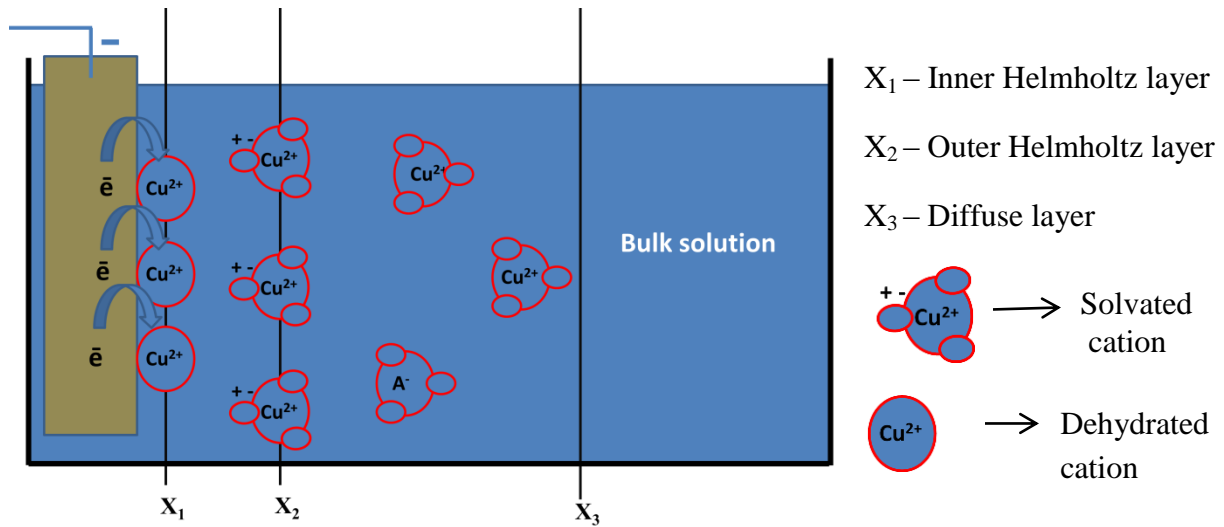
Figure 2.3 Schematic representation of the electric double layer in the electrodeposition in the contest of the copper deposition (Delgado et al. 2007).

2.2.2 DC magnetron sputter deposition

The process in which material is vaporized from the solid or the liquid source in the form of a vapor through vacuum or low pressure gaseous environment to the substrate where it condenses is known as physical vapor deposition (PVD) process. Sputtering is one of the most common PVD process for deposition of the copper thin films, in which due to high potential difference between the target and the substrate, plasma is generated from the inert gas and the ion bombardment is directed towards the target. Due to high energy bombardment of ions, the target gets eroded and gets deposited on the substrate. Sputtering could be broadly classified into two groups, based on the power source. They are i) DC magnetron sputtering, and ii) RF sputtering.

DC magnetron sputtering involves in creation of the plasma by the application of a large DC potential between two parallel plates (Mattox 1998). In DC magnetron sputtering, the electrons ejected from the cathode are accelerated away from the cathode and are not efficiently used for sustaining the discharge. By the suitable application of a magnetic field, the electrons could be deflected to stay near the target surface and by an appropriate

arrangement of the magnets, the electrons could be made to circulate on a closed path on the target surface. This high flux of electrons creates a high density plasma from which ions could be extracted to sputter the target material producing a DC magnetron sputtering configuration (Mattox 1998). In sputtering, the coating material is passed into the vapor phase, primarily, in atomic form by ion bombardment of a source electrode (target) composed of the coating material (Thornton 1977). Plasma confinement in the magnetron sputtering discharge is controlled by the magnitude and shape of the magnetic field above the sputtered target (Musil 1998). Sputtering method of deposition has many advantages as compared to other thin film depositions. DC magnetron sputtering is a convenient method for the preparation of dense, mechanically durable and well adherent films even at relatively low substrate temperature ($< 200°C$). The main advantage of the sputtering process is its capacity to pass materials into vapor phase while largely preserving their chemical compositions (Thornton 1977). Moreover sputtering is an environmentally clean deposition technique. According to Navinšek et al. (1999) "PVD coatings are more expensive than electroplating'' is no longer valid, if we take into account environmental limits, substrate material, size, quantity and the quality of the surface improvement. Large quantities of low-cost substrates could be successfully coated in an optimum reactor arrangement with a high deposition rate and the highest possible throughput of substrates can be achieved.

The ejection of the adatoms could be quantified by the term "sputtering yield", which is defined as the ratio of the atoms sputtered to the number of high energy incident particles (Example Cu=2.35 Atoms/Ar ions; Ag= 2.4 Atoms/Ar ions) (Ohring 2001). The deposition parameters, like target power, argon pressure, substrate temperature have a significant role in the microstructure and morphology of the coating. Sputter deposition of the film is a collision process and the deposition rate is limited by the target power density (Musil 1998). The relation between deposition rate and sputtering voltage are given by the Langmuir–Child relationship as given in equation (2.5) and (equation 2.6).

$$J_{ion} \, \alpha \, V_{dc}^{3/2} \tag{2.5}$$

$$KE_{av} \, \alpha \, V_{dc} \tag{2.6}$$

where, V_{dc} is the DC applied voltage, J_{ion} is the sputter deposition rate on argon ion flux, KE_{av} is the kinetic energy of the argon ion flux (Chan and Teo 2006). From the Langmuir–Child relationship, it is clear that flux density and energy of the sputtered ions are directly proportional to the applied voltage (V_{dc}). The applied voltage is proportional to the sputtering power. Hence, the sputtering rate as well as kinetic energy of the sputtered atoms increases with sputtering power. So at higher sputtering power, the crystallinity of the film is improved due to the higher surface mobility. Moreover, the nucleation and growth are faster at higher sputtering power and thereby the microstructure also improves (Le et al. 2010).

Along with better microstructure, adhesive quality of the coating on to the substrate is an important requirement for good antimicrobial copper coating. The negative bias to the substrate improves the adhesion strength (Ouis and Cailler 2013). Moreover, sputter cleaning (bombardment of the substrate surface prior to deposition) promotes better adhesion due to the removal of the adsorbed hydrocarbons and water molecules. During sputter cleaning, the nucleation density also increases, which helps to increase the adhesion strength (Singh and Wolfe 2005). During higher deposition range, better adhesion is obtained due to the better reflow of the copper atoms in to the grooves (Nguyen et al. 1997). The thin film with columnar morphology also exhibits a good adhesion because each column is separately bonded to the substrate (Mattox 1998).

2.2.3 Pretreatment on the aluminium substrate for improving adhesion strength

Poor adhesion strength of the copper thin film on to the aluminium substrate is the main problem of the copper coated aluminium. If adhesion strength is poor, coating becomes functionless (Gonczy and Randall 2005). The native oxide layer on the aluminium surface causes poor bonding between the substrate and the coating (Willigan et al. 2014).

So the removal of the oxide is necessary for the adherent copper coating. Due to the rapid formation of aluminium oxide, it is common to deposit thin zinc layer on to the aluminium *via* the ion exchange reaction between the aluminium and the zincate ions (Willigan et al. 2014 and Murakami et al. 2006). A zincate film formed by this process is thought to be thin since the cathodic reaction (precipitation of zinc) and the anodic one (dissolution of the aluminum into the zincate solution) immediately stops when the surface of the substrate is uniformly covered with the zinc film (Murakami et al. 2006). At higher value of pH, the oxide gets dissolved in the zinc bath initially (Ai et al. 2011). A more detailed explanation of the ion exchange reaction between the zinc and the aluminum is given in section 7.2.2.1(Chapter 7).

Zincate treatment could be done any number of times by repeating the dipping process over a fixed time interval followed by stripping in 50% nitric acid (Eg; double zincation, triple zincation etc.) (Parthasaradhy 1989). Murakami et al. (2006) has studied the efficiency of single, double and triple zincation process and concluded that double zincation is better. During double zincation, the uniform zincate film with better adhesive strength is achieved. During triple zincation, the adhesion is poor due to higher thickness of the zinc layer (Murakami et al. 2006). Similarly, single zinc deposition from zincate solution may not be providing adequate surface coverage, typically due to surface heterogeneity of the aluminum substrate (Willigan et al. 2014). Double immersion with acid etching between immersions is therefore standard practice prior to the copper deposition. It is reported that the incorporation of the sodium chloride into the bath also improves the adhesion strength of the copper thin film to the aluminium substrate (Bharucha and Janjua 1973).

2.3 Microstructural Characteristics of the Copper Coating

2.3.1 Nucleation and growth behavior of thin film

Microstructure of the thin film depends on the nucleation and growth mechanism. Singh and Wolfe (2005) have explained the growth mechanism of thin films, in which the structural evolution of the thin film undergoes three main stages:

(i) In the early stage, atoms will condense on the substrate and migrate to a site where lowest activation energy is available for the nucleation to occur. It is called as nucleation stage.

(ii) Next step is the incorporation of the incoming condensation flux into the growing individual units of the film structure. The condensate will try to re-structure in order to reduce surface free energy. This step is called crystal/film growth. Since, the free energy of the surface is generally an anisotropic property, crystal growth will take place initially in all directions to reduce the surface free energy.

(iii) Re-organize the unit structure of the film. It is called grain growth by coalescence. This depends upon the substrate deposition temperature, or total energy of the system.

According to the modes of growth, thin film is classified in to three categories *viz.* (i) island (or Volmer-Weber), (ii) layer (or Frank-van der Merwe), and (iii) Stranski-Krastanov, which are illustrated schematically in Figure. 2.4. Island growth occurs when the smallest stable clusters nucleate on the substrate and grow in three dimensions. This happens when atoms or molecules in the deposit are more strongly bound to each other than to the substrate. Many systems of metals on insulators, alkali halide crystals, graphite, and mica substrates display this mode of growth. The opposite characteristics are displayed during layer growth. Here the extension of the smallest stable nucleus occurs overwhelmingly in two dimensions resulting in the formation of planar sheets. In this growth mode, the atoms are strongly bound to the substrate than to each other. The

first complete monolayer is then covered with a somewhat less tightly bound second layer. The layer growth model is sustained if the bond energy is continuously decreasing towards the bulk crystal value. The layer plus island or Stranski-Krastanov (S.K.) growth mechanism is an intermediate combination of the aforementioned modes. In this case, after forming one or more monolayers, subsequent growth of layers become unfavorable and islands are formed (Le et al. 2010 and Ohring 2001).

ISLAND GROWTH

LAYER GROWTH

STRANSKI-KRASTANOV GROWTH
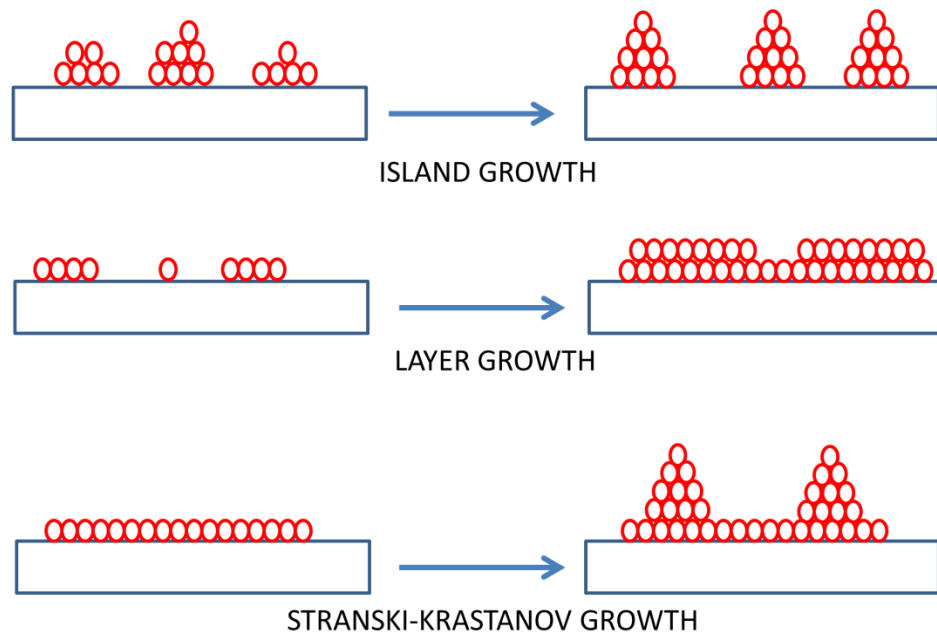
Figure 2.4 Schematic representations of growth modes.

In the case of sputtering, the morphology and growth behavior at different operating condition could be explained with the help of Thornton's structure zone model as given below.

2.3.1.1 Thornton's structure zone model

During growth, competition occurs between crystals of different orientations, and crystal with low surface energy will dominate and continue to grow (Singh and Wolfe 2005). Along with sputtering power, argon pressure also affects the microstructure of the thin

film. As the deposition pressure increases, the deposition rate decreases due to the collision scattering events between the sputtered copper atoms and the argon species in the deposition chamber (Chan and Teo 2006). So deposition is normally carried out at a sufficiently low pressure so that the flux undergoes an essentially collisionless transport to the substrate (Thornton 1977). The effect of the microstructure on the substrate temperature and argon pressure in sputtering could be explained by Thornton's structure zone model, which is schematically shown in Figure 2.5. In this model various growth morphologies are presented as a function of the substrate temperature and argon the pressure. According to this model, the deposit consists of tapered crystals with porosity between the tapered crystals. This is observed over a wide range of gas pressures but deposition temperature is relatively low. It is called as zone I. Zone II layer is formed at slightly higher temperature (0.5-0.6 T/T_m, where T and T_m are the substrate temperature and the target melting temperature in degree Kelvin, respectively). In Zone II, the growth process is dominated by surface diffusion of the adatom. In this region, surface diffusion allows the densification of the intercolumnar boundaries. However the basic columnar morphology remains. The grain size increases and the surface features tend to be faceted. Zone I and zone II is separated by a transition zone, called as zone T. In Zone T, the coating has a fibrous morphology. Formation of the Zone T material is due to the energetic bombardment from reflected high energy neutrals from the sputtering target at low gas pressures. These energetic high energy neutrals erode the peaks and fill-in the valleys to some extent. At higher temperatures, zone III morphology is observed. In Zone III, bulk diffusion allows recrystallization, grain growth and densification. Often the highly modified columnar morphology is detectable with the columns being single crystals of the coating material (Thornton 1977 and Ohring 2001).
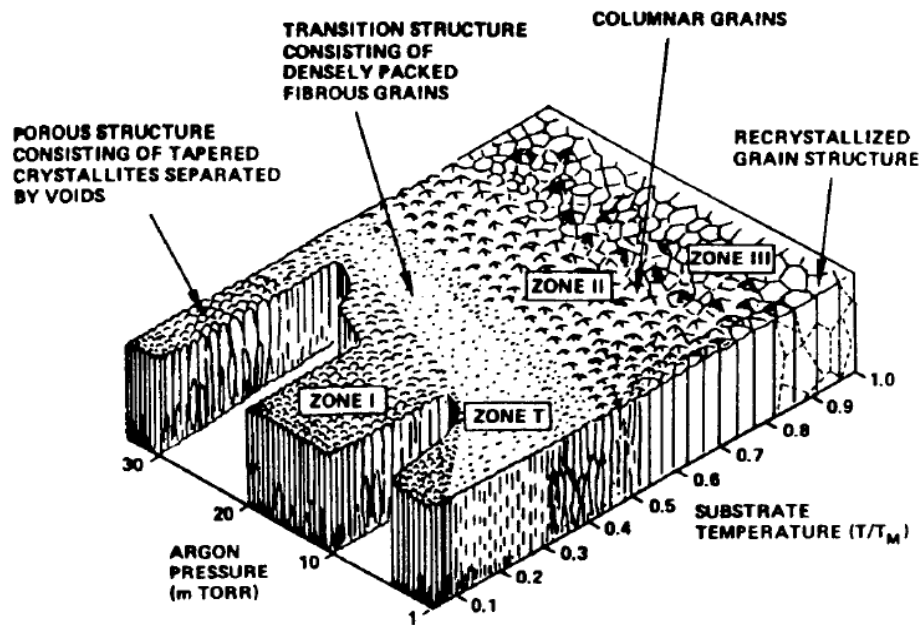
Figure 2.5 Structure zone model of the sputter deposited coating (Thornton 1977).

2.3.2 Nano-twin formation

Defects are necessary for the thermodynamic stability of real crystals. Twinning could be considered as a type of planar defect. In electroplating and sputtering, twins are formed due to error in stacking of unit cells when crystal first starts to grow. Copper has very low stacking fault energy (70-78 mJ m^{-2}) due to single valance electron of the copper (Zhao et al.2005 and Venables 1964). As a result, large numbers of stacking faults are formed easily in the copper thin film. Higher number of stacking faults together forms twins. So the introduction of nano-twins in the copper thin films is easily possible by controlling the operational parameters during electrodeposition and sputtering methods (Lu et al. 2009, Zhang et al. 2004a, Chen et al. 2008 and Zhang et al. 2004b).

Among various parameters, deposition rate has a significant role in the formation of the twins. The nucleation of twins has equal probability as perfect nucleus in the case of

higher deposition rate of low twin boundary energy materials. In the case of perfect nucleus (twin free nucleus), critical size

$$r^*_{perfect} = \frac{\gamma}{\Delta G} \tag{2.7}$$

Where, γ is the surface energy

ΔG is the bulk free energy.

In the case of twinned nucleus, critical size (Zhang et al. 2004a)

$$r^*_{twin} = \frac{\gamma}{\Delta G - \frac{\gamma_t}{h}} \tag{2.8}$$

Where, γ_t is the twin boundary energy, h is the height of the disc shaped nucleus. Note that ΔG is taken to be positive and hence, typically, $r^*_{perfect} < r^*_{twin}$ and nucleation of a perfect nucleus will be preferred to a twinned nucleus. However, if γ_t is very low and ΔG is very high, then the difference between $r^*_{perfect}$ and r^*_{twin} will be negligibly small, and the formation of twinned nuclei may occur freely during growth. Note that, ΔG is large at higher deposition rate (i.e., higher super saturation). Hence, in general, low γ_t and high deposition rate will favor deposition of films with twinned structures. For materials with relatively higher γ_t, sputter deposition at higher deposition rate is needed to form high twin densities (Zhang et al. 2004a). Hence at higher deposition rate, stable nano-twins are formed. In the case of elecrodeposition as well as sputtering, twins are formed with deposition rate of 10 nm sec^{-1} or higher (Lu et al. 2009 and Zhang et al. 2004a). Moreover, copper thin film have a tendency to grow parallel to (111) plane along [111] direction due to the low surface energy of (111) plane offered by its close packed structure (Zhou and Wadley 1999). In FCC, growth in (111) plane can only facilitate twin nucleation because for (111) plane ABCABC…..is the stacking sequence, but ABAB . . . is for both the (200) and the (220) planes. When adatom is deposited onto an ``A'' plane during [111] growth, it can either occupy the parent lattice ``B'' sites or the twin lattice (stacking faulted) ``C'' sites. Subsequent atoms that bond to this atom then form a nucleus

for either a regular lattice or a twin faulted one. However, during either [110] or [100] growth, the adatom can only occupy the parent ``B'' sites when dropped onto an ``A'' plane. As a result, twin nucleation is an intrinsic phenomenon accompanying deposition in the [111] direction but does not occur during growth in other principal crystal directions. Notice that the stacking sequence of an FCC (face centered cubic) crystal along the [111] (y) direction is ABCABC. . ., so an exchange of any two planes, say, A and B, leads to a shift in which A →B and B →A. The stacking sequence then becomes BACBACBAC which is in a twin orientation (Zhou and Wadley 1999). The schematic representation of normal as well as twinned crystal structure is shown in Figure 2.6.
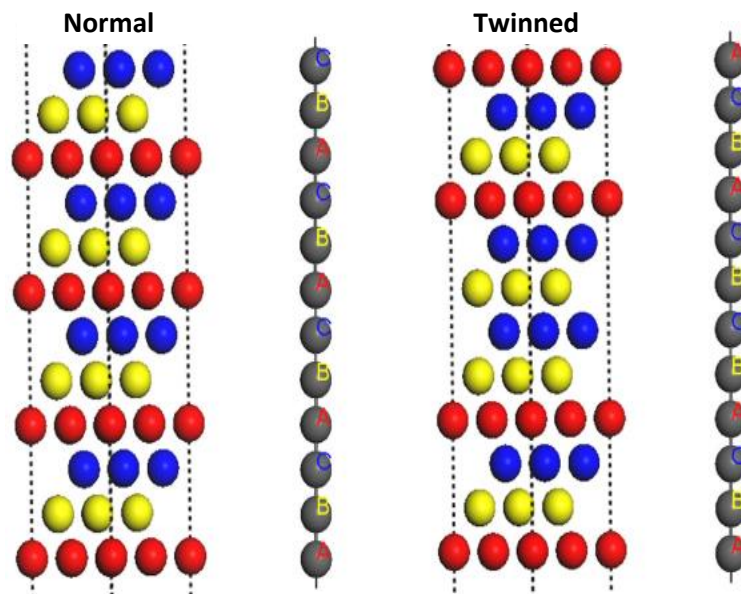
Figure 2.6 Schematic representation of the normal and the twinned crystal structure (Zhou and Wadley 1999).

2.3.3 Microstrain in the coating

Defects like twins and grain/crystallite boundaries introduce microstrain (lattice strain) in to the thin film coatings. Microstrain is thus the signature of defects density (Lu et al.

2000). In thin films, the excess energy is stored as microstrain and surface energy (Guazzone et al. 2006). Microstrain is a measure of the distribution of the lattice constants arising from crystal imperfections, such as, lattice dislocations, grain boundary triple junctions, stacking faults, and twins (Mote et al. 2012). It is a dimensionless value, which is usually assumed to be proportional to the square root of the density of dislocations (Rosenberg et al. 2000). In the studies carried out by Lu et al. (2009), it was explained that as twin density increases (twin space from 15 nm to 4 nm), the percentage of microstrain increases from 0.01% to 0.057%. In the case of nano crystalline palladium, microstrain decreased from 0.5% to 0.05% as the crystallite size increased from 10 nm to 100 nm (Guazzone et al. 2006). Since lattice strain certainly affects the properties of nano crystalline coatings, its measurement is important (Biju et al. 2008 and Qin and Szpunar 2005). X-ray profile analysis is a simple and powerful tool to estimate the crystallite size and lattice strain. These two characteristics could be extracted from the peak width analysis (Mote et al. 2012). Though the full pattern fitting methods are more rigorous, the analysis involved is quite complex and hence less direct analytical methods such as Warren-Averbach analysis or Williamson-Hall analysis is often employed. Warren-Averbach analysis requires at least two reflections along the same crystallographic direction and when higher angle reflections are weak and difficult to analyze, Williamson-Hall method is preferred.

Williamson-Hall analysis is carried out by assuming three different models, *viz.* (i) uniform deformation, (ii) uniform deformation stress and (iii) uniform deformation energy density (Biju et al. 2008). For metallic samples with cubic structures, the uniform deformation energy model is suitable (Mote et al. 2012 and Rosenberg et al. 2000). According to this model, the cause of lattice strain is assumed to be the density of deformation energy (Singla et al. 2013). The x-ray investigation showed that stress field coming from the grain boundaries would be the source for lattice strain. The high resolution electron microscope observations also shows that lattice strain exist mainly near the grain boundaries (Zak et al. 2011). The stress induced by the excess volume of the grain boundaries and twin boundaries is the principal reasons for microstrain in nano

crystallite coating (Biju et al. 2008). In small grains, strong stress fields from the grain boundaries tend to pull mobile dislocations out of the grains. So the grains with extremely small size experience the microstrain due to excess grain boundary volume. In bigger grains, the dislocations in the grains contribute to the microstrain (Qin and Szpunar 2005).

2.4 Mechanical Characteristics of the Copper Coatings

In electrodeposition and sputtering methods copper thin film is constituted by nano sized grains. The nano sized grains of the polycrystalline materials have the advantage of increased mechanical properties due to the hindering of dislocation movement. The strengthening originates from the fact that the grain boundaries block the dislocation movement. As a result plastic deformations become difficult (Lu et al. 2009). The empirical relation between grain size (crystallite size) and hardness is given by Hall – Petch relation. It is given in equation (2.9).

$$\sigma = \sigma_0 + K_0\, d^{\frac{-1}{2}} \tag{2.9}$$

where, d is the grain size in nm, σ is the yield stress, σ_0 and K_0 are Hall-Petch constants. Its values for nanocrystalline copper are 20 MPa and 0.14 MPa m$^{-1/2}$, respectively (Hansen 2004). From equation (2.9), it is inferred that hardness $\sim d^{\frac{-1}{2}}$ (Meriç et al. 1997). Hardness of thin films made up of copper as well as nickel has been measured and correlated with grain size by a number of authors (Schuh et al. 2002, Sanders et al. 1997, Lu et al. 2000 and Meriç et al. 1997). Yield strength of the nano crystalline copper is increased by 5-10 times from that of the annealed coarse grained copper (Sanders et al. 1997).The increased microhardness value of 1.2 GPa is reported in electrodeposited nanocrystalline copper, whereas, annealed copper showed 0.5 GPa (Lu et al. 2000). But if grain size becomes very small, dislocation pile ups can't be supported by grains (Bull and Berasetegui 2006). Such break down of Hall- Petch relation starts for copper below ~16

nm grain size (Sanders et al. 1997, Carlton and Ferreira 2007). This softening process could be attributed to the texture change, diffusion creep, triple junctions and sliding of grain boundaries (Sriraman et al. 2006 and Schiøtz et al. 1998).

Beegan et al. (2007) measured the coating hardness by following scratch test method. In scratch test method, the hardness is measured using equation (2.10).

$$Hs = (8F_N)/(\pi b^2) \tag{2.10}$$

Where, F_N is the normal force used and b is the average scratch width. In this method, the variation of the hardness could be estimated by taking the average scratch width on a larger length.

2.4.1 Effect of nano-twins on the mechanical properties

In addition to the nano-grains, nano-twins also contribute to increase in the strength of the copper thin films. The contribution of twins present in the copper thin films on the mechanical properties has been extensively studied (Lu et al. 2000, Zhang et al. 2004, Lu et al. 2005, Beegan et al. 2007 and Qian et al. 2005). As the density of the twins increases, the hardness obtained from nano indentation increased from 2 GPa to 2.6 GPa. Whereas the twin free ultrafine copper shows a maximum hardness of 1.6 GPa (Lu et al. 2005). The twin spacing has a significant role in the mechanical properties of the coating. On studying the samples having twin spacing ranging from 4 nm to 100 nm, it was seen that the mechanical strength continuously increased up to twin space of 15 nm. Below 15 nm twin space, the properties break down even though other structural parameters, such as, grain size and texture are unchanged (Lu et al. 2009). The uniaxial tensile true-stress true-strain curves for nano-twin copper samples of different twin spacing are shown in Figure 2.7.
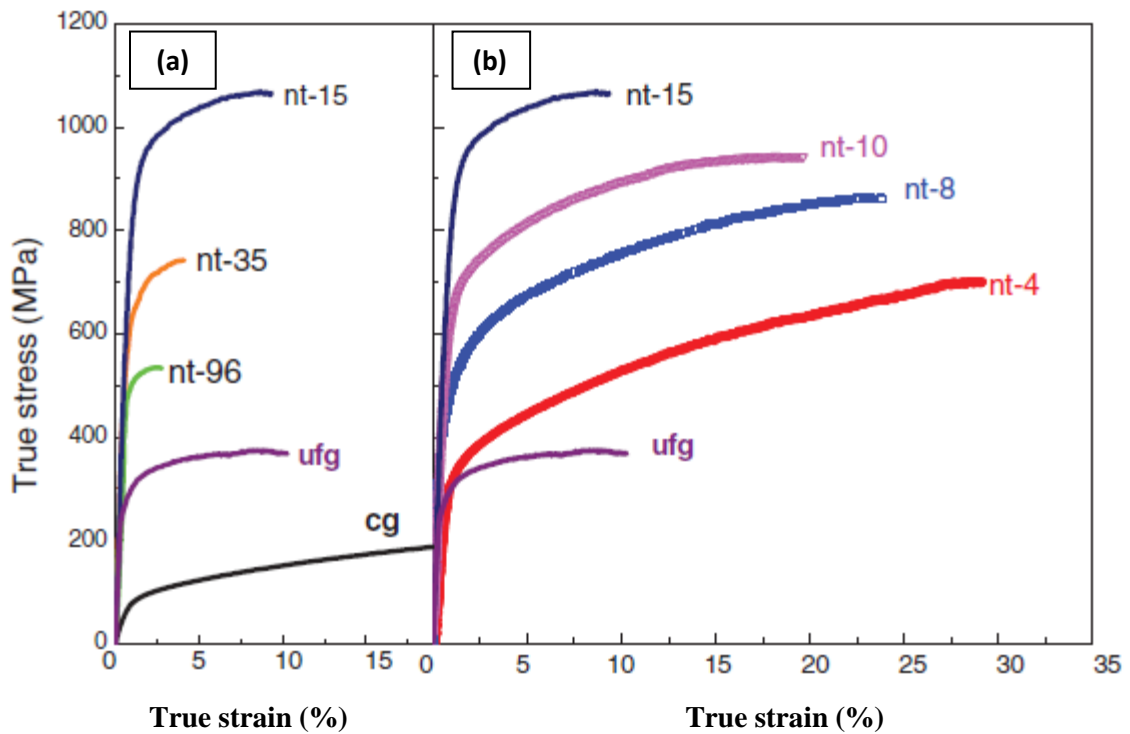
Figure 2.7 Uniaxial tensile true stress–true strain curves for nano-twinned (nt)-Cu samples tested at a strain rate of 6×10^{-3} s^{-1}, a) curves for samples with mean twin thickness varying from 15 to 96 nm, and b) curves for samples with mean twin thickness varying from 4 to 15 nm. For comparison, curves for a twin-free ultra-fine grain (ufg)-Cu with a mean grain size of 500 nm and for a coarse grained (cg)-Cu with a mean grain size of 10 mm are included (Lu et al. 2009).

The nano meter scale twin spacing is needed for higher strength because at higher twin spacing, dislocation pile-ups would form and the stress concentration from the pile-up would allow slip transmission across twin boundary at a lower applied stress, thereby reducing the strength of the material (Zhang et al. 2004a). The strain hardening behavior of nano-twinned copper samples is governed by two competing process; dislocation-dislocation interactions hardening in coarse grain and dislocation twin boundary interaction hardening in fine grains (Lu et al. 2009). Therefore in coarse grain materials,

if dislocations are made to move through grain interior, the twin boundaries can block effectively (Lu et al. 2005).

2.5 Antimicrobial Characterization Techniques

The antimicrobial properties of the copper and its reasons are explained in the section 2.1.2. These properties are commonly tested by the following methods.

i) Zone of inhibition method,

ii) Colony forming unit (CFU) counting technique

iii) Spectrophotometric method.

2.5.1 Zone of inhibition method

The zone of inhibition method is a semi quantitative test for the antibacterial sensitivity of a material. The zone of inhibition can be defined as the area of growth inhibition around a point source of antimicrobial agent, within a lawn of cultured organisms on a solid medium, due to the antimicrobial action of the source. In this test, samples containing antibacterial property are placed on an agar plate where bacteria have been placed, and the plate is left to incubate. If a sample which has antibacterial property stops the bacteria from growing or kills the bacteria, there will be an area around the sample where the bacteria have not grown enough to be visible. This area is called a zone of inhibition. The size of this zone depends on how effective the antibacterial sample is at stopping the growth of the bacterium. A stronger antibacterial agent will create a larger zone.

2.5.2 Colony forming unit (CFU) counting technique

The CFU counting method is an indirect measurement of cell density and reveals information related only to live bacteria. This method belongs to the quantitative test

methods of antimicrobial testing. The standard plate count method consists of diluting a culture with sterile saline solution, which is followed by treatment with antimicrobial substance. The dilution is continued until the bacteria are dilute enough to count accurately so that final plates in the series should have between 30 and 300 colonies because more than 300 colonies on a plate appear too close to each other and difficult to distinguish. The diluted culture is spread plated on agar plate. The assumption is that each viable bacterial cell is separate from all others and will develop into a single discrete colony (CFU). Thus, the number of colonies should give the number of bacteria that can grow under the incubation conditions employed. A wide series of dilutions (example; 10^4 to 10^{10}) is normally plated because the exact number of bacteria is usually unknown (JIS 2000). From the dilution factor, number of CFU and volume of culture plated, the number of cell could be calculated by using equation (2.11) as given below.

Number of bacteria = (Number of CFU) / (Volume plated $\times$ total dilution)   (2.11)

Usually Japanese Industrial Standard (JIS 2801:2000) is taken as the reference for testing antimicrobial materials in this method (JIS 2801: 2000, 2000).

2.5.3 Spectrophotometric method

The spectrophotometric method is based on turbidity and indirectly measures all bacteria (cell biomass), dead and lives. Increased turbidity in a culture is another index of bacterial growth and cell numbers (biomass). Here the amount of transmitted light decreases as the cell population increases. The transmitted light is converted to electrical energy, and this is indicated on a galvanometer. The reading, called absorbance or optical density, indirectly reflects the number of bacteria. This method is faster than the standard plate count but is limited because sensitivity is restricted to bacterial suspensions of 10^7 cells or greater.

2.6 Summary of the Literature Review

The summary of the literature review could be concluded as below: Infections are mainly occurring through the touch surfaces in the health care sector. The most common pathogens are *Escherichia coli* and *Staphylococcus aerous*. Copper has excellent antimicrobial properties and can be used in the design of antimicrobial touch surfaces. The multifaceted attack of the copper can kill the microbes effectively. The coating of copper is a potential method for converting existing non- antimicrobial aluminium touch surface to antimicrobial touch surface. Coatings by thin film deposition have the properties, like, excellent mechanical properties, easiness to coat on any complex shape and ability to tune the microstructure by controlling the coating parameters. Copper can be easily deposited on the aluminium substrate by electrodeposition and DC magnetron sputter deposition. Hence, the applicability of the copper by coating for antimicrobial touch surface application can be evaluated.

From the literature review, the research gaps have been identified and which are given below.

2.7 Research Gaps

The literature reviews indicates that health care associated infections (HCAI) are the severe problem in the health sector. The touch surfaces made of copper are one of the feasible solutions for preventing HCAI. But the study of antimicrobial activity of the copper coatings on the aluminium touch surface is not explored in detail. Moreover, the comparative study of the antimicrobial touch surfaces made by using bulk copper and coated one is absent in the literatures. The microstructural aspects of the copper coatings deposited by electrodeposition as well as DC magnetron sputter deposition at different coating parameters on the double zincated aluminium needs to be analyzed in detail. The impact of coating parameters on microstructure, mechanical properties and antimicrobial activities of the copper coating also not explored for the design of the better antimicrobial

touch surface. Literatures say that the exact mechanism of antimicrobial activity of copper is not yet clear.

The gap in literatures mentioned above leads to the formulation of research objectives and scope of work as given below.

2.8 Objectives and Scope of the Work

The aim of the current study is to prepare the antimicrobial touch surface particularly for hospitals, by depositing copper on aluminium products by following electrodeposition and DC magnetron sputter deposition methods and to investigate their microstructural features, mechanical properties and efficacy of the antimicrobial behaviour. Followings are the objectives of the present study:

➢ To optimise the coating parameters for the successful electrodeposition of the copper on the aluminium substrate using non-cyanide alkaline bath with and without the addition of ammonium nitrate.

➢ To optimise the coating parameters for the successful DC magnetron sputter deposition of the copper on the aluminium substrate.

➢ To characterize the microstructural features using scanning electron microscopy, transmission electron microscopy, x-ray diffractometer and energy dispersive spectroscopy of the electrodeposited as well as the DC magnetron sputter deposited copper coatings.

➢ To characterize the mechanical properties, like, adhesion strength and surface hardness of the electrodeposited as well as the DC magnetron sputter deposited copper coatings on the aluminium substrate.

➢ To estimate the biocidal efficacy of the copper coated by electrodeposition as well as DC magnetron sputter deposition on the aluminium substrate as compared to that of the bulk copper plate against gram negative and gram positive bacteria.

➢ To understand the mode of attack of copper on gram negative and gram positive bacteria using electron microscopy.

The scope of the work:

The scope of the present study can be divided as follows:

- Most of the hospital touch surfaces (especially in India) are made up of aluminium due to its advantages like less weight, easiness of making complex shapes, its recyclability, etc. So converting the existing aluminium touch surface to antimicrobial one by using copper coating is economically more feasible than replacing the same with the bulk copper.
- The deposition methods, such as, electrodeposition and sputter deposition methods have its own scope in different engineering applications. Complex shaped samples can be coated very easily by electrodeposition whereas, sputtering can be used for smooth and adherent coatings in large numbers of the samples.
- The microstructure of the coating can be tuned by adjusting the coating parameters. As a result, the copper coated aluminium surface can perform better than the bulk copper as an antimicrobial touch surface.
- The exact mechanism of the antimicrobial activity of the copper is not clearly revealed in the literatures. The electron microscopic study of the copper treated microbes can give better understanding in this regards.

Chapter 3

MATERIALS AND METHODOLOGY

Many of the hospital touch surfaces like doorknobs, push plates, bed rails and faucet handles are commonly made of commercially pure aluminium. In the present studies, the copper has been deposited on the commercially pure aluminium by using electrodeposition and sputter deposition techniques. The detailed explanation of the deposition procedures and the methodology for microstructural, mechanical and antimicrobial characterizations of the same are explained in the present chapter.

3.1 Substrate Preparation

Commercial pure aluminium plate of size 7 cm x 3 cm has been polished using buffing machine (1HP, 1500 rpm). The surface roughness is measured by using stylus profilometer (Mitutoyo SJ301) and confirmed that Ra (average value of surface roughness) value is in the range of 0.07 μm to 0.09 μm for all samples. The polished samples are degreased by using trichloroethylene and cleaned in ultrasonic cleaner for 10 minutes.

3.1.1 Double zincation process

Aluminium surface has an inherent oxide layer due to its exposure to the atmosphere. Such continuous oxide layer reduces the adhesion strength between the metallic coating and the substrate. This problem could be overcome by double zincation process (Willigen et.al. 2014). The detailed procedure for double zincation process is given below.

The polished commercial pure aluminium sheet is dipped in 50 mL of zinc bath containing ZnO (100 g/L), NaOH (525 g/L), $FeCl_2$ (1 g/L) and Rochelle salt (10 g/L) for

one minute and washed in distilled water. The zinc coating is stripped by 50% dilute nitric acid and this process is repeated for one more minute. As a result, the aluminium oxide is replaced with a thin zinc layer. The chemical reactions occurred during double zincation process is given in section 7.2.2.1 (Chapter 7). Figure 3.1 shows the photograph of different stages of double zincation process.
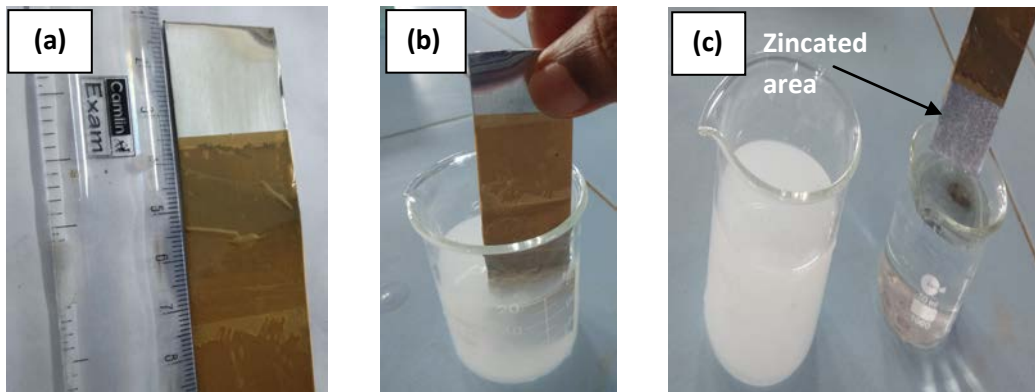
Figure 3.1 Photograph of double zincation process, a) polished aluminium substrate, b) dipping the sample in the zincate bath and c) zincated sample.

3.2 Copper Coating

The double zincated aluminium coupons are used as the substrate for the copper coating. The deposition process is carried out by the following deposition techniques *viz* i) Electrodeposition and ii) DC magnetron sputter deposition.

3.2.1 Electrodeposition of the copper on the double zincated aluminium

The copper is coated on the double zincated aluminium by electrodeposition. The non-cyanide alkaline bath has been used as the electrolyte for the deposition. The details of the bath preparation, bath optimization techniques and deposition process are given below.

3.2.1.1 Preparation of non-cyanide alkaline copper baths

In the present work, the electrodeposition has been carried out in non-cyanide alkaline bath. There are two set of coatings prepared. Initial one is prepared from the bath (electrolyte) containing ammonium nitrate (Bath-I). Since the commercial availability of the ammonium nitrate is restricted due to its explosive nature, second set of the copper coatings has been prepared from the bath which does not contain ammonium nitrate (Bath-II). The details of the bath preparation are given below.

i) Copper bath with ammonium nitrate (Bath-I)

The bath constitutes of 0.745 M of copper nitrate (Cu $(NO_3)_2.3H_2O$), 0.76 M of tetraethelenepentamine ($C_8H_{23}N_5$) and 0.21M of ammonium nitrate (NH_4NO_3). The tetraethelenepentamine and ammonium nitrate are used as the complexing agents (complexing agent: a compound in which independently existing molecules or ions of a nonmetal form coordinate bonds with a metal atom or ion). The optimization of the bath is carried out by following Hull cell optimization process, which is explained in section 3.2.1.2. The details of the chemicals used for the Bath-I are given in Table 3.1. The product details of the chemicals are given in Table 3.3.

Table 3.1 Chemical composition for the Bath-I

Name of the chemicals	Concentration
Copper nitrate (Cu $(NO_3)_2.3H_2O$),	0.745 M
Tetraethelenepentamine ($C_8H_{23}N_5$)	0.76 M
Ammonium nitrate (NH_4NO_3)	0.21M
Ammonia solution (NH_4OH)	0.1 M

The above mentioned chemicals are dissolved in 200 mL of distilled water, stirred using magnetic stirrer for 10 minutes and filtered with Whatman filter paper 40. The optimized pH for bright coating is found to be 7.9 and it is maintained by addition of the ammonia solution (NH_4OH) to the Bath-I.

ii) Copper bath without ammonium nitrate (Bath-II)

The commercial availability of the ammonium nitrate is restricted in many countries like India (Russia Today (2016), Government of the Netherlands (2010) , Sharma, A (2011)). So the new copper bath (Bath-II) is prepared with 0.4 M of copper nitrate, 0.4 M of tetraethelenepentamine and 3 mL of hydrochloric acid. The above mentioned chemicals are dissolved in 200 mL of distilled water, stirred using magnetic stirrer for 10 minutes and filtered with Whatman filter paper 40. The optimization of the bath is carried out by using Hull cell optimization process, which is explained in section 3.2.1.2. The optimized pH for bright coating is found to be 8.4 and it is maintained by addition of the concentrated hydrochloric acid to the Bath-II. The composition details of the Bath-II shown in Table 3.2 indicated that the Bath-II is simpler in composition as compared to that of the Bath-I.

Table 3.2 Chemical composition for the Bath-II

Name of the chemicals	Concentration
Copper nitrate (Cu $(NO_3)_2.3H_2O$),	0.4 M
Tetrathelenepentamine ($C_8H_{23}N_5$)	0.4 M
Hydrochloric acid	0.1 M

Table 3.3 Product details of the chemicals

Name of the chemicals	Manufacturer
Copper nitrate (Cu $(NO_3)_2.3H_2O$)	Nice chemicals
Tetrathelenepentamine ($C_8H_{23}N_5$)	Tokyo chemical industry
Ammonium nitrate (NH_4NO_3)	Nice chemicals
Zinc oxide (ZnO)	Nice chemicals
Sodium hydroxide (NaOH)	Nice chemicals
Ferric chloride ($FeCl_2$)	Nice chemicals
Rochelle Salt ($KNaC_4H_4O_6.4H_2O$)	Merck
Hydrochloric acid (HCl)	Nice chemicals
Nitric acid (HNO_3)	Nice chemicals
Trichloroethylene	Nice chemicals

3.2.1.2 Optimization process

Optimization of bath is important for obtaining good deposition. In electrochemistry, Hull cell method is the most commonly used technique for optimization (Parthasaradhy 1989). By this method, both coating current density and bath composition are optimized. The schematic sketch of the Hull cell along with the Hull cell scale is shown in Figure 3.2.

The bright and adhesive coating for the copper bath containing ammonium nitrate (Bath-I) is found to be achieved within the range of current density between 1 A dm^{-2} to 10 A dm^{-2}. The optimized coating current density for the Bath-II is 1 A dm^{-2} to 4 A dm^{-2}. The pH of the Bath-II is optimized as 8.4. The bath composition given in section 3.2.1.1 is obtained by using Hull cell test.
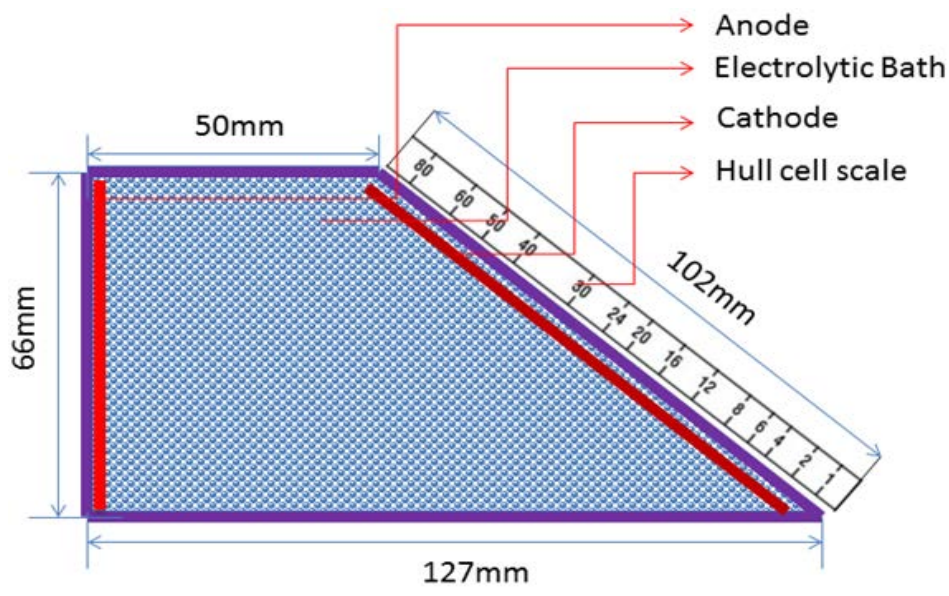
Figure 3.2 Schematic representation of the Hull cell.

3.2.1.3 Electrodeposition process

The double zincated aluminium sheet is fixed in the electrodeposition cell as the cathode and pure copper plate is fixed as the anode. The DC power source is connected with a variac to pass the required current density. The bath is continuously stirred during deposition. With an increment of 1 A dm^{-2} current density, copper is deposited from both type of copper baths (Bath-I and Bath-II). The coating is carried out at room temperature. The photographs of the copper bath, the deposition set up and the coated sample are given in Figure 3.3. The schematic diagram of cross section of the coated sample is shown in Figure 3.4.
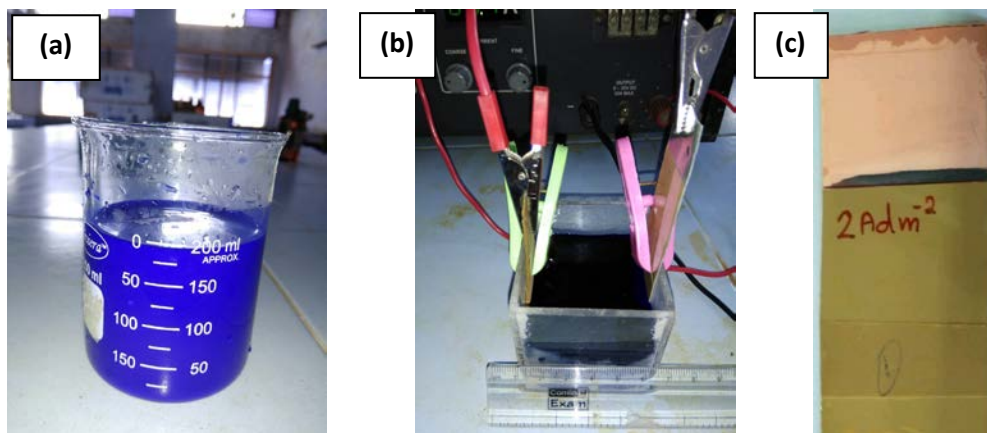
Figure 3.3 Photograph representing a) deposition bath, b) electrodeposition set up and c) coated sample.
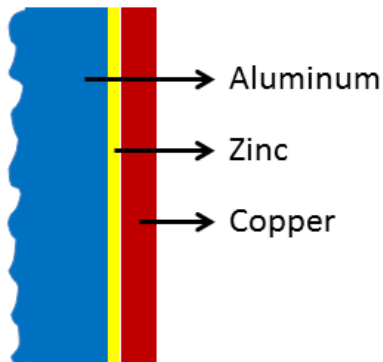
Figure 3.4 Schematic representation of cross section for the copper coated double zincated aluminium.

3.2.2 DC Magnetron sputter deposition of copper

The DC magnetron sputtering system (VR Technology, India) is used to deposit the copper on the double zincated aluminium substrate. The schematic diagram of the sputtering chamber is given in Figure 3.5. Before starting the sputtering process, the substrate and 99.99% pure copper target are fixed on its holders. Then the chamber has been evacuated with the help of the rotary pump and the diffusion pump. The 99.999 % pure argon gas is purged in to the chamber after the Penning gauge indicated a chamber pressure of 5×10^{-5} mbar. The argon flow rate is controlled by the mass flow controller (Aalborg). Once the argon flow is maintained at a rate of 17 mL/min, the DC power is supplied to the target. The deposition to the substrate is controlled by the shutter attached to the chamber. The sputtering power is varied from 50 W to 150 W by adjusting the DC power supply. The double zincated aluminium sample has been rotated with 100 rpm for obtaining uniform deposition. The heat generated on the target is absorbed by the cooling water. The deposition is carried out at room temperature. The optimized parameters are fixed by conducting a number of trial experiments, which is given in Table 3.4. The sputter deposited samples are prepared with the sputtering power of 50 W, 100 W and 150 W. The detailed mechanism of process of sputter deposition is given in section

7.1.2.1 (Chapter 7). The photographs of the sputtering chamber, the copper target and the coated sample are shown in Figure 3.6.
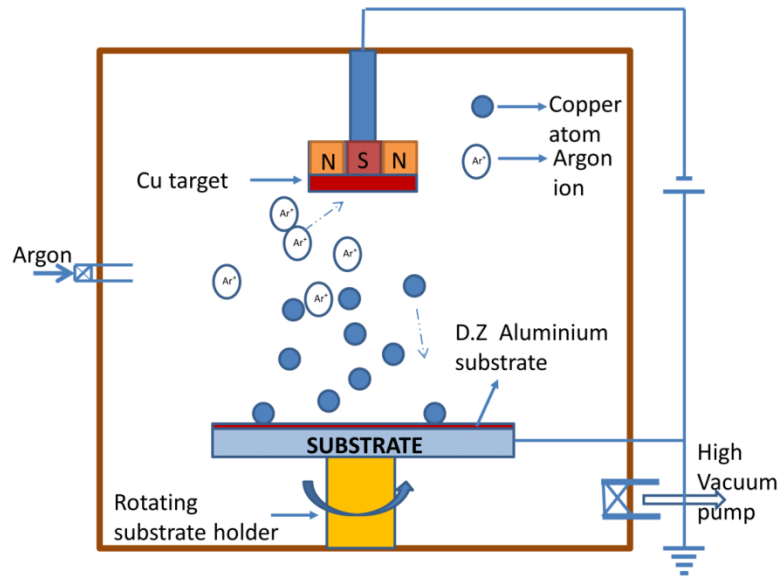
Figure 3.5 Schematic representation of the functioning of sputtering chamber with a sample.

Table 3.4 Process parameters of DC magnetron sputtering

Process parameter	Value
Argon flow rate	17 mL/min
Distance between the target and the substrate	12 cm
Substrate rotation speed	100 rpm
Initial pressure	5×10^{-5} mbar
Working pressure	0.012 mbar
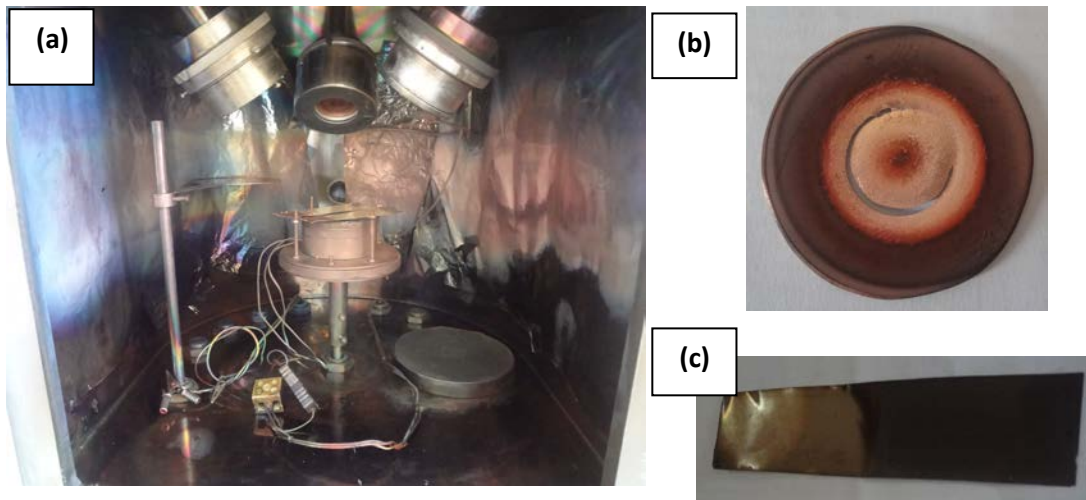
Figure 3.6 Photograph representing a) DC magnetron sputtering chamber, b) used copper target and c) coated sample.

The roughness of the coated samples deposited at different conditions has been measured and recorded by using stylus profilometer (Mitutoyo SJ301).

3.3 Microstructural Characterization

The microstructural characterization of the electrodeposited as well as sputter deposited copper coatings has been carried out by scanning electron microscope, transmission electron microscope, energy dispersive spectroscope and x-ray diffraction techniques.

3.3.1 Scanning electron microscopy (SEM) study

Analysis of the morphology is very important for understanding antimicrobial behavior of the coating. The surface roughness and hydrophilicity of the coating depends on the surface morphology. The surface morphology of the electrodeposited copper coating has been analyzed by using Scanning Electron Microscope (Model JSM-6380 LA, JEOL). The secondary electron images of top view and cross sectional view of coating have been used to analyses the growth of the coating which is carried out at different coating power.

3.3.2 Transmission electron microscopy (TEM) study

The characteristics of the coatings such as hardness, microstrain and surface energy are depending on the crystallite size of the coating. TEM is the most powerful tool to analyze the crystallite size, dislocation, twins, stacking faults and inter-planar spacing. TEM (JEOL, JEM-2100) is used to study the above ones of the copper coatings deposited on the double zincated aluminium. The extreme care is needed for the sample preparation of the coating, the details of which is given below.

3.3.2.1 Sample preparation for TEM

A disc of 3 mm diameter is punched out from the 60 micrometer thick copper coated double zincated aluminium. The 3mm diameter disc is dimpled in dimple grinder up to 40 micron thickness. It is further thinned down to 20 micron by ion milling equipment (Gatan, PIPS-691) in the presence of liquid nitrogen to prevent the grain growth. Milling at an angle of 5 degree is carried out from the substrate side. Initial milling is carried out with beam energy of 5 keV upto the point of formation of hole, cleaning is done at lower angle of 3 degree with beam energy of 3 keV. The TEM image is taken at the appropriate position as marked in the schematic diagram of ion milled sample in Figure 3.7. The micrographs have been taken in both cross sectional as well as topographical direction. The alignments of both directions are schematically shown in Figure 3.8.

49
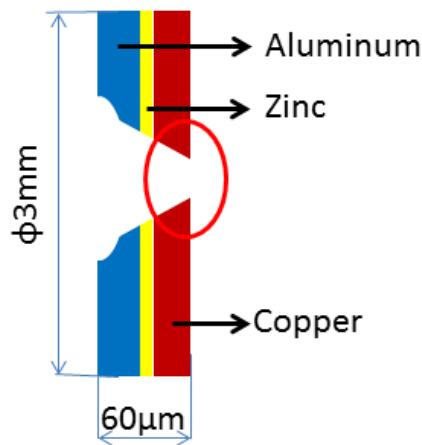
Figure 3.7 Schematic diagram of the ion milled sample.
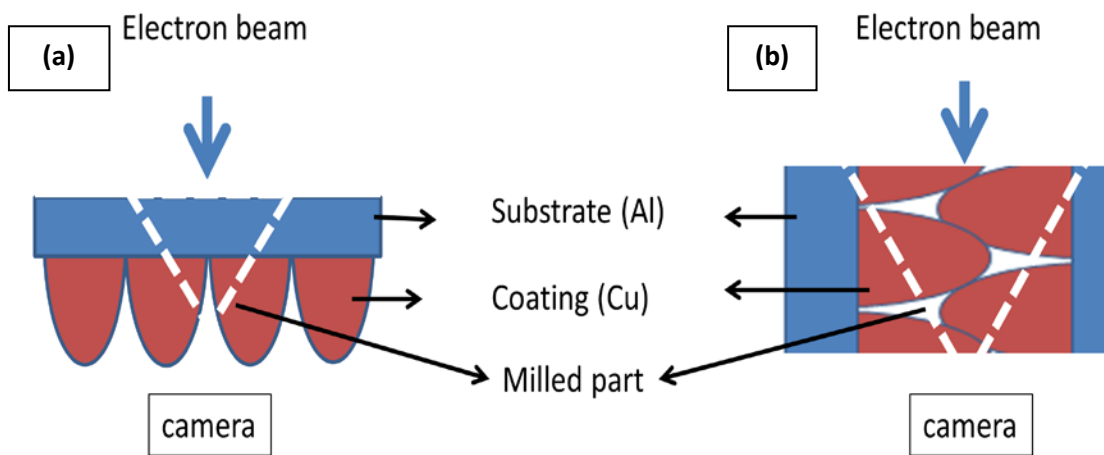
Figure 3.8 Schematic representations of the sample alignments for TEM micrograph in a) topographic direction and b) cross sectional direction, respectively.

3.3.3 X-ray diffraction spectroscopy (XRD)

X-ray diffraction pattern gives information about crystallite size, growth direction, percentage of crystallinity, phase structure, microstrain, etc. From the FWHM (full width half maxima) and Scherer formula, crystallite size could be readily calculated for nano sized crystallites. The copper coatings deposited at different coating parameters in

electrodeposition and sputter deposition have been studied by using x-ray diffractometer (JDX-8P JEOL) using Cu Kα (λ= 1.5406 Å) radiation with a scanning speed of 2 degree/min and 0.02 degree step size. The x-ray tube is operated with the power of 600 W. The 2θ value of the scanning is fixed in the range of 20° to 100°.

3.4 Mechanical Characterization

The mechanical characteristics like hardness and adhesion strength are the most essential properties required for the coating in the antimicrobial touch surface applications. The hardness of the copper coated aluminium touch surface has been tested by using scratch hardness test as well as microhardness test. The adhesion strength of the coatings to the double zincated aluminium is evaluated by cross-hatch cut test as well as pull-off adhesion test.

3.4.1 Hardness testing

The hardness of the coating has been evaluated by using scratch hardness as well as microhardness test. The details of the testing procedure are given below.

3.4.1.1 Scratch hardness test

Scratch hardness of the samples is measured by using scratch hardness tester (LINEARTESTER-249, Erichsen). The schematic representation of the test set up is shown in Figure 3.9. In this set up, the coated sample is drawn against a tungsten carbide stylus tip of 1mm diameter at a constant normal load of 10 N. The stroke length is fixed as 1 cm and stroke speed as 25 mm/s. The morphological study of the coating and width measurement of the scratches are carried out by using Scanning Electron Microscope (SEM, JSM-6380, JEOL make).
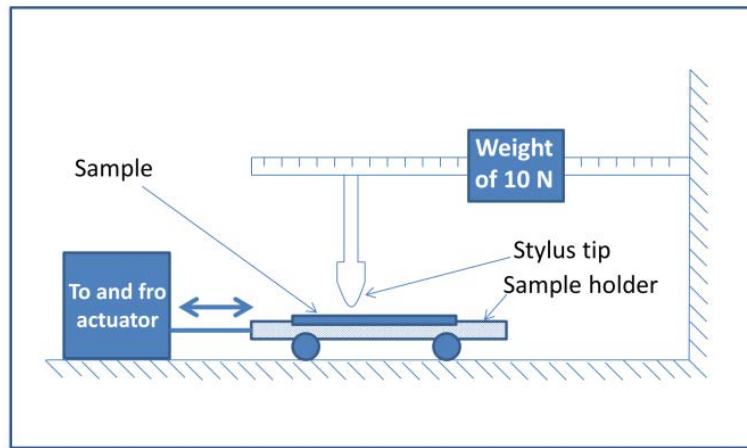
Figure 3.9 Schematic representation of the scratch hardness test set up.

3.4.1.2 Microhardness test

The static indentation hardness of the coated sample is measured using microhardness tester (CLEMEX, Japan). The load applied in this case is 50 g and dwell time is 15 sec.

3.4.2 Adhesion test

The adhesion strength of the coatings has been estimated by using pull-off adhesion test as well as cross-hatch cut test.

3.4.2.1 Pull-off adhesion test

The adhesive strength between the substrate and the coating is tested as per the specification ASTM D4541 with a pull-off adhesion tester (Positest AT, DeFelsko). A 20 mm diameter aluminium dolly with loading rate of 0.3 MPa/s is used for testing the adhesion strength. Epoxy patch adhesive (Loctite 907 Hysol) is used to fix the dolly on the coated samples four hours before the pull-off adhesion test. The schematic representation of pull- off adhesion test set up is shown in Figure 3.10.
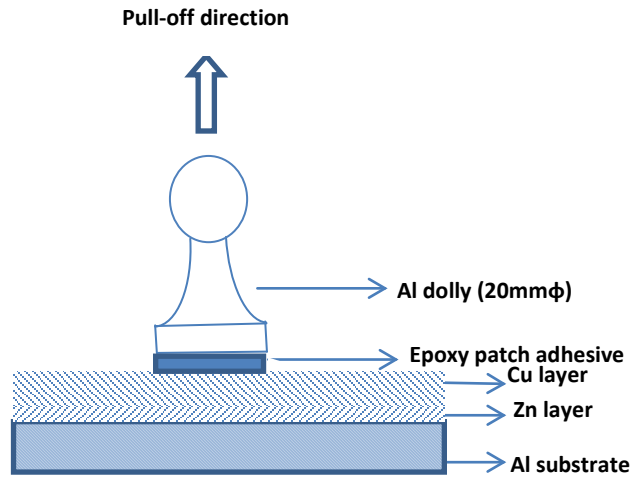
Figure 3.10 Schematic representation of the pull-off adhesion test set up.

3.4.2.2 Cross-hatch cut test

Cross hatch cut test is conducted to analyze the adhesion strength of the coating by using scratch hardness tester (Linear Tester 249, Erichsen). The test has been carried out as per ASTM D3359. The right angled lattice patterns on the samples with one mm spacing are made with the cross hatch cutter and are shown in Figure 3.11. The cutter is made out of hardened steel with a hardness of 60 Rc.

Figure 3.11 Photograph of the cross-hatch cutter.

3.5 Anti-bacterial Test

The antimicrobial activity of the copper coating has been estimated by the technique of counting the colony forming unit (CFU). The cultured microbes, namely, *Escherichia coli (E. coli:* ATCC 25922) and methicillin-resistant *Staphylococcus aureus* (MRSA: ATCC 43300) with concentration of 10^7 CFU/mL (0.5 McFarland standard) is dropped on 1.5 cm x 1.5 cm area of coupon of the copper coated aluminium. The culture is serially diluted after six hours of treatment on the metallic surface and spread on the agar plate. For *E. coli,* Müller-Hinton agar (MHA) and for *MRSA,* nutrient agar is used for plating. After 24 hours of incubation at 32 °C, the number of surviving *E. coli* bacteria on each agar plate is measured by the colony analyzer. Similarly, the coupons made by using uncoated aluminium and bulk copper are tested for their antimicrobial properties and the results are compared with that for copper coated aluminium coupons.

The SEM and TEM analysis are carried out to understand the changes in the cell structure of both *E.coli* and *MRSA* which had been exposed to copper coated surface and to compare the same with the other substrates, like, naked aluminium and the bulk copper surface. The presence of the copper in the cell is evaluated by using the EDS attached to SEM and TEM.

3.6 Summary of the Chapter

The present chapter explains about the experimental procedures followed for the sample preparation, copper coating and characterization with respect to microstructural, mechanical and antimicrobial properties. In the sample preparation, the polishing and double zincation procedures are explained. The double zincated samples are copper coated by following electrodeposition and DC magnetron sputter deposition route. For electrodeposition, the electrolyte has been prepared in two compositions, which is named as bath-I and bath-II. The pH, bath composition and coating current densities are optimized by using Hull-cell optimization technique. For the DC magnetron sputter

deposition, the target power is varied from 50 W to 150 W. The coated samples are microstructurally characterized with the help of SEM, TEM, XRD and EDS. The hardness of the coatings are tested by following scratch hardness and microhardness tests. The adhesive strength of the coating is evaluated by using cross-hatch cut test and pull-off adhesion test. The antimicrobial property of the coating is evaluated against gram positive bacteria (methicillin-resistant *Staphylococcus aureus*) and gram negative bacteria (*Escherichia coli*). The antimicrobial activity of the coating is compared with the bulk copper and the non- coated aluminium substrate (control) by CFU counting method. The microbes exposed to coatings are characterized by using SEM and TEM to understand the mechanism of the antimicrobial activity of the copper.

This page is intentionally left blank

Chapter 4

ELECTRODEPOSITED COPPER COATINGS: MICROSTRUCTURAL AND MECHANICAL CHARACTERIZATIONS

In the present chapter, the results of the electrodeposited copper coating on the double zincated aluminium substrate have been presented. The current chapter has been divided into two parts, which are: a) copper coating from the bath containing ammonium nitrate, which is mentioned as Bath-I, and b) copper coating from the bath without ammonium nitrate, which is mentioned as Bath-II.

4.1 Copper Coating from the Bath-I

In this section, the microstructure and mechanical properties of the copper deposits from Bath-I on the double zincated aluminium substrate have been characterized.

4.1.1 Physical observations

On macro observation, the coating was observed to be homogeneous and compact. The coatings produced at all levels of current density exhibited a salmon colour. At higher current densities (7 A dm^{-2} to 10 A dm^{-2}), the coating looked less bright than the coating produced using current density at medium range (4 A dm^{-2} to 6 A dm^{-2}). The roughness of the coatings was measured with a stylus profilometer. The variation in the Ra values (coating roughness) with the current densities is given in Table 4.1. Coatings produced at lower current densities ($\leq$3 A dm^{-2}) exhibited higher Ra values, indicating more surface roughness. Smoother coatings were observed in the middle range of current density (4 A dm^{-2} to 6 A dm^{-2}). At higher current densities ($\geq$7 A dm^{-2}), Ra values increased up to a

Table 4.1 Surface roughness of the coating deposited with different current densities

Coating current density, A dm^{-2}	1	2	3	4	5	6	7	8	9	10
Surface roughness (Ra) in μm	0.647 ±.019	0.643 ±.018	0.453 ±0.01	0.41 ±.01	0.40 ±.01	0.513 ±.015	0.563 ±.016	0.686 ±.012	0.757 ±.014	0.66 ±.01
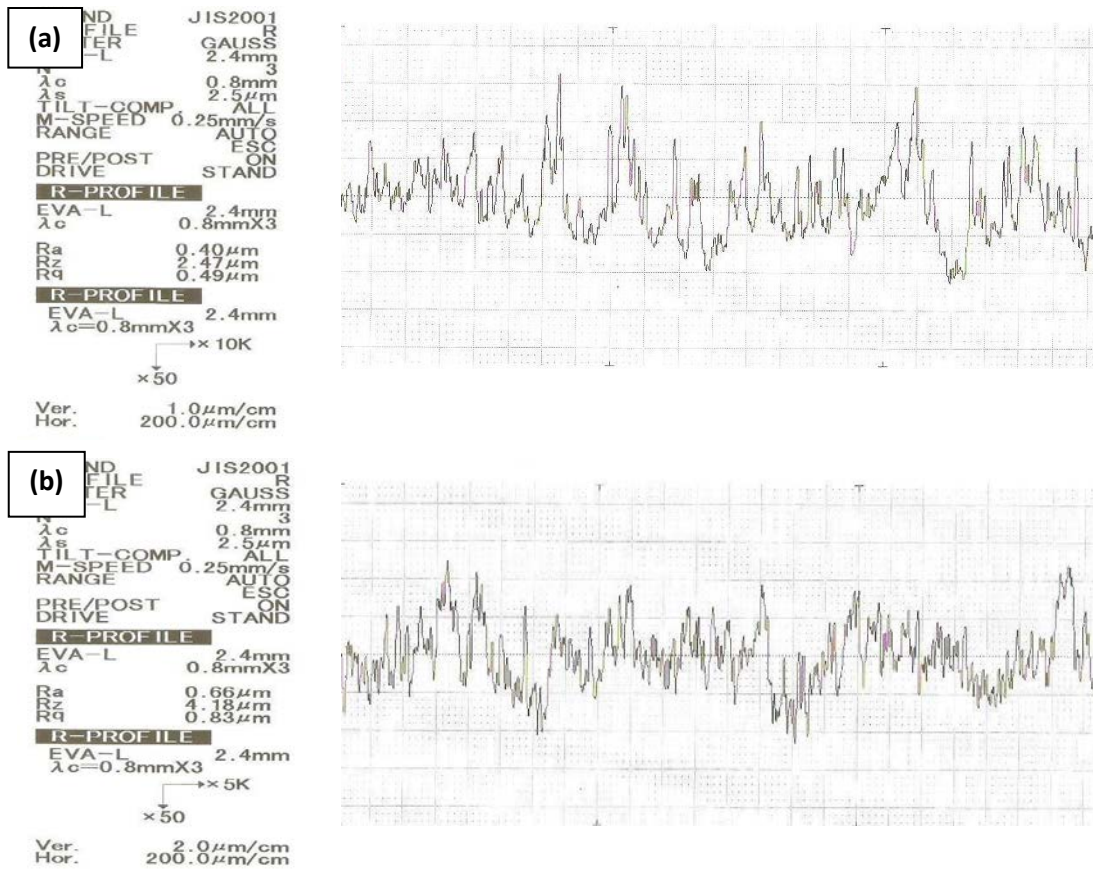
Figure 4.1 Roughness profiles of the coatings deposited by using current density of a) 5 A dm^{-2} and b) 10 A dm^{-2}, respectively.

maximum value of 0.757 µm. The roughness profiles corresponding to the coatings of 5 A dm^{-2} and 10 A dm^{-2} current densities are given in Figure 4.1.

4.1.2 Microstructural characterization

In this section, the microstructural characterization of the copper coatings deposited at different coating current densities by using SEM, TEM, XRD and EDS has been presented.

4.1.2.1 Scanning electron microscopic study

Figure 4.2 shows the SEM micrograph (topography) of the electrodeposited copper on the double zincated aluminium by using different coating current densities. As current density was increased from 1 A dm^{-2} to 10 A dm^{-2}, with fixed time of deposition, the morphology of the nodular structure continuously changed. Figure 4.2 (a - c) shows that the coatings with current densities of 1 A dm^{-2} to 3 A dm^{-2} are not continuous while the coatings using current densities greater than 3 A dm^{-2} are found to be continuous. To get more insight into morphology of the nodules, micrographs were taken at higher magnification and have been presented in Figure 4.3. At higher current densities ($\geq$ 7 A dm^{-2}), it is seen that the nodules protrude unevenly on the surface. This is depicted clearly in the cross sectional SEM micrograph of the coating corresponding to Figure 4.2 (e) and Figure 4.2 (i), in Figure. 4.4. It shows the columnar growth of the nodules perpendicular to the substrate. The average size of the nodules is 5.3 µm with a standard deviation of 1.44 µm. The distribution of nodules' size obtained from SEM micrograph is shown in Figure 4.5. The growth behavior of nodules at different current densities will be explained in the section 7.1.1.2 (Chapter 7). The purity of the electrodeposited copper coating was confirmed from the EDS profile, which has been presented in Figure 4.6.
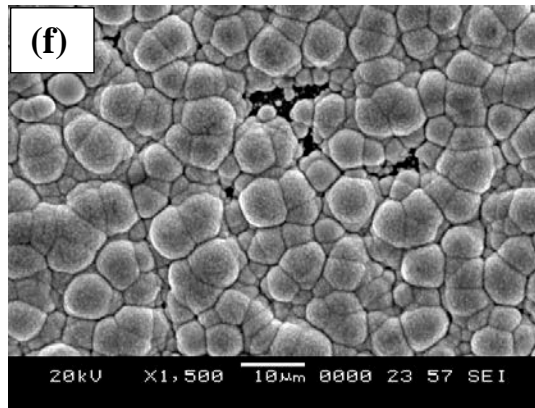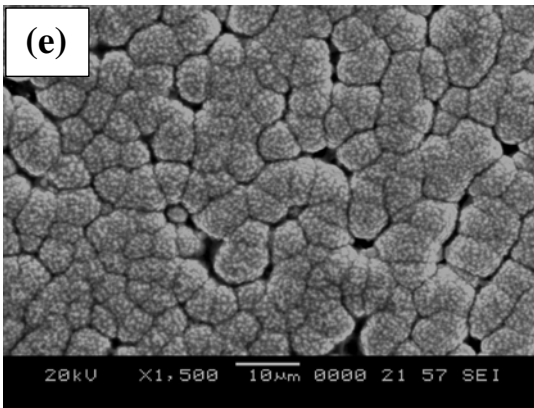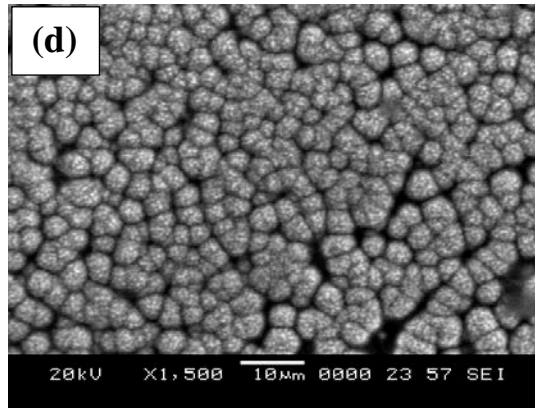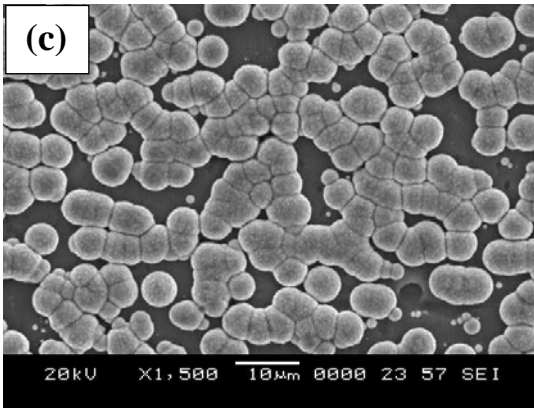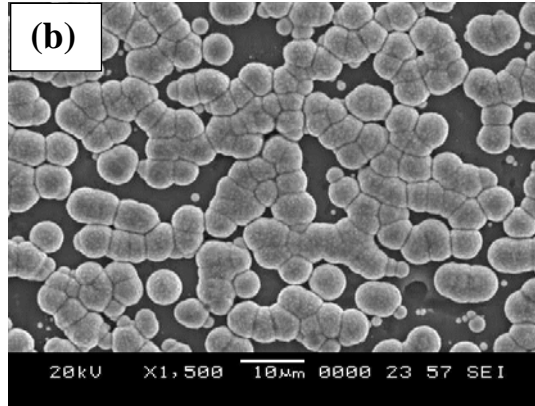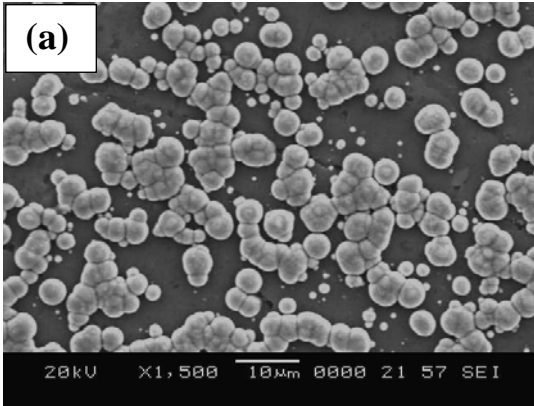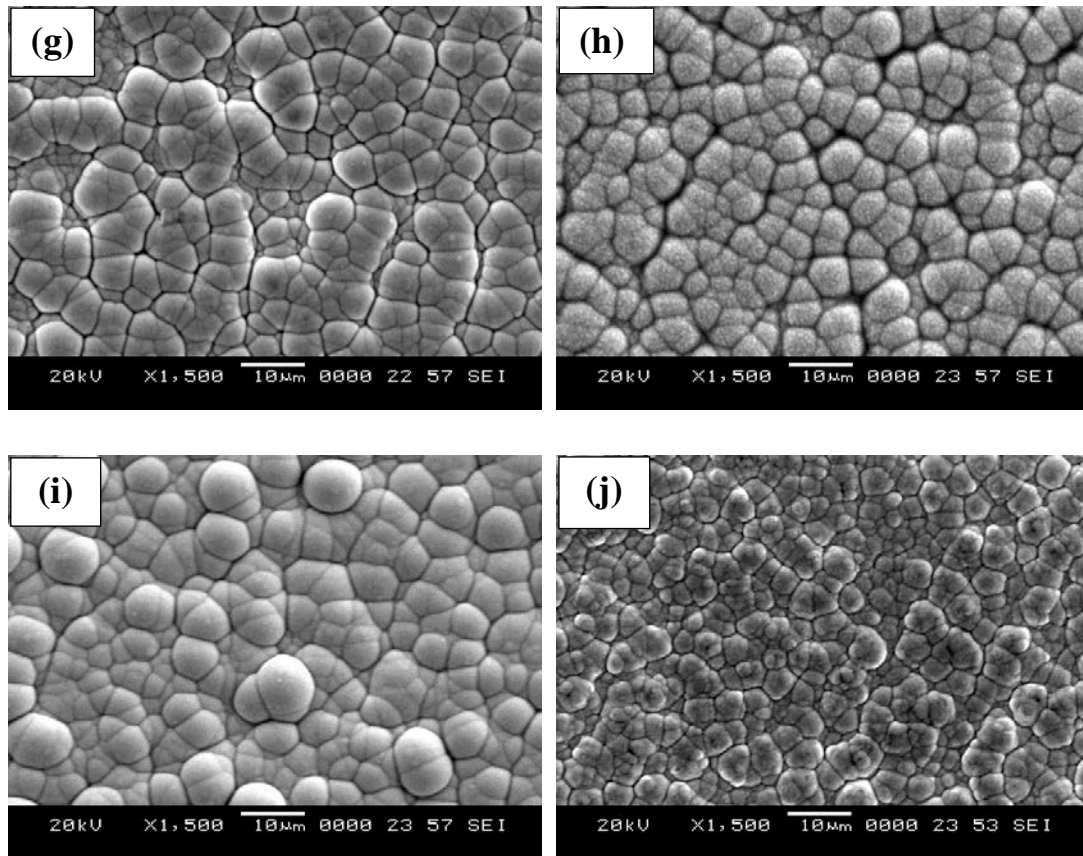
Figure 4.2 SEM micrographs revealing the topography of the copper coatings deposited on the double zincated aluminium with varying current densities a) 1 A dm^{-2}, b) 2 A dm^{-2}, c) 3 A dm^{-2}, d) 4 A dm^{-2}, e) 5 A dm^{-2}, f) 6 A dm^{-2}, g) 7 A dm^{-2} h) 8 A dm^{-2} i) 9 A dm^{-2} and j) 10 A dm^{-2}, respectively.
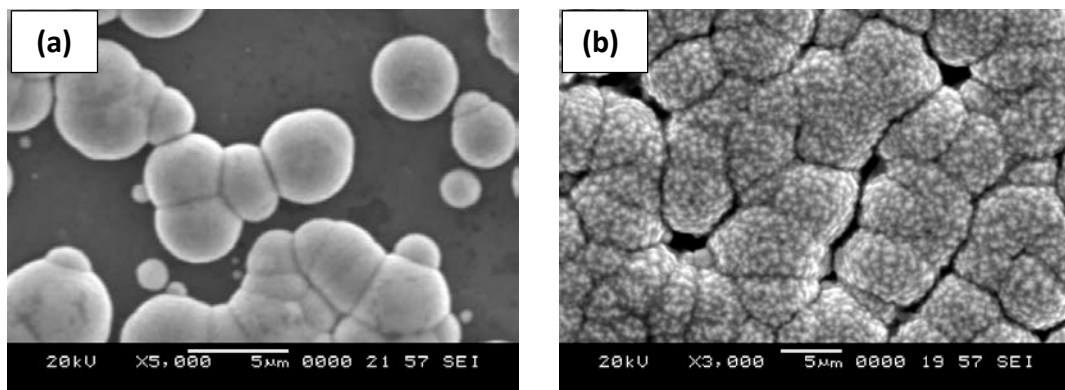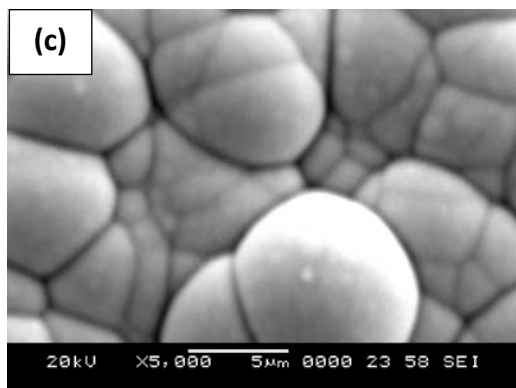
Figure 4.3 Higher magnification SEM micrographs (topography) of the copper deposits by using different coating current densities a) 2 A dm^{-2}, b) 5 A dm^{-2} and c) 9 A dm^{-2}, respectively.
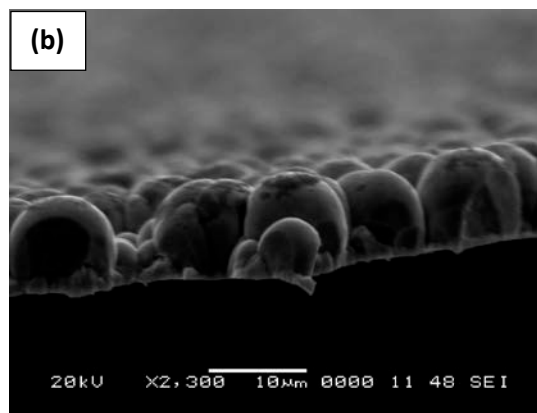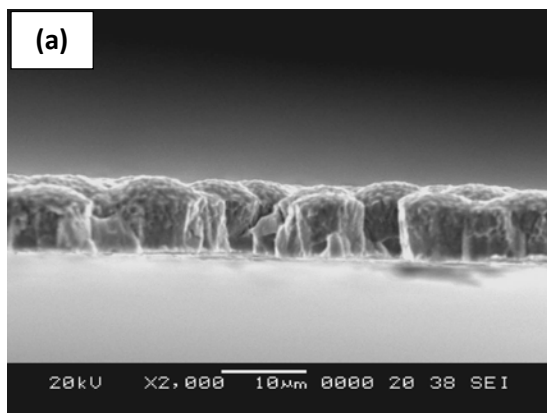
Figure 4.4 Cross section of the copper coating deposited at a) 5 A dm^{-2} and b) 9 A dm^{-2}.
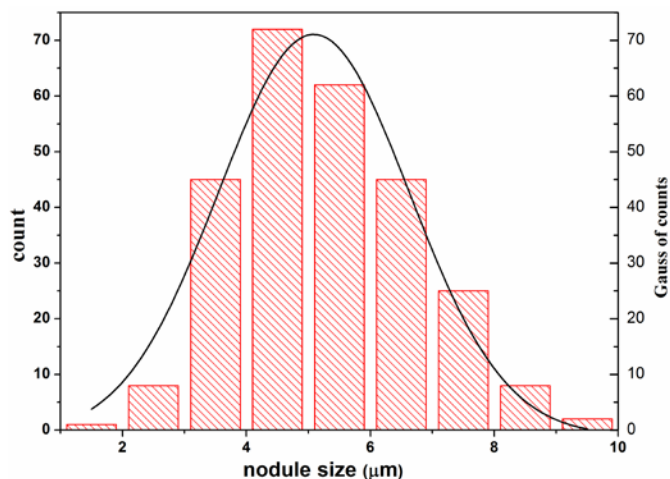
Figure 4.5 Nodules' size distribution of the copper coating deposited by using Bath-I.
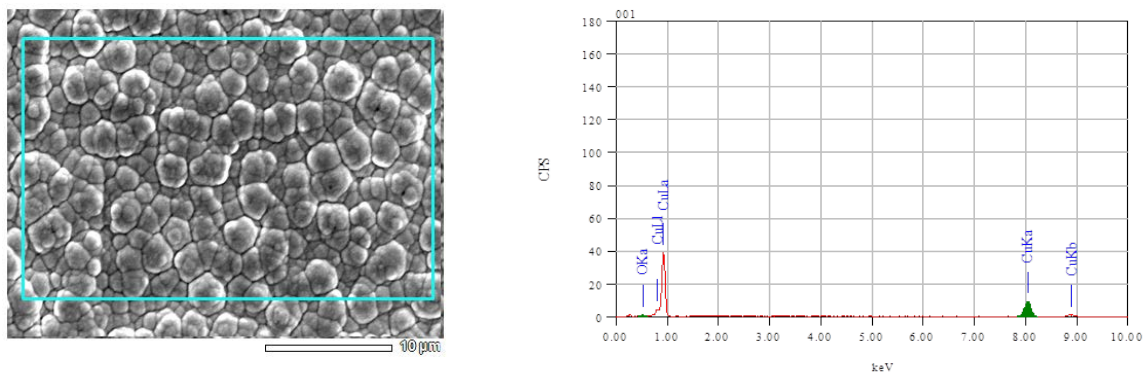
Figure 4.6 EDS result of the coating deposited by using 10 A dm^{-2} current density.

4.1.2.2 Transmission electron microscopic study

The TEM micrographs of the coating were taken in both, topographic as well as cross sectional directions. The schematic representation of the sample alignment for both topographic and cross sectional views is shown in Figure 3.8. In the text, the term 'TEM micrograph' represents the image along the topographic direction as shown in Figure 3.8 (a). In the case of TEM micrographs taken along the cross sectional direction, (as shown in Figure 3.8 (b)), the term 'cross sectional' is used.

Figure 4.7 (a) represents the bright field TEM micrograph of the copper coatings deposited using a coating current density of 2 A dm^{-2} (A visual image corresponding to Figure 4.7 (a) is given in Appedix-I). The crystallite size distribution was determined by measuring sizes of about 100 crystallites, and the size distribution is presented in Figure 4.7 (b). The average crystallite size is 63 nm and the standard deviation is 22.37 nm. SAED (selected area electron diffraction) pattern of the crystallite is shown in Figure 4.7 (c). The lattice image shown in Figure 4.7 (d) indicate the 'd' spacing of 0.208 nm corresponding to (111) plane.

Figure 4.8 (a) represent the bright field TEM micrograph of the copper deposition corresponding to the current density of 5 A dm^{-2}. The histogram representing crystallite size distribution of the same is shown in Figure 4.8 (b). At 5 A dm^{-2} coating current density, the average crystallite size was observed to be 44 nm with a standard deviation of 12.3 nm. The SAED pattern of the TEM micrograph given in Figure 4.8 (a) is shown in Figure 4.8 (c). Figure 4.9 (a) represents the bright field TEM micrograph of the copper deposit corresponding to current density of 10 A dm^{-2}. The histogram representing crystallite size distribution of the same is shown in Figure 4.9 (b). At 10 A dm^{-2} coating current density, the average crystallite size was observed to be 32 nm with a standard deviation of 10.47 nm. Figure 4.9 (c) represents the SAED pattern corresponding to the coating deposited by using current density of 10 A dm^{-2}.

In order to confirm the absence of epitaxial growth of the coating, TEM micrograph along cross sectional direction is presented in Figure 4.10 (a). The histogram corresponding to the Figure 4.10 (a) shown in Figure 4.10 (b) indicates the average crystallite size of 32 nm with a standard deviation of 8.3 nm. Figure 4.10 (c) represents the SAED pattern corresponding to the TEM micrograph. Moreover, TEM micrographs corresponding to higher current density contain planar defects like nano-twins. The detailed explanations are given below.
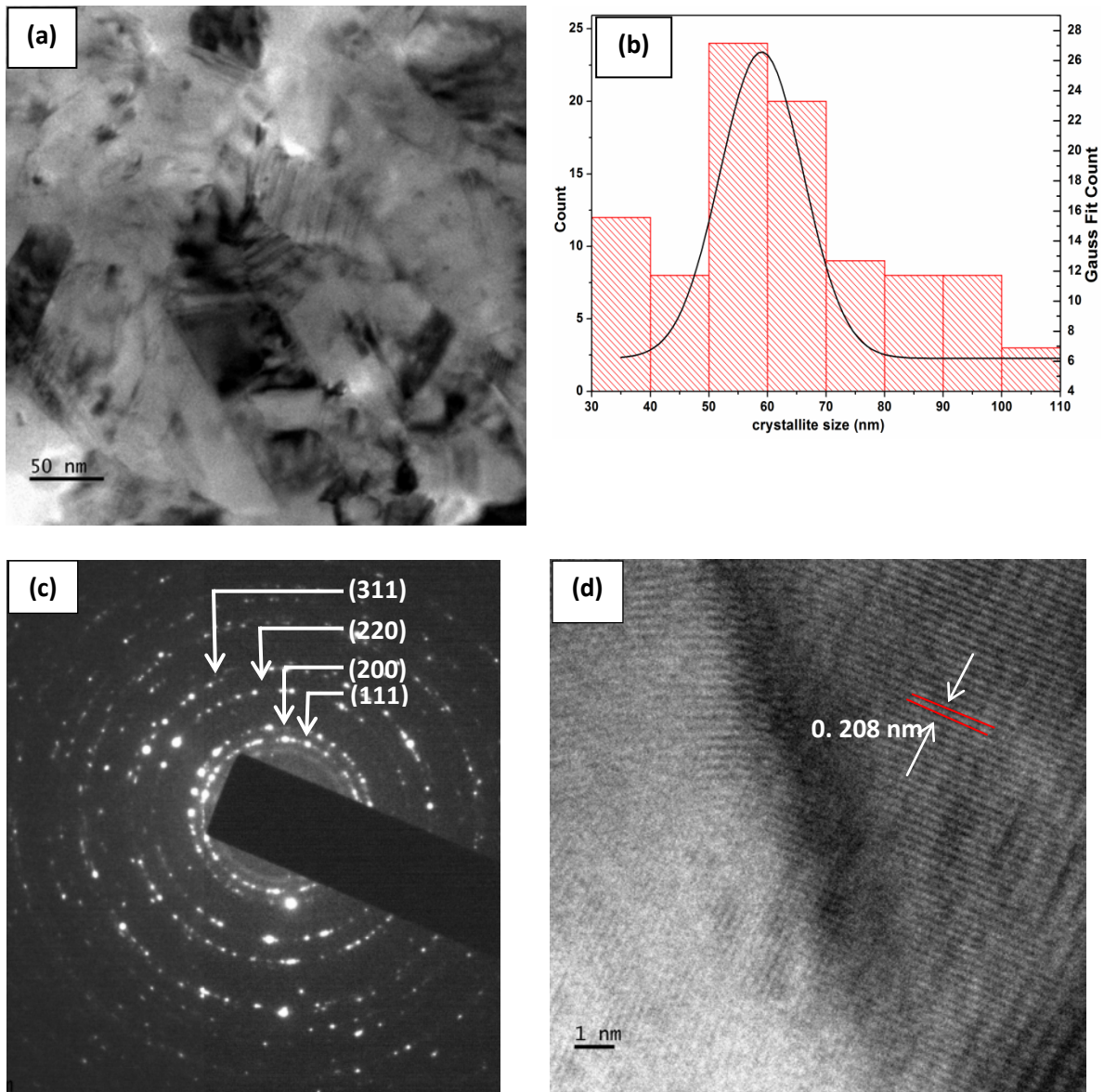
Figure 4.7 a) Bright field TEM micrograph of the copper coating deposited at 2 A dm^{-2} (lower current density), b) histogram representing the crystallite size distribution corresponding to Figure 4.7 (a), c) SAED pattern of the copper coating, and d) lattice image indicating 'd' spacing.
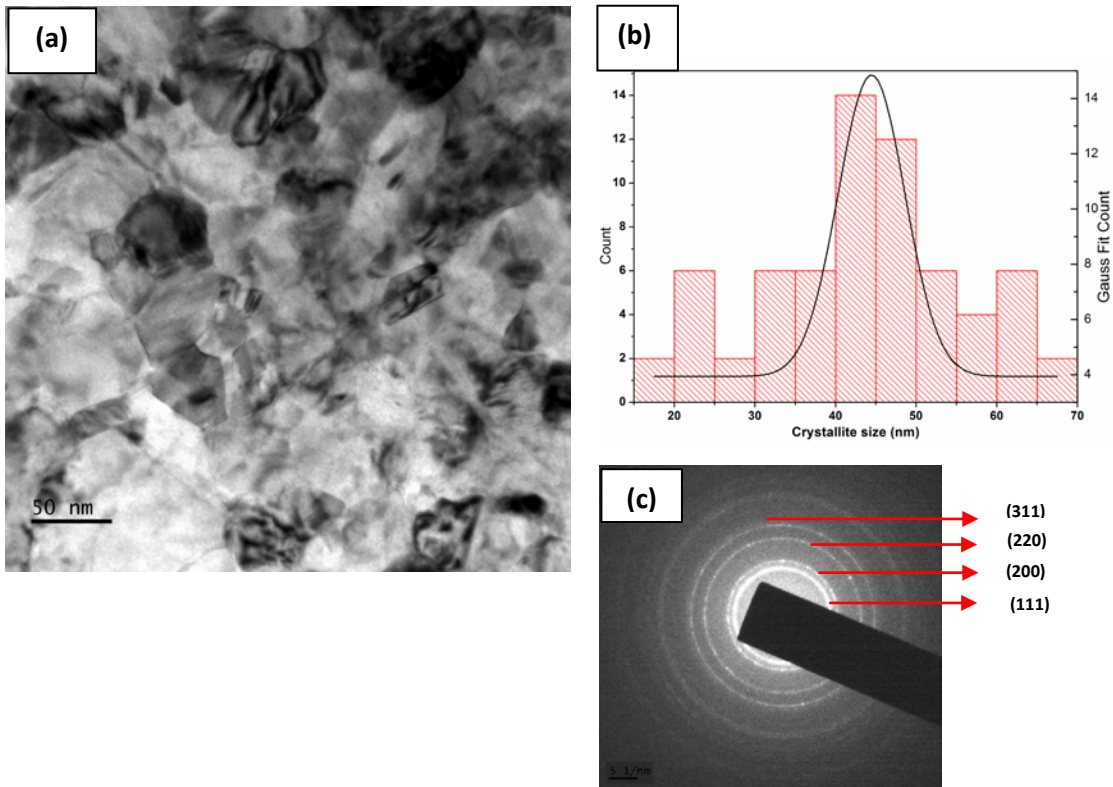
Figure 4.8 a) Bright field TEM micrograph of the copper coating deposited at 5 A dm^{-2} current density, b) histogram representing crystallite size distribution and c) SAED pattern corresponding to the same.
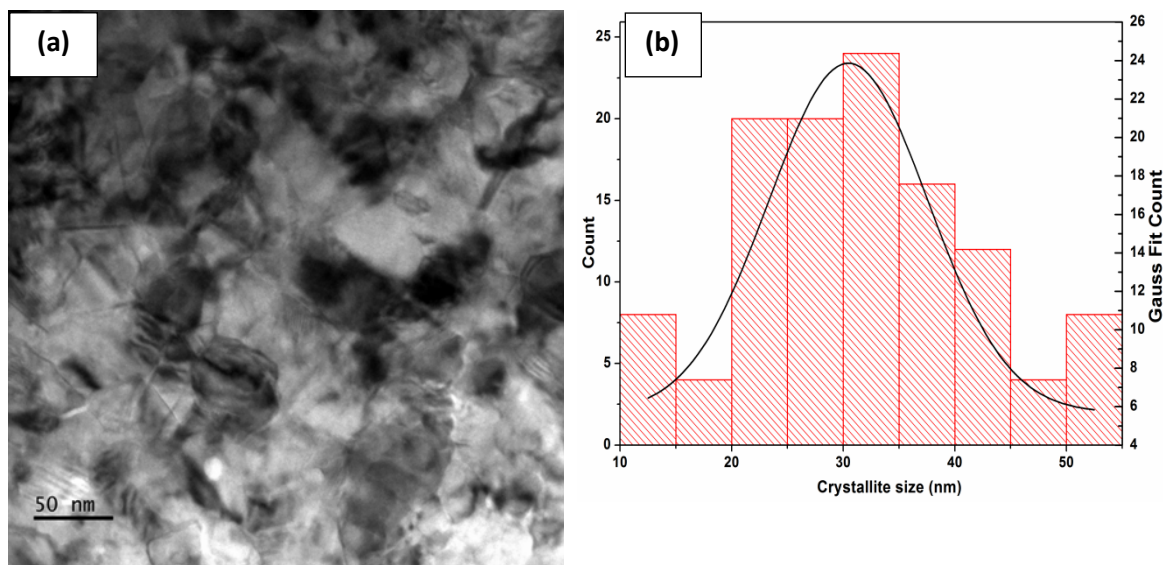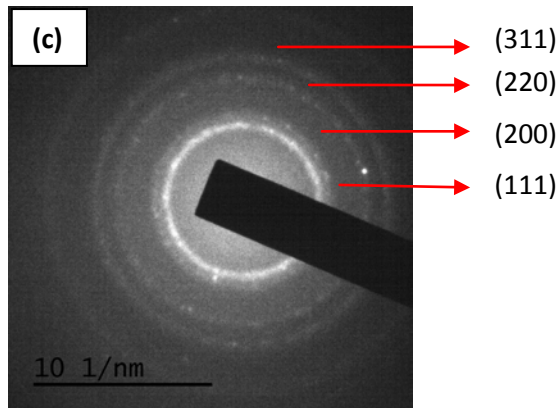
Figure 4.9 a) Bright field TEM micrograph of the copper coating deposited at 10 A dm^{-2} current density, b) histogram representing crystallite size distribution and c) SAED pattern corresponding to the same.
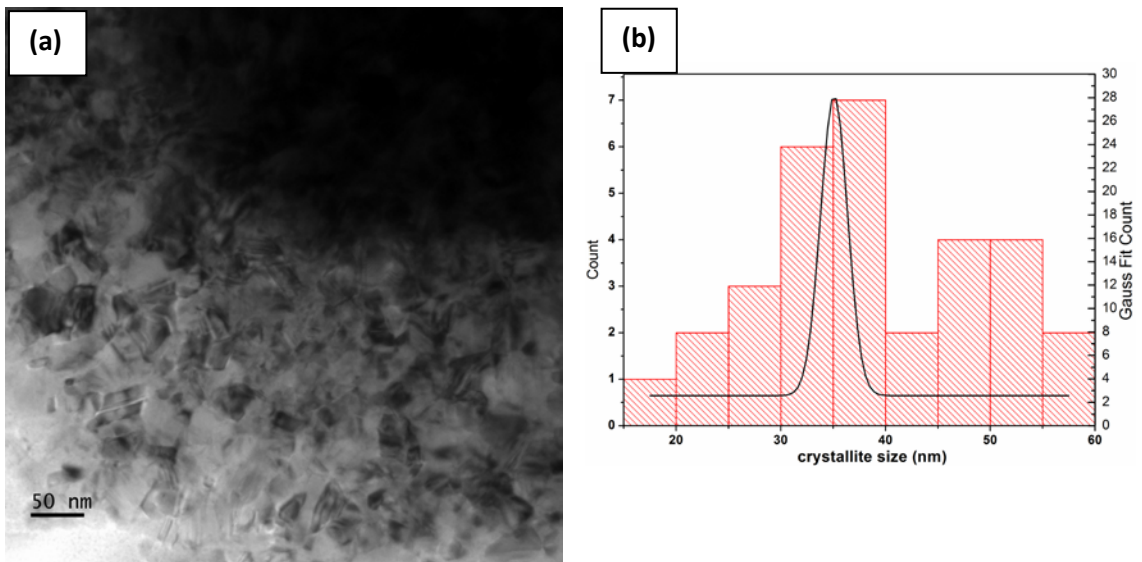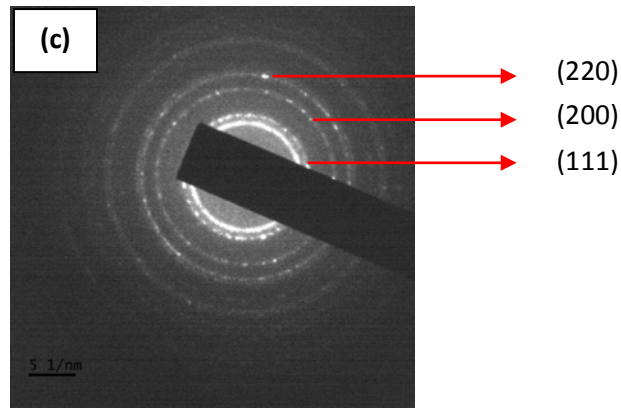
Figure 4.10 a) Bright field TEM micrograph (cross sectional) of the copper coating deposited at 10 A dm^{-2} current density, b) histogram representing crystallite size distribution and c) SAED pattern of the copper coating.

Nano-twins:

Figure 4.11 (a) represents the TEM micrograph of nano-twins (indicated by arrow marks) in the coating deposited at 10 A dm^{-2} current density. The magnified micrograph of the highlighted twin is shown in Figure 4.11 (b). It indicates that the width of the twins is in the range of 3 nm to 7 nm. The SAED pattern corresponding to the same is shown in Figure 4.11 (c). The density of nano-twins was estimated and it is in the range of approximately 400 numbers per square micrometer imaging area.
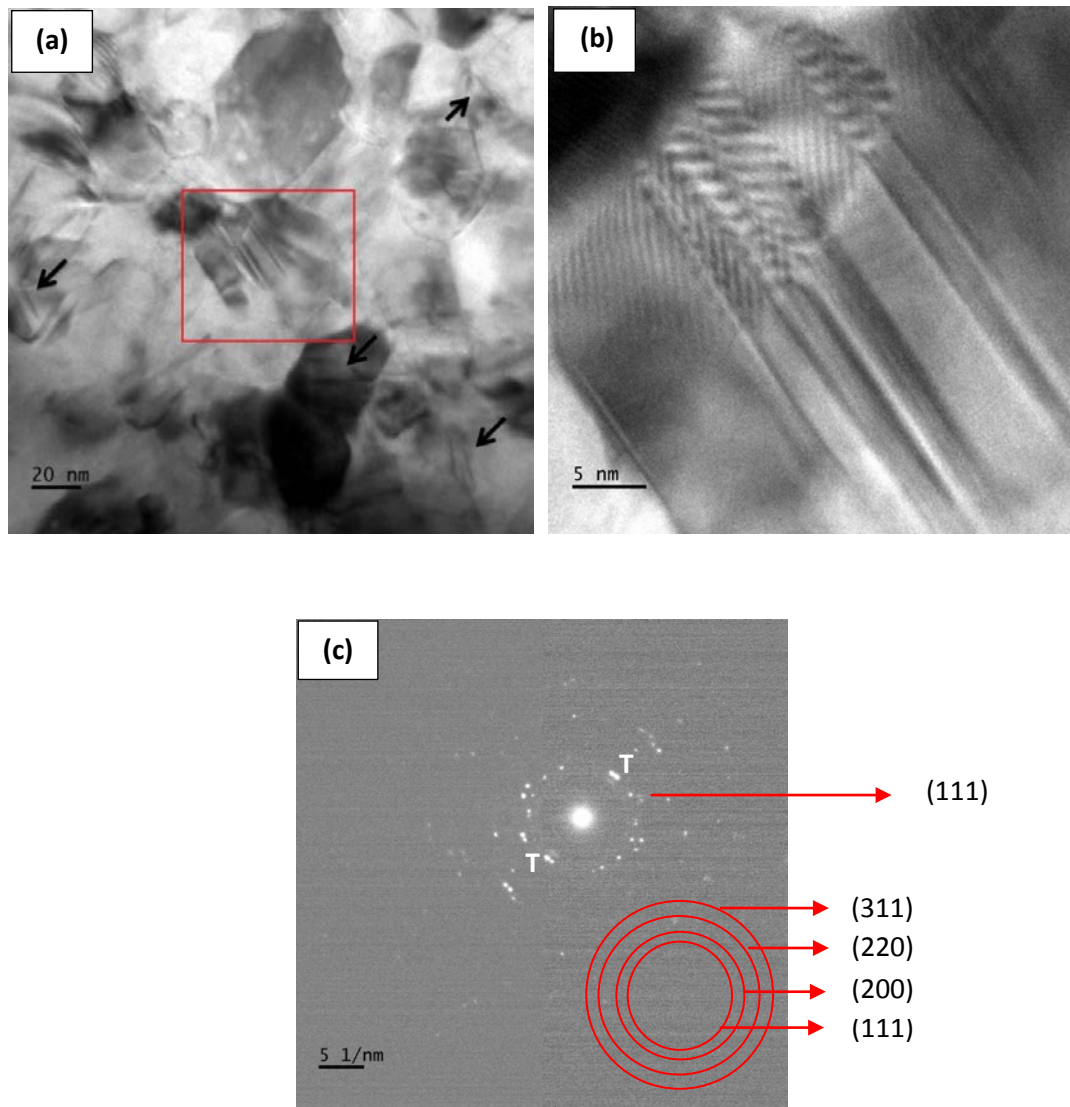
Figure 4.11 Bright field TEM micrograph corresponding to coating with 10 A dm^{-2} representing a) nano-twins, b) magnified micrograph of selected twins, and c) SAED pattern of the same indicated as 'T'.

4.1.2.3 X-ray diffraction study

Figure 4.12 shows the x-ray diffraction profiles of the copper coating corresponding to different coating current densities. The peak at 43.22° indicates the presence of a thin layer of zinc formed during double zincation of the aluminium substrate. The peaks at 43.316°, 50.448°,74.125°, and 89.94° represent the (111), (200), (220), and (311) planes

of the polycrystalline copper coating, respectively. The relative intensity of the peak corresponding to the (111) plane is observed to be higher as compared to that presented in ICDD#89-2838 file. The high value of the peak intensity of (111) plane is indicative of the preferred growth along (111) plane along [111] direction. This is confirmed from the XRD profile taken on the thicker coating (20 μm thick), as shown in Figure 4.13. Such coatings are prepared solely for the purpose of XRD studies. As the coating current density was increased, the full width half maxima (FWHM) of the peak increased. The increase of FWHM with increase in coating current density corresponding to the peak at 43.316° is shown in Figure 4.14. It is used for the estimation of the crystallite size and the microstrain. From the value of FWHM, the microstrain and crystallite size have been estimated by using Williamson-Hall method. The detailed explanation of the microstrain calculation and crystallite size estimation is given in the section 7.1.1.4 (Chapter 7).
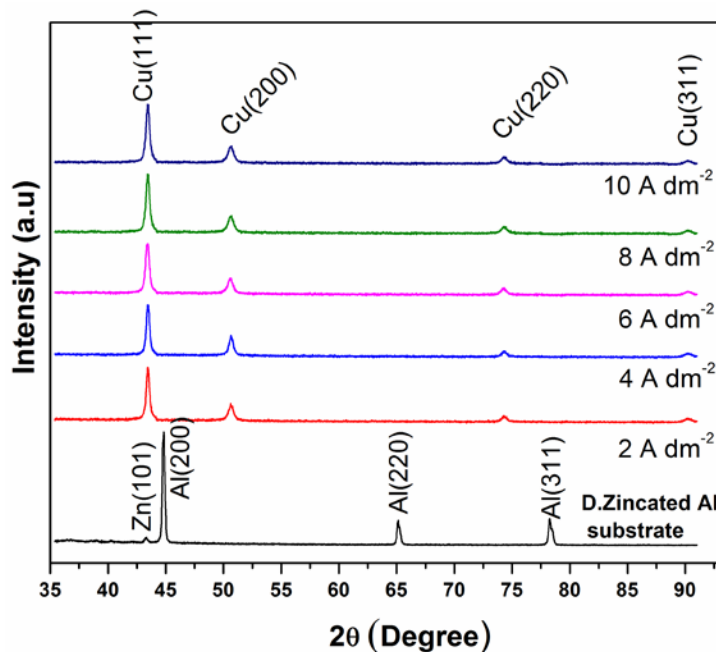
Figure 4.12 X-ray diffraction profiles of the copper coating deposited with different coating current densities (ICDD#89-2838).
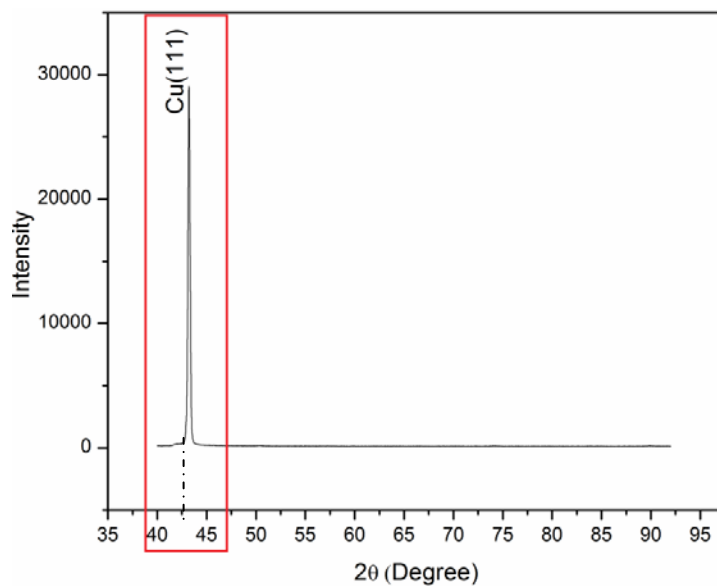
Figure 4.13 XRD profile corresponding to the thick coating deposited with 10 A dm^{-2} current density indicating (111) texture.
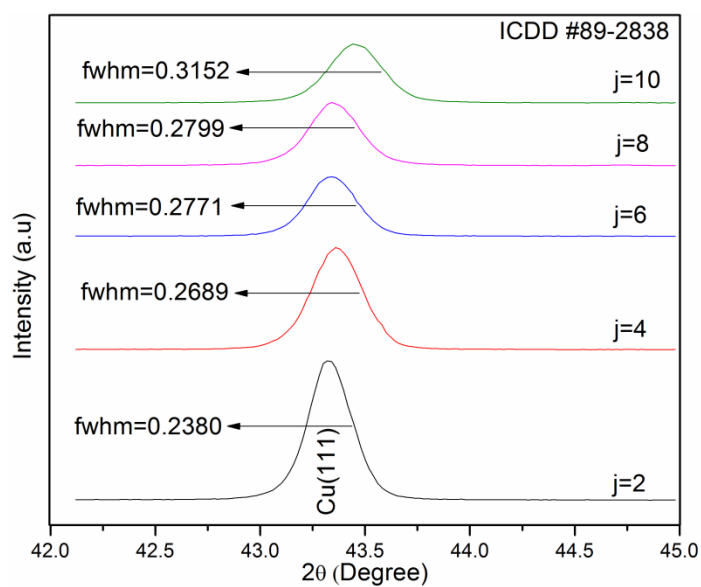
Figure 4.14 FWHM values at 43.316° corresponding to coating deposited with different coating current densities (j).

4.1.3 Mechanical characterization

Hardness and adhesion strength are the major mechanical characteristics of the coating required for the antimicrobial touch surface applications. The surface hardness of the coating is estimated by using scratch hardness test and microhardness test. The adhesion strength of the copper coating to the substrate is evaluated by using cross-hatch cut test and pull off adhesion test.

4.1.3.1 Scratch hardness test

Scratch hardness value gives the scratch resistance of the material against the indenter which moves tangentially along the sample surface. Scratch hardness depends on multiple parameters, like, coating material, friction between the coating and the indenter, surface roughness and thermal conductivity (ASTM G171-03). Figure 4.15 shows the top view of the scratches imprinted on the copper coating deposited with varying current densities. For this purpose, all the coatings have been produced with a fixed thickness of 20 ± 1 μm. The values of the scratch hardness (Hs) are obtained from equation (4.5) (Beegan et al., 2007).

$$Hs = (8F_N) / (\pi b^2) \tag{4.5}$$

where, 'F_N' is the normal force used and 'b' is the average scratch width. The average values of the scratch width and scratch hardness obtained by using equation (4.5) are tabulated in Table 4.2. It is seen that the scratch width is continuously varying with the current density. The highest hardness is obtained for the coating current density of 10 A dm^{-2}.
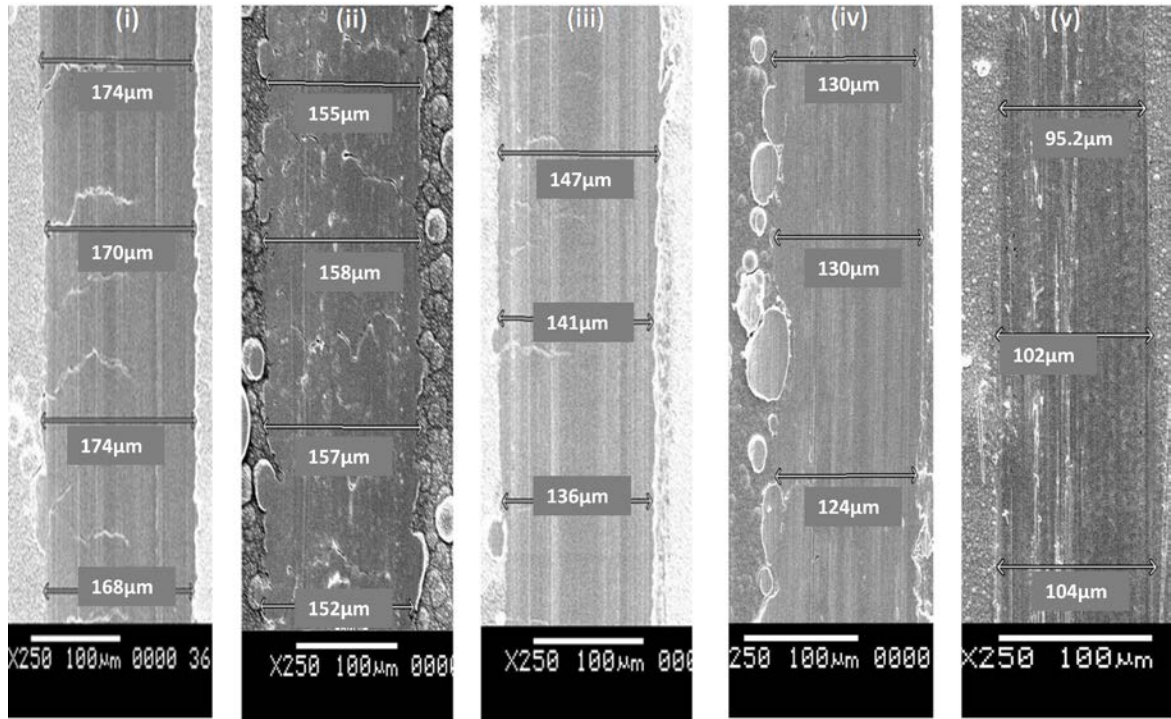
Figure 4.15 SEM micrographs of the scratches, with scratch width on the samples deposited with of (i) 2 A dm^{-2}, (ii) 4 A dm^{-2}, (iii) 6 A dm^{-2}, (iv) 8 A dm^{-2} and (v) 10 A dm^{-2}, respectively.

4.1.3.2 Microhardness analysis

Microhardness test is a static indentation hardness test and it gives indentation resistance of the material against the compression load acting perpendicular to the coating. Microhardness measurements on the copper coating deposited with different current densities are given in Table. 4.2. It reveals that as coating current density changes, the microhardness values vary. Among the measured values, highest microhardness of 2.05±0.11 GPa is recorded on the deposit in which the deposition current density was 10 A dm^{-2}. This value is about 4 times greater than that of the annealed copper (0.49 GPa) (European copper institute, 2015). Further, the microhardness values were closer to the scratch hardness values (Table 4.2), for a given coating.

Table 4.2 Scratch hardness and microhardness values of the coating deposited with different coating current densities

Current density (A dm^{-2})	Average scratch width (μm)	Scratch hardness (GPa)	Microhardness (GPa)
2	171	0.868	0.8±0.10
4	155	1.05	0.98±0.11
6	141	1.277	1.15±0.10
8	128	1.55	1.26±0.12
10	100.4	2.52	2.05±0.11

4.1.3.3 Cross-hatch cut test

According to ASTM D3359, the adhesive strength of the coating could be evaluated qualitatively by using cross-hatch cut test. SEM micrograph of the cross-hatch cut tested sample corresponding to 2, 5 and 10 A dm^{-2} current densities are shown in Figure 4.16, Figure 4.17 and Figure 4.18, respectively. The SEM micrograph in Figure 4.16 (a), Figure 4.17(a) and Figure 4.18 (a) indicates that none of the squares has completely
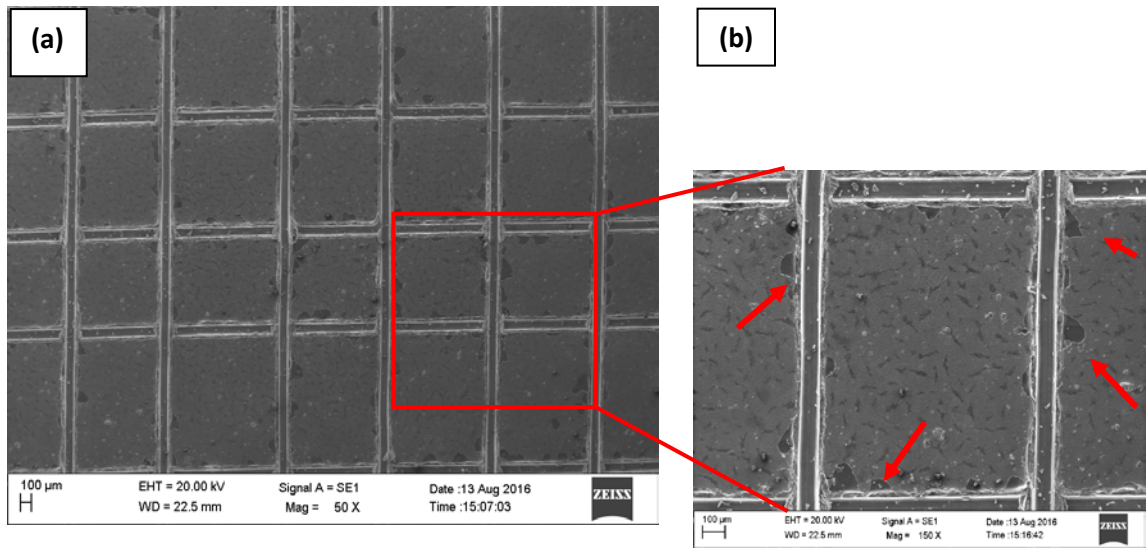
Figure 4.16 a) SEM micrograph of the cross-hatch cut tested sample deposited at 2 A dm^{-2}, and b) magnified images representing the affected area.
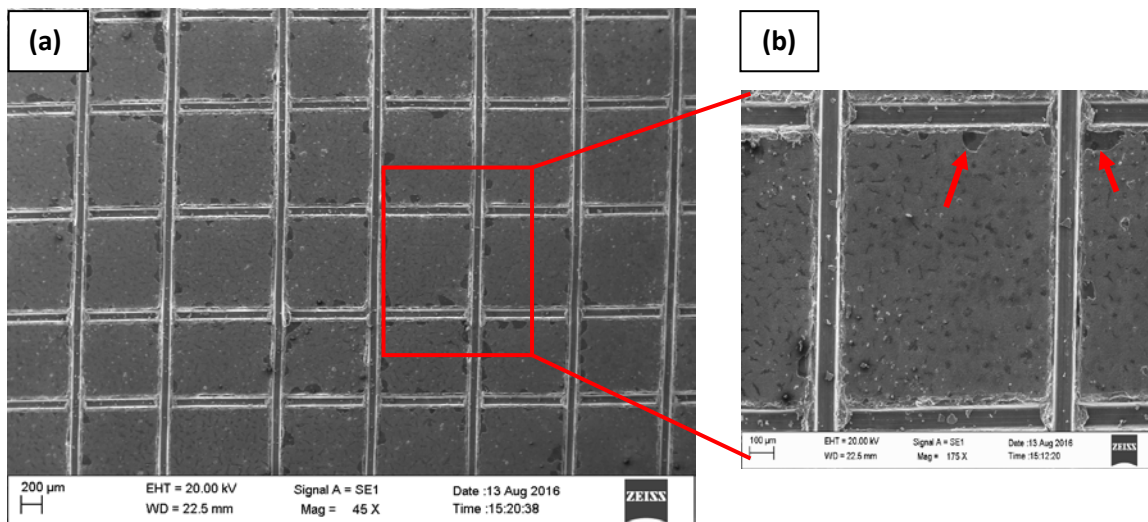
Figure 4.17 a) SEM micrograph of the cross-hatch cut tested sample deposited at 5 A dm^{-2}, and b) magnified image representing the affected area.

peeled-off from the substrate. But small flakes of the coating have been removed near to the cross cut. It is indicated by arrow marks in the magnified images shown in Figure 4.16 (b), Figure 4.17 (b) and Figure 4.18 (b), respectively. The affected area is less than
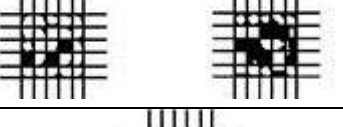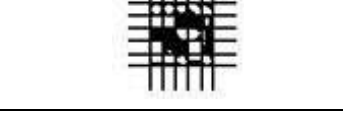
5% of the total cross-hatch tested area. The ASTM adhesion standard is shown in Table 4.3. The visual comparison of the tested sample with the standard indicates that the coating belongs to the 4B class, which represents adequate adhesion strength of the coating to the substrate.
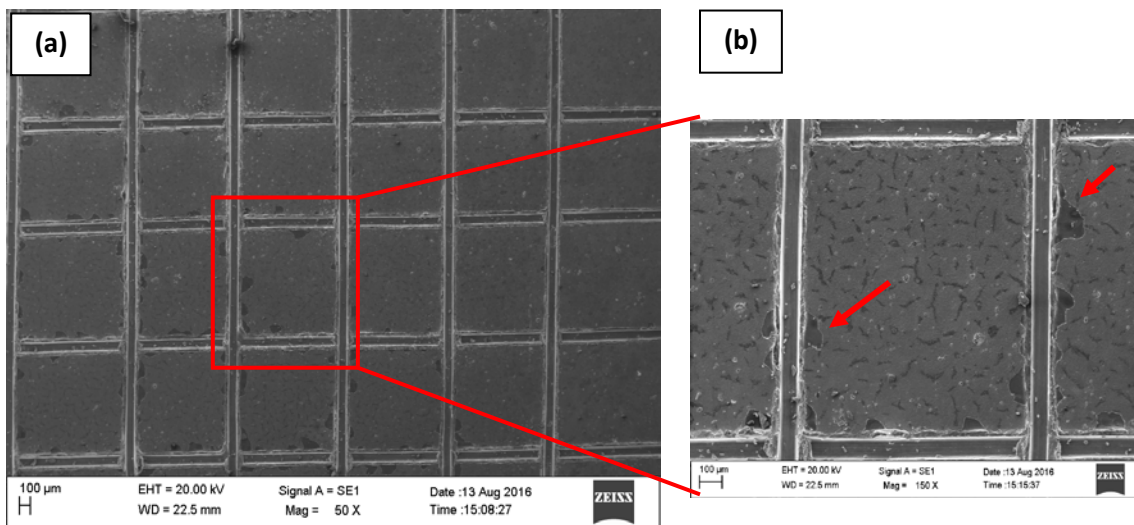
Figure 4.18 a) SEM micrograph of the cross-hatch cut tested sample deposited at 10 A dm^{-2}, and b) magnified image representing the affected area.

Table 4.3 Classification of the coating according to ASTM D3359 adhesion standards

Classification	Percentage area removed	Surface of the cross-cut area from which flaking has occurred for six parallel cut and adhesion range by percentage
5B	0%	
4B	Less than 5%	

3B	5-15%		
2B	15-35%		
1B	35-65%		
0B	Greater than 65%		

4.1.3.4 Pull-off adhesion test

According to ASTM D4541, the adhesion strength of the copper coating to the substrate could be evaluated quantitatively by using pull-off adhesion test. The test result shows that the coating is completely peeled off at 1.2±0.25 MPa pull-off strength. The photographs of the tested samples corresponding to different coating current densities are shown in Figure 4.19, which indicates the complete detachment of the coating from the substrate at the interface of the copper and zinc.
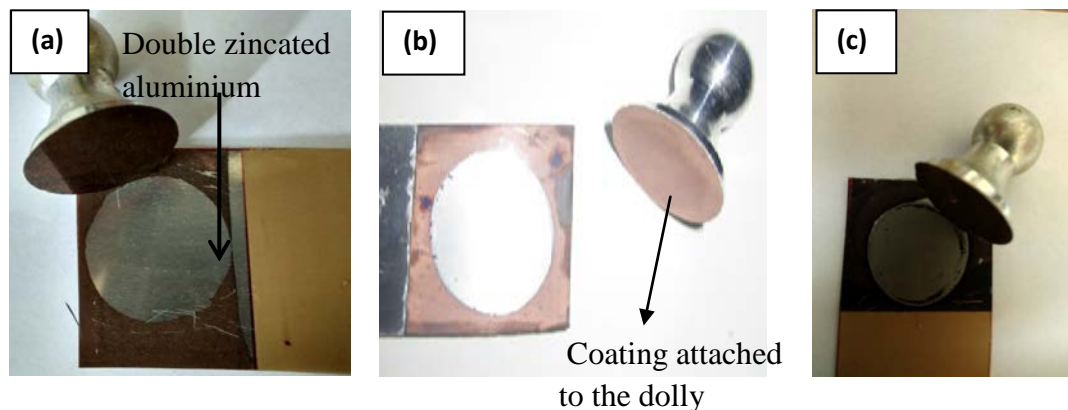
Figure 4.19 Photograph of the pull-off adhesion tested sample along with dolly, corresponding to a) 2 A dm^{-2}, b) 5 A dm^{-2} and c) 10 A dm^{-2} current density values.

4.2 Copper Coating from the Bath-II

In this section, the microstructural features and mechanical properties of the copper deposits from the Bath-II on the double zincated aluminium substrate have been presented.

4.2.1 Physical observations

The coated samples obtained from the optimized range of current densities (1A dm^{-2} to 4 A dm^{-2}) were observed as uniform and compact. The salmon colored shiny coating was observed for all the current densities used for the deposition. The variation in the Ra values (coating roughness) with the coating current density is given in Table 4.4. The roughness of the coating was varying from 0.262 μm to 0.453 μm when coating current density was varied from 1 to 4 A dm^{-2}. The roughness profile of the coating deposited by using current density 4 A dm^{-2} is shown in Figure 4.20.

Table 4.4 Variation of the surface roughness of the coating with the deposition current density

Coating current density, A dm^{-2}	1	2	3	4
Surface roughness (Ra), μm	0.262±0.007	0.322±0.009	0.453±0.009	0.40±0.008

STAND   JIS2001
PROFILE   R
FILTER   GAUSS
EVA-L   2.4mm
N   3
λc   0.8mm
λs   2.5μm
TILT-COMP.   ALL
M-SPEED 0.25mm/s
RANGE   AUTO
                 ESC
PRE/POST   ON
DRIVE   STAND
R-PROFILE
EVA-L   2.4mm
λc   0.8mmX3

Ra   0.40μm
Rz   2.47μm
Rq   0.49μm
R-PROFILE
EVA-L   2.4mm
λc=0.8mmX3
        →× 10K
    ×50

Ver.   1.0μm/cm
Hor.   200.0μm/cm
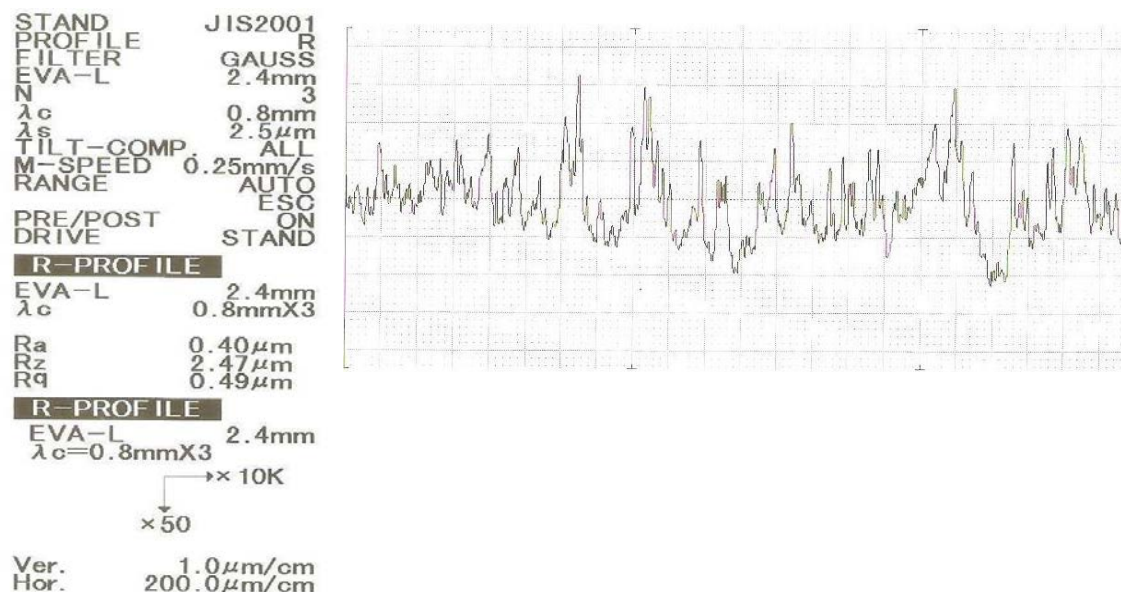
Figure 4.20 Roughness profile of the deposit corresponding to coating current density of 4 A dm^{-2}.

4.2.2 Microstructural characterization

In this section, the microstructural characterization of the copper deposited at different coating current densities by using SEM, TEM and XRD have been presented.

4.2.2.1 Scanning electron microscopic study

The SEM micrographs (topography) of the copper coatings deposited at different current densities are shown in Figure 4.21. It is observed that the coatings contain nodules of different sizes. With the increase in the coating current density, the size and distribution changed. At 1 A dm^{-2} current density, a primary layer is formed with a nodular diameter of 1.08±0.1μm. As coating current density is increased, the primary nodular size reduces. At 4 A dm^{-2}, the primary nodular size is 0.77± 0.1 μm. So, the increase in the current density during deposition from 1 A dm^{-2} to 4 A dm^{-2} reduces the primary nodular size by 28.7 %. As the coating current density increases, the nodules protrude unevenly and randomly in the perpendicular direction to the substrate as shown in Figure 4.21 (b-c).

79

The size of such nodules is 3.4±0.6 μm. The coating with 1 A dm^{-2} was observed as highly uniform compared to that deposited with higher current density. This could be clearly depicted in the higher magnified SEM micrographs shown in Figure 4.22. The cross sectional SEM micrograph shown in Figure 4.23 gives more insight about the growth nature of the coating. The average size of the nodules is 2.6 μm with a standard deviation of 1.36 μm. The distribution of nodules' size obtained from the SEM micrograph is shown in Figure 4.24. The ultrahigh purity of the coating has been confirmed from the EDS measurement. The result of the coating deposited by using 4 A dm^{-2} current density is given in Figure 4.25.
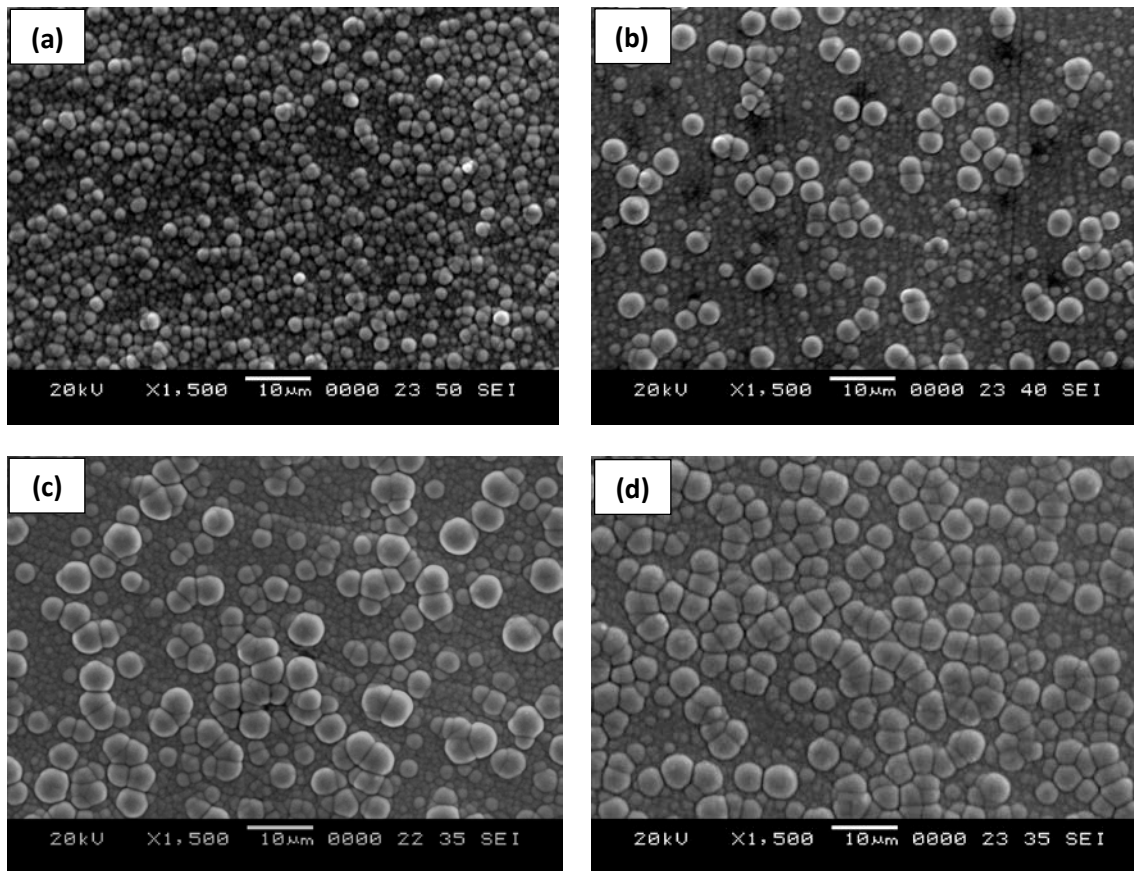
Figure 4.21 SEM micrographs (topography) of the copper coating on the double zincated aluminium deposited with different current densities a) 1 A dm^{-2}, b) 2 A dm^{-2}, c) 3 A dm^{-2}, and d) 4 A dm^{-2}, respectively.
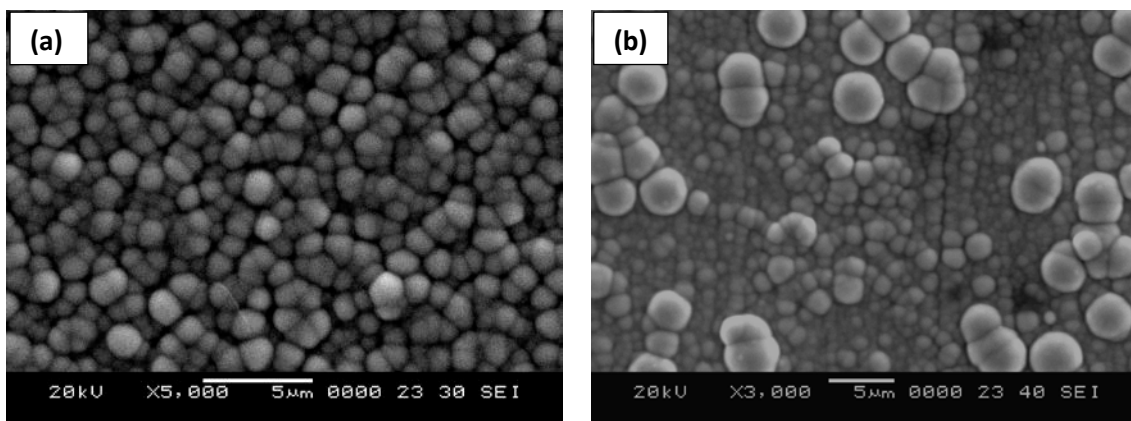
Figure 4.22 Magnified image of the coating deposited with current densities of a) 1 A dm^{-2} and b) 3 A dm^{-2}, respectively.
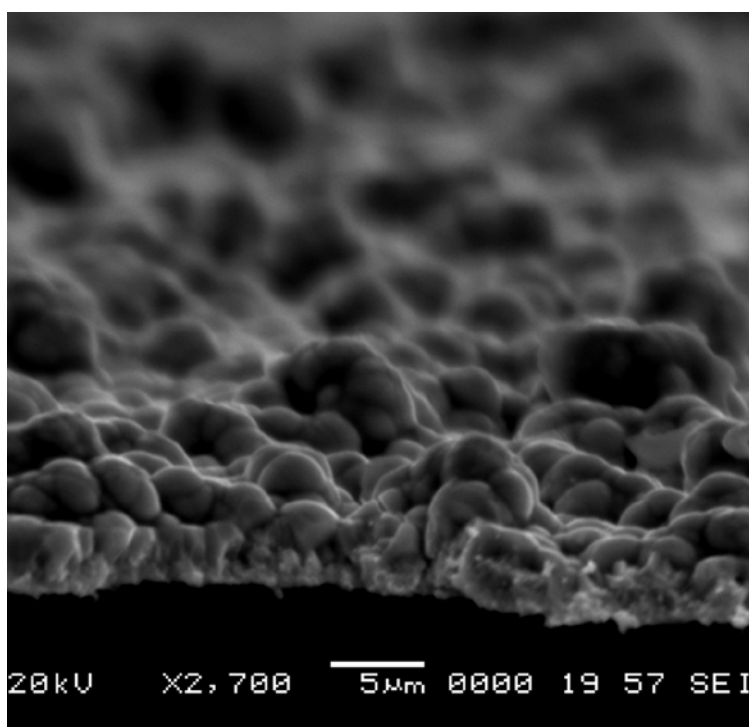
Figure 4.23 Cross sectional SEM micrograph of the coating deposited with 4 A dm^{-2} current density.
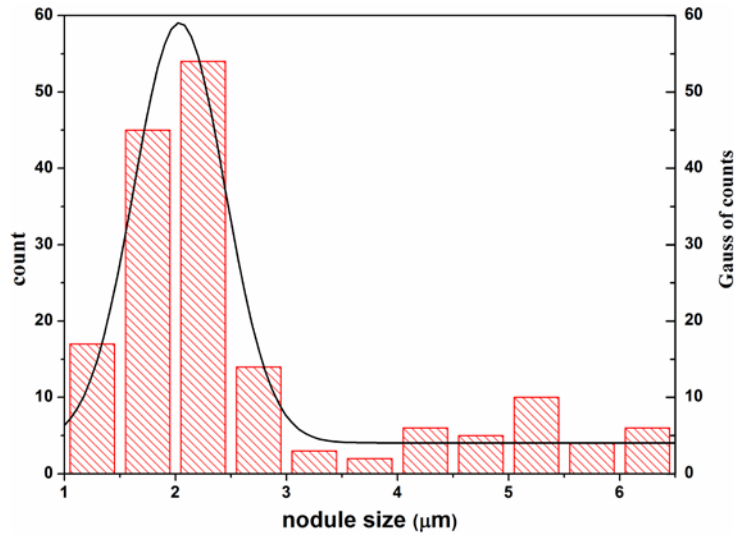
Figure 4.24 Nodules' size distribution of the copper coating deposited by using Bath-II.
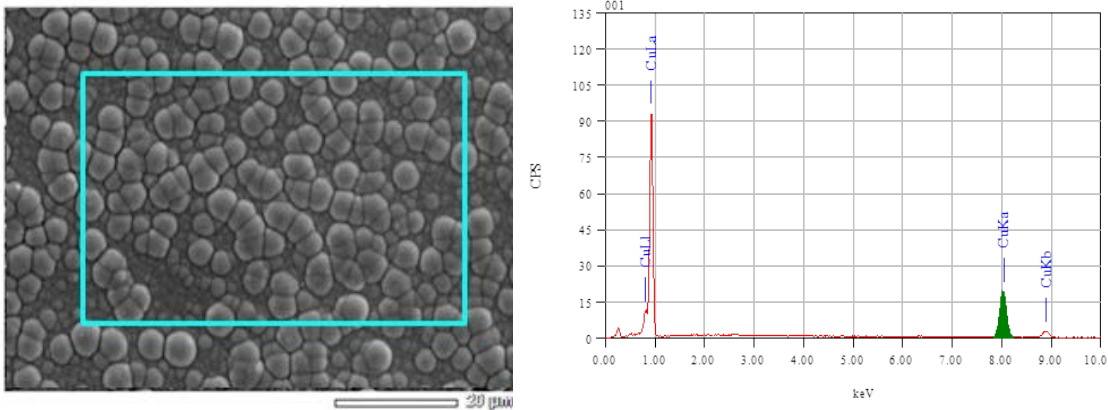
Figure 4.25 EDS results on the coating corresponding to 4 A dm^{-2} current density.

4.2.2.2 Transmission electron microscopic study

Transmission electron micrographs of the copper coatings on the double zincated aluminium which were deposited with a coating current density of 1 A dm^{-2} is shown in Figure 4.26 (a). The TEM micrograph showed that the coating is composed of fine, equiaxed copper crystallites. The crystallite size distribution is expressed by the histogram shown in Figure 4.26 (b). From the crystallite size distribution, the average size is obtained as 17.6 nm with a standard deviation of 5.4 nm. The nucleation density of

the copper crystallite was found to be 4.2×10^{11} cm^{-2}. The continuous rings in the SAED pattern shown in Figure 4.26 (c) indicate the nano size of the crystallites.
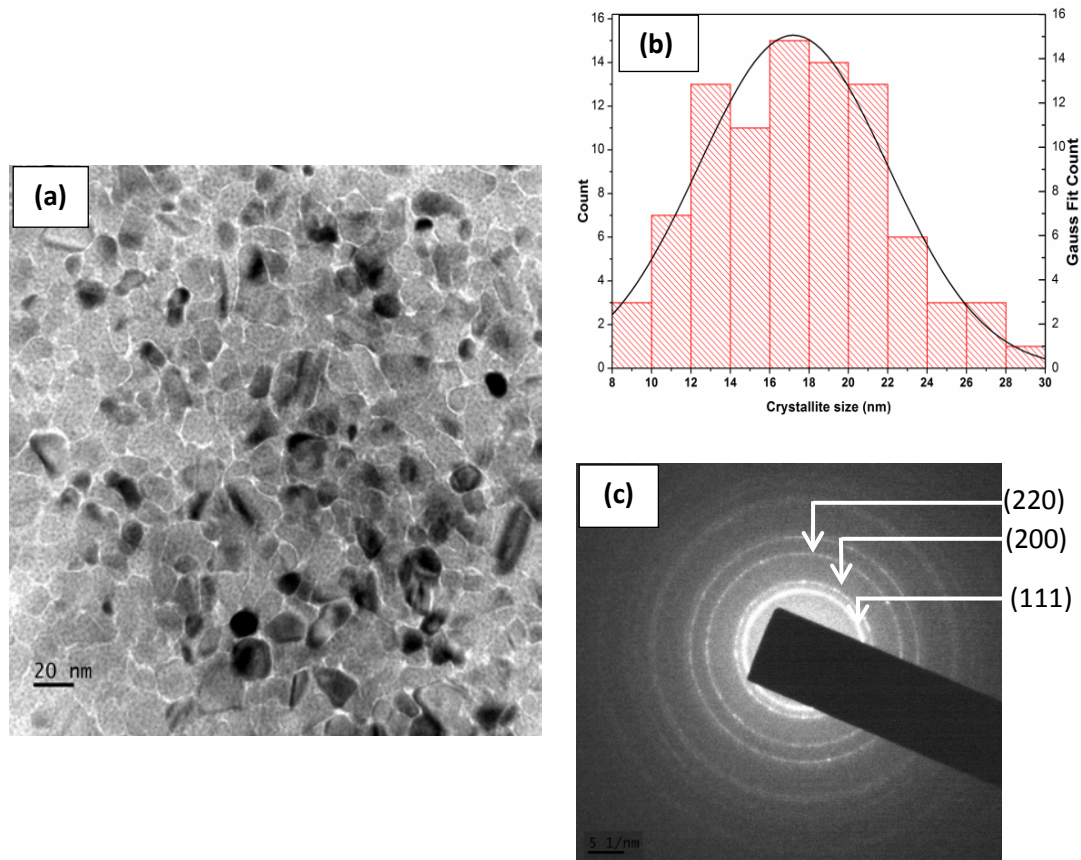
Figure 4.26 (a) Bright field TEM micrograph of the copper coating deposited at current density of 1 A dm^{-2}, (b) histogram representing the crystallite size distribution and (c) SAED pattern of the coating.

Figure 4.27 (a) shows the bright field TEM micrograph of the coating deposited with a current density of 4 A dm^{-2}. The micrograph indicates that the coating consists of equiaxed crystallites. Moreover some of the crystallites contain nano sized twins (indicated by arrow marks in Figure 4.27 (a)). Figure 4.27 (b) shows one of the twins at higher magnification, where the width of the twins is less than 5 nm. Crystallite size distribution is expressed by the histogram shown in Figure 4.27 (c). From the large
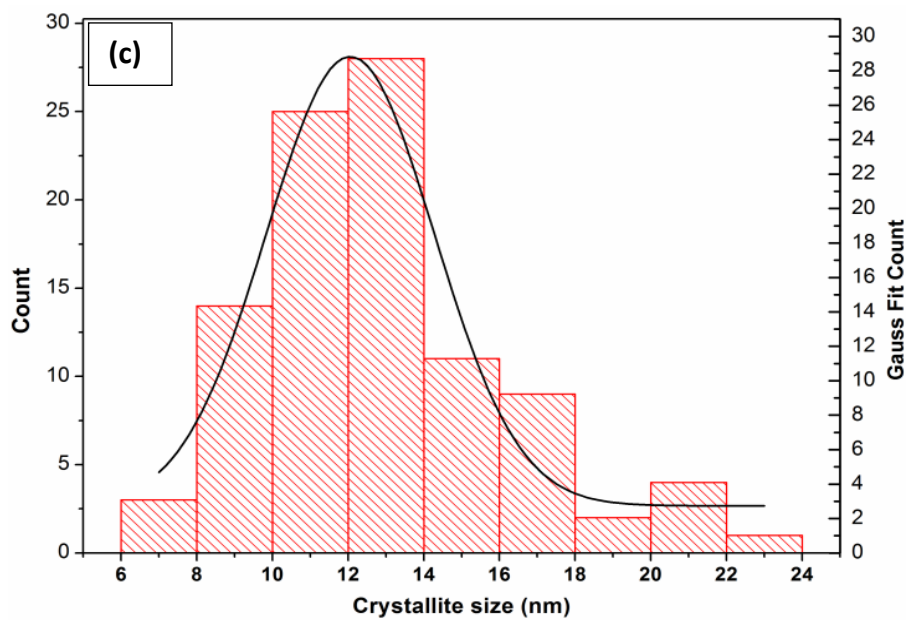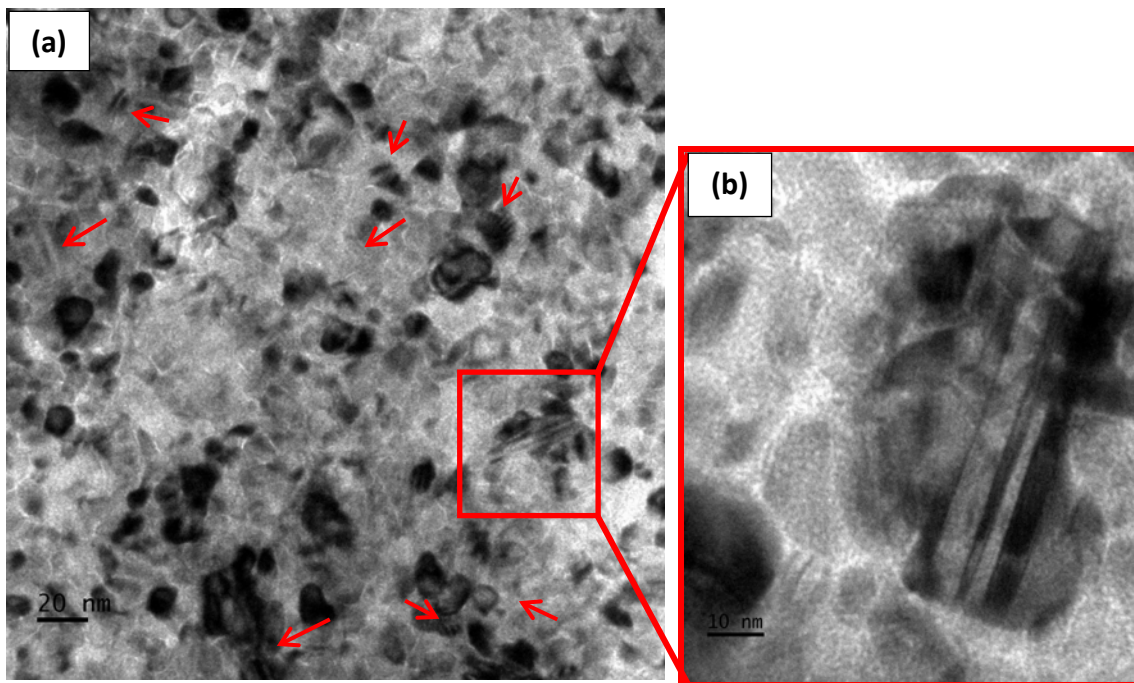
Figure 4.27 (a) Bright field TEM micrograph of the copper coating deposited with the current density of 4 A dm^{-2} , (b) magnified image of nano-twins, and (c) histogram of the crystallite distribution corresponding to Figure 4.27(a).
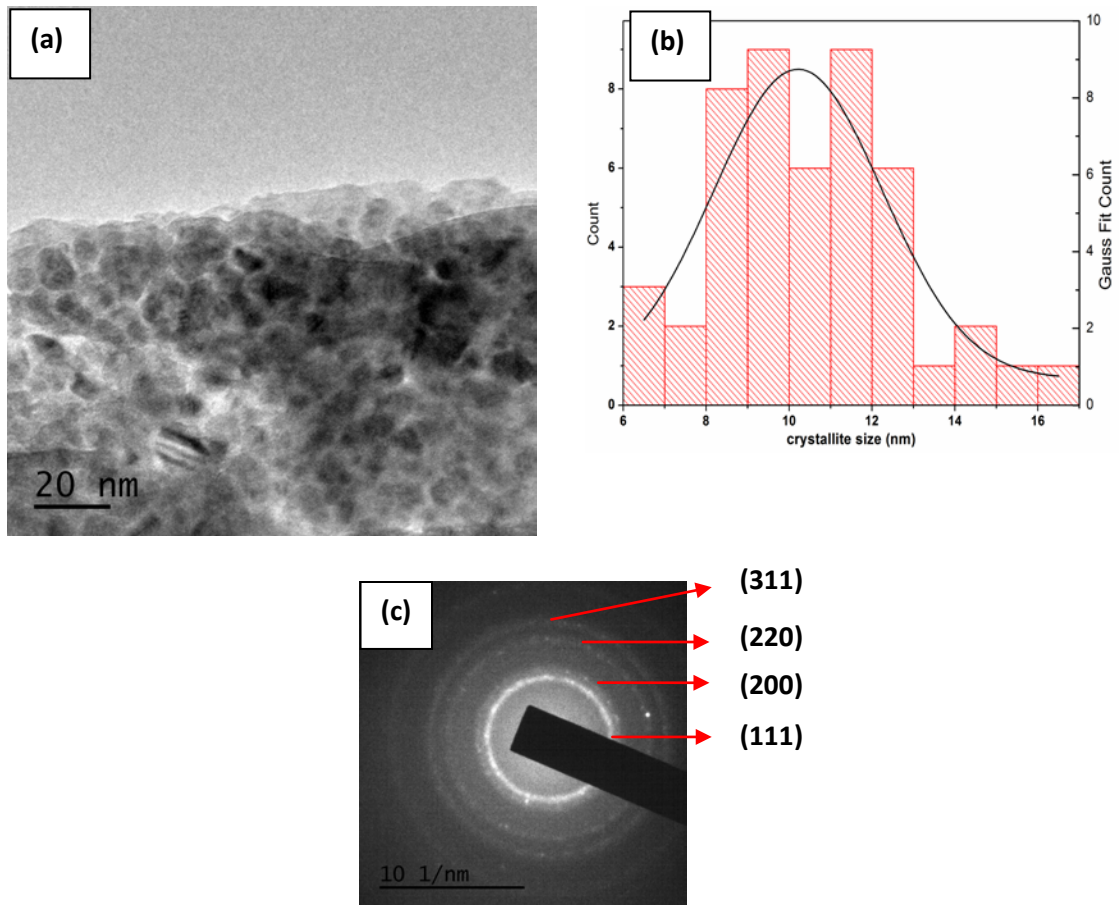
Figure 4.28 a) Bright field TEM micrograph (cross sectional) of copper coating deposited with the current density of 4 A dm^{-2} , b) histogram representing the crystallite size distribution and c) SAED pattern of the same.

numbers of crystallite size measurement, the average crystallite size was obtained as 12.9 nm with a standard deviation 3.6 nm. Because of such ultra-fine crystallites, the nucleation density of copper crystallite in 4 A dm^{-2} was found to be 6.8 x 10^{11} per cm^2.

4.2.2.3 X-ray diffraction study

The x-ray diffraction patterns of the copper coating deposited with different current densities are shown in Figure 4.29. The diffraction peaks corresponding to different crystallographic planes were analyzed and found that FWHM (full width half maxima) of

the peaks was increased with increase in the coating current densities. This could be attributed to the reduction in the crystallite size as well as increase in the microstrain (Biju et al. 2008). The microstrain and crystallite size has been calculated from the XRD profile corresponding to different coating current densities using Williamson-Hall method. The detailed explanation for the estimation of the microstrain and the crystallite size from Williamson-Hall method is given in section 7.1.1.4 (Chapter 7).
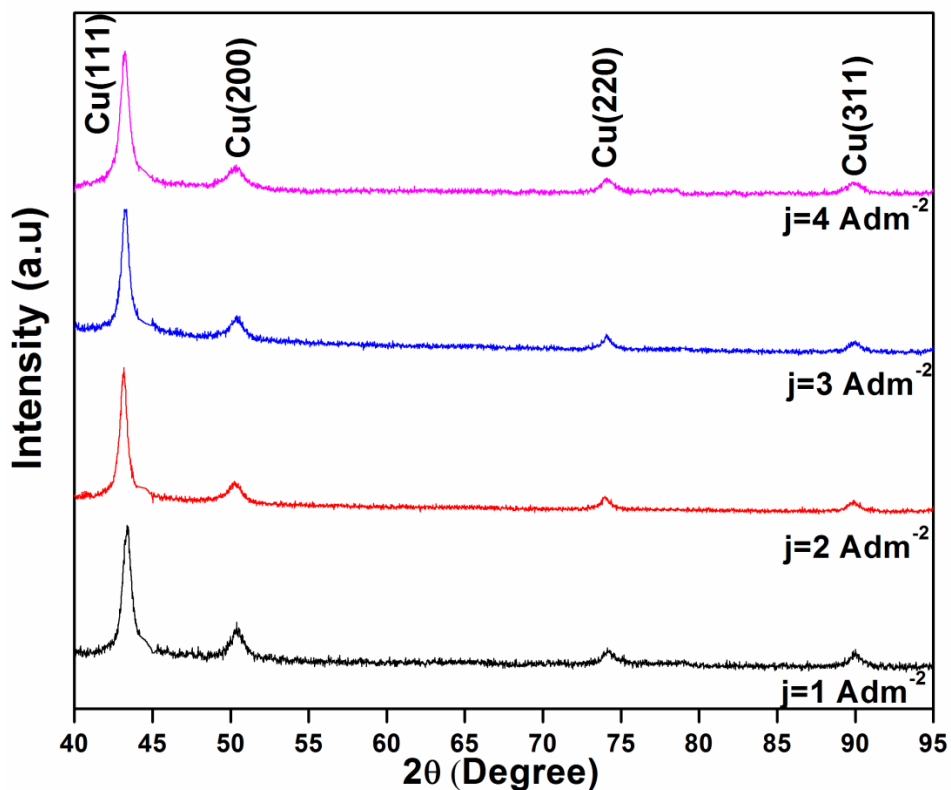
Figure 4.29 X-ray diffraction profile of the copper coatings deposited with different current densities (j).

4.2.3 Mechanical characterization

The mechanical characteristics of the coatings such as hardness and adhesion strength have been evaluated for the coatings deposited with different current densities. The surface hardness is estimated by using scratch hardness test and the microhardness test.

The adhesion strength has been evaluated by using the cross-hatch cut test and pull-off adhesion test.

4.2.3.1 Scratch hardness test

Figure 4.30 shows the SEM images of the scratch hardness tested samples deposited at different coating current densities. The average value of the scratch width corresponding to each current density is shown in Table 4.5. The scratch hardness of the each coating is calculated by using equation 4.5 given in Table 4.5. The maximum hardness value is obtained for the coating deposited with current density of 1 A dm^{-2}.
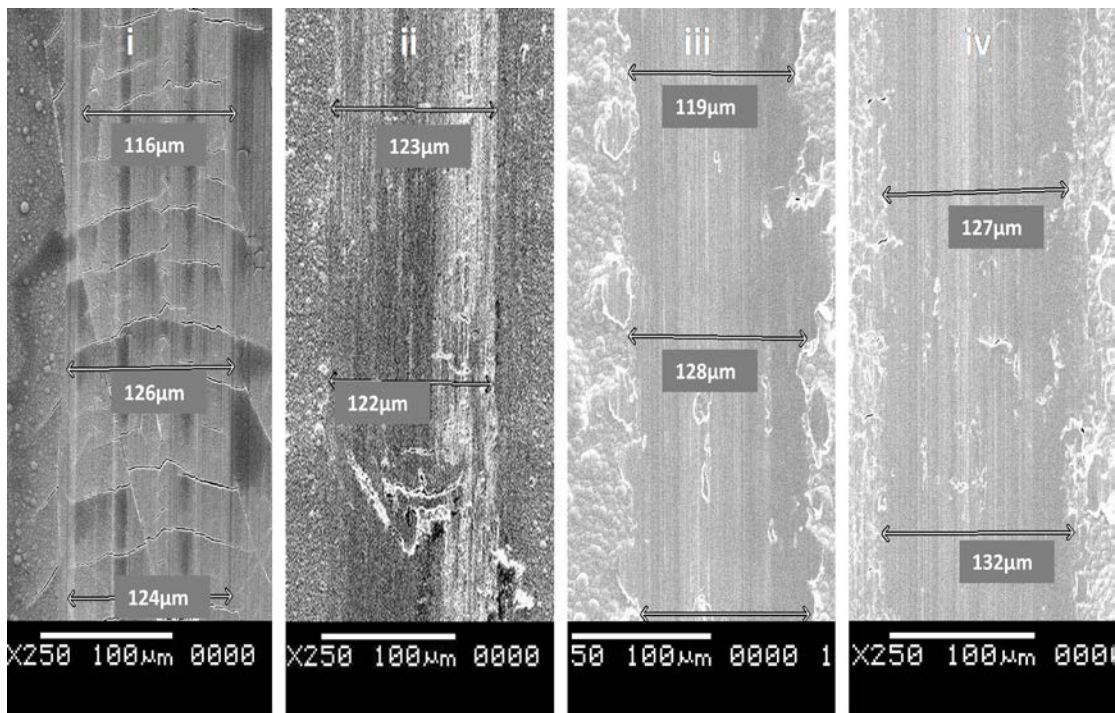
Figure 4.30 SEM micrographs of the scratches on the coated samples with the scratch width dimensions on it. The micrographs correspond to coating deposited with current densities of (i) 1 A dm^{-2}, (ii) 2 A dm^{-2}, (iii) 3 A dm^{-2}, and (iv) 4 A dm^{-2}, respectively.

4.2.3.2 Microhardness test

The microhardness values of the coating deposited with different coating current densities are given in Table 4.5. The highest value of the microhardness is registered for the coating deposited with 1 A dm^{-2}. There is not much difference in the hardness values among the coatings deposited with different current densities.

Table 4.5 Scratch hardness and microhardness values of the coating deposited with different coating current densities

| Current density (A dm^{-2})	Average scratch width (μm)	Scratch hardness (GPa)	Microhardness (GPa)
1	121.7	1.72	1.46±0.12
2	123	1.68	1.41±0.09
3	125	1.62	1.34±0.08
4	130	1.5	1.22±0.9

4.2.3.3 Cross-hatch cut test

Adhesion strength between the copper coating and the double zincated aluminium substrate was evaluated qualitatively by using cross-hatch cut test. Figure 4.31 and Figure 4.32 shows the SEM images of the cross-hatch cut tested sample deposited with 1 A dm^{-2} and 4 A dm^{-2}, respectively. None of the cross-hatched squares were detached as shown in Figure 4.31 (a) and Figure 4.32 (a). The magnified images shown in Figure 4.31 (b) and Figure 4.32 (b) indicate that the coating flakes are also not removed at the intersection of the cross-hatch. As a result, the percentage area affected by the cross-hatch test is zero. So, as per the visual comparison with ASTM D3359 standard shown in Table 4.3, the coating could be included in the category of 5B class.
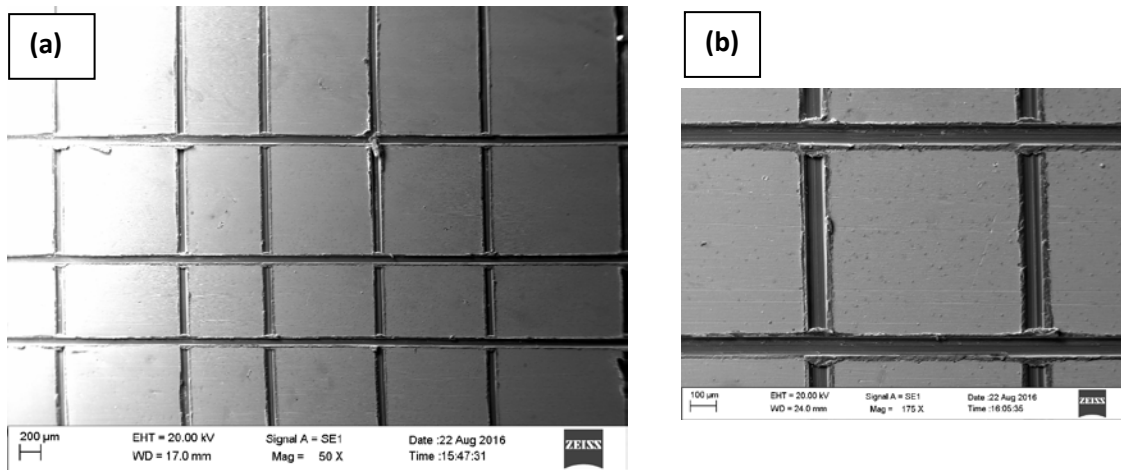
Figure 4.31 a) SEM micrograph of the cross-hatch cut tested sample deposited with coating current density of 1 A dm^{-2}, and b) magnified image representing affected area**.**
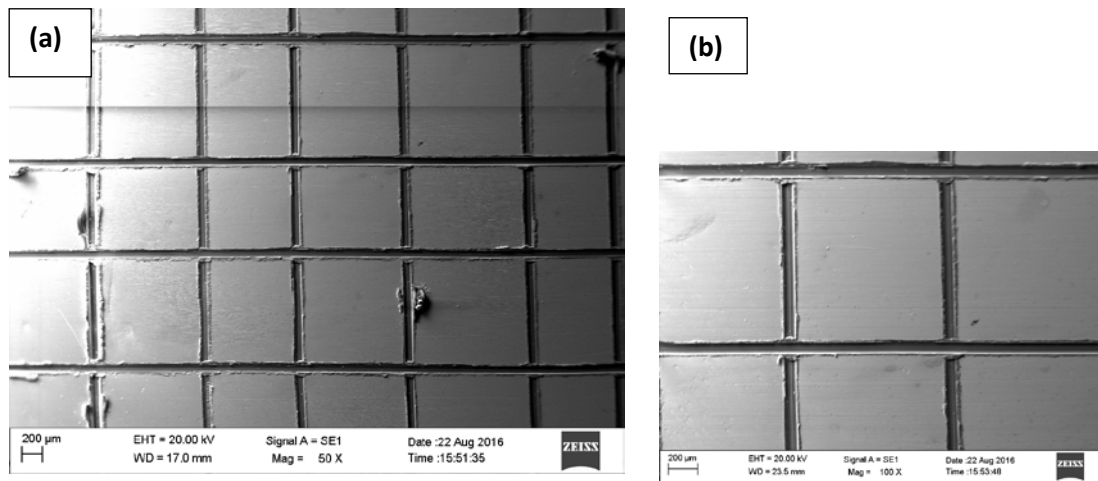
Figure 4.32 a) SEM micrograph of the cross-hatch cut tested sample deposited with coating current density of 4 A dm^{-2}, and b) magnified image representing affected area.

4.2.3.4 Pull-off adhesion test

Adhesive strength of the coating with the substrate deposited at different current densities has been measured using pull-off adhesion tester. All samples are showing excellent adhesive strength to the double zincated aluminium substrate. The dolly has detached

from the copper coating at pull-off adhesion strength of 1.9±.2 MPa irrespective of the coating current density used. The photograph of the pull-off adhesion tested samples corresponding to 1A dm^{-2} and 4 A dm^{-2} are shown in Figure 4.33. Hence it is concluded that the coatings do have an adhesion strength >1.9 MPa.
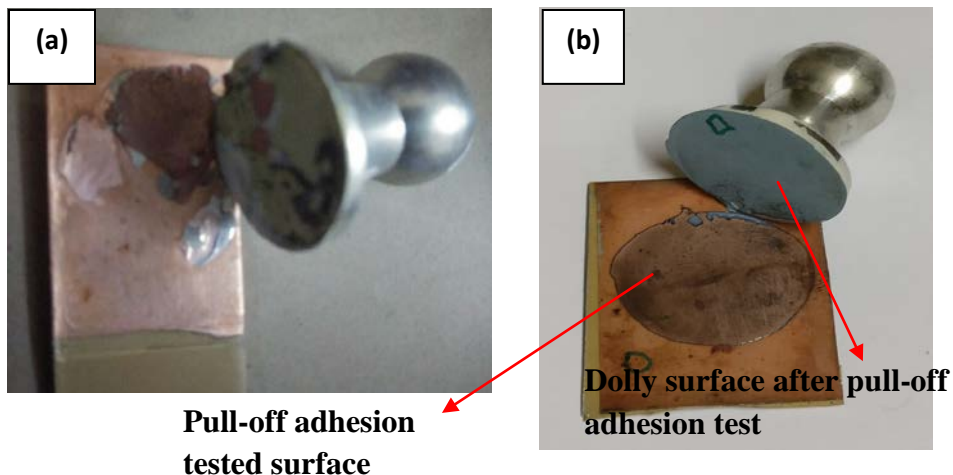
Figure 4.33 Photograph of the pull-off adhesion tested samples with the dolly for the coating deposited with the coating current density of a) 1 A dm^{-2} and b) 4 A dm^{-2}, respectively.

4.3 Summary of the Chapter

a) Copper coating from the Bath-I

The copper coating deposited from the Bath-I with optimized current density range of 1 A dm^{-2} to 10 A dm^{-2} has been characterized for microstructural features and mechanical properties. Physical observation shows that the coating has a salmon colour. The morphological study of the coating by using SEM shows the nodular structure with a nodular size of 4 μm to 6 μm. The TEM micrographs of the coating show that each nodule is formed by nano sized crystallites of average size varying from 63 nm to 32 nm. The crystallite size varies with the coating current density. At higher deposition current density, the presence of nano-twins of 3 nm to 7 nm width was confirmed. The preferred orientation along (111) plane of the copper coatings is confirmed by using XRD. As the

coating current density increases, FWHM of the peaks increases. The hardness of the coating has been tested by using scratch hardness test and microhardness tests. The highest value of the hardness is observed for the coating corresponding to 10 A dm^{-2} current density. The adequate adhesion strength of the coating to the substrate was confirmed from the cross-hatch cut test and the pull-off adhesion test.

b) Copper coating from the Bath-II

Adherent and shiny coating was obtained from the newly optimized non-cyanide alkaline bath. The optimized current density was in the range of 1 A dm^{-2} to 4 A dm^{-2}. The SEM study showed that the coating constitutes nodules ranging in size from 0.77 μm to 1.08 μm. Each nodule is composed of nano sized crystallites of size varying from 12.9 nm to 17.6 nm which change with coating current density. As coating current density increases, the crystallite size reduces. At higher coating current densities, some of the crystallites contain nano-twins. The preferred growth of the copper coating along (111) direction is confirmed from the XRD profiles. The surface hardness of the coating has been tested by using scratch hardness test and microhardness tests. It is inferred that as the coating current density increases, the hardness value reduces. The adhesion strength of the coating with the double zincated aluminium substrate was tested by using cross-hatch cut test and pull-off adhesion tests. Excellent adhesion strength was observed in both cross-hatch cut test and pull-off adhesion tests.

List of publications related to Chapter 4

1. Arun Augustin, Udaya Bhat.K, K. Rajendra Udupa, Chitharanjan Hegde (2015). "Electron Microscopic Study of Nodules formed during Electrodeposition of Copper on Aluminium". Materials Science Forum, Trans Tech Publications, vols. 830-83: pp 371-374.

2. Arun Augustin, Udupa, K.R. and Bhat, K.U. (2016). "Effect of coating current density on the wettability of electrodeposited copper thin film on aluminium substrate", Perspectives in Science Elsevier Publishing, vols. 8: pp 472-474.

3. Arun Augustin, K. Rajendra Udupa, and Udaya Bhat (2016). "Crystallite size measurement and micro-strain analysis of electrodeposited copper thin film using Williamson-Hall method." Proceeding of International Conference on Condensed Matter and Applied Physics, AIP Publishing, Vol. 1728. No. 1.

4. Arun Augustin, Huilgol, P., Udupa, K.R. and Bhat, U. (2016). "Effect of Current Density during Electrodeposition on Microstructure and Hardness of Textured Cu Coating in the Application of Antimicrobial Al Touch Surface." Journal of the Mechanical Behavior of Biomedical Materials, Elsevier Publishing 63, 352–360.

5. Udaya Bhat K, Arun Augustin, Suma Bhat and Udupa K. (2018). "Preparation and characterization of copper thin films for antimicrobial applications" Microscopy Applied to Materials Sciences and Life Sciences, Apple Academic Press.

Chapter 5

DC MAGNETRON SPUTTER DEPOSITED COPPER COATINGS: MICROSTRUCTURAL AND MECHANICAL CHARACTERIZATIONS

In this section, the microstructural features and mechanical properties of the DC magnetron sputter deposited copper coating on the double zincated aluminium substrate has been discussed.

5.1 Physical Observations

Uniform adherent coating was observed for the sputtering power in the range of 50W to 150W. Dark salmon colored coating was observed irrespective of the sputtering power. The variation in the Ra value (coating roughness) with the sputtering power is given in Table 5.1. The Ra value varies from 0.14 μm to 0.18 μm. A typical roughness profile obtained from stylus profilometer corresponding to the coating at 150 W is given in Figure 5.1.

Table 5.1 Variation in the surface roughness of the coating with different sputtering powers

Sputtering power, W	50	100	150
Surface roughness (Ra) in μm	0.18±0.01	0.17±0.01	0.14±0.01
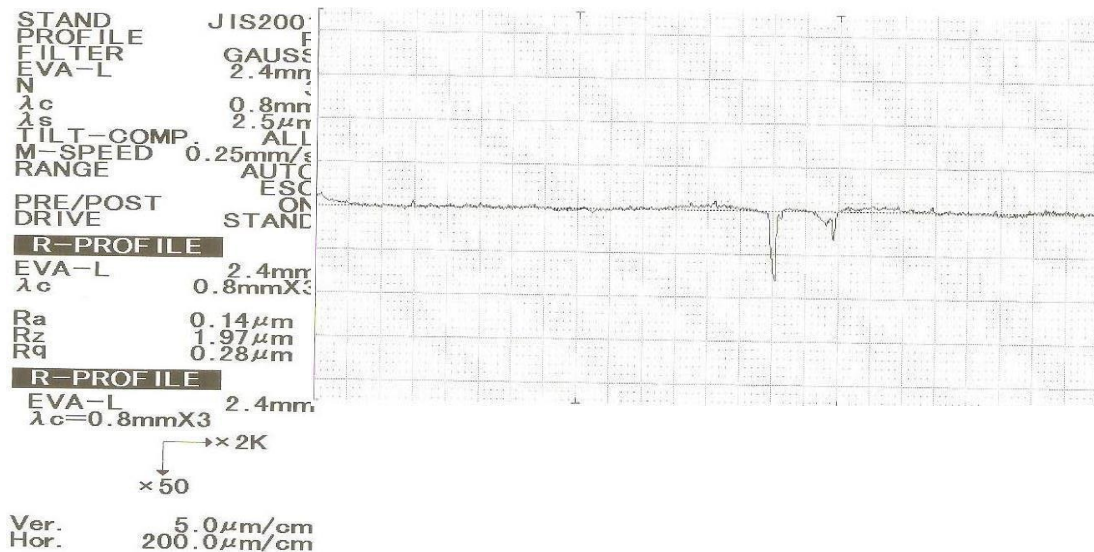
Figure 5.1 Roughness profile corresponding to coating deposited at sputtering power of 150 W.

5.2 Microstructural Characterization

In this section, the microstructural characterization of the copper coatings deposited using different sputtering power is presented. Tools like SEM, TEM and XRD were used for the microstructural characterization.

5.2.1 Scanning electron microscopic study

The SEM micrographs of the copper coating deposited on the double zincated aluminium by using different DC magnetron sputtering power have been shown in Figure 5.2. The coating constitutes uniformly distributed copper nodules with globular topography. As the sputtering power increases from 50 W to 150 W, the size of the nodules decreases. These are given in Table 5.2. Figure 5.3 shows the cross sectional image of the coating corresponding to 50 W and 150 W. It indicates the columnar growth behavior. The EDS result shown in Figure 5.4 indicates that the coating is made up of pure copper. The

94

presence of zinc in the EDS spectra is attributed to the zinc layer in between the copper and the aluminium due to the intermediate zincating step.
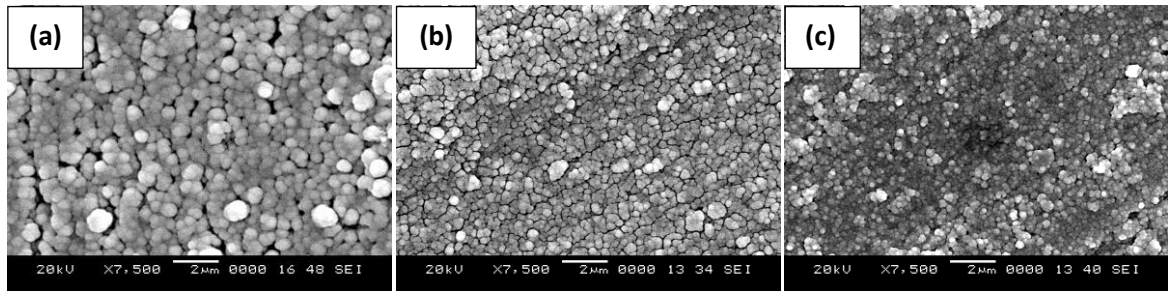
Figure 5.2 SEM micrograph of the sputtered copper coatings with sputtering power of a) 50 W, b) 100 W and c) 150 W, respectively.
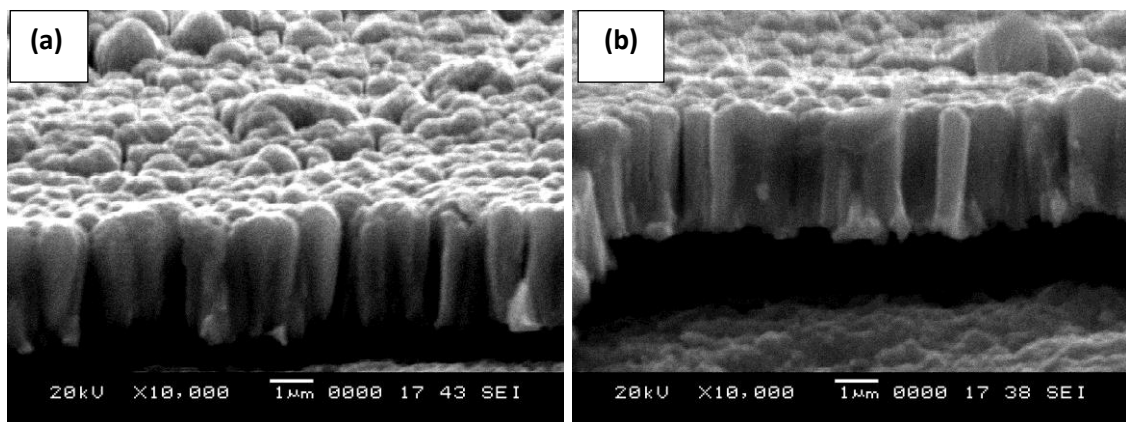
Figure 5.3 Cross sectional SEM micrograph of the sputter deposited copper coating with a sputtering power of a) 50 W and b) 150 W respectively.

Table 5.2 Variation of nodule's size with sputtering power

Sputtering power (W)	50	100	150
Nodule's size (nm)	477.2±36.2	301.15±24	193.4±16.2
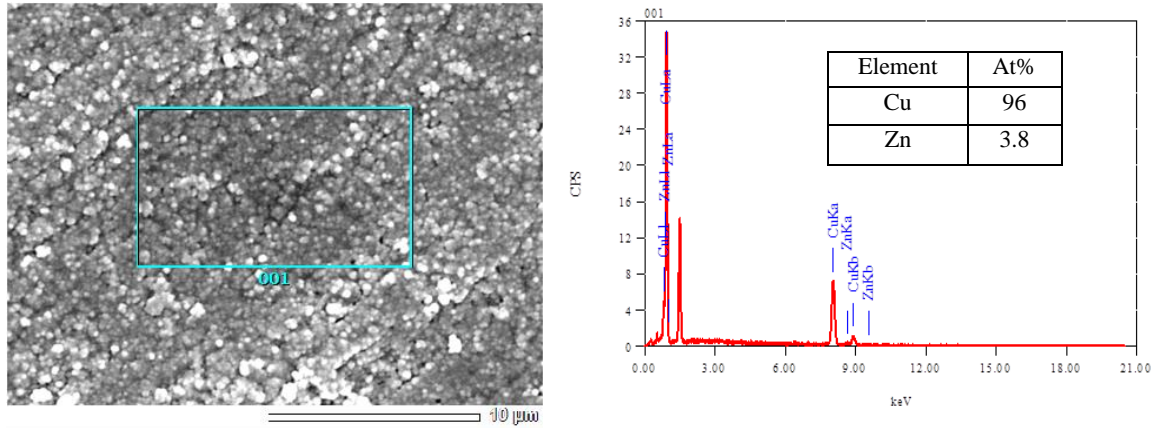
Figure 5.4 EDS results of the selected area in the coating.

5.2.2 Transmission electron microscopic study

Figure 5.5 (a) shows the TEM micrograph of the DC magnetron sputtered copper coatings at sputtering power of 50 W. The average crystallite size is observed as 49 nm with a standard deviation of 15.5 nm. Each nodule is composed of these nano crystallites. The low magnified TEM micrograph of the Figure 5.5(a) shown in Figure 1 (Appendix 1) also proves the same. The continuous rings in the SAED pattern shown in Figure 5.5 (b) indicate the presence of nano sized crystallites corresponding to different crystallographic planes. The histogram shown in Figure 5.5 (c) corresponding to the same indicates the crystallite size distribution.

Figure 5.6 (a) shows the TEM micrograph of the coating deposited with a sputtering power of 100 W. The coating has an average crystallite size of 33.36 nm with a standard deviation of 10.6 nm. The histogram shown in Figure 5.6 (b) shows the crystallite size distribution. Figure 5.7 (a) shows the TEM micrograph of the coating at a sputtering power of 150 W. It shows that the average crystallite size is 18 nm with a standard deviation of 5.24 nm. The histogram shown in Figure 5.7 (c) shows the crystallite size distribution corresponding to Figure 5. 7 (a). As the sputtering power increases from 50 W to 150 W, the crystallite size reduces from 49 nm to 18 nm. Moreover, at higher sputtering power, some crystallites contain nano-sized twins, as shown in Figure 5.7 (d).

The magnified image of the selected twin, shown in Figure 5.7 (e) indicates that twins have a width in the range of 3 nm to 8 nm.
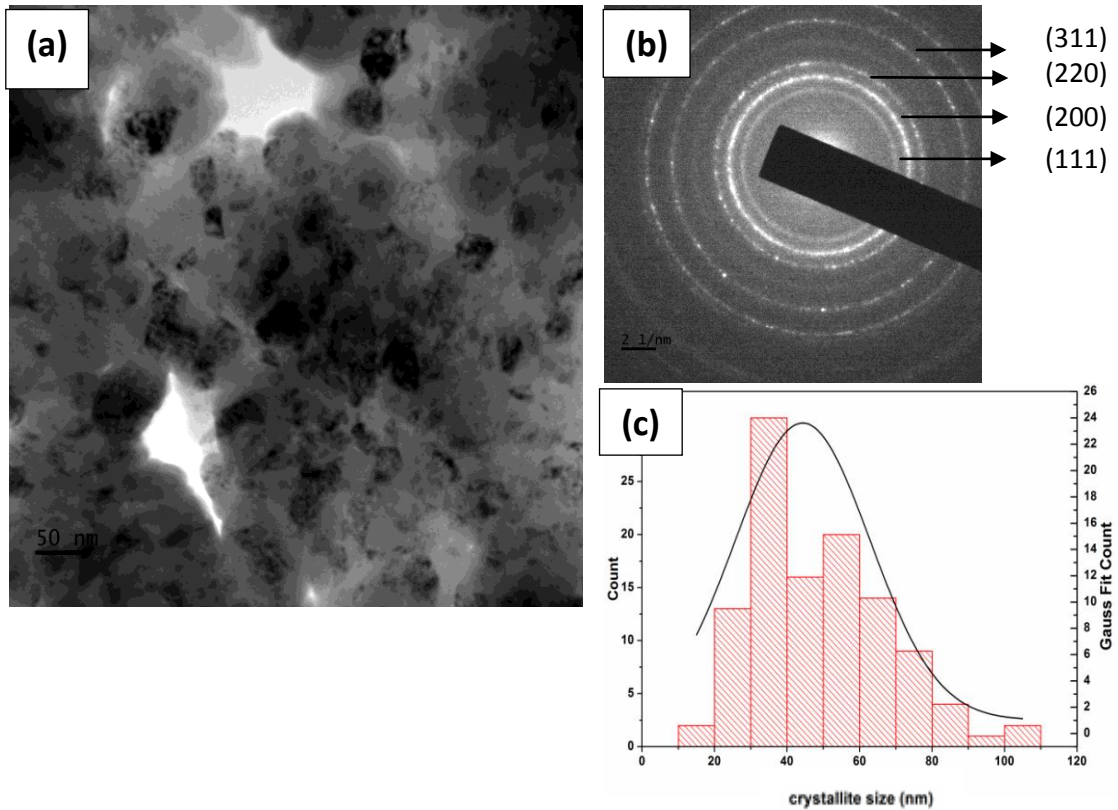
Figure 5.5 a) Bright field TEM micrograph of the copper coating deposited at the sputtering power of 50 W, b) SAED pattern corresponding to the TEM micrograph and c) histogram showing the crystallite size distribution in the deposit corresponding to 50 W.
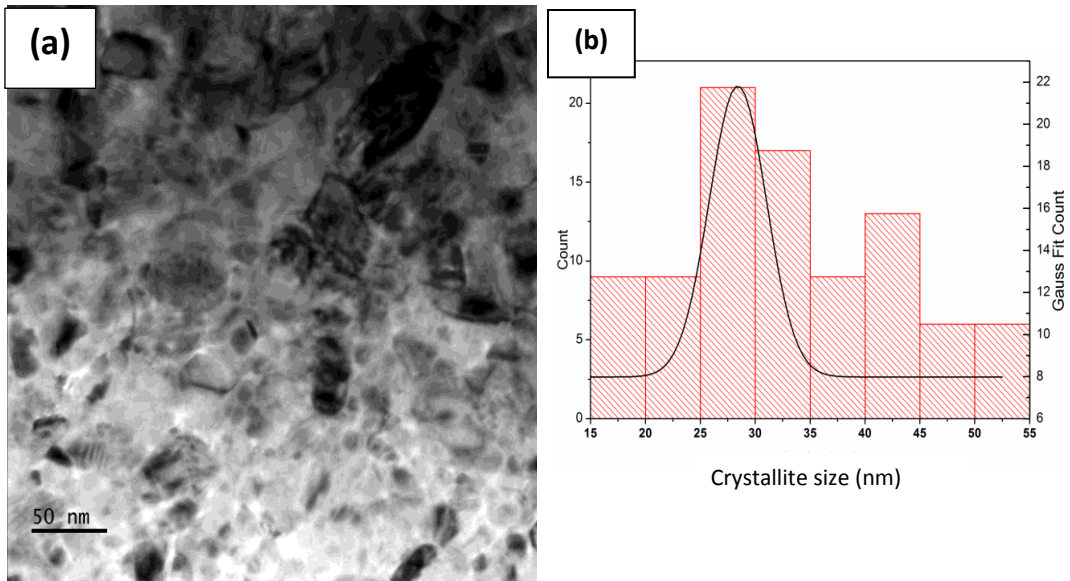
Figure 5.6 a) Bright field TEM micrograph of the copper coating deposited at the sputtering power of 100 W, and b) histogram showing the crystallite size distribution in the micrograph.
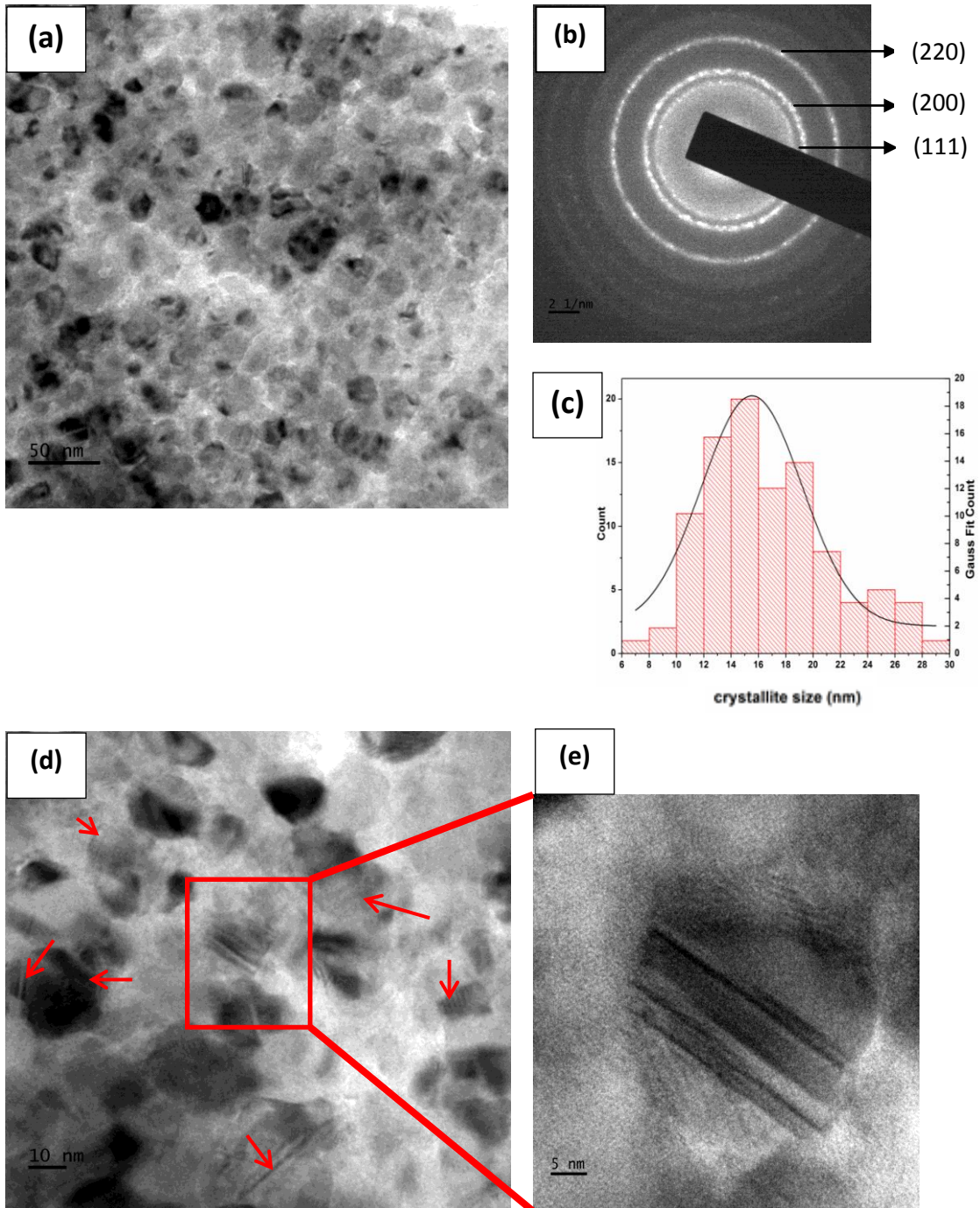
Figure 5.7 a) Bright field TEM micrograph of copper coating at the sputtering power of 150 W, b) SAED pattern of the TEM micrograph, c) histogram showing the crystallite size distribution corresponding to 150 W, d) and e) nano-twins observed at higher magnifications.

In order to confirm the absence of epitaxial growth of the coating, TEM micrograph in cross sectional direction is presented in Figure 5.8 (a). The SAED pattern of the TEM micrograph is shown in Figure 5.8(b). The histogram corresponding to Figure 5.8 (a) is shown in Figure 5.8(c), in which the average crystallite size is observed as 17.6 nm with a standard deviation of 3.72 nm.
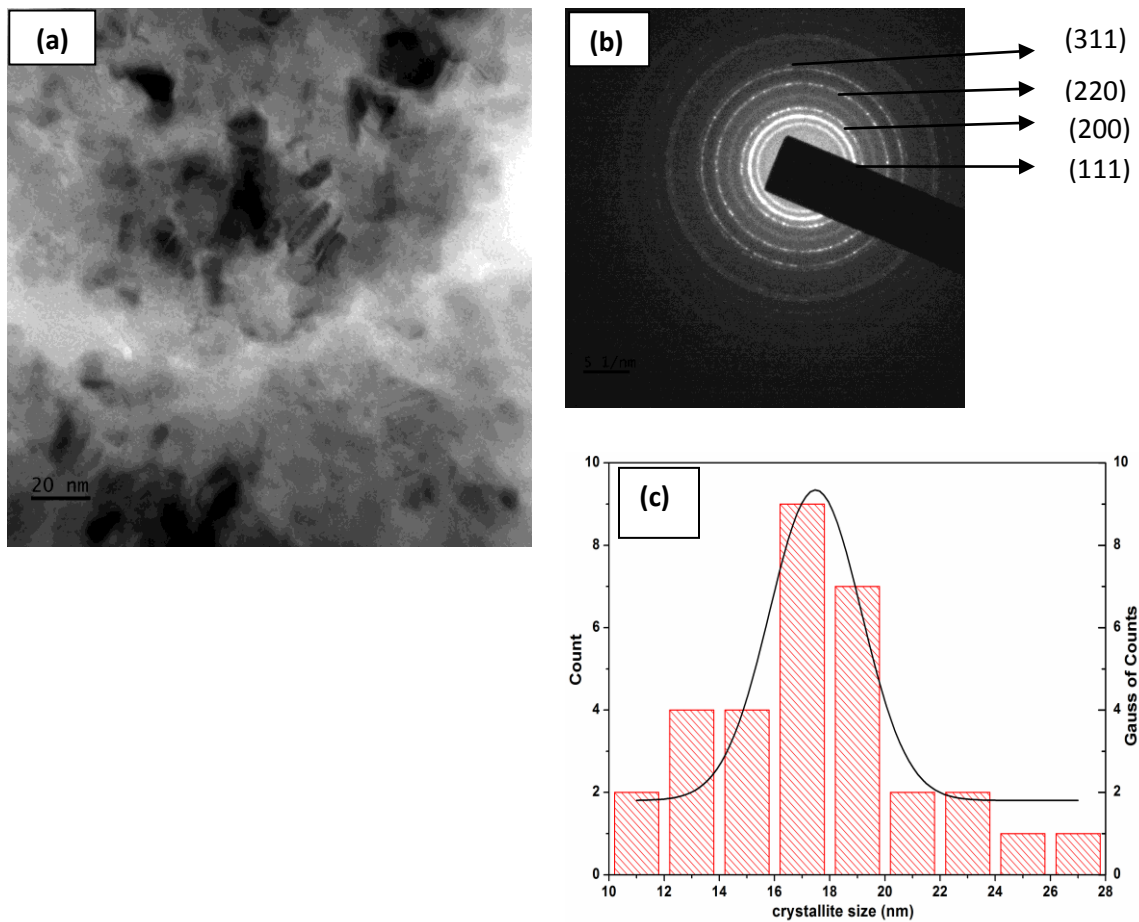
Figure 5.8 a) Bright field TEM micrograph (cross section) of the copper coating at the sputtering power of 150 W, b) SAED pattern of the TEM micrograph and c) histogram showing the crystallite size distribution in the coating corresponding to 150 W.

5.2.3 X-ray diffraction study

XRD profile of the DC magnetron sputtered copper coatings at different sputtering power is shown in Figure 5.9. The FWHM of the peaks increase with the increase in sputtering power. Since the peaks are observed only for three crystallographic planes, microstrain calculation is difficult (Biju et al. 2008). The relative intensity ratio of peak for (111) plane is higher as compared to that of the standard copper file (ICDD # 89-2838). This is attributed to the preferred texture of the coating along (111) plane along [111] direction.
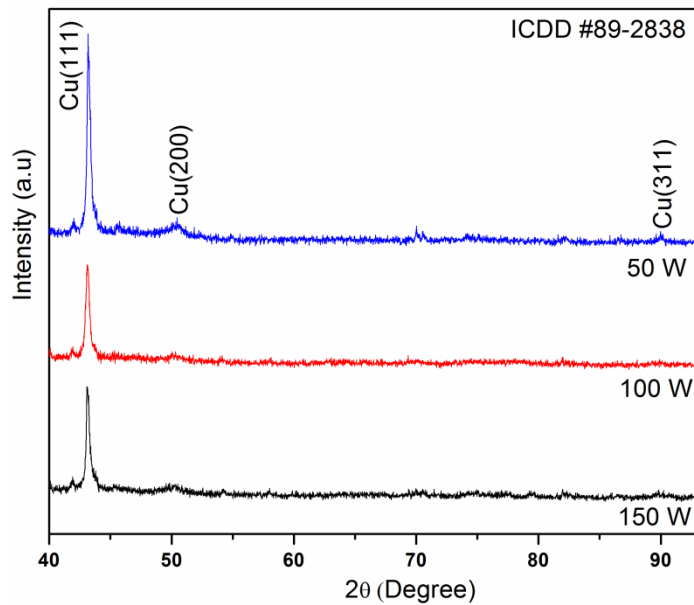
Figure 5.9 XRD profile of the copper coating deposited at different sputtering powers.

5.3 Mechanical Characterization

5.3.1 Scratch hardness test

Scratch resistance is one of the major mechanical properties required for the antimicrobial coatings. The SEM images of the scratch tests on the sputtered copper coatings are shown in Figure 5.10. The variation of the scratch width (average value) with sputtering power is given in Table 5.3. The scratch hardness of the coating deposited at different sputtering power has been calculated using equation 4.5, and is given in Table

5.3. The scratch hardness is seen to increase from 1.21 GPa to 1.72 GPa with increase in the sputtering power from 50 W to 150 W.
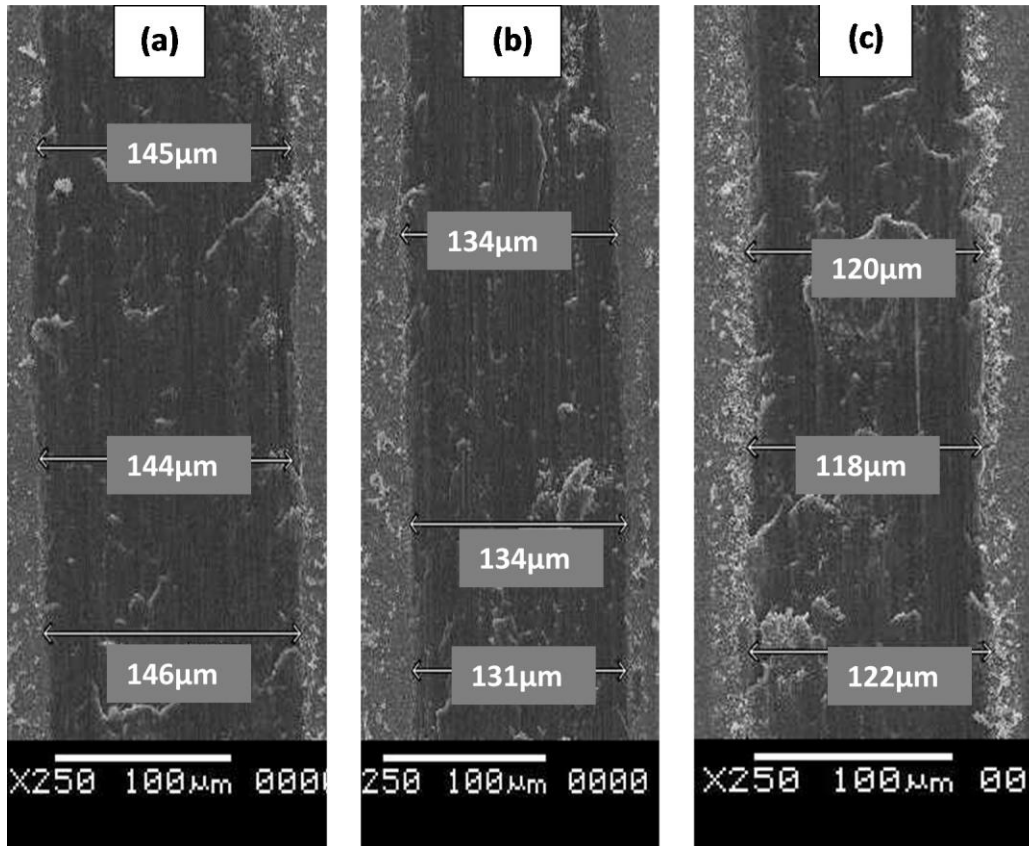
Figure 5.10 SEM micrographs of the scratches, with scratch width dimensions on the coated samples deposited at different sputtering power of (a) 50 W, (b) 100 W, and (c) 150 W, respectively.

5.3.2 Microhardness test

The resistance against the static indentation of the coating has been measured by using microhardness test. The test results for the coatings at the different sputtering power have been given in Table 5.3. Maximum hardness value is observed for the coating at sputtering power of 150 W. Compared to scratch hardness values, microhardness values are higher. This is attributed to the severe plastic deformation having occurred during

scratch test. The highest surface hardness of the coating at 150 W was three times higher than that of annealed copper (European copper institute, 2015).

Table 5.3 Scratch hardness and microhardness values for the copper coatings deposited with different sputtering powers.

Sputtering power (W)	Average scratch width (μm)	Scratch hardness (GPa)	Microhardness (GPa)
50	145.1	1.21	1.01±0.9
100	136.8	1.36	1.26±0.11
150	121.7	1.71	1.49±0.11

5.3.3 Cross-hatch cut test

The qualitative adhesion strength of the coating to the substrate is evaluated by cross-hatch cut test, carried out as per ASTM D3359. Figure 5.11 and Figure 5.12 show the SEM images of the cross-hatch cut tested sample deposited with 50 W and 150 W sputtering powers, respectively. Figure 5.11 (a) and Figure 5.12 (a) indicate that none of the squares are detached from the substrate after removing the pressure sensitive tape from the cross-hatched surface. The magnified images shown in Figure 5.11 (b) and 5.12 (b) indicate that the coating flakes are also not removed at the intersection of the cross-hatch. As a result, the percentage area affected by the cross-hatch cut test is zero. So, as per the visual comparison with ASTM D3359 standard shown in Table 4.3, the coating is included in the category of 5B class.
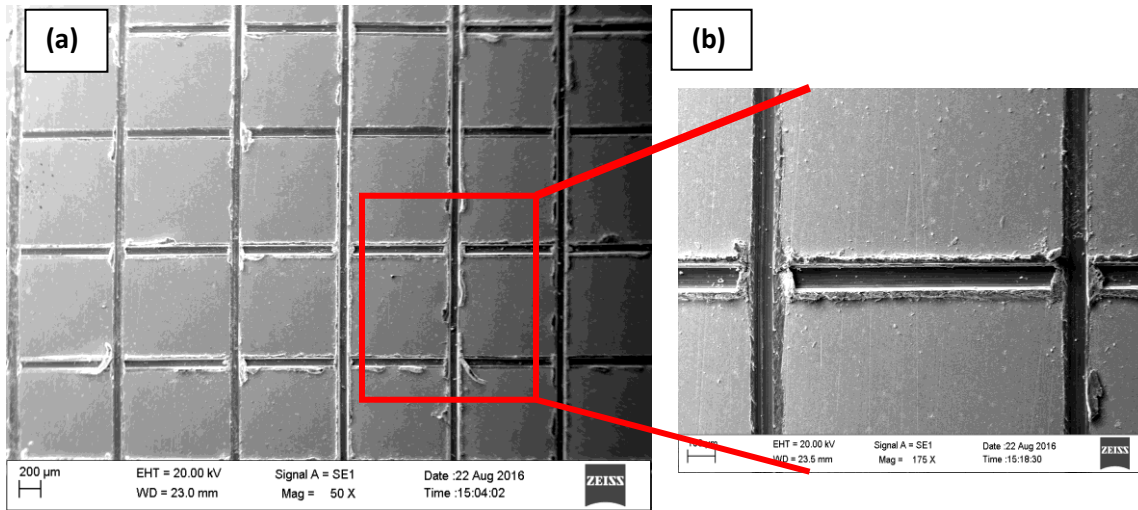
Figure 5.11 a) SEM micrograph of the cross-hatch cut tested sample deposited with 50 W power and b) magnified images representing affected area.
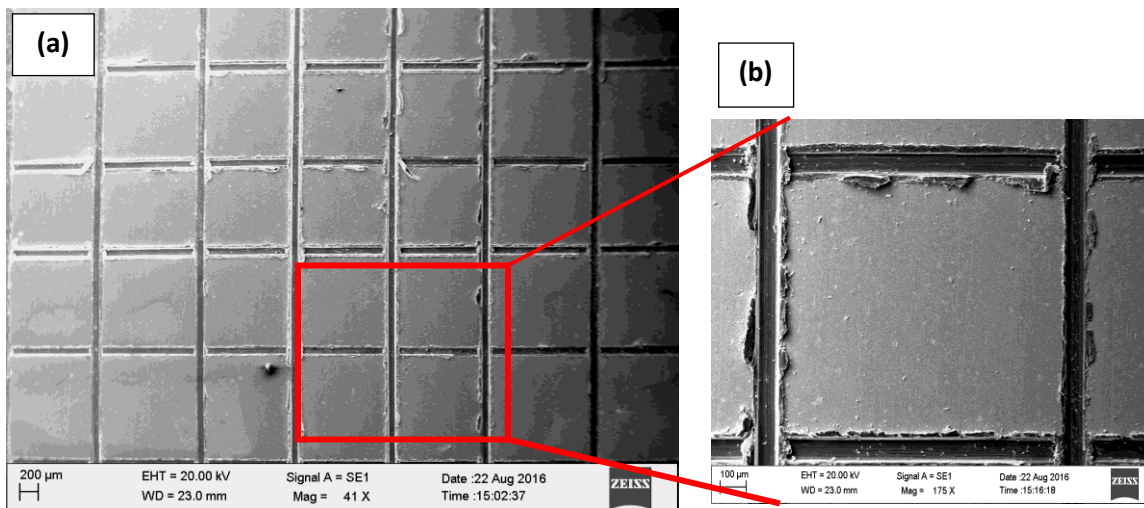
Figure 5.12 a) SEM micrograph of the cross-hatch cut tested sample deposited with 150W power, and b) magnified images of the cross hatched portion.

5.3.4 Pull-off adhesion test

The adhesion strength of the copper coating with the double zincated aluminium substrate has been quantified by following pull-off adhesion test. The photograph of the adhesion tested sample is shown in Figure 5.13. At a pull-off adhesion strength of 1.7±0.2 MPa,

the dolly detaches from the coating irrespective of the sputtering power. But the coating is not completely detached from the substrate. Hence, it is inferred that the coating has an adhesion strength >1.7±0.2 MPa.
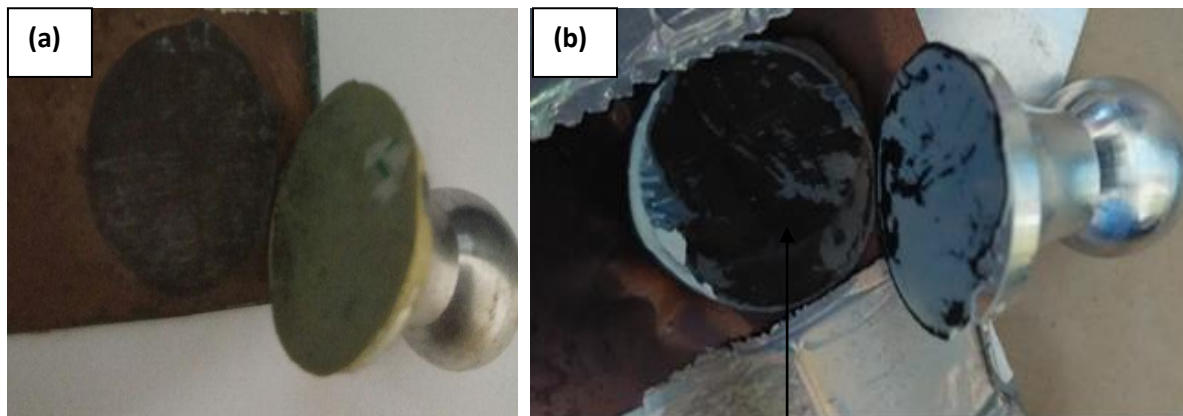
Copper coating remains on the substrate after pull-off adhesion test

Figure 5.13 Pull- off adhesion tested sample with the dolly for the copper coating with sputtering power of a) 50 W, and b) 150 W, respectively.

5.4 Summary of the Chapter

The copper coating was successfully deposited on the double zincated aluminium by the DC magnetron sputter deposition technique. The deposition was carried out with an optimized target power of 50 W, 100 W and 150 W. The SEM study of the sputter deposited coating reveals its nodular morphology with globular topography. The size of the nodules is reduced with increase in the sputtering power. The TEM study reveals that each nodule is made up of nano-sized crystallites. The crystallite size reduces from 49 nm to 18 nm with an increase in target power from 50 W to 150 W. The TEM micrographs show that at higher sputtering power, some of the crystallites contain nano-twins. The preferred growth of the copper coating along (111) direction is confirmed from the XRD profiles. The surface hardness of the coating has been tested by using scratch hardness test and microhardness tests. It is inferred that as the coating sputtering power increases, the hardness value increases. The adhesion strength of the coating with the double zincated aluminium substrate was tested by using cross-hatch cut test and pull-off

adhesion tests. Excellent adhesion strength was observed in both cross-hatch cut test and pull-off adhesion tests. The coating hardness belongs to 5B class as per ASTM D3359.

List of publications related to Chapter 5

1. Arun Augustin, K. Rajendra Udupa, Udaya Bhat K. (2015), "Effect of Pre-Zinc Coating on the Properties and Structure of DC Magnetron Sputtered Copper Thin Film on Aluminium" American Journal of Materials Science, Scientific & Academic Publishing. vol. 5(3C): pp 58-61.

2. Udaya Bhat K, Arun Augustin, Suma Bhat and Udupa K. (2018), "Preparation and characterization of copper thin films for antimicrobial applications" Microscopy Applied to Materials Sciences and Life Sciences, Apple Academic Press.

Chapter 6

ANTIMICROBIAL ACTIVITY OF THE COPPER COATINGS

In the present chapter, the results obtained from the antimicrobial characterizations have been presented. The antimicrobial activity of both electrodeposited and sputter deposited coatings have been tested against both gram negative and gram positive bacteria. The Escherichia .coli (E. coli) and Methicillin-resistant Staphylococcus aureus (MRSA) are taken as the model of pathogenic gram negative and gram positive bacteria respectively. The biocidal efficacy of the copper coated aluminium has been quantitatively estimated by CFU (colony forming unit) counting technique. The results were compared with the uncoated aluminium (control) and the bulk copper plate. In order to understand the structural changes happening in the bacterial cell after the copper treatment, the electron microscopic (SEM and TEM) study results are presented. From the contrast of the TEM micrographs, dense cellular bodies and liquidus soft media could be distinguished in the bacteria cell and thereby loss of fluid from the cell due to copper treatment could be identified. The SEM micrographs of the bacteria help to understand the morphological changes of the copper treated cells with respect to the non-copper treated cells. Moreover, the EDS attached to TEM and SEM is used to find the presence of the copper in the cell after the copper treatment.

6.1 Antimicrobial Study against Gram Negative Bacteria (*E. coli*)

The antimicrobial activities and its mechanism of gram negative and gram positive bacteria are different due to their difference in cell wall structure. *E. coli* is one of the most common gram negative pathogenic bacteria present on the hospital touch surfaces.

In the present section, the survivability of the *E.coli* on the copper coatings as compared to the bulk copper and the uncoated aluminium as well as the electron microscopic study of the same has been presented.

6.1.1 CFU count results

Figure 6.1 represents the photographs of the *E.coli* colonies corresponding to the uncoated aluminium, the bulk copper and the copper coated aluminum. Figure 6.1(a) represents the colonies corresponding to the uncoated aluminium sample of dimension 1.5 cm x 1.5 cm and surface roughness of 0.07 μm. Because of its zero antimicrobial activity, ~ 200 colonies of *E.coli* bacteria were observed in Figure 6.1(a). For the comparison of the antimicrobial activity of the coating, uncoated aluminium is used as the control. Figure 6.1(b) represents the colonies corresponding to the bulk copper with the same dimensions and roughness as that of the uncoated aluminium (control). Even though the copper has biocidal activity, Figure 6.1(b) exhibits ~23 colonies of *E. coli*. Hence in the present study, bulk copper has an antimicrobial activity of ~88% as compared to the control sample. Figure 6.1(c-e) represents the colonies growing on the copper coatings deposited on the aluminium substrate of dimension 1.5 cm x 1.5 cm. Figure 6.1 (c) represents the colonies growing on the coating deposited from the electrolytic Bath-I (current density = 9 Adm^{-2}), Figure 6.1(d) represents the colonies growing on coating from the electrolytic Bath-II (current density = 4Adm^{-2})and Figure 6.1(e) represents the colonies growing on coating by DC magnetron sputter deposition technique (sputtering power=150 W). Compared to the colonies growing on the bulk copper samples (Figure 6.1(b)), copper coated samples have lesser number of colonies. This is due to the better antimicrobial activity of the copper coatings as compared to that of the bulk copper. Among the coated samples, colonies growing on the coating deposited using Bath-II (Figure 6.1(d)) show lesser number of colonies as compared to that of other coatings, shown in Figure 6.1(c) and Figure 6.1(e). Hence coatings obtained from the Bath-II have better performance in antimicrobial activities among the coatings. The reasons for improved antimicrobial activity of the copper coatings as compared to
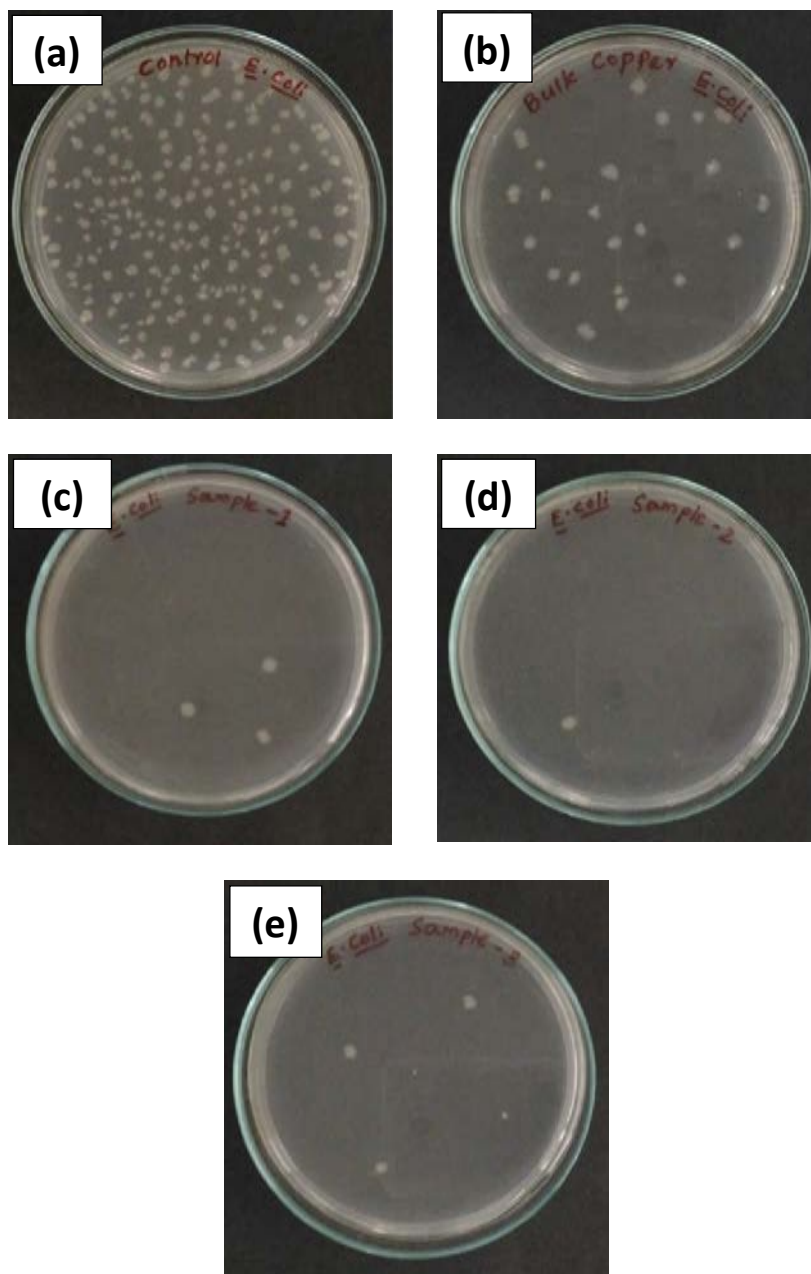
Figure 6.1 Photographs of *E. coli* colonies formed after six hours exposure on a) uncoated aluminium (control), b) bulk copper c) copper coated aluminium from the Bath-I, d) copper coated aluminium from the Bath-II and e) copper coated aluminium by DC magnetron sputtering method, respectively.

the bulk copper as well as the variations of antimicrobial activities among the coatings is attributed to the difference in the morphological and microstructural features of the coatings. The detailed discussion is given in section 7.3.2 (Chapter 7).

6.1.2 Electron microscopic test results

The CFU study results showed that the copper coating can kill the *E.coli* bacteria more effectively. But the mechanism of killing microbes by the copper is not yet clearly understood (Augustin et al. 2016c). The electron microscopic study of the copper treated *E.coli* helps to understand its structural and morphological changes due to the attack of the copper. Thereby mechanism of the antimicrobial activity of the copper on the gram negative microbes could be revealed up to a certain level. In the present section, the micrographs obtained from the SEM and TEM analysis of the bacteria along with EDS results have been presented.

6.1.2.1 Scanning electron microscopic study of the *E. coli*

Figure 6.2 and Figure 6.3 represents the SEM micrographs of the *E. coli*. The *E. coli* cells which are exposed to the copper coatings for six hours is shown in Figure 6.2, whereas, the *E. coli* cell treated on the uncoated aluminium plate (control) is shown in Figure 6.3. Compared to the copper treated *E.coli* cell, the non-treated cells were healthy and rod shaped. The copper treated *E. coli* cells were wrinkled and damaged as shown in Figure 6.2 (a). Due to the copper treatment, holes are formed on the cell surface as shown by the arrow mark in Figure 6.2 (b). The EDS corresponding to the selected area in Figure 6.2 (b) is shown in Figure 6.2 (c). It indicates that the copper treated *E. coli* contains copper ions. This may either be on the cell wall or inside the cell structure. Cells which are treated with the uncoated aluminium do not show the presence of the copper, as seen in Figure 6.3 (b). Hence, it is proved that the copper ions were accumulated in the cell due to its exposure to the copper coatings.

110

Element	Cu	C	O
At. %	0.67	64.86	34.47
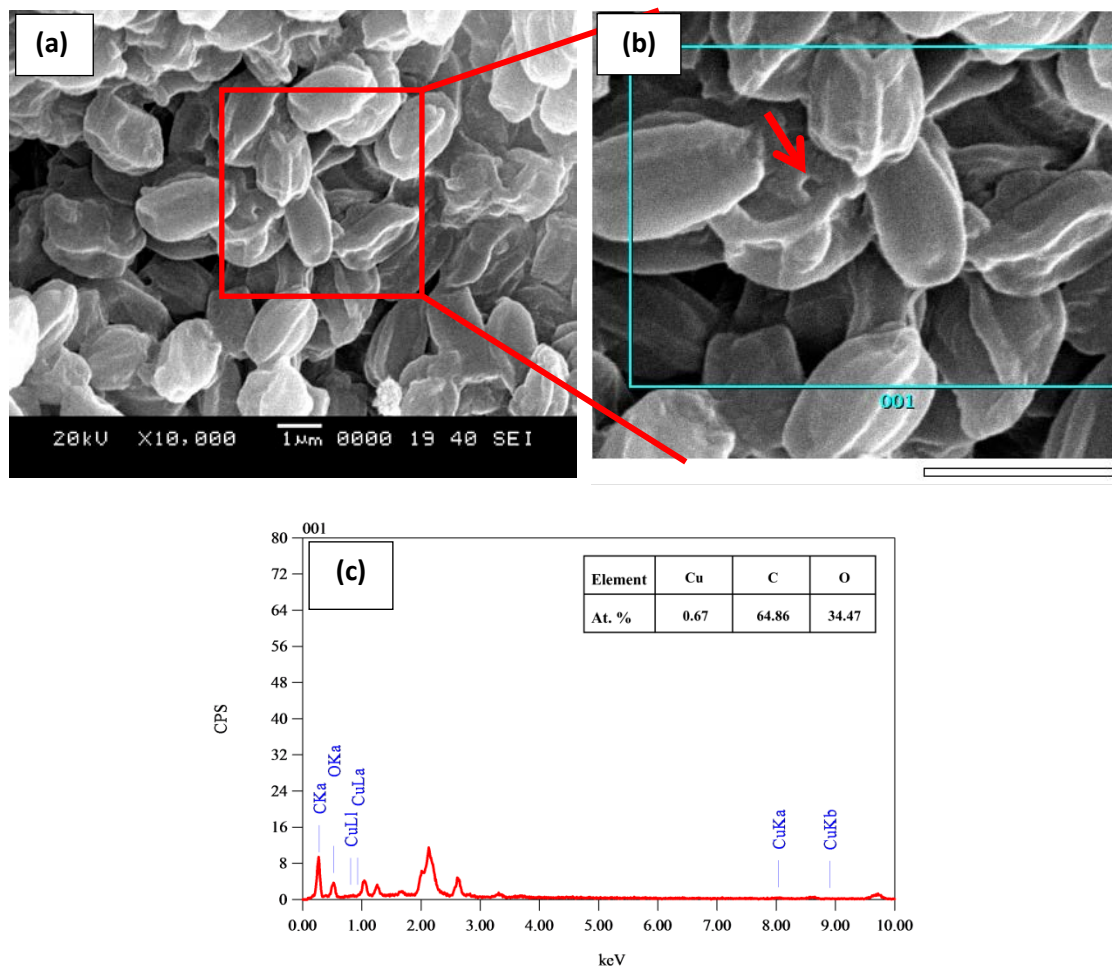
Figure 6.2 a) SEM micrograph of the copper treated *E. coli,* b) enlarged view of the Figure 6.2 (a) and c) EDS corresponding to the selected area in Figure 6.2 (b), respectively.
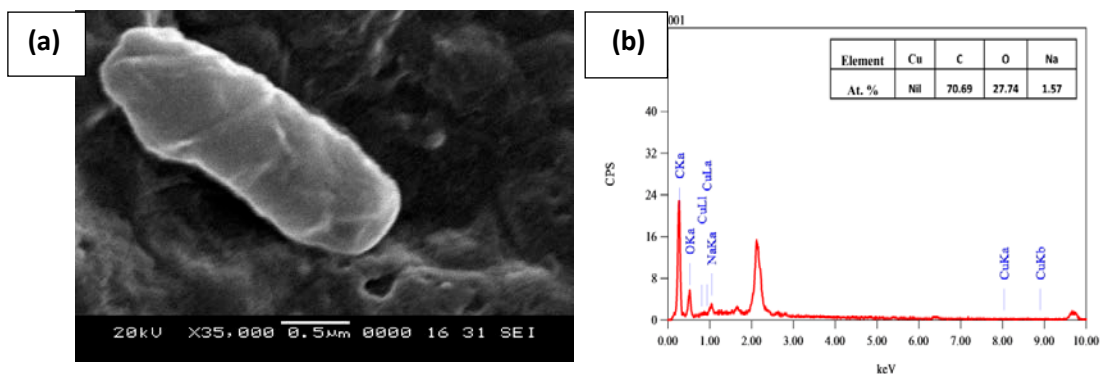
Figure 6.3 a) SEM micrograph of the *E. coli* exposed to the uncoated aluminium and b) EDS corresponding to the same.

6.1.2.2 Transmission electron microscopic study of the *E. coli*

Figure 6.4 represents the TEM micrographs of both the copper treated and the non-copper treated *E. coli* cells along with their corresponding EDS results. Figure 6.4 (a) represents the *E. coli* cells exposed to the copper coated aluminium, whereas Figure 6.4 (c) represents the *E.coli* which is treated with the uncoated aluminium substrate. Figure 6.4 (b) and Figure 6.4 (d) represents the EDS corresponding to the copper treated as well as the non-copper treated cells respectively. The copper treated cells were damaged and shrunken as compared to the non-copper treated cells. The cells which were exposed to the non-copper coated surface maintained their rod shape and healthiness. The white region in the TEM micrographs of cells corresponding to the uncoated aluminum (Figure 6.4 (c)) represents the fluid present in the cell structure. The dark regions of *E. coli* represent the solid part in the cell. The complete dark region in the copper treated cell shown in Figure 6.4 (a) indicates the complete leakage of the fluid from the cells. As a result, the copper treated cells were shrunken to ~ 80% as that of the non-copper treated cells. The detailed discussion of the results is given in section 7.3.1.1(Chapter 7).
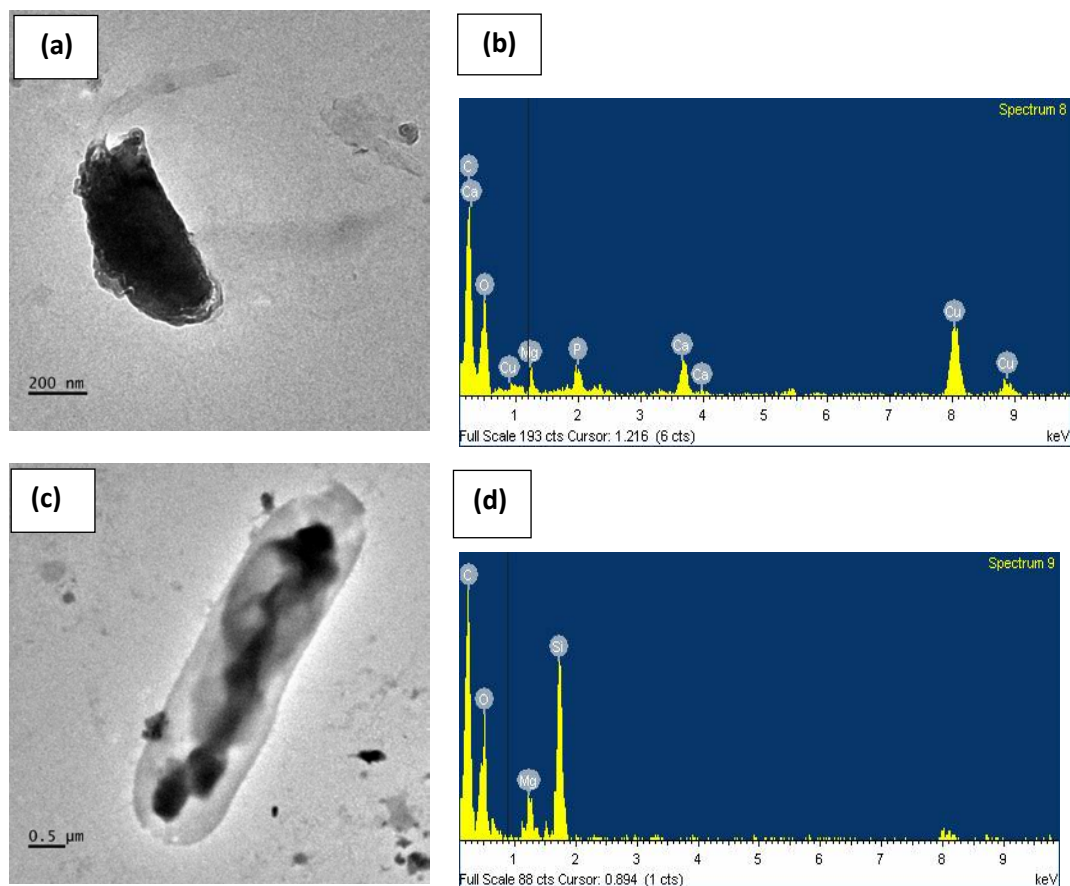
Figure 6.4 a) TEM micrograph of the copper treated *E. coli,* b) EDS corresponding to the same, c) TEM micrograph of the *E. coli* without copper treatment and d) EDS results corresponding to the same, respectively.

6.2 Antimicrobial Study against the Gram Positive Bacteria (*MRSA*)

MRSA is the most predominant pathogen causing infection through hospital touch surfaces (World Health Organization 2011). Moreover, the *MRSA* is considered as a typical model for gram positive groups of the bacteria. Hence the antimicrobial activities of the *MRSA* have been estimated by CFU counting method and the structural and

morphological changes due to the copper treatment has been presented in the current section with the help of the micrographs obtained by using the electron microscopes.

6.2.1 CFU count results

The antimicrobial activities of the copper coatings deposited by different ways are quantitatively estimated by counting the number of CFUs of *MRSA*. The Figure 6.5 (a) represents the colonies formed after treated the bacteria with the uncoated aluminium, which is taken as the control sample. Figure 6.5 (b) represents the colonies corresponding to the bulk copper plate of same dimension and roughness as that of the control. Figure 6.5 (b) contains ~20 colonies of *MRSA*. Figure 6.5 (c) and Figure 6.5 (d) represents the colonies corresponding to the electrodeposited coating obtained by using Bath-I and Bath-II respectively. Figure 6.5 (e) represents the colonies grown on the sputter deposited coatings. The number of *MRSA* colonies grown on the electrodeposited coatings was almost nil. It indicates that 100% antimicrobial activity of the electrodeposited coatings
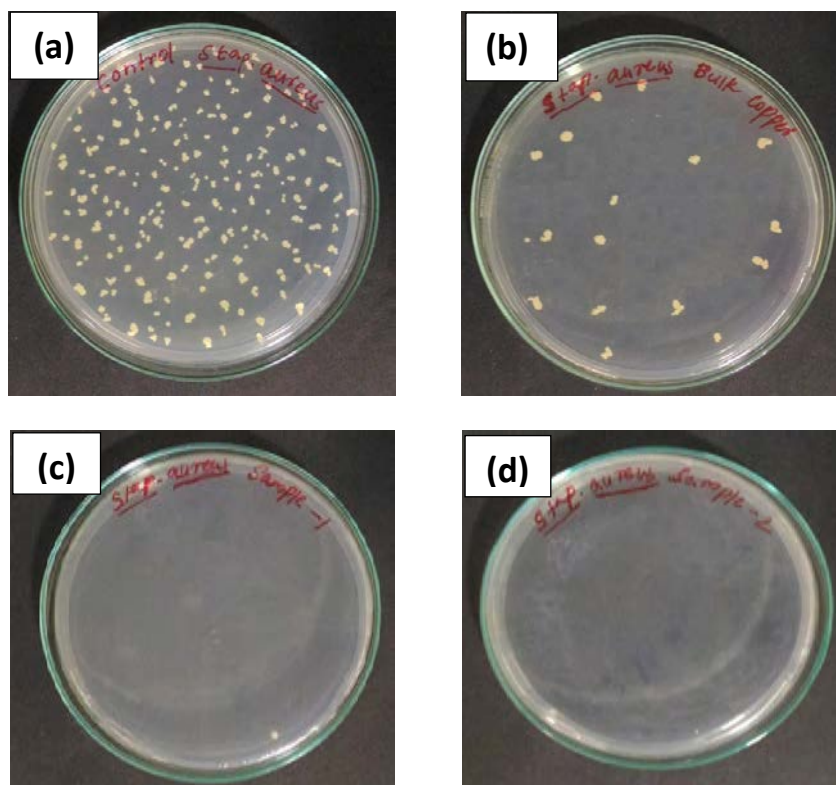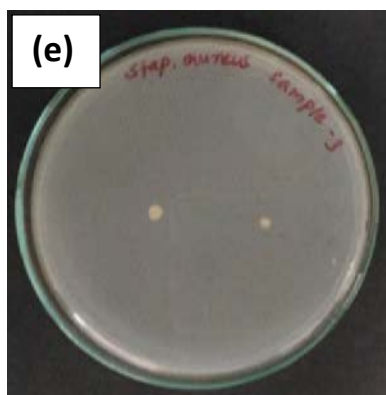
Figure 6.5 Photographs of the *MRSA* colonies formed after six hours of exposure on a) uncoated aluminium (control), b) bulk copper c) copper coated aluminium from Bath-I, d) copper coated aluminium from Bath-II and e) copper coated aluminium deposited by using DC magnetron sputtering method, respectively.

against *MRSA* within six hours of exposure with the coatings. The sputter deposited coating was slightly less antimicrobial as compared to the electrodeposited coatings. The microstructural and morphological difference could be the reasons for such variations in the antimicrobial activities. The detailed discussions on these factors are given in section 7.8 (Chapter 7).

6.2.2 Electron microscopic test results

As mentioned in the literature survey, the cell wall of gram positive and gram negative bacteria has significant difference in structure as well as composition. As a result, the mode of attack of the copper and the mechanism for killing the gram positive bacteria are expected to be different as compared to the gram negative bacteria.

6.2.2.1 Scanning electron microscopic study of *MRSA*

Figure 6.6 represents the SEM micrographs of the *MRSA*. The *MRSA* cells which are treated with copper are shown in Figure 6.6 (a). Figure 6.6 (b) and Figure 6.6 (c)

represent the *MRSA* cells which were not exposed to copper surface. Compared to the non-copper treated cells, copper treated cells do not show much deformation in their spherical shape. But copper treated cells have many pits on the cell wall, as indicated by the arrow mark in Figure 6.6 (a). The *MRSA* cells exposed to the uncoated aluminium substrate were free from such damage, as seen in Figure 6.6 (c). Moreover, the cell divisions (mitosis and meiosis) observed in the marked region in Figure 6.6 (b) indicates a favorable environment for the growth of *MRSA* on the uncoated aluminium substrate as compared to that of the copper coated surface.
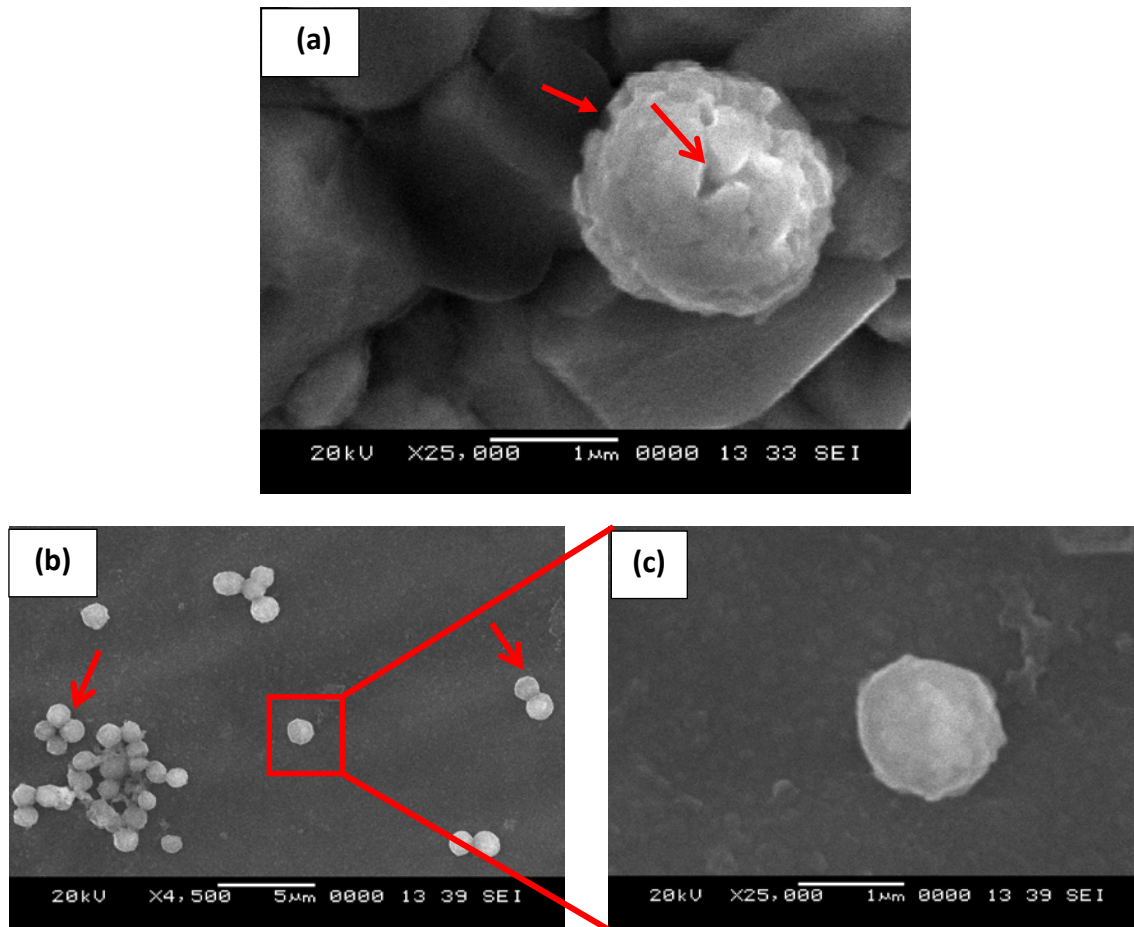
Figure 6.6 a) SEM micrograph of the copper treated *MRSA*, b) SEM micrograph of non-copper treated *MRSA* showing cell divisions, and c) Magnified image of the *MRSA* selected from Figure 6.6 (b).

6.2.2.2 Transmission electron microscopic study of the *MRSA*

Figure 6.7 represents the TEM micrograph of the copper treated *MRSA* along with its EDS data. Figure 6.8 represents the TEM micrograph and the EDS results of the non-copper treated *MRSA*. The presence of copper in the *MRSA* cell shown in Figure 6.7 (a) was confirmed from the EDS, as given in Figure 6.7 (b). The TEM image showed that the cell wall of the copper treated *MRSA* was damaged, as marked in Figure 6.7 (a). Such cell damages were absent in the *MRSA* cells which were not treated with the copper (exposed to uncoated aluminium). Moreover, these cells had undergone cell divisions. Such healthy cells after divisions are shown in Figure 6.8 (a). The initial stage of cell division (mitosis) of *MRSA* that occurred on the non-coated aluminium is given in Figure 6.8 (b). As reported by Hong and Koo (2005), the spherical shape of the *MRSA* cells was not distorted due to the exposure to the copper (Figure 6.7 (a)). However, the cell dimension was reduced to 10-15% as compared to the non-copper treated cells. The detailed explanation of the structural changes of the *MRSA* cells due to the copper treatment is given in section 7.3.1.2 (Chapter 7).
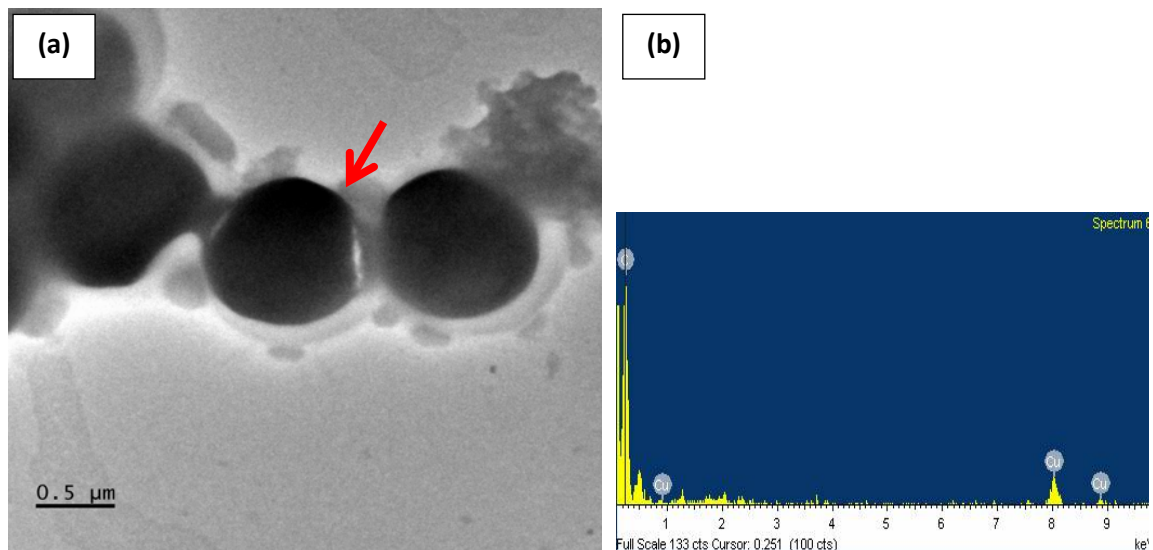
Figure 6.7 a) TEM micrograph of the damaged *MRSA* cells during copper treatment and b) The EDS of the damaged *MRSA* cells.
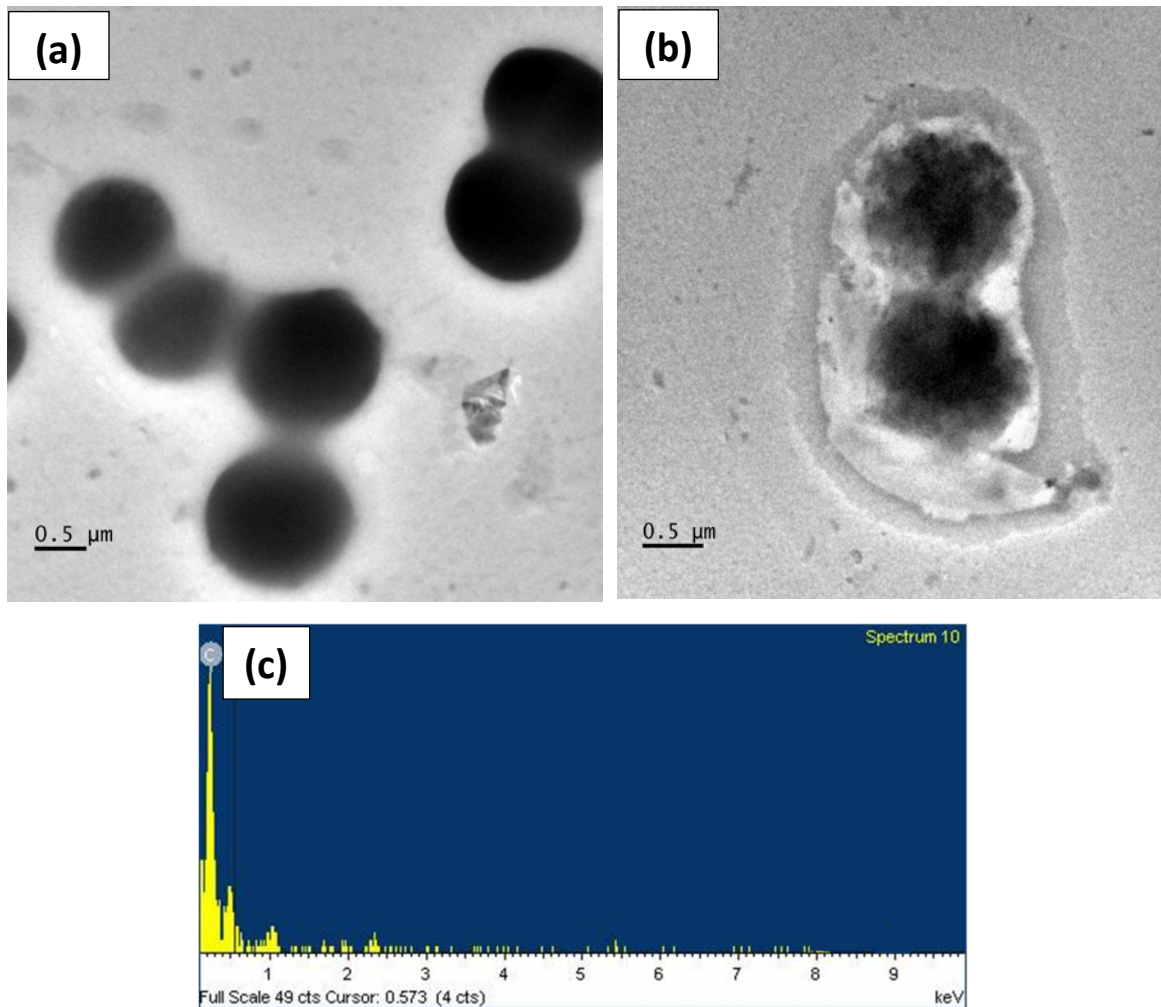
Figure 6.8 a) TEM micrograph of the non-copper treated *MRSA*, b) Initial stages of cell divisions on the uncoated aluminium substrate and c) EDS of the same.

6.3 Summary of the Chapter

The antimicrobial activity of the copper coating on the aluminium substrate deposited by electrodeposition and DC magnetron sputtering technique has been evaluated against gram negative bacteria (*E.coli*) and gram positive bacteria (*Methicillin-resistant Staphylococcus aureus (MRSA)*). The CFU (colony forming unit) count of the bacteria after six hours of exposure to the coating showed that the copper coating has better

antimicrobial activity as compared to that of the bulk copper sample. The TEM and SEM analysis of the microbes revealed that the cell wall is the primary target of attack of the copper in both *E.coli* and *MRSA*. The EDS results of the bacteria cells which are exposed to the coatings shows the presence of the copper in the cells. The copper treated *E.coli* cells were damaged and shrunken as compared to the non-treated *E.coli* cells and the copper treated *MRSA* cells contain pits on the cell wall as compared to that of the non-copper treated cells. The cell integrity of the MRSA cells, however, is maintained due to its thicker cell wall structure.

List of publications related to Chapter 6

1. Augustin, A., Thaira, H., Bhat, K.U. and Udupa, K.R. (2016). Effect of Electrodeposited Copper Thin Film on the Morphology and Cell Death of *E. Coli*; an Electron Microscopic Study. In Biotechnology and Biochemical Engineering, (Springer), pp 227–232.

2. Arun Augustin, Huilgol, P., Udupa, K.R. and Bhat, U. (2016). "Effect of Current Density during Electrodeposition on Microstructure and Hardness of Textured Cu Coating in the Application of Antimicrobial Al Touch Surface." Journal of the Mechanical Behavior of Biomedical Materials, Elsevier Publishing 63, 352–360.

This page is intentionally left blank

Chapter 7

DISCUSSION

The copper coating on the double zincated aluminium is carried out by two processes: (i) Electrodeposition and (ii) DC magnetron sputter deposition. The results of the microstructural, mechanical and antimicrobial characterization of the coatings have been presented in chapters 4, 5, and 6, respectively. The detailed discussion of the obtained results is presented in the current chapter.

7.1 Microstructural Analysis

The antimicrobial activities and mechanical properties of the copper coatings are very much dependant on its microstructural features. The difference in antimicrobial activity of the copper coating compared to that of the bulk copper could be easily explained with the help of the microstructural study. The results obtained from the microstructural characterization of the copper coating using SEM, TEM, EDS and XRD have been presented in Chapters 4 and 5. The detailed analysis of the obtained results of the electrodeposited as well as DC magnetron sputtered copper coatings on the double zincated aluminium is explained in the present section.

7.1.1 Electrodeposited copper coatings

The microstructural characteristics of the electrodeposited copper coatings are mainly dependent on its process of deposition. Hence, before coming to the topic of microstructural features, we take a brief look on the process of electrodeposition.

7.1.1.1 Process of electrodeposition

During the electrodeposition of the copper, the copper is dissociated into the electrolyte by oxidation at the copper anode, whereas at the cathode, the copper is are deposited by reduction. The oxidation and reduction reactions are given below.

$$Cu \rightarrow Cu^{2+} + 2e \text{ (Anode)} \tag{7.1}$$

$$Cu^{2+} + 2e \rightarrow Cu \text{ (Cathode)} \tag{7.2}$$

The bond dissociation energy of Cu^+-Cu=155.2±7.7 kJ/mol (Delley et al. 1983).

The copper ions are supplied from the copper anode. The energy for the reduction of the copper is provided by the external DC power source. During deposition, fully solvated copper ions formed by ligands (an ion or molecule attached to a metal atom by coordinate bonding) of tetra ethelyne pentamine (complexing agent- a compound in which independently existing molecules or ions of a nonmetal form coordinate bonds with a metal atom or ion) get attracted towards oppositely charged electrode surface by Coulombic forces. The electrical double layer or Helmholtz double layer formation (as shown in Figure 2.3) during electrodeposition is broken by continuous stirring of the bath near the cathode. More details on the electrical double layer are explained in section 2.2.2.1(Chapter 2). Copper ions are adsorbed onto the cathode (double zincated aluminium) surface by displacing the attached water molecules and ligands. Upon continuous depletion of the copper ions from the double layer region, fresh copper ions are supplied from the bulk electrolytes by either one or a mix of three different processes, namely, i) diffusion due to the concentration gradient, ii) electric field assisted migration and iii) convection current in the electrolyte due to the stirring action (Ray 2015).

The electrodeposition of the copper takes place in three steps (Ray 2015).

i. Copper ion migration

The solvated copper ions (copper ions in the bath) in the electrolyte migrate towards the cathode under the influence of an applied potential as well as through diffusion and/or convection.

ii. Electron transfer

At the cathode surface, the solvated copper ions enter the diffusion layer (shown in Figure 2.3), where the water molecules of the hydrated ion are aligned by the weak field present in this layer. Eventually, the copper ions enter the fixed Helmholtz layer, where, due to the higher field present, the hydrated ions and ligand's shell is lost as shown in Figure 2.3. Subsequently, the individual ion is neutralized by electron transfer from the cathode and is adsorbed at the cathode surface.

iii. Incorporation of the copper into the surface

In this last step, the adsorbed atom is drifted to a growth point on the cathode and is incorporated in the growing lattice. The process continues as long as the applied potential is near to the reduction potential of the ion.

Even though the bath concentration, pH, additives and type of cations affect the deposition, coating current density determines, in particular, the rate of the deposition of the cations and hence microstructure of the deposited coatings (Paunovic and Schlesinger 2006). More copper ions are formed with increase in the current density of the coating.

7.1.1.2 Morphological analysis of the electrodeposited copper coatings

Nodular shaped morphology was observed in the electrodeposited coatings in the present investigation. Similar morphology was reported by De Almeida et al. (2002), Balaraju and Rajam (2005), Kanungo et al. (2003), and Grujicic and Pesic (2002). The SEM micrographs of the coating deposited from Bath-I is shown in Figure 4.2. From the

micrographs, it is inferred that the coverage of the coating increased with the increase in the coating current density. At lower current densities, the coating contains semispherical and distinct nodules (shown in Figure 4.2 (a-c)). As a result, the coating coverage is discontinuous, revealing the underneath double zincated aluminium surface. Such discontinuous coatings are produced because not enough copper ions are transferred to the substrate to promote sufficient nucleation and growth of nodules. In this case, copper ions would move to the selected region (preferred sites) and grow, rather than supporting fresh nucleation event. At lower coating current density, copper ions get sufficient time to choose the preferred sites due to its slower movement. At moderate current densities, the nodules grew up to the physical impingement of the same and covered the entire substrate, which is clear from the SEM images shown in Figure 4.2 (d-e). This is due to the adequate availability of the copper ions at moderate current densities. This uniform growth was confirmed from the SEM micrographs taken over the cross section of the deposited sample, as shown in Figure 4.4 (a). Further, at higher current densities, the substrate is covered completely with the unevenly grown nodules. This could be attributed to the supply of the excess amount of the copper ions to the cathode due to over-potential at higher current densities as reported by Rashidi and Amadeh (2008) and Ebrahimi and Ahmed (2003). As a result, uniform layers of the nodules are formed at initial stage and few nodules among the existing ones further grow in a perpendicular direction, as shown in Figure 4.2 (f-j) and Figure 4.4 (b). As a result, the coating roughness is more at higher coating current density. It is given in Table 4.1 and 4.4 (Chapter 4). The above mentioned three types of morphology are schematically represented in Figure 7.1.

(a)

Islands of copper nodules at lower coating current density

(b)

Continuous layer of copper nodules at medium coating current density

(c)

Copper nodules protrudes unevenly from primary nodules at higher coating current density
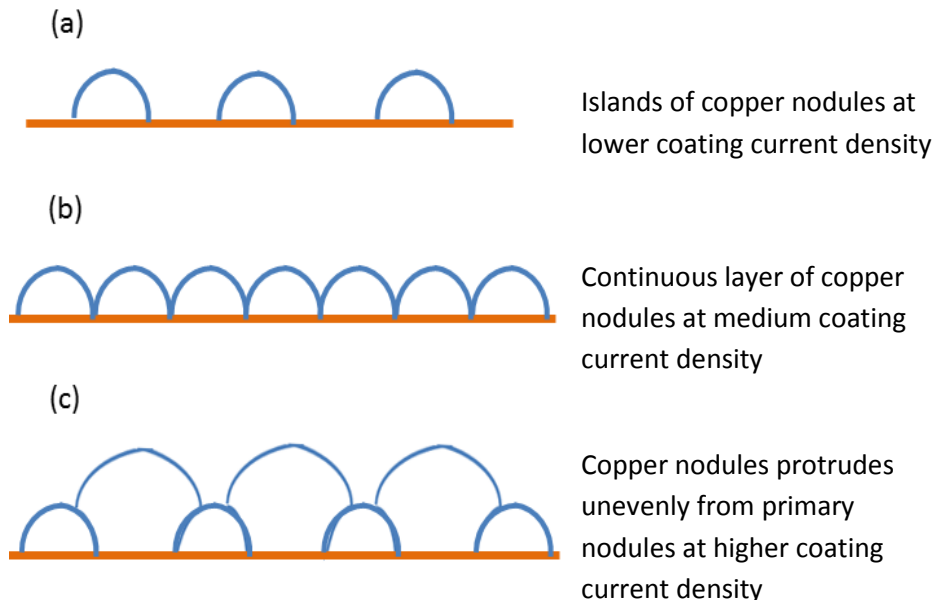
Figure 7.1 Schematic diagram showing different types of morphologies of nodular growth based on current density.

The formation of such morphology could be explained by the schematic representation of the mechanism of electrodeposition as shown in Figure 7.2. In accordance with the variation of the current density, the copper ion flux density varies because current density is the driving force for the ion movement (Pradhan and Reddy 2009). At lower coating current densities, fewer copper ions are transferred from the anode to the cathode through the electrolyte, as depicted in Figure 7.2 (a). At this stage, the rate of nucleation being very small, only few nuclei occur on the double zincated aluminium plate. These nuclei grew to form semi-spherical shaped nodules and have an island like morphology. These features are visible in SEM micrographs presented in Figure 4.2. In this case, only the most favorable site on the zinc surface happened to be selected for the process of the nucleation. Soon after the nucleation, growth can be conceived to be occurring by 'smooth plane front' crystallization, in which each copper atom gets an opportunity to occupy a kink position. At moderate current densities, sufficient copper flux towards the

cathode from the anode creates uniform nodular coating as shown in Figure 7.2 (b). At this stage, all the sites on the plates are occupied without much preference for the 'most favorable site' as the urge for nucleation is high due to high rate of arrival of Cu^{++} ions to the surface of the plate. Of course, growth stops because of the impingement of growing nuclei from all the directions. These results in a smooth surface of the deposits as shown in the SEM micrographs presented in Figure 4.2 (d-e). At higher coating current densities, the copper flux densities are higher than the previous ones, as shown in Figure 7.2 (c). As a result, initially, copper nodules of uniform size form similar to Figure 7.2 (b), followed by preferred copper nodules growing perpendicular to the substrate due to the rapid copper ion enrichment in the vicinity of the surface. Finally, uneven growth of copper nodules occurs as shown in Figure 7.2 (c). The uneven growth of the copper nodules is due to the reduction in the effective coating current density. This happens due to increase of the surface area. The change in the surface area could be estimated as given below.

If the substrate is assumed as flat with dimension of $2r \ x \ 2 \ r$

$$\text{Initial area ofthe substrate} = 4r^2 \qquad (7.3)$$

If the nodules are assumed as semi-spheres of radius 'r'

$$\text{Surface area after forming uniform nodules} = {4\pi r^2}/{2} \qquad (7.4)$$

Hence,

Increase in the surface area of the cathode after forming uniform nodules $= \frac{\pi}{2}$ times that of the initial area. As a result, surface area has increased after forming uniform nodular surface by ~ 57 % compared to the flat substrate. So the effective current density (current per unit area) gets reduced. As a result, selected nodules grow perpendicular as shown in Figure 7.2 (c). Moreover, the protruded nodules are bigger in size as compared to the initially formed nodules as shown in Figure 4.2 (j) and Figure 4.21 (b). Once the nodules start protruding, the copper ions get attracted towards the protruded nodules compared to other nodules due to their closeness to the anode, which is indicated by dotted arrow

marks in Figure 7.2 (c). Hence, more copper ions get deposited on the protruded nodules and as a result these nodules are bigger in size. This is more common in those coating deposited with higher coating current densities. Such morphology offers more surface area on the coating. The growth modes of the electrodeposited coating resembled the Stranski-Krastanor type among the three types of growth modes reported by Le et.al (2010) and Ohring (2001). It is shown in Figure 2.4.
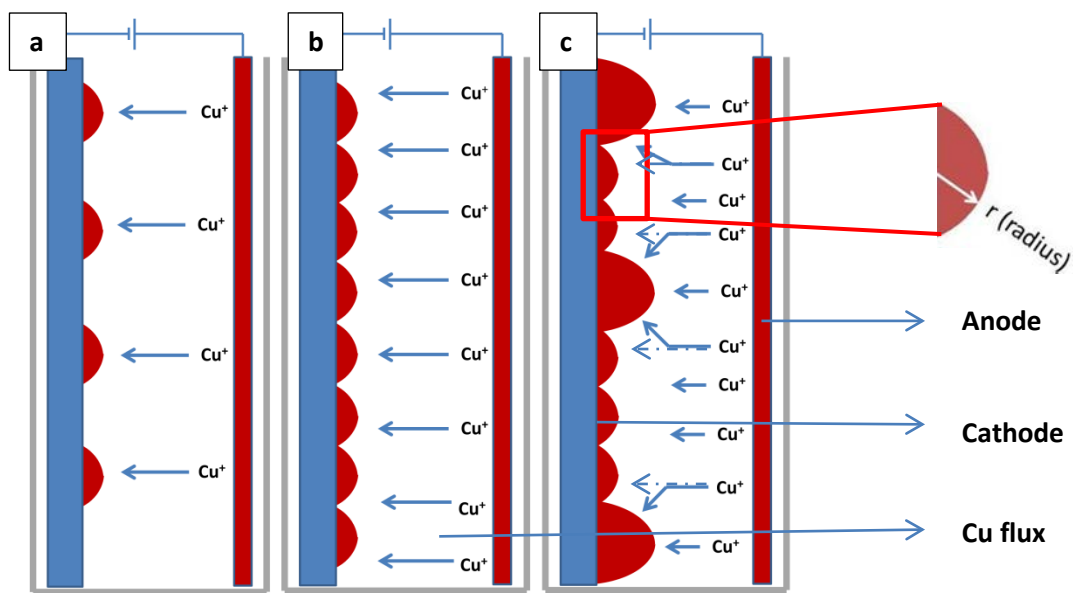
Figure 7.2 Copper flux distributions in electrolytic cell for a) lower current density, b) medium current density, and c) higher current density, respectively.

In the case of electrodeposited coatings from the Bath-II, similar type of coating morphology was observed as shown in Figure 4.21. But the size of the nodules became smaller compared to that of the coating from Bath-I. For the coating from Bath-I, the nodule size was in the range of 4 μm - 7 μm, whereas that for the coating from the Bath-II was 0.77 μm - 3.4 μm. So the reduction in the nodules' size was observed in the case of the coating formed by using Bath-II. This is attributed to the increase of nucleation density of copper nodules formed in the case of the coating from the Bath-II as compared to that from the Bath-I. The presence of the chloride ions from the hydrochloric acid

added to the bath may have facilitated the increased nucleation in the case of the Bath-II (Dini and Snyder 2011). The pH and chemical concentration of the copper salts may also have affected the size of the nodules.

As a conclusion, it is observed that the electrodeposited copper from the Bath-I and Bath-II offer more surface area which have a bearing on three dimensional contacts for the microbes on the surface of the copper deposit carried out at higher deposition current density as compared to that at lower coating current densities.

7.1.1.3 Analysis of the crystallites structure of the electrodeposited copper coatings

In the case of the electrodeposition, the crystallite size of the copper coating from the Bath-I for a coating current density of 2 A dm^{-2} was 63 nm as shown in Figure 4.7, whereas the crystallite size for the same bath at 10 A dm^{-2} was 32 nm, as shown in Figure 4.9. Similarly, for the copper coating from the Bath-II, the crystallite size for 1 A dm^{-2} was 17.6 nm and that for 4 A dm^{-2} was 12.9 nm. The reduction in the crystallite size of the electrodeposited coating is achieved in both types of baths (Bath-I and Bath-II) by increasing the current density. This is schematically shown in Figure 7.3. While increasing the current density, deposition rate of the copper is increased by increasing the number of copper ion flux as shown in Figure 7.2. Due to higher density of the copper ion flux, the nucleation density increases (Rashidi and Amadeh 2008 and Ebrahimi and Ahmed 2003). As a result, the growth of the crystallite is restricted, and more number of nucleation has occurred.
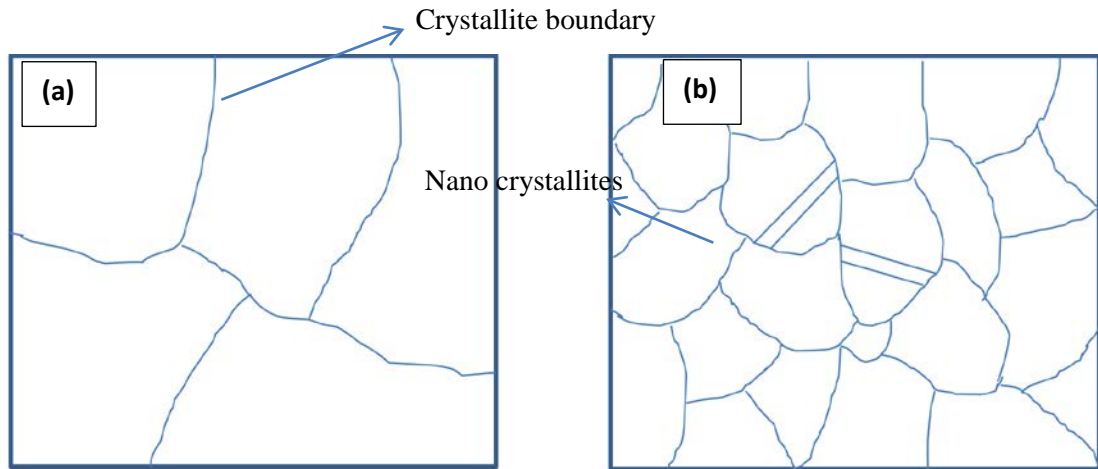
Figure 7.3 Schematic representation of crystallite size distribution at a) lower current density and b) higher coating current density, respectively.

In the case of coating from the Bath-II, the crystallites are equiaxed in shape as compared to that from the Bath-I. The histogram representing the crystallite size distribution shown in Figure 4.26 (b) and Figure 4.27 (c) also indicate that the coating from the Bath-II gives more uniformity in the size of crystallites as compared to that of Bath-I, as shown in Figure 4.7 (b) and Figure 4.9 (b). The SAED pattern of continuous rings shown in Figure 4.26 (c) also indicates the ultra-fine crystallite structure of the same. The cross sectional TEM micrographs shown in Figure 4.10 and Figure 4.28 proved that the coating is made up of nano sized crystallites. This means that the epitaxial growth was absent. Such nanocrystallites were formed in the copper coating due to the following reasons.

a) Lattice mismatch

Lattice mismatch between the substrate and the coating leads to the high density of dislocations. As a result, the thin film could become polycrystalline (Mattox 1994). The lattice mismatch could be calculated using the equation (7.5).

$$\text{Lattice mismatch} = (a_s - a_f)/a_f \qquad (7.5)$$

where 'a_s' is the lattice parameter of the substrate and 'a_f' is that of the film. In the case of the double zincated aluminium substrate, $a_s = 2.4735$ Å and that of copper the film $a_f =$

2.0871 Å. Hence the lattice mismatch is obout 18%. This results in tensile stress on the copper thin film as shown in Figure 7.4. As a result, the coated sample tries to bend towards the coated side.
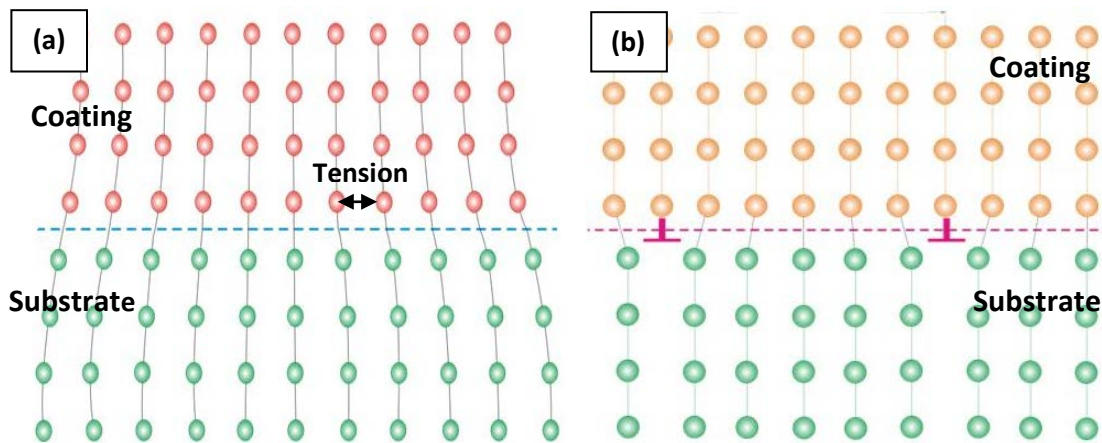
Figure 7.4 Schematic representation of the lattice mismatch between the substrate and the coating results a) tension in the coating and b) dislocations in the coating.

b) Polycrystallinity of the substrate

The polycrystalline aluminium is used as the substrate. A zinc layer is coated on it by using double zincation process. The TEM micrograph shown in Figure 2 (Appendix I) of the double zincated aluminium substrate indicates that the crystallite size of the zincated coating is ~20 nm. As a result, the copper coating has a tendency to grow in polycrystalline nature (Mattox 1994).

c) Preferred nucleation at the intersection of the crystallite

The intersection of two adjacent crystallites can act as the nucleation point. As a result, instead of growth of existing crystallites, nucleation of new crystallites occurs. This is attributed to the lower energy required to nucleate a crystallite at crystallite boundary intersections than the growth of the existing crystallites. As a result, the growth of the

existing copper crystallites stops at certain point and thereby the epitaxial growth was absent in the coatings. This is schematically shown in Figure 7.5.
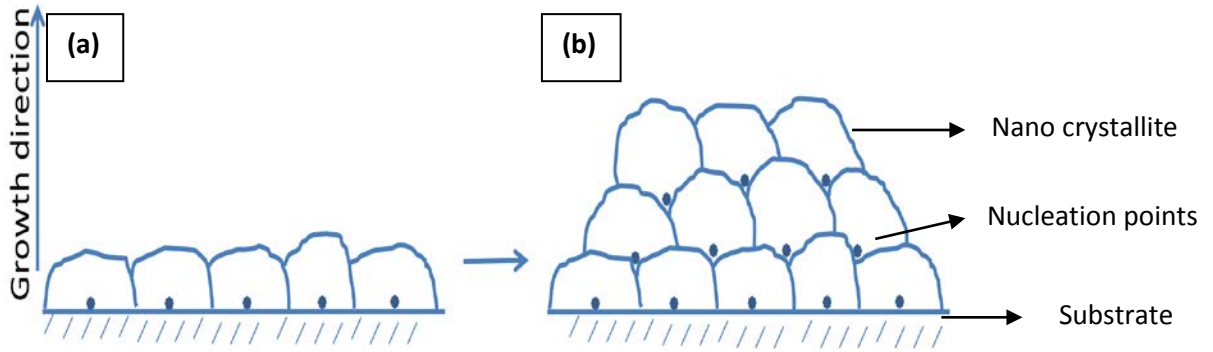
Figure 7.5 Schematic representation of the crystallite growth with nucleation point at a) initial stage and b) grown up stage.

i) How reduction in the crystallite size occurred at higher deposition rate?

According to Ohring (2001), the critical size of the nuclei decreases with increase in the deposition rate. On decrease of critical nuclei size, growth has been restricted and more number of nucleation occurred. The decrease in the critical nuclei size (r*) with increase in the deposition rate ($\dot{R}$) occurs because first derivative of r* w.r.t deposition rate ($\dot{R}$), at fixed temperature is less than zero (Ohring 2001). The above statement is rewritten as below

$$\left(\frac{\partial r*}{\partial \dot{R}}\right)_T < 0 \tag{7.6}$$

From Maxwell–Boltzmann relation, the change in the chemical free energy occurring during deposition is

$$\Delta Gv = -\frac{k_B T}{\Omega} \ln\left(\frac{\dot{R}}{\dot{R}_e}\right) \tag{7.7}$$

The first derivative of the equation (7.7) with respect to $\dot{R}$ is given as

$$\frac{\partial \Delta Gv}{\partial \dot{R}} = -\frac{k_B T}{\Omega \dot{R}} \tag{7.8}$$

From the thermodynamic equilibrium condition given in the Appendix-II

$$r* = \frac{-2(a_1\gamma_{fv}+a_2\gamma_{fs}-a_2\gamma_{sv})}{3a_3\Delta Gv} \qquad (7.9)$$

The first derivative of the equation (7.9) with respect to ΔGv is given as

$$\frac{\partial r*}{\partial \Delta Gv} = -\frac{-2(a_1\gamma_{fv}+a_2\gamma_{fs}-a_2\gamma_{sv})}{3a_3(\Delta Gv^2)}$$

Hence $$\frac{\partial r*}{\partial \Delta Gv} = -\frac{r*}{\Delta Gv} \qquad (7.10)$$

Where,

k_B is the Boltzmann constant (=1.38064852 × 10^{-23} m^2 kg s^{-2} K^{-1})

Ω is the atomic volume

T is the temperature (K)

$\dot{R}$ is the equilibrium deposition rate (atoms/cm^2-sec)

ΔGv is the chemical free energy change per unit volume (J/m^3)

γ is the interfacial tension (J/m^2)

$\dot{R}_e$ is the equilibrium desorption rate from the film nucleus at the substrate temperature 'T'(atoms/cm^2-sec)

Equation (7.6) is rewritten using direct chain rule with the equation (7.8) and (7.10) as below

$$\left(\frac{\partial r*}{\partial \dot{R}}\right)_T = \left(\frac{\partial r*}{\partial \Delta Gv}\right)\left(\frac{\partial \Delta Gv}{\partial \dot{R}}\right) \qquad (7.11)$$

$$= \left(-\frac{r*}{\Delta Gv}\right)\left(-\frac{k_B T}{\Omega \dot{R}}\right) \qquad (7.12)$$

Since ΔGv is negative from the equation (7.6), the overall sign is negative.

So it is proved that
$$\left(\frac{\partial r*}{\partial \dot{R}}\right)_T < 0$$

Hence it is inferred that the decrease in the size of the critical nucleus occurs with increase in the deposition rate.

ii) How twins are forming at higher deposition rate?

At higher deposition current densities, few crystallites in the coating contain nano sized twins. This indicates that the nucleation of twins is easier at higher coating current densities for copper. In the case of higher current densities, the deposition rate is faster. In such cases, the critical size of the twinned nucleus is almost equal to that of the perfect nucleus (twin free nucleus), due to the higher value of the bulk free energy (ΔG) and lower twin boundary energy for the copper.

The condition for the twin formation at higher deposition rate is explained as follows

Assume a perfect nucleus of disc shape having radius 'r' and height 'h'(shown in Figure 1 in Appendix III)(Zhang et al. 2004a).

$$\text{Its total free energy } (\Delta G_1) = 2\pi rh\gamma - \pi r^2 h \Delta G_a \tag{7.13}$$

Where γ is the surface free energy and ΔG_a is bulk free energy per unit volume driving the nucleation.

On the first derivation of ΔG_1 with respect to 'r' equating zero,

$$\text{If} \quad r = r^*, \quad \text{then} \quad \frac{d(\Delta G_1)}{dr} = 0$$

Then, $\quad$ critical radius of the perfect nucleus $r^* = \gamma / \Delta G_a$ $\tag{7.14}$

Assuming that if twins are forming in the crystallite with a twin boundary energy γ_t, then equation (7.13) is rewritten as

$$\Delta G_2 = 2\pi rh\gamma - \pi r^2 h \Delta G_a + \pi r^2 \gamma_t \tag{7.15}$$

Hence the critical radius of the twinned nucleus $r^*_{twin} = \gamma/(\Delta G_a + \gamma_t/h)$ (7.16)

In normal case, $r^* < r^*_{twin}$, and a perfect nucleus (twin free nucleus) will nucleate. However, in the case of higher deposition rate for the copper, the bulk free energy (ΔG_a) will be higher. Moreover copper has lower twin boundary energy (24 mJ m^{-2}) (Jain 2007). As a result, the difference between r^* and r^*_{twin} is negligibly small. Thus the probability of the nucleation of the twins is more or equal to the perfect nuclei during the growth at higher deposition rate during the copper coating.

The excess energy during rapid deposition of the copper is thus accommodated by the formation of the nano-twins (Augustin et al. 2016). The (111) texture of the copper also has a prominent role in the nucleation of twins. The (111) texture in the copper thin film growth is observed from the XRD analysis. The mechanism of the formation of the twins along (111) plane is explained in section 2.3.2 (Chapter 2).

To conclude, TEM study of the electrodeposited copper coating reveals that each nodule is composed of nano sized crystallites. Some of the crystallites in the coating deposited with higher current densities contain nano-twins. The overall observation is schematically shown in Figure 7.6.
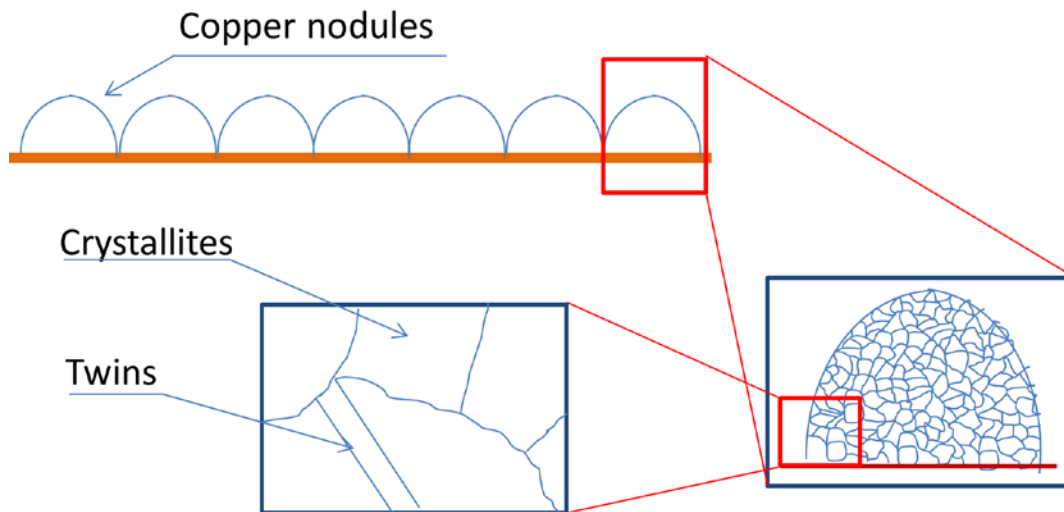
Figure 7.6 Schematic representation of the microstructure in the nodules of the copper coating as revealed by TEM studies.

7.1.1.4 Microstrain and texture analysis of the electrodeposited copper coatings

The XRD results of the electrodeposited coating deposited using both types of bath (Bath-I and Bath-II) are shown in Figure 4.12 and 4.29, respectively. The XRD profiles indicate the presence of the peaks corresponding to the crystallographic planes of (111), (200), (220) and (311), respectively. From the analysis of the XRD peaks, it is observed that as the current density increases during electrodeposition of the coating using both Bath-I and Bath-II, the FWHM of the XRD peaks are increased. As an example, the magnified profile corresponding to the (111) plane of the coating from the Bath-I is shown in Figure 4.14. This is attributed to the decrease in the crystallite size as well as increase in the microstrain, with the increase in the coating current density used for the electrodeposition (Singla et al. 2013). The crystallite size and microstrain in the coating is estimated by using Williamson-Hall method. This is shown below.

i) Crystallite size and microstrain measurement using Williamson-Hall method

Microstrain is calculated from the XRD profile using Williamson-Hall (W.H) method. This method consist of three models, *viz.* Uniform deformation model (UDM), Uniform stress deformation model (USDM), and Uniform deformation energy density model (UDEDM) (Singla et al. 2013). UDEDM is the most suitable for cubic crystal structured metallic samples (Rosenberg et al. 2000). In Uniform deformation energy density model of Williamson-Hall analysis, the material is assumed to be anisotropic in microstrain and is due to density of deformation energy (u) (Biju et al. 2008). The breadth of the XRD peak is the sum of the instrumental effect, crystalline size and microstrain. $(\beta_{hkl})_{measured}$ of the Bragg's peak is calculated by using a self-consistent profile fitting technique using a regular Pearson VII function, which assumes that the peak shape is symmetrical (Singla et al. 2013).The corrected instrumental broadening (β_{hkl}) is obtained by subtracting the breadth of the XRD peak obtained from the annealed copper.

$$\beta_{hkl} = [(\beta_{hkl})^2_{measured} - \beta^2_{instrumental}]^{0.5} \qquad (7.17)$$

Williamson-Hall method assumes that the peak broadening(β_{hkl})is exclusively originates from small crystallite size and microstrain.

So

$$\beta_{hkl} = \beta_{crystallite\ size} + \beta_{strain\ effect} \tag{7.18}$$

We have

$$\beta_{crystallite\ size} = \frac{K\lambda}{t\cos\theta_{hkl}} \quad \text{(Scherrer formula)} \tag{7.19}$$

$$\beta_{strain\ effect} = 4\varepsilon\tan\theta_{hkl} \quad \text{(Wilson formula)} \tag{7.20}$$

K is the shape factor, λ is x-ray wave length, t is the effective crystallite size normal to *hkl* planes, ε is the root mean square value of the microstrain and θ is the Bragg's angle. Substituting Scherrer formula and Wilson formula in equation (7.18) gives

$$\beta\cos\theta = \frac{K\lambda}{t} + 4\varepsilon\sin\theta_{hkl} \tag{7.21}$$

Equation (7.21) is known as Williamson-Hall equation. Assuming that microstrain is induced by deformation energy density (u). Using Hook's law u=$\varepsilon_{hkl}^2 E_{hkl}/2$,Williamson-Hall equation could be rewritten as below

$$\beta_{hkl}\cos\theta_{hkl} = \frac{K\lambda}{t} + \left[4\left(\frac{2}{E_{hkl}}\right)^{\frac{1}{2}}\sin\theta_{hkl}\right]u^{1/2} \tag{7.22}$$

Equation (7.22) represents the uniform deformation energy model of Williamson-Hall method. For cubic crystal, Young's modulus

$$E_{hkl}=s_{11} - (2s_{11} - 2s_{12} - s_{44})[(k^2l^2 + l^2h^2 + h^2k^2)/(h^2 + k^2 + l^2)^2] \tag{7.23}$$

Where s_{11} , $s_{12}$and s_{44} are the elastic compliances and their values for copper are 1.50x10^{-11}, -6.3x10^{-11} and 1.33x10^{-11} Pa^{-1}, respectively (Love 1944 and Xu et al. 2000). The Young's modulus of cubic structured copper is calculated as E_{111}=0.55x10^{-11}, E_{200}= 1.59x10^{-11}, E_{220}=0.8125x10^{-11} and E_{311}=1.1x10^{-11} Pa^{-1}. The slope of the linear fitted line

represents $u^{1/2}$ and y intercept represents $\frac{K\lambda}{t}$. The Williamson-Hall plot for current density of 10 A dm^{-2} is shown in Figure 7.7. From the y-intercept value and slope value obtained from Figure 7.7, crystallite size and microstrain along [111] direction was found to be 38.1 nm and 0.172 % respectively. The crystallite size and percentage of microstrain for the remaining coating current densities of Bath-I are also estimated in the same method and values are tabulated in Table 7.1. The average crystallite size obtained from TEM analysis at 2 A dm^{-2} and 10 A dm^{-2} current densities are in agreement with the crystallite size values obtained by using Williamson-Hall method. Hence it is assumed that microstrain values obtained from Williamson-Hall method is free from error. Similarly, the microstarin obtained from the XRD profile of the coating corresponding to the Bath-II is given in Table.7.2.
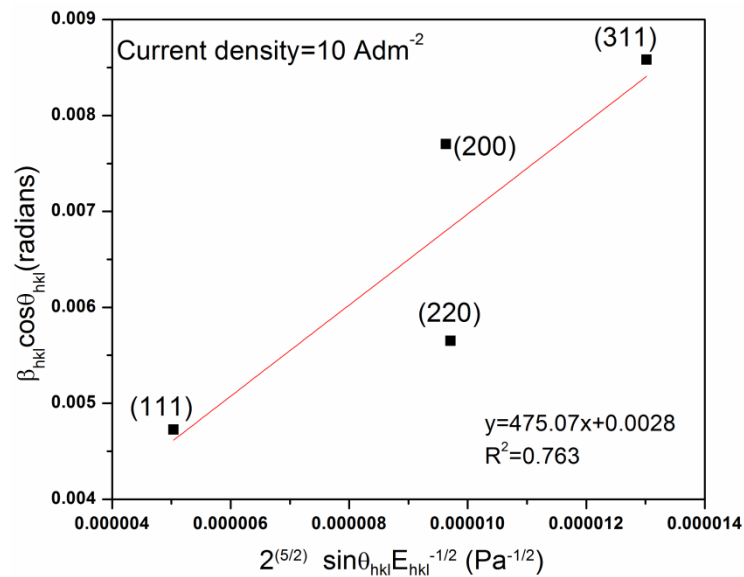
Figure 7.7 Williamson-Hall plot for the deposit using coating current density of 10 A dm^{-2} using Bath-I.

Table 7.1 Crystallite size and microstrain measurement using Williamson-Hall method for the coating using Bath-I

Current density (A dm^{-2})	Crystallite size (nm)	% of microstrain along (111) plane
2	78.0	0.030
4	70.6	0.051
6	56.2	0.090
8	52.0	0.142
10	38.1	0.172

Table 7.2 Crystallite size and microstrain measurement using Williamson-Hall method for the coating using Bath-II

Current density (A dm^{-2})	Crystallite size (nm)	% of microstrain along (111) plane
1	25.6	0.182
2	22.8	0.186
3	19.1	0.194
4	16.8	0.202

As per the data presented in Table 7.1 and Table 7.2, the value of microstrain increases with increase in the current density. This is attributed to the decrease in the crystallite size with increase in the coating current density. The reason for the decrease in the crystallite size with increase in the coating current density is due to the increase of nucleation with increase in the copper ion supply, as explained in the Figure 7.2. With the reduction in the size of the crystallites in the nano structured copper coating, the crystallite boundary volume increases. The copper atoms get attracted from the crystallite to the boundary due to the large amount of vacancies at crystallite boundaries. As a result, certain amount of elastic strain develops as shown in Figure 7.8. As reported by Qin and Szpunar (2005), such elastic strain is more near the crystallite boundaries as compared to the interior of

the crystallites. Thus in small crystallites, the mobile dislocations are pulled to the crystallite boundaries. This is evidenced by the dislocation free crystallites in the TEM micrographs of copper coatings. The arrows shown in Figure 7.8 indicate the pulling direction of the copper atoms from the crystallites into boundary volumes. If microstrain exceeds elastic limit, plastic deformation like stacking faults and twins are formed in the copper coatings (Qin and Szpunar 2005). Moreover at higher deposition current density, due to increased energy, twins are quite common in copper coatings. Such growth twins and stacking faults also contribute to the microstrain. Because of the increase in volume of defects with increase in the current density of the nano structured coating, the copper atoms experience a pulling force into it. Certain amount of microstrain thus developed in the lattices near the defects like crystallite boundaries (Qin and Szpunar 2005). The tabulated values of microstrain is given in Table 7.1 and Table 7.2 also support this.
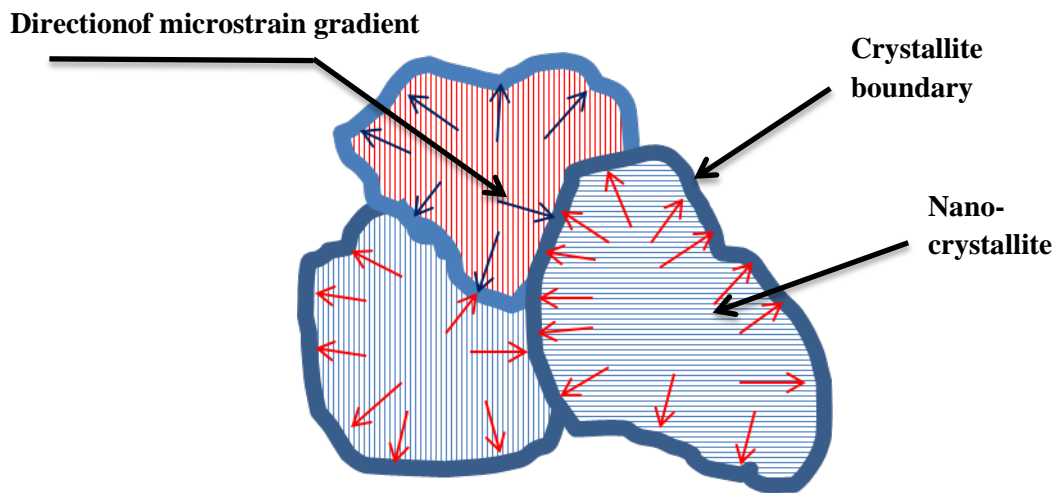
Figure 7.8 Schematic representation of microstrain gradient directions in nano crystallites.

ii) Texture analysis of the electrodeposited copper coating

The XRD profile of the electrodeposited coating given in Figure 4.12 and Figure 4.29 showed that intensity ratio for the peak corresponding to the (111) plane at 43.16° is

higher compared to that for the same recorded in ICDD # 89-2838 (International Centre for Diffraction Data). Such higher intensity ratio represents the texture of the (111) plane in the coating. The preferred growth direction of the deposited copper is confirmed from the XRD profile of the coating (as shown in Figure 4.13), which has been deposited for longer duration to get a higher thickness. In Figure 4.13, only peak at 43.16° corresponding to (111) plane of the copper is observed. The absence of all other peaks in the XRD pattern indicates that the coating is deposited in highly preferred orientation parallel to (111) plane along [111] direction. The preferred growth of (111) plane in<111> direction is due to its minimum growth strain as compared to other planes in FCC crystal structure (Sriraman et al. 2006). The (111) plane is the most densely packed plane in FCC crystal structure. The (111) growth texture facilitates the nucleation of the nano-twins because it is known that in FCC metals, twins can form only in (111) plane (Zhou and Wadley 1999). The mechanism of nano-twin formation is schematically explained in section 2.3.2 (Chapter 2) with the help of Figure 2.6.

7.1.2 DC Magnetron Sputter Deposition

The microstructural characteristics of the sputter deposited copper coatings are mainly dependant on its process of deposition. Hence before coming to the microstructural features, a brief look on the process of DC magnetron sputter deposition is given below.

7.1.2.1 Process of sputter deposition

Sputter deposition is the process of deposition of the atoms from the target surface by momentum transfer due to bombarding energetic atomic sized particle (Mattox 1998). The process of sputter deposition could be divided into three steps *viz* i) sputtering of the copper, ii) transportation of the ejected (sputtered) copper atoms and iii) deposition of the copper on the substrate (Ohring 2001).

i) Sputtering of copper

The sputtering chamber contain high vacuum with adequate amount of argon gas. Because of higher negative potential applied to the copper target, the electrons are released from the target and hit the neutral argon gas atom. As a result, the argon atoms become positively charged argon ions (Ar^+). The reaction is given below.

$$Ar + e^- \rightarrow Ar^+ + 2e^- \tag{7.24}$$

Because of the positive charge, the argon ions get accelerated to the negatively charged copper target. As a result, the copper atoms sputter off from the target surface by getting knocked out. The knocking of the copper atom is possible by momentum transfer between the energetic argon ions and the atoms on the surface of the copper target. This is schematically shown in Figure 3.5.

The ratio of the number of sputtered atoms to the number of incident ions is known as 'sputtering yield'. The sputtering yield could be related to the momentum transfer by the empirical relation given in equation (7.25) (Ohring 2001).

$$\text{Sputtering Yield} = \frac{3\alpha}{4\pi^2} \frac{4m_i m_t}{(m_i + m_t)^2} \frac{E_i}{U} \tag{7.25}$$

Where 'm_i' is the atomic mass of the bombarding (or incident) argon ion (=40 amu), 'm_t' is the atomic mass of the copper target (= 63 amu), 'U' is the binding energy of the surface atom of the target, 'E_i' the energy of the incident ion, and α is the ratio of m_i/m_t.

From the equation (7.25), it is clear that the sputtering yield is proportional to the energy of the incident ion. The energy of the incident ion is proportional to the target power (sputtering power) because as the sputtering power increases, more electrons are released from the copper surface and hit the argon atoms.

ii) Transportation of the ejected copper atoms

Due to the bombardment of the argon ions, the copper atoms are ejected from the target surface. Once the copper is ejected, these atoms can travel to the double zincated aluminium substrate through high vacuum. The vacuum pressure is important in the morphology of the coating because the growth behavior of the copper coatings depends on the kinetic energy of the ions that arrive at the substrate and the mean free path of the particle, which allows an increase or decrease in the bombardment of the copper atoms to the surface of the double zincated aluminium substrate. The coating morphology at different argon pressure is illustrated with the help of the structure zone model given in section 2.3.1(Chapter 2).

iii) Deposition of the copper

The copper atoms released from the targets impinge on the double zincated aluminium substrate and condense on the substrate by losing their energy. The energy loss occurs by chemical reaction with the substrate surface atoms, finding preferential nucleation sites (e.g lattice defects, atomic steps), collision with the other diffusing surface atoms and collision with the adsorbed surface species (Mattox 1994). The condensed atoms are bonded to the atoms which are already deposited (Cu or Zn) by chemical reactions. The chemical bonding may be metallic bonding where the copper atoms share orbital electrons. The bonding takes place at preferred nucleation sites. The SEM micrograph of the double zincated aluminium is shown in Figure 4 (Appendix I). In which the unevenness on the surface could act as the nucleation sites. The mobile surface adatoms could also nucleate by collision with other similar adatoms to form a cluster of atoms and then stable nuclei (Mattox 1998). The interaction of the copper to the zinc at the Cu-Zn interface is one of the major factors deciding the mobility of the copper atoms on the substrate. The nuclei grow by collecting adatoms which either impinges on the nuclei directly or migrate over the surface to the nuclei. Types of nucleation depending on the nature of the interaction between the depositing atoms and the substrate material are

142

given in section 2.3.1 (Chapter 2). In which the present deposition is under the Stranski-Krastanov (S-K) mechanism. The S-K mechanism is common with metal on metal deposition and at low temperatures where the surface mobility is low (Mattox 1994).

7.1.2.2 Morphological analysis of the sputter deposited copper coatings

In the case of DC magnetron sputter deposited copper coatings, nodular morphology with globular shaped topography was observed by the SEM study. The SEM micrographs are shown in Figure 5.2 and Figure 5.3. With increase in the sputtering power, the nodules' size of the copper reduces as shown in Table 5.2. This is attributed to the increase of the copper flux density towards the substrate with increase of Ar^+ bombardment on the copper target. The bombardment of the Ar^+ is increased due to the increase of the target power. Consequently, the copper atom flux density towards the substrate is increased because sputtering yield is proportional to the target power, as given in equation 7.25. With increase in the copper atom flux density, the nucleation density is increased. This is similar to the case of the electrodeposition. As a result, smaller nodular shaped morphology is observed on the topography of the coating deposited using higher sputtering power.

In the cross-sectional study, columnar structure is observed as illustrated in SEM images presented in Figure 5.3. According to the structure zone model shown in Figure 2.5, the present copper sputter deposition belongs to Zone-I because the values of T/Tm <2.5 (where T =300 K (substrate temperature) and Tm =1356 K (melting temperature of the target)) and the argon pressure was maintained at 10 mTorr. The low argon pressure was maintained to ensure an essentially collisionless transport of the copper flux to the substrate. Since sputtered atoms are deposited along the line of site, the deposition is more uniform. The deposit is observed as smoother compared to the coating deposited by using electrodeposition method. The roughness values given in Table 5.1 also indicate the same.

7.1.2.3 Analysis of crystallite structure in the sputter deposited copper coatings

TEM micrographs of sputtered copper coating corresponding to the sputtering powers of 50 W, 100 W, and 150 W are shown in Figure 5.5, Figure 5.6 and Figure 5.7, respectively. The average crystallite size measured from the above mentioned TEM micrographs corresponding to different sputtering power is graphically shown in Figure 7.9. The graph shown in Figure 7.9 indicates that sputtering power is linearly proportional to the crystallite size in the power range between 50W to 150 W under a given set of operating parameters, given in Table 3.4. As the sputtering power increases from 50 W to 150 W, the average crystallite size is reduced from 49 nm to 18 nm. The TEM micrograph at lower magnification shown in Figure 1 (Appendix I) indicates that each copper nodule is composed of nano sized crystallites. The cross sectional TEM micrographs shown in Figure 5.8 proves that the epitaxial growth was absent. The absence of epitaxial growth is attributed to the reasons like lattice mismatch, polycrystallinities of the substrate and rapid deposition as explained in the case of the electrodeposition given in section 7.1.1.3.
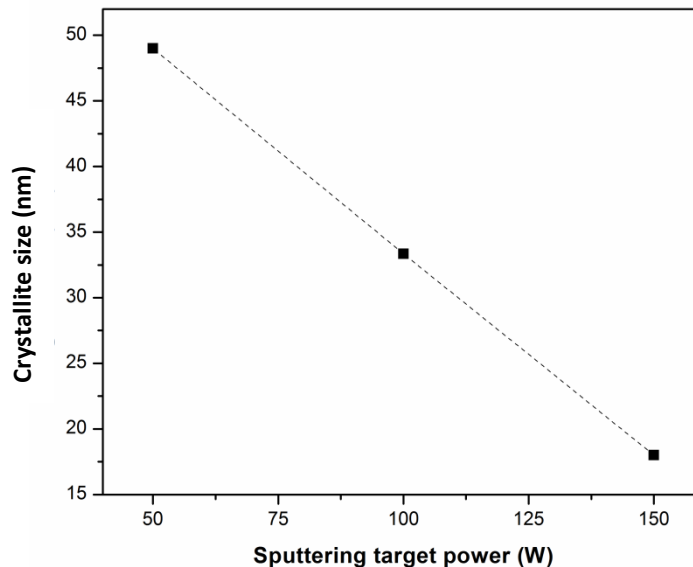
Figure 7.9 Variation of the crystallite size with sputtering power in DC magnetron sputter deposited copper coating.

In the present study, since the deposition parameters other than the sputtering power remain same, it is observed that the change in the crystallites' size is due to the variation of sputtering power. As the sputtering power increases, crystallite size of the coating reduces. Similar results are given by Le et al. (2010). Due to the increase in the sputtering power, more argon ions bombard the copper target. As a result, more number of copper species get sputtered from the copper target and deposited on the substrate. Because of more copper flux density towards the substrate at higher sputtering power, more nucleation sites are activated. Hence, crystallite size becomes reduced with increase in the sputtering power. The variation of copper flux at lower and higher sputtering power is schematically shown in Figure 7.10. This phenomenon is similar to that of increase in the current density during the electrodeposition. At lower copper flux density, the condensed copper species on the substrate surface may move on the surface to nucleate at preferred sites or to the nucleated crystallite. As a result, less number of nucleation as well as more growth occurs at lower sputtering power. At higher sputtering power, the copper crystallites nucleate at the condensing point without much surface movement. The growth gets stopped due to the physical impingement as compared to that at lower sputtering power. As a result, crystallites size becomes smaller as compared to that in the coating deposited with lower sputtering power. The above mechanism is schematically shown in Figure 7.10.
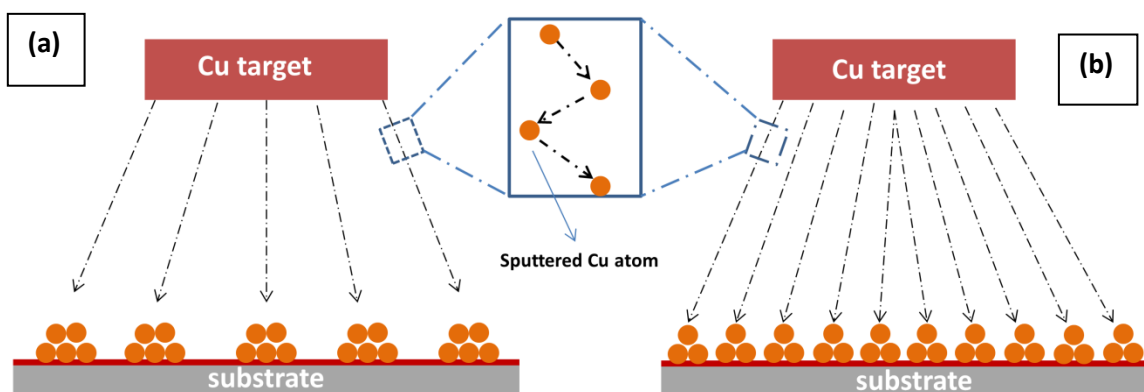
Figure 7.10 Schematic representation of the copper flux during DC magnetron sputtering at a) low sputtering power and b) higher sputtering power.

In the sputter deposited copper coatings, as in the case of the electrodeposited coatings, nano-twins are observed when deposition is carried out at higher sputtering power (Figure 5.7 (d)). An occurrence of twins at this condition is mainly due to the higher deposition rate. As mentioned in the case of the electrodeposition, critical size of the twinned nucleus is almost equal to perfect nucleus (twinned free nucleus) at higher deposition rate during sputtering. This is due to the increased bulk free energy (ΔG) during rapid deposition. Moreover, copper has less twin boundary energy (24 mJ/m^2) on (111) planes, which is less than that of the crystallite boundaries (625 mJ/m^2) (Zhou and Wadley 1999). Thus, such nano-twinned crystallites are energetically stable. The detailed mechanism of the same is given in section 7.1.1.3 (ii).As explained in the section 2.3.2 (Chapter 2), the twins can nucleate only in (111) plane for FCC crystal structure. So the (111) texture revealed from XRD of the sputtered copper coatings supports our proposition.

7.1.2.4 Microstrain and texture analysis of the sputter deposited copper coatings

The XRD profiles of the sputter deposited copper coatings deposited at different sputtering power is shown in Figure 5.9. The peaks corresponding to the crystallographic planes of (111), (200) and (311) are indicative of the crystalline nature of the copper coatings deposited by sputtering method. The FWHM of the XRD peaks are found to increase with increase in the sputtering power. The major reason for increase in the peak width is attributed to the decrease in the crystallite size which occurs with increase in the sputtering power. This is confirmed from the analysis of the TEM micrograph of the sputter deposited copper coatings. The reduction in the crystallite size with increase in sputtering power is obvious. This is attributed to the increased flux density of copper as explained in section 7.1.2.3. Since the crystallite size of DC magnetron sputtered copper coating is in the range of 49 nm to 18 nm, a considerable amount of microstrain is expected as in the case of the electrodeposited copper coatings. But the quantitative estimation of the microstrain of the DC magnetron sputter deposited coating is difficult due to the presence of less number of peaks in the x-ray diffraction profile. It is reported

that at least four peaks are needed for microstrain measurement by using Williamson-Hall method (Biju et al. 2008). The absence of dislocations in the crystallites is attributed to the pulling of mobile dislocations to the crystallite boundaries due to the microstrain (Qin and Szpunar 2005).

The increased value of the peak intensity of (111) with respect to the ICDD#89-2838 represents the preferred growth of the copper coatings. This is attributed to the minimum growth strain associated with (111) plane in <111> direction as reported in the case of electrodeposited copper coatings. Due to the preferred growth of (111) along <111> direction, nano-twins are formed in the nano sized crystallites. Such nano-twins also contributed to the microstrain in the copper coatings.

7.2 Mechanical Characterizations

Determination of mechanical properties like surface hardness and substrate adhesion strength of the coating are important because they indicate their ability to withstand the abuse during its handling as a touch surface. The hardness of the copper coating on the aluminium substrate is obtained from the scratch hardness test as well as the microhardness test. Similarly, adhesion strength of the coatings to the substrate is obtained by using the cross-hatch cut test as well as the pull-off adhesion test. The results are presented in section 4.1.3, 4.2.3, and 5.3 (Chapter 4 and Chapter 5). The detailed discussion of the obtained results is given in the present section.

7.2.1 Hardness analysis of the copper coatings

Scratch hardness test as well as microhardness test are used to evaluate the hardness of the coatings. The soft metallic coatings (hardness <5 GPa), like, copper undergo plastic deformation during the scratch test (Bull and Berasetegui 2006). In scratch hardness test, the copper coated substrate is drawn against the stylus tip. This results in the shearing of copper layers. Therefore if cohesive bond strength value is higher, it is expected to show a higher value of the scratch hardness. Hence, scratch hardness is an indirect measure of

the cohesive bond strength of the coatings. Schuh et al. (2002) and Vencl et al. (2011) have proved by their experimental work that increase in the cohesive bond strength is also an indication of the improved wear resistance of the coating. Microhardness test, on the other hand, is a static indentation hardness test and it gives indentation resistance of the material against the compressive load acting perpendicular against the coating at selected points.

7.2.1.1 Electrodeposited copper coatings

In the electrodeposited copper coatings, both scratch hardness as well as microhardness test results are given Table 4.2 and Table 4.5. Table 4.2 represents the hardness values of the coating deposited by using Bath-I. From Table 4.2, it is inferred that both scratch hardness as well as microhardness values increase with increase in the coating current density. Further, the microhardness values are closer to the scratch hardness values. The slight increase in the scratch hardness values as compared to the microhardness values is due to the severe plastic deformation occurring during the scratch test. Similar findings were reported by Beegan et al. (2007). Scratch hardness values increased from 0.868 GPa to 2.52 GPa, whereas microhardness values increased from 0.8±0.1 GPa to 2.05±0.1GPa with increase in the coating current density. Among the measured values of the hardness of the coatings from the Bath-I, highest microhardness of 2.05±0.11 GPa is recorded on the deposit in which the crystallite size is 38.1 nm. This value is about four times greater than that of annealed copper which recorded 0.49 GPa, as given by European Copper Institute, (2015). With increase in the coating current density from 2 A dm^{-2} to 10 A dm^{-2}, crystallite size decreased from 78 nm to 38.1 nm, as given in Table 7.1. It is thus inferred that reduction in the crystallite size is the reason for increasing hardness of the coating. According to Hall-Petch relation, hardness is inversely proportional to the square root of crystallite size (Meriç et al. 1997). As the crystallite size reduces, more number of dislocations accumulated at the crystallite boundary. This is well proved by TEM images in which high proportion of crystallite boundary area is visible. As a result, the dislocation movement became difficult during plastic deformation. This is schematically

148

shown in Figure 7.11 where 'x' indicates the distance of the dislocation movement in coarser crystallite (Figure 7.11 (a)) and 'y' indicates the same in the smaller crystallite (Figure 7.11 (b)). From the Figure 7.11, it is clear that, the distance of dislocation movement in finer crystallites is smaller than that in the coarser crystallite (i.e x>y). The reason for x>y is attributed to the reduction in the crystallite size. At the crystallite boundary, the dislocation movements are blocked. These types of strengthening in metals are generally known as grain boundary strengthening mechanism (Dieter and Bacon 1986).
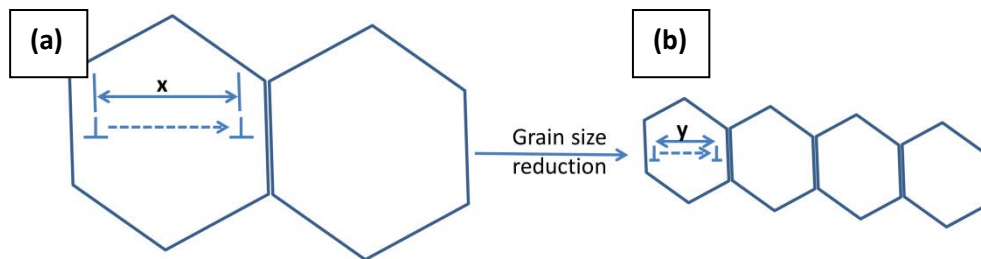
Figure 7.11 Schematic representation of the dislocation hindering by the crystallite boundary in a) coarse crystallite and b) fine crystallite, respectively.

Moreover, the XRD analysis shows that the coating has a preferred growth parallel to (111) plane along [111] direction. The (111) plane has higher value of Young's modulus (172 GPa) due to its denser packing as compared to other planes in the FCC structure of the copper (Love 1944 and Xue et al. 2000). As reported in many literatures, the presence of the nano-twins also increases the hardness of the coating (Lu et al. 2009, Zhang et al. 2004a, Zhang et al. 2004b, Lu et al. 2004, and Lu et al. 2005). The detailed explanation on the effect of the nano-twins on the hardness of the copper coatings is given in section 7.2.1.3. Many of these factors in combination pertaining to nano crystallites are contributing to the high value of the coating hardness.

Table 4.5 shows the microhardness and the scratch hardness results of the coating deposited using Bath-II. This coating also exhibits good coating hardness values, similar to the coating from the Bath-I. This is attributed to its nano-crystallinity and preferred texture of (111) plane along <111> direction. Similar to the coating from the Bath-I, the

crystallite size is reduced with increase in the coating current density. The XRD measurement shows that crystallite size decreased from 25.6 nm to 16.8 nm with increase in the coating current density from 1 A dm^{-2} to 4 A dm^{-2} (Table 7.2). But the scratch hardness as well as the microhardness values reduced with the decrease in the crystallite size. This is attributed to the softening phenomenon of the nano-crystallites due to its ultra-fine crystalline size. It is known as reverse Hall-Petch effect. Literatures reported that softening phenomenon of the copper nano-crystallites starts for the crystallites size less than ~16 nm (Sanders et al. 1997). In the present investigation, the crystallite size of the coating measured from the TEM micrographs, was in between 17.6 nm to 12.9 nm. This is given in section 4.2.2.2 (Chapter 4). Compared to the TEM values, crystallite size measured from the XRD was a little higher. This may be due to the experimental error. The crystallite size is in the reverse Hall-Petch region if the TEM results are considered. It is argued by Zhang et al. (2004) that the phenomenon of reverse Hall-Petch relation is due to incomplete densification of the crystallite boundary region which gives rise to occurrence of crystallite boundary sliding, like Coble creep, even at room temperature. But the coating deposited with the current density of 4 A dm^{-2} hasn't shown much softening during hardness test as compared to the samples deposited with the lower coating current densities. The obtained hardness was three times higher than that of the annealed copper. It is attributed to the large number of nano-twins present in the nano-crystallites in the coating deposited with the higher coating current densities. The reasons for the nucleation of the twins in the coating deposited with higher deposition rate are given in section 7.1.1.3 (ii). The role of the twins on the hardness of the coating is explained in the section 7.2.1.3.

7.2.1.2 DC magnetron sputter deposited copper coatings

The hardness of the sputter deposited copper coating has been evaluated by using the scratch hardness test as well as the microhardness test. The scratch hardness test result of the sputtered coating is given in section 5.3.1. Similarly, the microhardness test results are given in section 5.3.2. The obtained values for both the scratch hardness and the

microhardness tests are given in Table 5.3. Both scratch hardness as well as microhardness values are increased with the sputtering power. As explained in the TEM micrograph analysis of sputtered coating (section 7.1.2.3), the crystallite size is reduced from 49 nm to 18 nm due to the increase in the sputtering power from 50 W to 150 W. The increase in the hardness is attributed to the reduction in the crystallite size. The highest value of the microhardness is 1.49 GPa. It is registered for the coating corresponding to the 150 W sputtering power. The scratch hardness values are slightly higher than that of the microhardness, which is similar to the case of the electrodeposition. The increased hardness of the sputtered copper coating as compared to the annealed bulk copper could be attributed to the factors like nano-crystallites, preferred texture and presence of the nano-twins. The detailed explanations are given below.

i) Nano-crystallite structure

Crystallite boundaries are strong obstrucles for the dislocation movement. As the crystallite size reduces, crystallite boundary volume increases. As a result, more number of dislocation movements gets blocked at crystallite boundaries and thereby plastic deformation become difficult (Dieter and Bacon 1986). This increases the hardness as well as the strength of the coating. The relation between the crystallite size and the strength of the coating is expressed by Hall-Petch relation, which is given in Equation (7.26). The mechanisms are similar to as explained in the case of electrodeposition, given in section 7.2.1.1.

ii) Preferred texture

The XRD study of the sputter deposited coating exhibits the preferred texture of the (111) plane along <111> direction. In copper, (111) plane is the close packed one, offering highest value of Young's modulus compared to other crystallographic planes in the copper (Love 1944 and Xue et al. 2000). As a result the mechanical strength of the coating became higher compared to the polycrystalline bulk copper. In the study of

titanium, similar observation is reported by Bahl et al. (2014). Similar observations have been made in the case of the electrodeposited copper film too.

iii) Presence of nano-twins

Similar to the electrodeposited copper coatings, sputter deposited copper coatings also contain nano sized twins in the crystallites. Such twins are more prominent in the coatings deposited at higher sputtering power (150W). Along with the crystallite boundaries, such nano-twins also hinder the dislocation movement during plastic deformations. The TEM micrograph corresponding to the 150 W (shown in Figure 5.7 (d) and (e)) indicated that the coating contains a good number of twins. This is due to the increased deposition rate of the copper atoms. The reasons of nucleation of the nano-twins at higher deposition rate are given in section 7.1.1.3 (ii). The condition for nucleating nano-twins in sputtering has been explained by Zhang et.al (2004b). It is given in the section 2.3.2 (Chapter 2).

7.2.1.3 Influence of the nano-twins on the hardness of coating

The presence of nano-twins at higher coating current densities is confirmed by the TEM micrographs. In order to analyse the influence of such nano-twins on the hardness of the coating, the values of the hardness measured by experimental technique as well as empirical relation were compared for the coating obtained from the Bath-I. The experimental measurements are carried out by the scratch hardness test and the microhardness test. Whereas, Hall-Petch relation is used to measure the hardness by empirical method. The estimated values of the hardness are plotted against different crystallite size, obtained by varying the coating current densities is shown in Figure 7.12. The Hall-Petch relation is given in equation (7.26) (Meriç et al. 1997).

$$\sigma = \sigma_0 + K_0 d^{-1/2} \tag{7.26}$$

Where, d is the crystallite diameter, σ is the yield stress, σ_0 and K_0 are Hall-Petch constants. Its values for nano-crystalline copper are 20 MPa and 0.14 MPa m$^{-1/2}$, respectively (Hansen 2004). Scratch hardness and static microhardness values showed similar behavior with the variation in the crystallite size. Maximum values of the scratch

hardness and the microhardness values are obtained in the case of the coating having a crystallite size of 38.1 nm. At lower crystallite size, there is sudden shoot up of both the microhardness and the scratch hardness values. The scratch hardness showed 2.52 GPa whereas the microhardness test shows 2.05±0.11 GPa for the deposit having a crystallite size of 38.1nm. This maximum value of the hardness is much higher than the hardness values obtained from Hall-Petch relation (1.52 GPa). This is attributed to the presence of nano-twins in addition to the reduction in the crystallite size as well as the (111) texture.
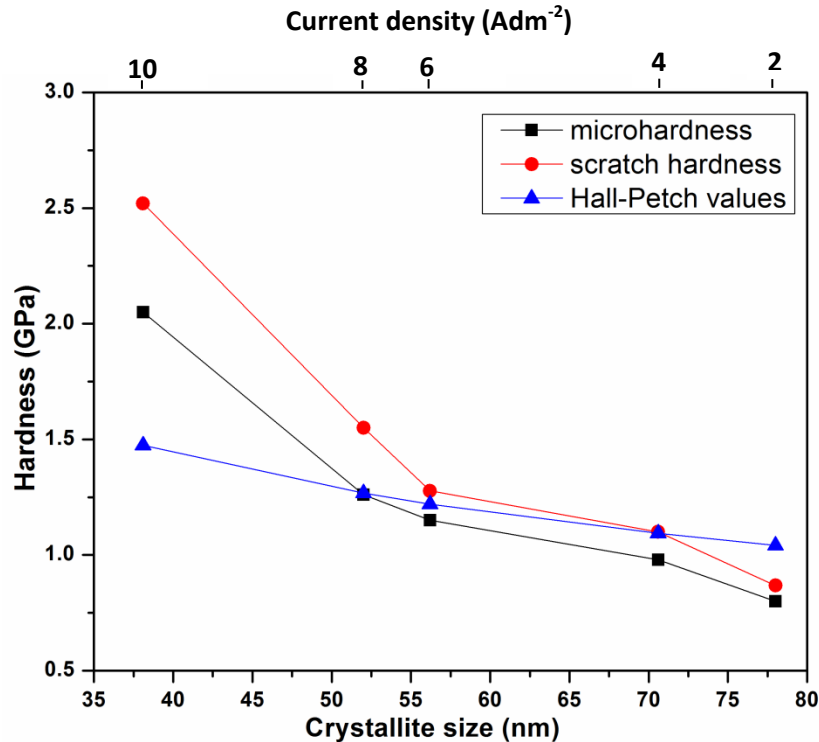
Figure 7.12 Comparison between the scratch hardness values, microhardness values and hardness from Hall-Petch relation against different crystallite sizes and coating current densities.

Figure 4.11 shows a TEM micrograph corresponding to the coating current density of 10 A dm^{-2}, in which a large number of nano- twins are visible. One of the crystallite with nano-twins is magnified and presented in Figure 4.11 (b). Its SAED pattern is given in Figure 4.11(c). Width of the nano-twins is in the range of 3-7 nm. The density of the

nano-twins is estimated and it is in the range of approximately 400 twins per square micrometer imaging area. The nucleation of such twins is attributed to the excess energy developed in the coating deposited with the high coating current density (Simões et al. 2010). Zhang et al. (2004a) elucidated how twins of few nanometers thick help to improve the hardness of the copper thin film. Such twins can effectively obstruct the easy movement of the dislocations, leading to dislocation pile-up. This is schematically shown in Figure 7.13.
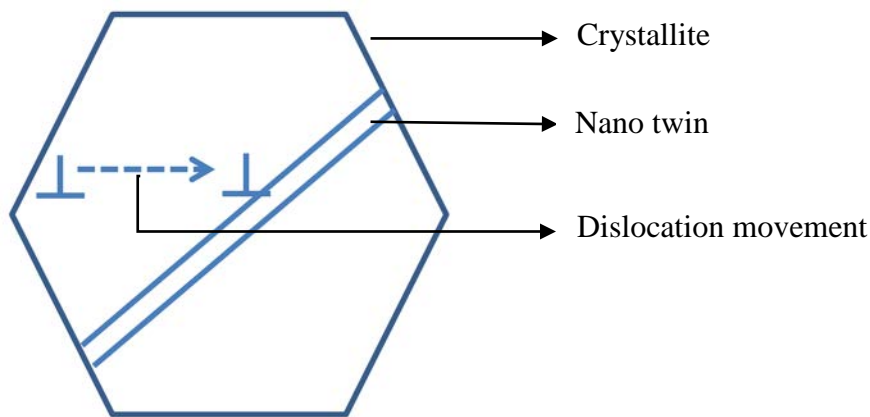
Figure 7.13 Schematic representation of the dislocation pile-up within twinned crystallite.

7.2.2 Adhesion strength analysis of the copper coatings to the substrate

Any coating becomes non-functional, if it does not possess sufficient adhesive strength with the substrate. So, the analysis of the adhesion strength of the coating to the substrate and its improvement has more significance.

7.2.2.1 Adhesion strength improvement of the copper coating to the substrate by using double zincation process

In the present study, copper coating by the electrodeposition and DC magnetron sputtering has been carried out on the double zincated aluminium, because our

preliminary experimental results showed that the double zincated aluminium substrate offered 4-6 times higher adhesion strength to the copper coatings compared to that of the bare aluminium substrate. The literatures also reported similar observations (Monteiro et al. 1991). During the zincation process, the aluminium oxide layer on the aluminiumsubstrate is removed by the dissolution of the aluminium in the zincate bath due to its high alkalinity, which has registered a pH of 12.4. Higher alkalinity of the bath is maintained by the presence of the NaOH kept at a concentration of (525 g/l). During one minute dipping of the aluminium substrate into the zincate bath, the exchange reactions between the aluminium and the zincate ions take places. Such a reaction could be represented by following reactions as envisioned by Willigan et al. (2014).

(i) Dissolution of the aluminium and formation of the aluminate

$$Al + 3OH^- \rightarrow Al\,(OH)_3 + 3\,e^- \tag{7.27}$$

$$Al(OH)3 \rightarrow AlO_2^- + H_2O + H^+ \tag{7.28}$$

(ii) Reduction of the zincate and the deposition of the aluminium

$$Zn(OH)_4{}^{2-} \rightarrow Zn^{2+} + OH^- \tag{7.29}$$

$$Zn^{2+} + 2e^- \rightarrow Zn \tag{7.30}$$

Once the thin layer of the zinc is deposited, further dissolution of the aluminium will be stopped by the adherent zinc layer between the aluminium and the solution. But a single time zinc deposition does not gives adequate surface coverage and smooth surface. Thus, the zincation process is needed to be carried out twice (double zincation) for better surface coverage and surface smoothness as reported by Murakami et.al (2006). The detailed procedure of the double zincation process is given in the section 3.1.1 (Chapter 3).

The zincated aluminium enables direct contacts of the copper to the zinc. The chemical interaction of metal to metal contact gives better bond strength than that of the metal to ceramic (Al_2O_3) contacts (Finnis 1996). The improvement in the adhesion strength of the

zincated substrate is also facilitated by the lower value of the lattice mismatch between the copper and the zinc as compared to that of the copper to the aluminium oxide.

7.2.2.2 Adhesion strength analysis of the electrodeposited and sputter deposited copper coatings

The adhesive strength of the electrodeposited copper coating as well as the sputtered coating on the double zincated aluminium substrate has been evaluated by using cross-hatch cut test and pull-off adhesion test. Cross-hatch cut test is used to analyze the coating qualitatively, whereas Pull-off adhesion test is used to evaluate the adhesion strength quantitatively. The obtained results are presented in Chapter 4 and Chapter 5. The data given in Table 7.3 shows the comparison of the adhesion test results for different types of the coatings. For the purpose of comparison of the adhesion strength between different types, uniform coating thickness of 5 μm was used. The data in the Table.7.3 shows that the adhesion strength of the copper coating obtained from the Bath-II and sputtered coating is better as compared to the copper deposit obtained from the Bath-I.

The adhesion strength of the copper coatings to the substrate depends on the nucleation density of the nano sized crystallites on the substrate (Mattox 1994). The nucleation density of the nano-crystallites is inversely proportional to the crystallite size. The coating from the Bath-I has more crystallite size as compared to coating from the Bath-II and the sputter deposited coating. The detailed comparison is given in Table 7.3. The increased adhesion strength of the coating obtained from the Bath-II and sputtered coating is attributed to its increased nucleation density.

Along with the nucleation, the width of the columnar/ nodular structure also affects the adhesion strength. As the width of the columns or nodules becomes narrow, the adhesion strength of the coating increases because each column or nodule is separately bonded to the substrate and poorly bonded to each other (Prater and Moss 1983). In the case of copper coating from the Bath-I, Bath-II and DC magnetron sputtering, the width of the

156

nodules are different as given in Table 7.3. The coating obtained from the Bath-II and the sputtered ones have smaller in nodular or columnar width. This is also a reason for the improved adhesion strength of these two type of coating as compared to that from the Bath-I.

Table 7.3 Comparison of the adhesion strength values and other related parameters of the coating obtained by different methods

	Electrodeposited coating from		DC magnetron sputter coating
	Bath-I	Bath-II	
Nucleation density	~1200 / μm^2	~7000 / μm^2	~4000 / μm^2
Width of the nodules/columns	4 μm -6 μm	0.77 μm -3.4 μm	0.2 μm -1 μm
Cross-hatch cut test results (As per ASTM D3359)	4B	5B	5B
Pull-off adhesion test results (As per ASTM D4541)	1.2±0.2 MPa	>1.9 MPa	>1.9 MPa

7.3 Antimicrobial Characterizations

The antimicrobial activity of the copper coating deposited by using electrodeposition as well as DC magnetron sputter deposition has been evaluated by CFU (colony forming unit) counting technique, as given in Figure 6.1 and Figure 6.5, respectively. The coating has better antimicrobial activity as compared to the bulk copper. In the present section, the mechanism of antimicrobial activities as well as the reasons for better antimicrobial activity of the copper coatings compared to the bulk copper has been discussed separately.

7.3.1 Mechanism of antimicrobial activity of the copper against bacteria

Escherichia coli (E. coli) and methicillin-resistant *Staphylococcus aureus* (*MRSA*) are the bacteria which were taken for antimicrobial testing of the copper coated aluminium samples in the present study. *E. coli* was taken as a typical example for gram negative and *MRSA* as an example for gram positive group of bacteria. Since the cell wall structure for the gram negative and gram positive are different, the mechanism of antimicrobial activity is also expected to be different. The results of the electron microscopic (SEM and TEM) studies of the copper exposed and non-copper exposed bacteria and their EDS results have been presented in section 6.1.2 and section 6.2.2 (Chapter 6), respectively. From the results obtained from the electron microscopic study of the bacteria, the mechanism of the antimicrobial activity of the copper against bacteria has been explained below.

7.3.1.1 Gram negative bacteria (*E. coli*)

E.coli is one of the major pathogens in the group of gram negative bacteria for major infections from the hospital touch surfaces (World Health Organization, 2011). The structure of the *E.coli* bacteria has been explained in the section 2.1.2.1 (Chapter 2). The schematic diagram of the cell wall structure of the typical gram negative bacteria is given in Figure 2.2 (a). From the electron microscopic study, it is proved that the copper treated cells are wrinkled and damaged as compared to the control (non-copper treated bacteria) cells. Moreover, the EDS results obtained with SEM and TEM studies shown in the Figure 6.2 and Figure 6.4 indicated the presence of the copper in the copper treated *E.coli* cell.

The wrinkling occurred due to the leakage of the body fluids to the extra cellular space. The outer membrane of the *E. coli* is made up of lipopolysaccharides, phospholipids and proteins (Bai et al. 2007). Lipopolysaccharide contains negatively charged groups which attracts Cu^+ and Cu^{2+} ions from the copper surfaces (Pal et al. 2007). These copper ions

steal the electrons from the cell wall and affect its integrity. The damage to the cell membrane by the copper is reported by Santo et al. (2011) and Ben-Sasson et al. (2013). When a bacterium comes in contact with the copper surface, a short circuiting of the current in the cell membrane could occur between the positively charged copper ions and the negatively charged cell wall. This weakens the membrane and creates holes (Rai and Duran 2011). Moreover, it disturbs the selective permeability of the plasma membrane. As a result, the efflux and influx of the cell gets imbalanced and loss of K^+ ions from the cytoplasm reduces its conductivity (Bai et al. 2007). Along with that, the copper controlling enzymes like CopA, CueO and CuS are also inactivated. Further, the proteins are inactivated due to the breakage of the Fe–S bonds in cytoplasmic hydratases, like, dihydroxy-acid dehydratase in the common branched chain pathway and isopropylmalate isomerase (IPMI) in the leucine-specific branch as reported by Macomber and Imlay (2009). The inherent affinity of the copper ions to the sulphur makes the rapid cell death and prolonged exposure of the cells results in permanent damage of the cell wall.

Another possibility reported is the formation of the reactive oxygen species (ROS) at the intracellular region due to the presence of the copper ions in the aqueous medium. This generates oxidative stresses in the bacteria followed by the DNA damage and finally failure (Shi et al. 2012). The above mentioned mechanisms are schematically shown in Figure 7.14. It is essential to note that the exact mechanism for the microbial damage by the copper is not fully understood. Our TEM micrographs indicate a reduction in the cell volume to 80 % of the initial volume as shown in Figure 6.4. This is possible only if the membrane is damaged and cell fluid flows out from the cell.

7.3.1.2 Gram positive bacteria (methicillin-resistant *Staphylococcus aureus*)

In order to understand the antimicrobial activity of the copper against the gram positive bacteria, *Staphylococcus aureus* (MRSA) is exposed with the copper coatings and electron microscopic studies were carried out as presented in section 6.2.2 (Chapter 6).

The structural details of the *MRSA* are given in section 2.1.2.1 (Chapter 2). Moreover, the schematic representation of the *MRSA* shown in Figure 2.2 indicates that the thick cell

wall of the peptidoglycon contains teichoic acid. The negatively charged teichoic acid attracts the positively charged copper ions (Lemire et al. 2013). Hence, the copper ions could be easily attracted to the cell wall. As a result, the copper ions steal the electrons from the cell wall and create pits in it. Such pits are observed in the SEM micrograph of copper exposed *MRSA,* as shown in Figure 6.6 (a). But the spherical shape of the cell structure is maintained even after the copper ions attack the cell wall. This is attributed to the increased thickness of the cell wall as compared to the cell wall of *E.coli* (Hong and Koo 2005). The rigidity of the cell wall is mainly attributed to the thick peptidoglycan. The spherical shape of the *MRSA* also contributes to the structural integrity of the cell wall after the copper attack. When compared to the rod shape of *E.coli*, spherical shaped *MRSA* helps to accommodate more pressure against the breakage of the cell wall. So in gram positive bacteria, the cell is not completely wrinkled and shrunken as in the case of the *E.coli.* But, the CFU study shows that *MRSA* has less resistance to the copper as compared to the *E.coli.* This is attributed to the absence of outer membrane and the presence of negatively charged teichoic acid molecule within the thick peptidoglycan layer (20 nm to 80 nm) on the surface of *MRSA* as reported by Li et al. (2015). It is reported that the rapid killing of the gram positive bacteria during copper treatment is not by the membrane damage, but due to the loss of the cell respiration (Antimicrobial Copper Cu+, 2015). The schematic representation of the different ways of the copper attack on the bacterial cell is shown in Figure 7.14.
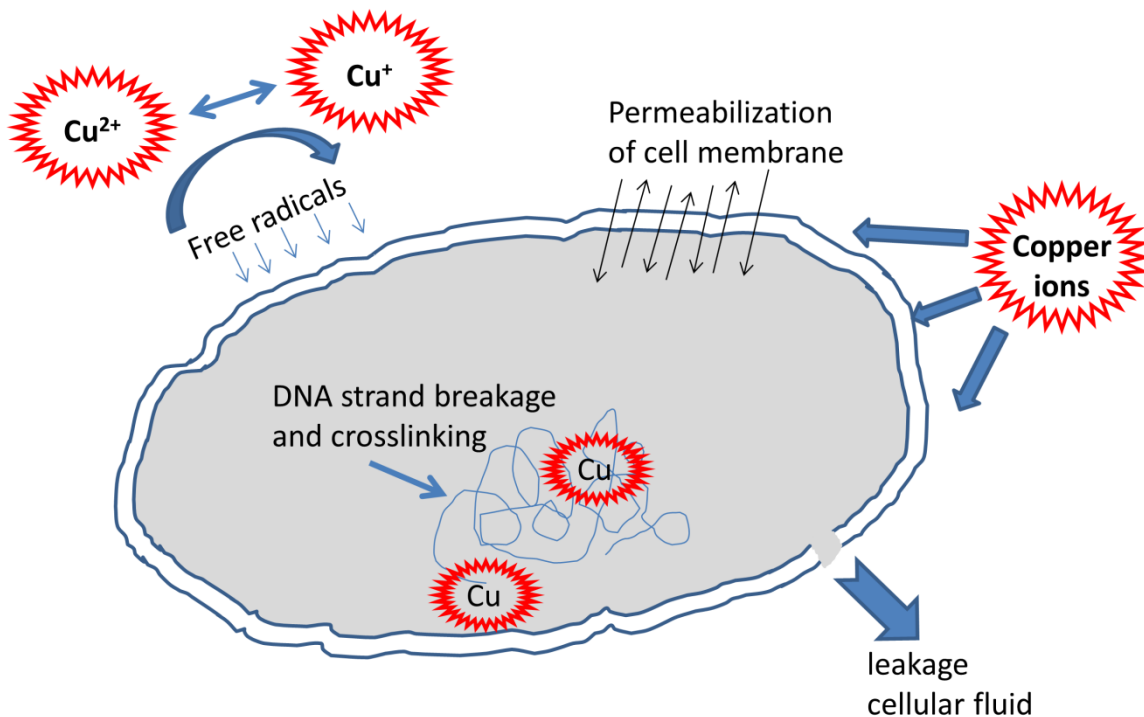
Figure 7.14 Schematic diagram showing different ways of the copper attack on the bacterial cell.

7.3.2 Reasons for increased antimicrobial activities of the copper coatings

The CFU study reveals that the copper coating either by electroplating or by DC magnetron sputter deposition exhibits better antimicrobial efficacy as compared to the bulk copper. The major reasons for the better antimicrobial activity of the copper coatings as compared to the bulk copper are (i) three dimensional (3D) contacts of the coatings with the microbe surface, (ii) (111) texture of the coating, (iii) nano-crystallites in the coatings and (iv) ultra-high purity of the coatings.

7.3.2.1 Three dimensional (3D) surface of the copper coating

According to the literature survey, it is well proved that the contact between the copper and cell wall of the bacteria is the primary reason for the antimicrobial activity of the

copper (Santo et al. 2011 and Warnes et al. 2012). Hence, uneven copper surface can offer better antimicrobial activity compared to the smooth copper surface. In the present case, copper coatings produced with higher current density have an uneven nodular morphology as shown in Figure 4.2 and Figure 4.21. Similarly, sputter deposited coatings also has nodular morphology as shown in Figure 5.2. Such uneven nodular morphology offers contacts with the microbes in three dimensions. This is schematically shown in Figure 7.15. Such 3D surface contacts are more predominant in the electrodeposited copper coating as compared to the DC sputter deposited one. In the case of the DC magnetron sputtering, the nodules are grown uniformly. The *E.coli* has a size of 3 μm length and 1 μm diameter. For *MRSA*, the diameter is 2 μm. In the case of electrodeposited coatings, the inter-nodular spacing is in the range of 5-7 μm. Hence, the electrodeposited coatings at higher coating current densities could offer efficient 3D contact with the copper surface. But in the case of bulk copper of surface roughness of 0.07 μm, bacteria are on the flat surface (ideally). As a result, the bacteria surface is in contact in only two dimensions. So the three dimensional surface of the coatings is attributed as one of the major reasons of the increased antimicrobial activity of the same as compared to the bulk copper.
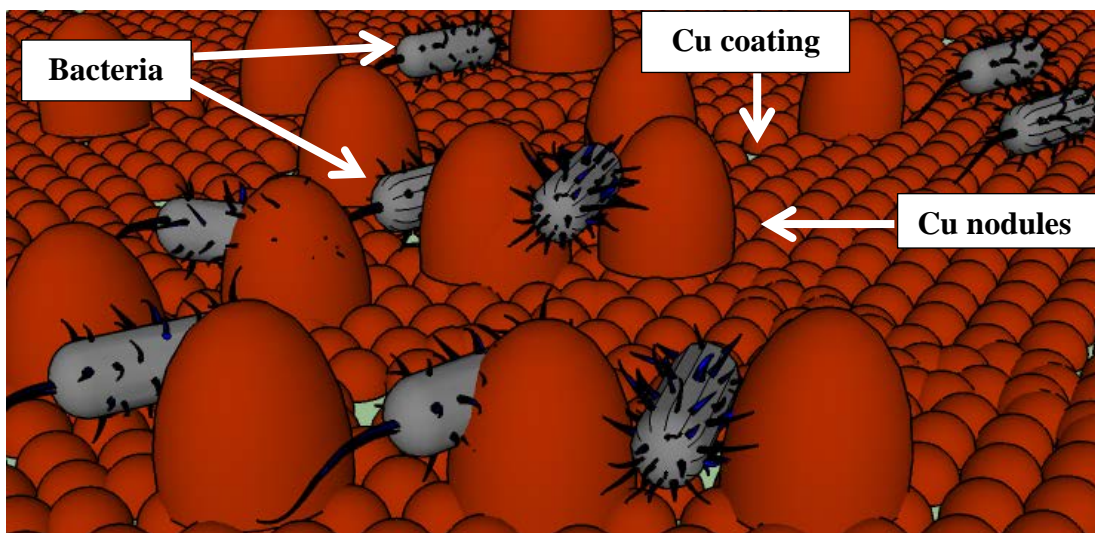
Figure 7.15 Schematic representation of 3D contact of the bacteria with the copper coating.

7.3.2.2 (111) texture of the copper coating

The XRD results of both the electrodeposited as well as the sputter deposited coatings exhibit (111) texture. In the case of copper, (111) plane is the close packed plane of highest density. The growth of (111) plane along [111] direction for the coating indicated that the exposed surface of the coating contains higher density of the copper atoms. But in the case of the bulk copper, such preferred texture was absent. So it is expected that more copper atoms are in surface contact with the microbes in the case of the textured copper coatings as compared to the bulk copper. As a result, the antimicrobial activity of the coatings enhanced than that of the bulk copper. Similar effect is reported in the case of (111) plane of the silver nano particles (Pal et al. 2007).

7.3.2.3 Nano-crystallites in the copper coatings

The nano-crystallanity of the copper coatings deposited by both sputtering as well as electrodeposition has been explained in detailed with the help of TEM micrographs (in sections 4.1.2.2, 4.2.2.2 and 5.2.2). They show that the electrodeposited copper coating has a minimum crystallite size of 32 nm (from Bath-I) and 12.9 nm (from Bath-II), and that of the sputter deposited coating is 18 nm. The crystallite size (grain size) of the bulk copper was in the range of 10 μm, as shown in Figure 2 (Appendix III). Because of the nano-crystallinity, the coating has more crystallite boundary volume. It is expected that crystallite boundary has more surface energy as compared to the inside of the crystallite. Moreover, microstrain is also experienced in the crystallites due to such large crystallite boundaries. The microstrain on the periphery of the fine crystallites increases the energy of the atoms near the boundary. These factors help to increase the surface energy of the coating as compared to that of the bulk copper. In the present antimicrobial testing method (CFU counting technique), aqueous culture was dropped on the coating as well as on the bulk copper. The spreading rate of the culture medium is faster on the coating due to their higher surface energy as compared to that of the bulk copper. The higher wettability of the surface helps to increase the contacts of the microbes with the copper

(Nie et al. 2010). As a result, the coating exhibits more antimicrobial activity as compared to bulk copper.

7.3.2.4 Ultra-high purity of the copper coatings

The antimicrobial activity of the copper is mainly due to the contact between the copper atom and the cell wall of the microbes (Santo et al. 2011 and Warnes et al. 2012). So the rapidity of the antimicrobial activity is proportional to the number of the copper atoms which are in contact with the microbial cell. In this context, the coated copper could offer better antimicrobial activity as compared to the bulk copper. This is attributed to the ultra-high purity of the coatings along with other properties of the coatings, such as, 3D surface, (111) texture and nano-crystallites. There is no other metallic ion co-deposited with the copper during electrodeposition. Similarly, during sputter deposition, ultra-high pure copper plate was used as the target. The EDS results of the coating also agreed to the same result. But the bulk copper which is used for antimicrobial test is commercially pure. This is another factor in the increased antimicrobial activity of the copper coated surface as compared to the bulk copper.

7.4 Summary of the Chapter

The microstructural, mechanical and antimicrobial properties of the copper coatings deposited by using electrodeposition and DC magnetron sputter deposition have been discussed in the current chapter.

The microstructural aspects are discussed based on the results obtained from SEM, TEM and XRD study of the coating. It includes morphology, crystallite size, nano-twins, microstrain and texture of the copper coatings. Since the microstructure depends on the process of deposition, a brief discussion on the process of electrodepostion as well as sputter deposition have been included in the section of the microstructural analysis. The electrodeposited and DC magnetron sputter deposited coatings contains nodules having nano sized crystallites. The size of the crystallites decreased with increase in the deposition rate. Moreover, the defects, like twins also observed in the nano crystallites

deposited with higher deposition rate. Because of the nano-crystallites, small amount of microstrain was observed in the XRD analysis of the coatings. The (111) texture of the coating along <111> direction is confirmed from the XRD analysis. The detailed discussion on the above characteristics of the coating has been included in the section 7.1.

The mechanical properties required for the antimicrobial touch surface like hardness and adhesion strength of the coating have been discussed in section 7.2. The coating hardness (scratch hardness and microhardness) values are increased with decrease in the crystallite size up to the Hall-Petch break down point. Along with the reduction in the crystallite size, the presence of the nano-twins and the (111) texture also promote the hardness of the coating. The adhesion strength of the coating was improved by the pre-treatment of the aluminium substrate, such as, double zincation process. The adhesion strength of the copper coatings on the double zincated aluminium has been evaluated qualitatively and quantitatively by using the cross-hatch cut test and the pull-off adhesion test, respectively. The coating of both electrodeposited and DC magnetron sputter deposited showed adequate adhesion strength to the double zincated aluminium substrate. Among the coatings, deposition by using Bath-II and by using DC magnetron sputtering method exhibits better adhesion strength as compared to electrodeposition using Bath-I.

The antimicrobial properties of the coating were tested against *E.coli* (gram negative bacteria) and *MRSA* (gram positive bacteria). One set of samples have been selected from each category of the coating (coating from Bath-I, Bath-II and DC magnetron sputtering) based on the characteristics, like, surface area, crystallite size, and hardness of the coatings. The obtained antimicrobial results were compared with the non-coated aluminium and the bulk copper available in the market. The copper coated aluminium samples have better biocidal efficacy as compared to the bulk copper due to the characteristics of the coatings like a) three dimensional surface, b) (111) texture, c) nano crystallites and d) ultra-high purity. The mechanisms of the attack of copper on the microbes were explained with the help of SEM, TEM and EDS results of copper treated and non-treated bacteria. The less resistance of *MRSA* against copper attack as compared

to the *E.coli* is observed during the six hours of exposure of copper coatings. This is attributed to the presence of teichoic acid and the absence of outer membrane in the cell wall of *MRSA*.

List of publications related to Chapter 7

1. Arun Augustin, Udaya Bhat.K, K. Rajendra Udupa, Chitharanjan Hegde (2015). "Electron Microscopic Study of Nodules formed during Electrodeposition of Copper on Aluminium". Materials Science Forum, Trans Tech Publications.

2. Arun Augustin, Udupa, K.R. and Bhat, K.U. (2016). "Effect of coating current density on the wettability of electrodeposited copper thin film on aluminium substrate", Perspectives in Science, Elsevier Publishing.

3. Arun Augustin, K. Rajendra Udupa, and Udaya Bhat (2016). "Crystallite size measurement and micro-strain analysis of electrodeposited copper thin film using Williamson-Hall method." Proceeding of International Conference on Condensed Matter and Applied Physics, AIP Publishing.

4. Arun Augustin, Huilgol, P., Udupa, K.R. and Bhat, U. (2016). "Effect of Current Density during Electrodeposition on Microstructure and Hardness of Textured Cu Coating in the Application of Antimicrobial Al Touch Surface." Journal of the Mechanical Behavior of Biomedical Materials, Elsevier Publishing.

5. Arun Augustin, K. Rajendra Udupa, Udaya Bhat K. (2015), "Effect of Pre-Zinc Coating on the Properties and Structure of DC Magnetron Sputtered Copper Thin Film on Aluminium" American Journal of Materials Science.

6 Augustin, A., Thaira, H., Bhat, K.U. and Udupa, K.R. (2016). Effect of Electrodeposited Cu Thin Film on the Morphology and Cell Death of *E. Coli*; an Electron Microscopic Study. Biotechnology and Biochemical Engineering, (Springer).

7. Udaya Bhat K, Arun Augustin, Suma Bhat and Udupa K. (2018) Preparation and characterization of copper thin films for antimicrobial applications *Microscopy Applied to Materials Sciences and Life Sciences,* Apple Academic Press.

CONCLUSIONS AND SCOPE FOR FURTHER

RESEARCH

The major conclusions derived from the results and discussion of the research work is given below:

1. Copper coating on the aluminium substrate was deposited successfully by electrodeposition and DC magnetron sputter deposition techniques. In electrodeposition technique, coating was carried out in the range of current density from 1 A dm^{-2} to 10 A dm^{-2} for bath-I and from 1 A dm^{-2} to 4 A dm^{-2} for bath-II. Similarly, for DC magnetron sputter deposition, coating was carried out in the range of sputtering power from 50 W to 150 W.

2. The surface morphology obtained from SEM micrographs revealed that electrodeposited and DC magnetron sputter deposited coating exhibits nodular morphology. The average size of the nodules in the coating from bath-I was 5.3 μm and that of bath-II was 2.6 μm. The uneven growth of the nodules presented at higher current density helped to offer a three dimensional surface contacts with microbes. In DC magnetron sputter deposited coating, the nodules' size was decreased from 0.48 μm to 0.2 μm with increase in the sputtering power.

3. The topographic as well as the cross sectional TEM micrographs of the electrodeposited and the sputter deposited coatings revealed that coating consists of nano sized crystallites. The crystallite size in the bath-I decreased from 63 nm to 32 nm with increase in the coating current density from 1 A dm^{-2} 10 A dm^{-2}. Similarly in bath-II, crystallite size decreased from 17.6 nm to 12.9 nm with increase in the coating current

density from 1 A dm^{-2} to 4 A dm^{-2}. In DC magnetron sputter deposition, crystallite size was decreased from 49 nm to 18 nm with increase in the sputtering power from 50 W to 150 W.

4. The preferred growth of the coating in (111) plane along <111> direction was confirmed from XRD studies. Moreover, the microstrain in the coating due to the nano sized crystallite structure was estimated by Williamson-Hall method. The results showed that microstrain increased with decrease in the crystallite size.

5. The scratch resistance of the coating was calculated in terms of scratch hardness. The values increased with decrease in the crystallite size and presence of the defects, like, twins of the coating. The maximum value of scratch hardness for the coating from the bath-I was 2.52 GPa and for the bath –II was 1.72 GPa. Similarly, for sputter deposited coating, the maximum value of the scratch hardness was 1.71 GPa.

6. The hardness of the coated samples was measured by using microhardness tester and the maximum value for the coating from the bath-I was 2.05 GPa and that for the bath –II was 1.46 GPa. Similarly, for sputter deposited coating, the maximum value of the scratch hardness was recorded as 1.49 GPa.

7. The increased hardness of the coating compared to the annealed copper is attributed to the nano-crystallinity, preferred texture and presence of the nano-twins in the coating.

8. The adhesion strength of the coating evaluated by using cross-hatch hardness and pull-off adhesion test shows adequate adhesion strength of the coating to the substrate. This is attributed to the double zincation process prior to the copper deposition.

9. The copper coatings exhibits good antimicrobial activities against *E.coli* (gram negative bacteria) and *MRSA* (gram positive bacteria) in the colony forming unit count test. The antimicrobial activity of coated sample was better than that of the commercial pure copper against *E.coli* and *MRSA*. This is attributed to the i) three dimensional

surface of the copper coatings, ii) (111) texture of the coating, iii) nano-crystallinity in the coatings and iv) ultra-high purity of the coatings.

10. The electron microscopic study showed that the gram negative bacteria (*E.coli*) which are exposed to the copper was found to be wrinkled and damaged as compared to the non-treated cell because the cell wall was broken and intracellular fluid was leaked out to the extracellular space. Whereas, in the case of gram positive bacteria (*MRSA*), small pits were developed on the copper treated cells as compared to the non-treated ones. However, the morphology of the cell was maintained due to the thick cell wall in the gram positive bacteria.

Scope for Further Research

The scope for further study of the current research work can be concluded as given below:

- The corrosion study of the coated sample at different environmental conditions can be explored.

- The heat treatment of the coated samples and its morphological change as well as alloy formation can be studied.

- The oxidation behavior of the coated samples can be evaluated.

- The surface treatment of the coated sample for improving the antimicrobial applications can be studied.

- The role of the coating parameters can be studied by modeling software.

This page is intentionally left blank

REFERENCES

Ai, J., Liu, S., Widharta, N.A., Adhikari, S., Anderegg, J.W. and Hebert, K.R. (2011). "Copper Layers Deposited on Aluminum by Galvanic Displacement." *The Journal of Physical Chemistry C*, *115* (45), 22354–22359.

Allegranzi, B., Nejad, S.B., Combescure, C., Graafmans, W., Attar, H., Donaldson, L. and Pittet, D. (2011). "Burden of endemic health-care-associated infection in developing countries: systematic review and meta-analysis." *The Lancet*, *377* (9761), 228–241.

Antimicrobial Copper Cu+ (2014). "Introduction to Antimicrobial Copper." http://www.antimicrobialcopper.org/uk/introduction-to-antimicrobial-copper (Oct. 5, 2016)

Antimicrobial Copper Cu+ (2015) "How does copper kill pathogens?" https://www.antimicrobialcopper.org/uk/faqs#t678n12637 (Oct. 15, 2016).
ASTM G171-03. Standard Test Method for Scratch Hardness of Materials Using a Diamond Stylus.

Augustin, A., Huilgol, P., Udupa, K.R. and Bhat, U. (2016a). "Effect of Current Density during Electrodeposition on Microstructure and Hardness of Textured Cu Coating in the Application of Antimicrobial Al Touch Surface." *Journal of the Mechanical Behavior of Biomedical Materials*, *63* 352–360.

Augustin, A., Thaira, H., Bhat, K.U. and Udupa, K.R. (2016c). Effect of Electrodeposited Copper Thin Film on the Morphology and Cell Death of E. Coli; an Electron Microscopic Study. In Biotechnology and Biochemical Engineering, (Springer), pp 227–232.

Augustin, A., Udupa, K.R. and Bhat, U. (2016b). Crystallite size measurement and micro-strain analysis of electrodeposited copper thin film using Williamson-Hall method. In International Conference on Condensed matter and Applied Physics (ICC 2015): Proceeding of International Conference on Condensed Matter and Applied Physics, (AIP Publishing), p 020492.

Bahl, S., Suwas, S. and Chatterjee, K. (2014). "The importance of crystallographic texture in the use of titanium as an orthopedic biomaterial." *RSC Advances*, *4* (72), 38078–38087.

Bai, W., Zhao, K. and Asami, K. (2007). "Effects of copper on dielectric properties of E. coli cells." *Colloids and Surfaces B: Biointerfaces*, *58* (2), 105–115.

Balaraju, J. and Rajam, K. (2005). "Electroless deposition of Ni–Cu–P, Ni–W–P and Ni–W–Cu–P alloys." *Surface and Coatings Technology*, *195* (2), 154–161.

Beegan, D., Chowdhury, S. and Laugier, M. (2007). "Comparison between nanoindentation and scratch test hardness (scratch hardness) values of copper thin films on oxidised silicon substrates." *Surface and Coatings Technology*, *201* (12), 5804–5808.

Bharucha, N. and Janjua, M. (1973). "Method of plating copper on aluminum (Google Patents).

Biju, V., Sugathan, N., Vrinda, V. and Salini, S.L. (2008). "Estimation of lattice strain in nanocrystalline silver from X-ray diffraction line broadening." *J Mater Sci*, *43* (4), 1175–1179.

Borkow, G. and Gabbay, J. (2005). "Copper as a biocidal tool." *Curr. Med. Chem.*, *12* (18), 2163–2175.

Bull, S. and Berasetegui, E. (2006). "An overview of the potential of quantitative coating adhesion measurement by scratch testing." *Tribology International*, *39* (2), 99–114.

Cabiscol, E., Tamarit, J. and Ros, J. (2010). "Oxidative stress in bacteria and protein damage by reactive oxygen species." *International Microbiology*, *3* (1), 3–8.

Carlton, C.E. and Ferreira, P.J. (2007). "What is behind the inverse Hall–Petch effect in nanocrystalline materials?" *Acta Materialia*, *55* (11), 3749–3756.

Chan, K.-Y. and Teo, B.-S. (2006). "Atomic force microscopy (AFM) and X-ray diffraction (XRD) investigations of copper thin films prepared by dc magnetron sputtering technique." *Microelectronics Journal*, *37* (10), 1064–1071.

Chen, K.-C., Wu, W.-W., Liao, C.-N., Chen, L.-J. and Tu, K. (2008). "Observation of atomic diffusion at twin-modified grain boundaries in copper." *Science*, *321* (5892), 1066–1069.

De Almeida, M., Carlos, I., Barbosa, L., Carlos, R., Lima-Neto, B. and Pallone, E. (2002). "Voltammetric and morphological characterization of copper electrodeposition from non-cyanide electrolyte." *Journal of Applied Electrochemistry*, *32* (7), 763–773.

Delgado, Á.V., González-Caballero, F., Hunter, R., Koopal, L. and Lyklema, J. (2007). "Measurement and interpretation of electrokinetic phenomena." *Journal of Colloid and Interface Science*, *309* (2), 194–224.

Delley, B., Ellis, D., Freeman, A., Baerends, E. and Post, D. (1983). "Binding energy and electronic structure of small copper particles." Physical Review B, 27 (4), 2132.

Dieter, G.E. and Bacon, D.J. (1986). "Mechanical metallurgy (McGraw-Hill New York). Dini, J.W. and Snyder, D.D. (2011). "Electrodeposition of copper." *Modern Electroplating, Fifth Edition*, 33–78.

Ebrahimi, F. and Ahmed, Z. (2003). "The effect of current density on properties of electrodeposited nanocrystalline nickel." *Journal of Applied Electrochemistry*, *33* (8), 733–739.

European Copper Institute (2012). " Mechanical properties of copper." http://www.copperalliance.eu/about-copper/properties/mechanical-properties (Nov. 08, 2015).

Finnis, M. (1996). "The theory of metal-ceramic interfaces." *Journal of Physics: Condensed Matter*, *8* (32), 5811.

Gonczy, S.T. and Randall, N. (2005). "An ASTM standard for quantitative scratch adhesion testing of thin, hard ceramic coatings." *International Journal of Applied Ceramic Technology*, *2* (5), 422–428.

Government of Netherlands (2010) " Ban on Selling Ammonium Nitrate Fertilizers Containing More Than 16 % of Nitrogen to the Private Sector." https://www.government.nl/latest/news/2010/06/25/ban-on-selling-ammonium-nitrate-fertilizers-containing-more-than-16-of-nitrogen-to-the-private-sector (Sep. 01, 2016).

Grass, G., Rensing, C. and Solioz, M. (2011). "Metallic copper as an antimicrobial surface." *Applied and Environmental Microbiology*, *77* (5), 1541–1547.

Grobe, C., Schleuder, G., Schmole, C. and Nies, D.H. (2014). "Survival of Escherichia coli cells on solid copper surfaces is increased by glutathione." *Applied and Environmental Microbiology*, *80* (22), 7071–7078.

Grujicic, D. and Pesic, B. (2002). "Electrodeposition of copper: the nucleation mechanisms." *Electrochimica Acta*, *47* (18), 2901–2912.

Guazzone, F., Payzant, E.A., Speakman, S.A. and Ma, Y.H. (2006). "Microstrains and Stresses Analysis in Electroless Deposited Thin Pd Films." *Ind. Eng. Chem. Res.*, *45* (24), 8145–8153.

Hamid, Z.A. and Aal, A.A. (2009). "New environmentally friendly noncyanide alkaline electrolyte for copper electroplating." *Surface and Coatings Technology*, *203* (10–11), 1360–1365.

Hansen, N. (2004). "Hall–Petch relation and boundary strengthening." *Scripta Materialia*, *51* (8), 801–806.

Hong, I. and Koo, C.H. (2005). "Antibacterial properties, corrosion resistance and mechanical properties of Cu-modified SUS 304 stainless steel." *Materials Science and Engineering: A*, *393* (1), 213–222.

Huslage, K., Rutala, W.A. and Weber, D.J. (2010). "A quantitative approach to defining 'high-touch' surfaces in hospitals." *Infection Control and Hospital Epidemiology*, *31* (8), 850–853.

Inweregbu, K., Dave, J. and Pittard, A. (2005). "Nosocomial infections." *Continuing Education in Anaesthesia, Critical Care & Pain*, *5* (1), 14–17.

Isa, N.N.C., Mohd, Y., Zaki, M.H.M. and Mohamad, S.A.S. (2017). "Characterization of Copper Coating Electrodeposited on Stainless Steel Substrate." *International Journal of Electrochemical Science*, *12* (7), 6010–6021.

Iwase, T., Uehara, Y., Shinji, H., Tajima, A., Seo, H., Takada, K., Agata, T. and Mizunoe, Y. (2010). "Staphylococcus epidermidis Esp inhibits Staphylococcus aureus biofilm formation and nasal colonization." *Nature*, *465* (7296), 346–349.

Jain, V.V. (2007). Microstructure and properties of copper thin films on silicon substrates. Texas A&M University.

JIS, Z. (2000). "2801: 2000." *Antimicrobial products—Test for Antimicrobial Activity and Efficacy*,.

Kang, S.-W., Yun, J.-Y. and Rhee, S.-W. (2002). "Microstructure of copper films deposited on TiN substrate by metallorganic chemical vapor deposition." *Journal of The Electrochemical Society*, *149* (1), C33–C36.

Kanungo, M., Mishra, K. and Das, S. (2003). "Study on morphology of copper deposited onto aluminium by immersion plating from an oxalate bath containing perchloric acid." *Minerals Engineering*, *16* (12), 1383–1386.

Keevil, C. (2003). "Rapid detection of biofilms and adherent pathogens using scanning confocal laser microscopy and episcopic differential interference contrast microscopy." *Water Science & Technology*, *47* (5), 105–116.

Le, M.-T., Sohn, Y.-U., Lim, J.-W. and Choi, G.-S. (2010). "Effect of sputtering power on the nucleation and growth of Cu films deposited by magnetron sputtering." *Materials Transactions*, *51* (1), 116–120.

Lemire, J.A., Harrison, J.J. and Turner, R.J. (2013). "Antimicrobial activity of metals: mechanisms, molecular targets and applications." *Nature Reviews Microbiology*, *11* (6), 371–384.

Li, H., Chen, Q., Zhao, J. and Urmila, K. (2015). "Enhancing the antimicrobial activity of natural extraction using the synthetic ultrasmall metal nanoparticles." *Scientific Reports*, *5*.

Love, A.E.H. (1944). "A treatise on the mathematical theory of elasticity (New York: Dover Publications).

Lu, L., Chen, X., Huang, X., Lu, K., Lu, L., Chen, X., Huang, X. and Lu, K. (2009). "Revealing the Maximum Strength in Nanotwinned Copper." *Science*, *323* (5914), 607–610.

Lu, L., Schwaiger, R., Shan, Z.W., Dao, M., Lu, K. and Suresh, S. (2005). "Nano-sized twins induce high rate sensitivity of flow stress in pure copper." *Acta Materialia*, *53* (7), 2169–2179.

Lu, L., Shen, Y., Chen, X., Qian, L. and Lu, K. (2004). "Ultrahigh Strength and High Electrical Conductivity in Copper." *Science*, *304* (5669), 422–426.

Lu, L., Sui, M. and Lu, K. (2000). "Superplastic extensibility of nanocrystalline copper at room temperature." *Science*, *287* (5457), 1463–1466.

Lunder, O., Olsen, B. and Nisancioglu, K. (2002). "Pre-treatment of AA6060 aluminium alloy for adhesive bonding." *International Journal of Adhesion and Adhesives*, *22* (2), 143–150.

Macomber, L. and Imlay, J.A. (2009). "The iron-sulfur clusters of dehydratases are primary intracellular targets of copper toxicity." *Proceedings of the National Academy of Sciences*, *106* (20), 8344–8349.

Marais, F., Mehtar, S. and Chalkley, L. (2010). "Antimicrobial efficacy of copper touch surfaces in reducing environmental bioburden in a South African community healthcare facility." *J. Hosp. Infect.*, *74* (1), 80–82.

Mattox, D. (1998). Handbook of physical vapor deposition processing-film formation, adhesion, surface preparation and contamination control." *Noyes publications*, New Jersey, USA, Film Growth, 496-498.

Meriç, C., Atik, E. and Engez, T. (1997). "Application of the Hall-Petch Relation to Microhardness Measurement on AA 1030, Cu, CuSn7, CuZn30 and 6114 Alloys." *Mathematical and Computational Applications*, *2* (2), 71–77.

Molteni, C., Abicht, H.K. and Solioz, M. (2010). "Killing of bacteria by copper surfaces involves dissolved copper." *Applied and Environmental Microbiology*, *76* (12), 4099–4101.

Monteiro, F., Barbosa, M., Ross, D. and Gabe, D. (1991). "Pretreatments of improve the adhesion of electrodeposits on aluminium." *Surface and Interface Analysis*, *17* (7), 519–528.

Mote, V., Purushotham, Y. and Dole, B. (2012). "Williamson-Hall analysis in estimation of lattice strain in nanometer-sized ZnO particles." *Journal of Theoretical and Applied Physics*, *6* (1), 1–8.

Murakami, K., Hino, M., Hiramatsu, M., Osamura, K. and Kanadani, T. (2006). "Effect of zincate treatment on adhesion of electroless nickel-phosphorus coating for commercial pure aluminum." *Materials Transactions*, *47* (10), 2518–2523.

Musil, J. (1998). "Low-pressure magnetron sputtering." *Vacuum*, *50* (3), 363–372.

Natter, H. and Hempelmann, R. (1996). "Nanocrystalline Copper by Pulsed Electrodeposition: The Effects of Organic Additives, Bath Temperature, and pH." *J. Phys. Chem.*, *100* (50), 19525–19532.

Navinšek, B., Panjan, P. and Milošev, I. (1999). "PVD coatings as an environmentally clean alternative to electroplating and electroless processes." *Surface and Coatings Technology*, *116* 476–487.

Nguyen, T., Charneski, L.J. and Evans, D.R. (1997). "Temperature dependence of the morphology of copper sputter deposited on TiN coated substrates." *Journal of the Electrochemical Society*, *144* (10), 3634–3639.

Nie, Y., Kalapos, C., Nie, X., Murphy, M., Hussein, R. and Zhang, J. (2010). "Superhydrophilicity and antibacterial property of a Cu-dotted oxide coating surface." *Annals of Clinical Microbiology and Antimicrobials*, *9* (1), 1.

Ohring, M. (2001). "Materials science of thin films (Academic press), 174-175.

Okamoto, N., Takahashi, S., Saito, T. and Kondo, K. (2009). "Formation factor of nodule by copper electrodeposition." *ECS Transactions*, *16* (22), 49–57.

Ondok, V., Musil, J., Meissner, M., Čerstvỳ, R. and Fajfrlik, K. (2010). "Two-functional DC sputtered Cu-containing TiO 2 thin films." *Journal of Photochemistry and Photobiology A: Chemistry*, *209* (2), 158–162.

Organization, W.H. and others (2011). "Report on the burden of endemic health care-associated infection worldwide".

Ouis, A. and Cailler, M. (2013). "Effects of substrate bias voltage on adhesion of DC magnetron-sputtered copper films on E24 carbon steel: investigations by Auger electron spectroscopy." *Journal of Adhesion Science and Technology*, *27* (21), 2367–2386.

Pal, S., Tak, Y.K. and Song, J.M. (2007). "Does the antibacterial activity of silver nanoparticles depend on the shape of the nanoparticle? A study of the gram-negative bacterium Escherichia coli." *Applied and Environmental Microbiology*, *73* (6), 1712–1720.

Parthasaradhy, N. (1989). "Practical Electroplating HandbookPrentice Hall.

Paunovic, M. and Schlesinger, M. (2006). "Fundamentals of electrochemical deposition (john wiley & sons).

Perreault, F., De Faria, A.F., Nejati, S. and Elimelech, M. (2015). "Antimicrobial properties of graphene oxide nanosheets: why size matters." *ACS Nano*, *9* (7), 7226–7236.

Pradhan, D. and Reddy, R. (2009). "Electrochemical production of Ti–Al alloys using TiCl 4–AlCl 3–1-butyl-3-methyl imidazolium chloride (BMImCl) electrolytes." *Electrochimica Acta*, *54* (6), 1874–1880.

Prater, J. and Moss, R. (1983). "Effect of the coating structure on the adherence of sputter-deposited oxide coatings." *Thin Solid Films*, *107* (4), 455–462.

Qian, L., Li, M., Zhou, Z., Yang, H. and Shi, X. (2005). "Comparison of nano-indentation hardness to microhardness." *Surface and Coatings Technology*, *195* (2), 264–271.

Qin, W. and Szpunar, J.A. (2005). "Origin of lattice strain in nanocrystalline materials." *Philosophical Magazine Letters*, *85* (12), 649–656.

Rashidi, A. and Amadeh, A. (2008). "The effect of current density on the grain size of electrodeposited nanocrystalline nickel coatings." *Surface and Coatings Technology*, *202* (16), 3772–3776.

Ray, A. (2015). "Electrodeposition of Thin Films for Low-cost Solar Cells.".

Reed, D. and Kemmerly, S.A. (2009). "Infection control and prevention: a review of hospital-acquired infections and the economic implications." *The Ochsner Journal*, *9* (1), 27–31.

Rosenberg, Y., Machavariani, V.S., Voronel, A., Garber, S., Rubshtein, A., Frenkel, A.I. and Stern, E.A. (2000). "Strain energy density in the x-ray powder diffraction from mixed crystals and alloys." *J. Phys.: Condens. Matter*, *12* (37), 8081–8088.

Roy, K., Hilliard, G.M., Hamilton, D.J., Luo, J., Ostmann, M.M. and Fleckenstein, J.M. (2009). "Enterotoxigenic Escherichia coli EtpA mediates adhesion between flagella and host cells." *Nature*, *457* (7229), 594–598.

Russia Today. (2016). " Turkey bans sale of ammonium nitrate fertilizers after terror attack spike." https://www.rt.com/news/346044-turkey-terror-fertilizers-ban (Oct. 01, 2016).

Sallee, N., Cromer, M. and Vittori, O. (1994). "Electroplating of Copper on Aluminium with Direct and Pulsed Currents." *Canadian Metallurgical Quarterly*, *33* (2), 155–162.

Sanders, P.G., Eastman, J.A. and Weertman, J.R. (1997). "Elastic and tensile behavior of nanocrystalline copper and palladium." *Acta Materialia*, *45* (10), 4019–4025.

Santo, C.E., Lam, E.W., Elowsky, C.G., Quaranta, D., Domaille, D.W., Chang, C.J. and Grass, G. (2011). "Bacterial killing by dry metallic copper surfaces." *Applied and Environmental Microbiology*, *77* (3), 794–802.

Schiøtz, J., Di Tolla, F.D. and Jacobsen, K.W. (1998). "Softening of nanocrystalline metals at very small grain sizes." *Nature*, *391* (6667), 561–563.

Schmidt, M.G., Attaway, H.H., Sharpe, P.A., John, J., Sepkowitz, K.A., Morgan, A., Fairey, S.E., Singh, S., Steed, L.L., Cantey, J.R. and others (2012). "Sustained reduction of microbial burden on common hospital surfaces through introduction of copper." *Journal of Clinical Microbiology*, *50* (7), 2217–2223.

Schuh, C., Nieh, T. and Yamasaki, T. (2002). "Hall–Petch breakdown manifested in abrasive wear resistance of nanocrystalline nickel." *Scripta Materialia*, *46* (10), 735–740.

Schwechheimer, C. and Kuehn, M.J. (2015). "Outer-membrane vesicles from Gram-negative bacteria: biogenesis and functions." *Nature Reviews Microbiology*, *13* (10), 605–619.

Sharma, A. (2011). "Govt bans open sale of ammonium nitrate." Indiatoday, http://indiatoday.intoday.in/story/government-bans-sale-of-ammonium-nitrate/1/146320.html%20Hand%20wash (Sept. 01, 2016).

Simões, S., Calinas, R., Vieira, M.T., Vieira, M.F. and Ferreira, P.J. (2010). "In situ TEM study of grain growth in nanocrystalline copper thin films." *Nanotechnology*, *21* (14), 145701.

Singh, J. and Wolfe, D. (2005). "Review Nano and macro-structured component fabrication by electron beam-physical vapor deposition (EB-PVD)." *Journal of Materials Science*, *40* (1), 1–26.

Singla, G., Singh, K. and Pandey, O.P. (2013). "Williamson–Hall study on synthesized nanocrystalline tungsten carbide (WC)." *Appl. Phys. A*, *113* (1), 237–242.

Sriraman, K., Raman, S.G.S. and Seshadri, S. (2006). "Synthesis and evaluation of hardness and sliding wear resistance of electrodeposited nanocrystalline Ni–W alloys." *Materials Science and Engineering: A*, *418* (1), 303–311.

Sunada, K., Minoshima, M. and Hashimoto, K. (2012). "Highly efficient antiviral and antibacterial activities of solid-state cuprous compounds." *Journal of Hazardous Materials*, *235* 265–270.

Tay, S.L., Wei, X., Chen, W., Yao, C. and Gao, W. (2014). "Microstructures and Properties of Electrodeposited Cu-Bi Composite Coatings." *Int. J. Electrochem. Sci*, *9* 2266–2277.

Thornton, J.A. (1977). "High rate thick film growth." *Annual Review of Materials Science*, *7* (1), 239–260.

Vasilev, K., Sah, V., Anselme, K., Ndi, C., Mateescu, M., Dollmann, B., Martinek, P., Ploux, L. and Griesser, H.J. (2009). "Tunable antibacterial coatings that support mammalian cell growth." *Nano Letters*, *10* (1), 202–207.

Venables, J. (1964). "The electron microscopy of deformation twinning." *Journal of Physics and Chemistry of Solids*, *25* (7), 685IN1691–690IN6692.

Vencl, A., Arostegui, S., Favaro, G., Zivic, F., Mrdak, M., Mitrović, S. and Popovic, V. (2011). "Evaluation of adhesion/cohesion bond strength of the thick plasma spray coatings by scratch testing on coatings cross-sections." *Tribology International*, *44* (11), 1281–1288.

Warnes, S., Caves, V. and Keevil, C. (2012). "Mechanism of copper surface toxicity in Escherichia coli O157: H7 and Salmonella involves immediate membrane depolarization followed by slower rate of DNA destruction which differs from that observed for Gram-positive bacteria." *Environmental Microbiology*, *14* (7), 1730–1743.

Weaver, L., Michels, H. and Keevil, C. (2010). "Potential for preventing spread of fungi in air-conditioning systems constructed using copper instead of aluminium." *Letters in Applied Microbiology*, *50* (1), 18–23.

Weber, D.J., Rutala, W.A., Miller, M.B., Huslage, K. and Sickbert-Bennett, E. (2010). "Role of hospital surfaces in the transmission of emerging health care-associated pathogens: norovirus, Clostridium difficile, and Acinetobacter species." *American Journal of Infection Control*, *38* (5), S25–S33.

Willigan, R.R., Chen, L. and Jaworowski, M.R. (2014). "Bimetallic zincating processing for enhanced adhesion of aluminum on aluminum alloys.

World Health Organization, and others (2011). "Report on the burden of endemic health care-associated infection worldwide".

Xu, F.F. and Imlay, J.A. (2012). "Silver (I), mercury (II), cadmium (II), and zinc (II) target exposed enzymic iron-sulfur clusters when they toxify Escherichia coli." *Applied and Environmental Microbiology*, *78* (10), 3614–3621.

Xue, X., Kozaczek, K., Kurtz, D. and Kurtz, S. (2000). "Estimating residual stress tensor in aluminum and copper thin films and interconnects." *Advances in X-Ray Analysis*, *42* 612.

Yousuf, B., Ahire, J.J. and Dicks, L.M. (2016). "Understanding the antimicrobial activity behind thin-and thick-rolled copper plates." *Applied Microbiology and Biotechnology*, 1–12.

Yueh, M.-F., Taniguchi, K., Chen, S., Evans, R.M., Hammock, B.D., Karin, M. and Tukey, R.H. (2014). "The commonly used antimicrobial additive triclosan is a liver tumor promoter." *Proceedings of the National Academy of Sciences*, *111* (48), 17200–17205.

Zak, A.K., Majid, W.A., Abrishami, M.E. and Yousefi, R. (2011). "X-ray analysis of ZnO nanoparticles by Williamson–Hall and size–strain plot methods." *Solid State Sciences*, *13* (1), 251–256.

Zeiger, M., Solioz, M., Edongué, H., Arzt, E. and Schneider, A.S. (2014). "Surface structure influences contact killing of bacteria by copper." *Microbiologyopen*, *3* (3), 327–332.

Zhang, X., Misra, A., Wang, H., Nastasi, M., Embury, J.D., Mitchell, T.E., Hoagland, R.G. and Hirth, J.P. (2004b). "Nanoscale-twinning-induced strengthening in austenitic stainless steel thin films." *Applied Physics Letters*, *84* (7), 1096–1098.

Zhang, X., Misra, A., Wang, H., Shen, T.D., Nastasi, M., Mitchell, T.E., Hirth, J.P., Hoagland, R.G. and Embury, J.D. (2004a). "Enhanced hardening in Cu/330 stainless steel multilayers by nanoscale twinning." *Acta Materialia*, *52* (4), 995–1002.

Zhang, Z., Wang, J., Zhang, B., Liu, H., Song, W., He, J., Lv, D., Wang, S. and Xu, X. (2013). "Activity of antibacterial protein from maggots against Staphylococcus aureus in vitro and in vivo." *International Journal of Molecular Medicine*, *31* (5), 1159–1165.

Zhou, X.W. and Wadley, H.N.G. (1999). "Twin formation during the atomic deposition of copper." *Acta Materialia*, *47* (3), 1063–1078.

Appendix-I
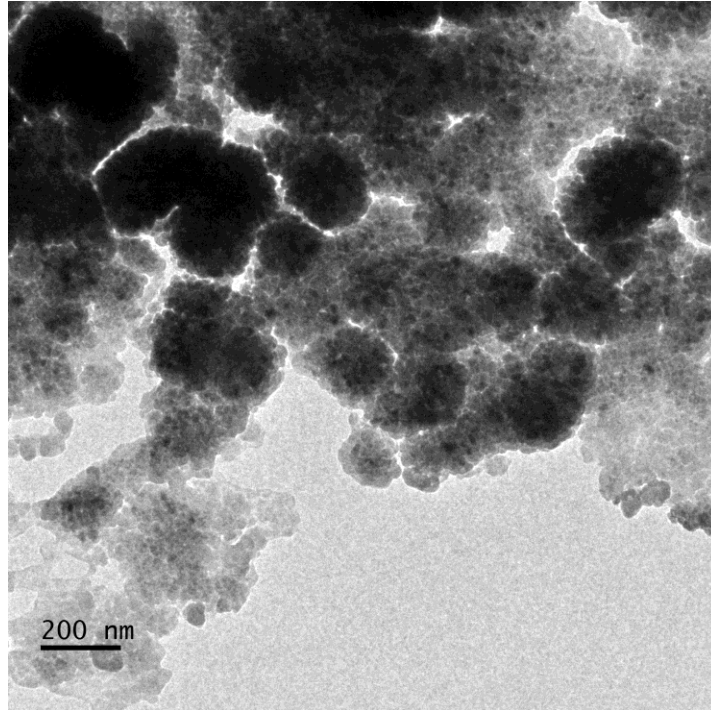
Figure 1 Low magnified TEM micrograph of DC magnetron spurred coating at 50 W sputtering power.
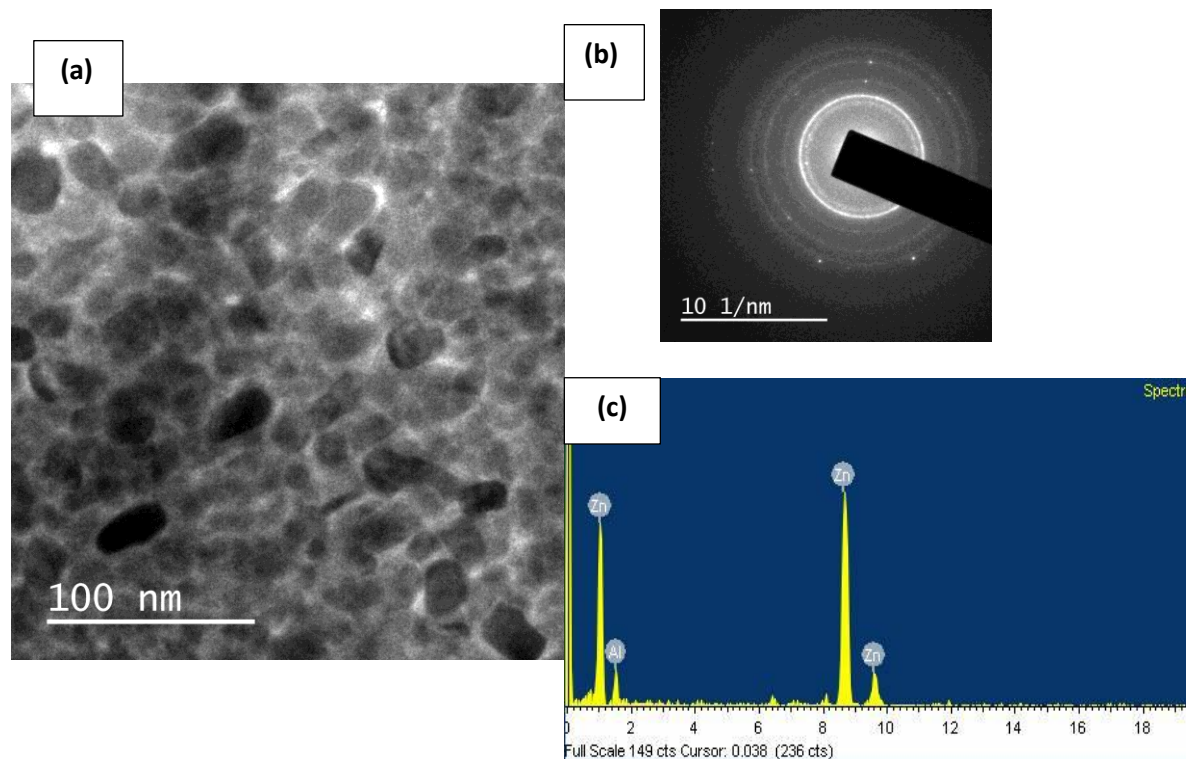
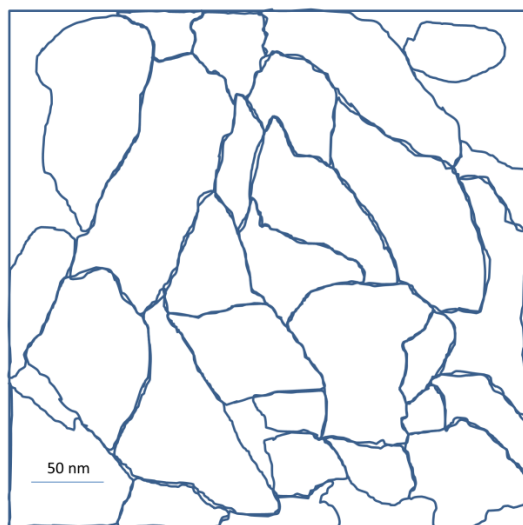**Figure 2** a) TEM micrograph of double zincated aluminium, b) SAED pattern of the Figure 2 (a) and c) EDS corresponding to Figure 2 (a), respectively.

Figure 3 Visual image corresponding to the TEM micrograph shown in Figure 4.7.

Appendix-II

Heterogeneous nucleation

Assume copper film forming atoms in the vapour phase impinge on the substrate creating nuclei of dimension 'r'. The free energy change during the formation of film can be expressed as

$$\Delta G = a_3 r^3 \Delta G + a_1 r^2 \gamma_{fv} + a_2 r^2 \gamma_{fv} + a_2 r^2 \gamma_{fs} - a_2 r^2 \gamma_{sv} \tag{1}$$

Where ΔG is the chemical free energy change per unit volume.

γ is the interfacial tension, are identified by the subscripts f, s, v representing film, substrate, and vapour, respectively. For the spherical cap-shaped solid nucleus shown in Figure 1, the curved surface area ($a_1 r^2$), the projected circular area on the substrate ($a_2 r^2$), and the volume ($a_3 r^3$) are involved, and the corresponding geometric constants are

$$a_1 = 2\pi(1 - \cos\theta), \quad a_2 = \pi \sin^2\theta \quad \text{and} \quad a_3 = \frac{\pi}{3}(2 - 3\cos\theta + \cos^3\theta)$$

From the Young's equation $\gamma_{sv} = \gamma_{fs} + \gamma_{fv} \cos\theta$ $\tag{2}$
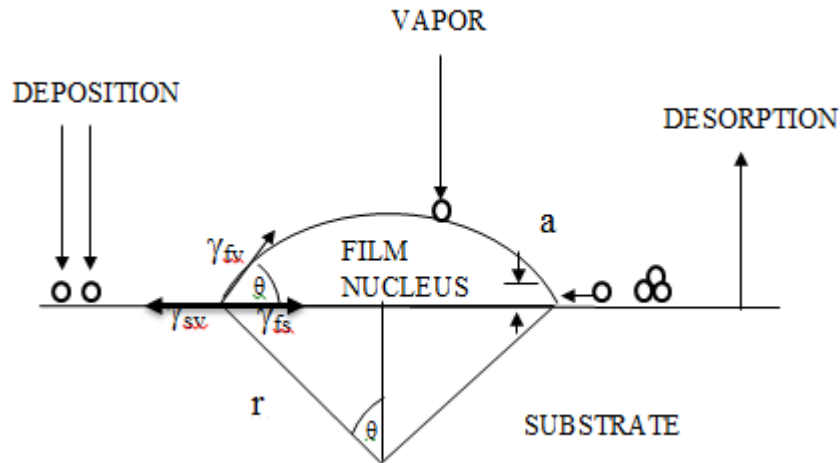
Figure 1 Schematic representation of the nucleation process on the substrate surface.

From the equation (1), it is inferred that if new interface appears, there is an increase in surface free energy and hence the positive sign for the first two surface terms. Similarly the loss of the circular substrate-vapour interface under the cap implies a reduction in system energy and a negative contribution to ΔG. The thermodynamic equilibrium is achieved when $\frac{d\Delta G}{dr} = 0$, which occurs at a critical nucleus size $r = r^*$

Hence $r^* = \frac{-2(a_1\gamma_{fv} - a_2\gamma_{fs} - a_2\gamma_{sv})}{3a_3\Delta G_v}$ (3)

Appendix-III

Figure 1 Schematic representation of perfect nucleus of disc shape having radius 'r' and height 'h'.
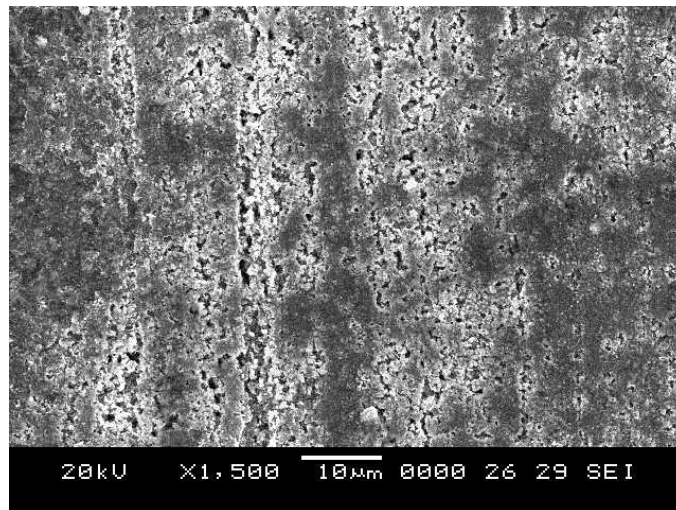
Figure 2. SEM micrograph of double zincated aluminium.
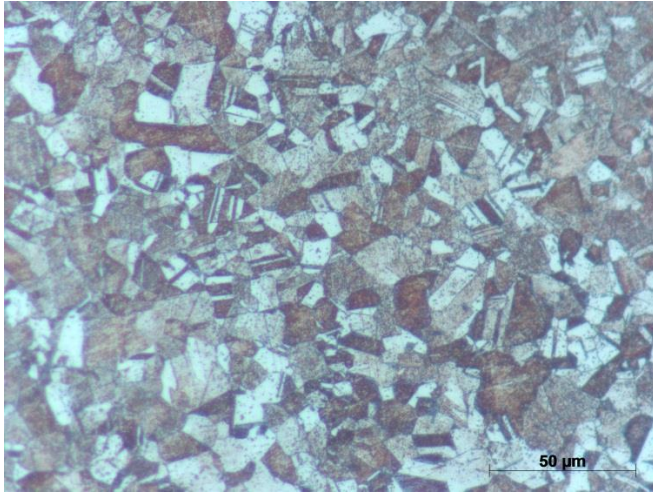
Figure 3 Optical microscopic image of bulk copper.

List of Publications based on PhD Research Work

[to be filled-in by the Research Scholar and to be enclosed with Synopsis Submission Form]

Sl. No.	Title of the paper/book chapter	Authors (in the same order as in the paper. Underline the Research Scholar's name)	Name of the Journal/book Conference/ Symposium, Vol., No., Pages	Month & Year of Publication	Category *
1	Effect of Current Density during Electrodeposition on Microstructure and Hardness of Textured Cu Coating in the Application of Antimicrobial Al Touch Surface	Arun Augustin, Huilgol, P., Udupa, K.R. and Bhat, U.	*Journal of the mechanical behavior of biomedical materials*, Volume 63, Pages 352-360.	Oct, 2016	1
2	Electron Microscopic Study of Nodules formed during Electrodeposition of Copper on Aluminium	Arun Augustin, Udaya Bhat.K, K. Rajendra Udupa, Chitharanjan Hegde	*Materials Science Forum*, Volume. 830, pages 371-374.	Sept, 2015	1
3	Effect of coating current density on the wettability of electrodeposited copper thin film on aluminium substrate	Arun Augustin, Udupa, K.R. and Bhat, K.U	*Perspectives in Science.* Volume 8 Pages 472-474.	Sept, 2016	1
4	Effect of Pre-Zinc Coating on the Properties and Structure of DC Magnetron Sputtered Copper Thin Film on Aluminium	Arun Augustin, K. Rajendra Udupa, Udaya Bhat K.	*American Journal of Materials Science*, volume. 5(3C), pages 58-61	December, 2015	1

5	Crystallite size measurement and micro-strain analysis of electrodeposited copper thin film using Williamson-Hall method	<u>Arun Augustin</u>, K. Rajendra Udupa, and Udaya Bhat	*Proceeding of International Conference on Condensed Matter and Applied Physics,* Volume. 1728, page-20492.	May, 2016	3
6	Effect of Electrodeposited Copper Thin Film on the Morphology and Cell Death of *E. coli*; an Electron Microscopic Study	<u>Arun Augustin,</u> Harsha Thaira, Udaya Bhat K and K Rajendra Udupa	*Biotechnology and Biochemical Engineering*, Springer, Page 227-232.	Sept, 2016	5, Book Chapter
7	Preparation and characterization of copper thin films for antimicrobial applications	Udaya Bhat K, <u>Arun Augustin,</u> Suma Bhat and Udupa K.	*Microscopy Applied to Materials Sciences and Life Sciences,* CRC Press, Page 91-131	April, 2018	5, Book Chapter
8	Characterization of DC Magnetron Sputtered Copper Thin Film on Aluminium Touch Surface	Arun Augustin, Udupa, K.R. and Bhat, U	*Transactions of the Indian Institute of Metals,* Springer Publications	Under Review	1

* Category: 1. Journal paper, full paper reviewed   2. Journal paper, Abstract reviewed
         3. Conference/Symposium paper, full paper reviewed   4. Conference/Symposium paper, abstract reviewed
         5. Others (including papers in Workshops, NITK Research Bulletins, Short notes etc.)
           (If the paper has been accepted for publication but yet to be published, the supporting documents must be attached.)

Research Scholar
Name & Signature, with Date

                                     Research Guides
                                     Name & Signature, with Date

BIO-DATA

Name   : ARUN AUGUSTIN

Date of Birth   : 13-05-1986

Permanent address   : Ayyankanal House

                                     Kamballur PO

                                     Cherupuzha, Kasargod Dt

                                      Kerala-670511

E-mail   : arunmalabar@yahoo.com

                                      arunmecce@gmail.com

Contact number   : +91-8921171940

                                     +91-9740641930

Academic Qualification

Bachelor of Technology (B.Tech): Mechanical Engineering, Department of Mechanical Engineering, Kannur University, Batch: 2003-2007.

Master of Technology (M.Tech.): Production Technology, Department of Mechanical Engineering, Basaveshwar Engineering College (Autonomous), Bagalkot, Visvesvaraya Technological University Belagavi, Karnataka, Batch: 2009-2011.

P.G. Diploma: Welding Engineering, Annamalai University, Tamilnadu.

Work Experience

Industrial Experience: 1 year in Simplex Infrastructure Ltd. Gujarat

Teaching Experience: 3.5 Years (LBS Engg. College Kasargod, Vimal Jyothi Engg. College Kannur and Christ College of Engg., Irinjalakuda, Kerala)